Innovation and Discovery in Russian Science and Engineering

Balgaisha Mukanova
Igor Modin

The Boundary Element Method in Geophysical Survey

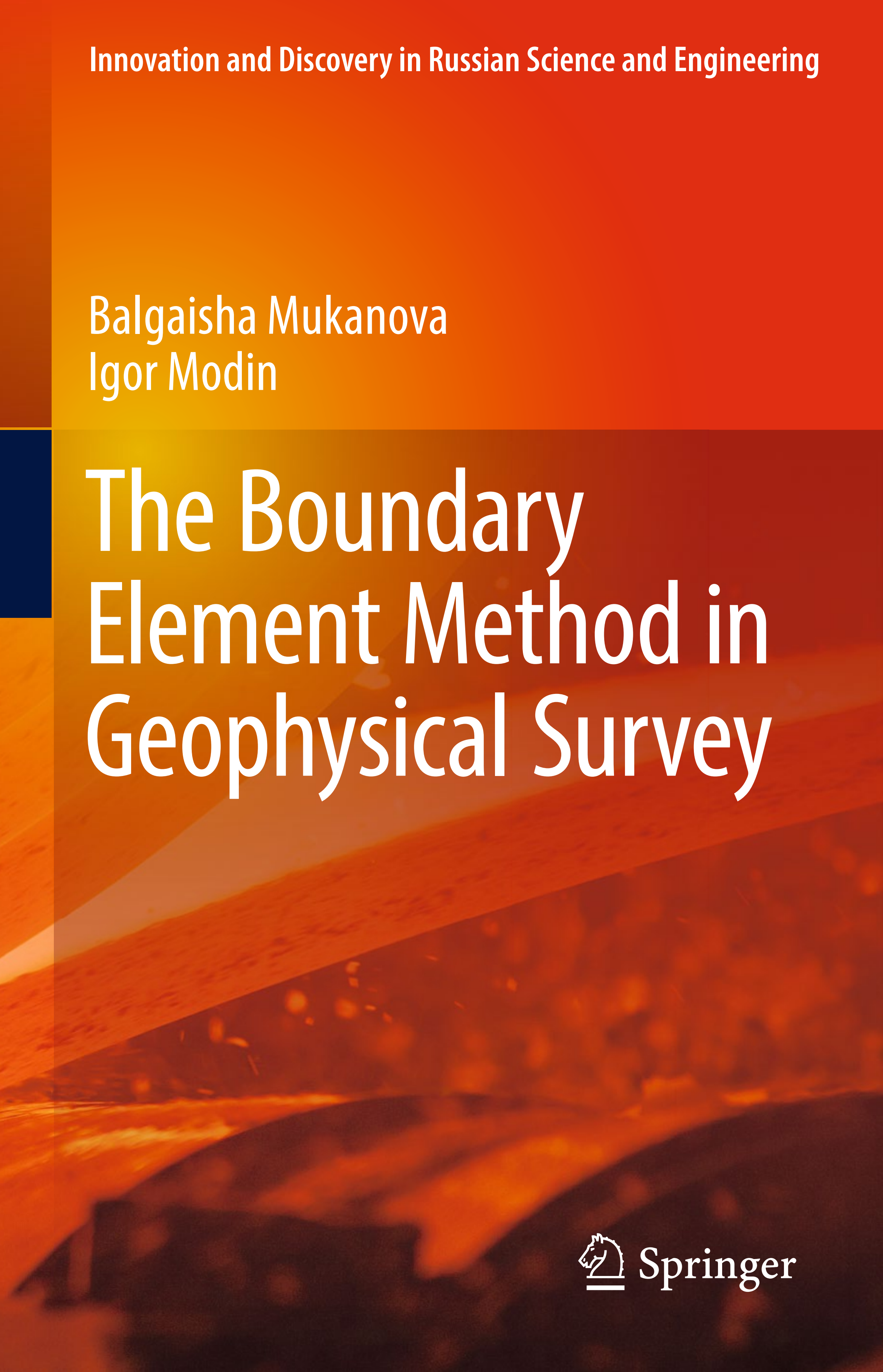

Springer

Innovation and Discovery in Russian Science and Engineering

More information about this series at http://www.springer.com/series/15790

Balgaisha Mukanova • Igor Modin

The Boundary Element Method in Geophysical Survey

Springer

Balgaisha Mukanova
L.N. Gumilyov Eurasian
National University
Astana, Kazakhstan

Igor Modin
Lomonosov Moscow State University
Moscow, Russia

ISSN 2520-8047 ISSN 2520-8055 (electronic)
Innovation and Discovery in Russian Science and Engineering
ISBN 978-3-319-72907-7 ISBN 978-3-319-72908-4 (eBook)
https://doi.org/10.1007/978-3-319-72908-4

Library of Congress Control Number: 2017962697

© Springer International Publishing AG 2018
This work is subject to copyright. All rights are reserved by the Publisher, whether the whole or part of the material is concerned, specifically the rights of translation, reprinting, reuse of illustrations, recitation, broadcasting, reproduction on microfilms or in any other physical way, and transmission or information storage and retrieval, electronic adaptation, computer software, or by similar or dissimilar methodology now known or hereafter developed.
The use of general descriptive names, registered names, trademarks, service marks, etc. in this publication does not imply, even in the absence of a specific statement, that such names are exempt from the relevant protective laws and regulations and therefore free for general use.
The publisher, the authors and the editors are safe to assume that the advice and information in this book are believed to be true and accurate at the date of publication. Neither the publisher nor the authors or the editors give a warranty, express or implied, with respect to the material contained herein or for any errors or omissions that may have been made. The publisher remains neutral with regard to jurisdictional claims in published maps and institutional affiliations.

Printed on acid-free paper

This Springer imprint is published by Springer Nature
The registered company is Springer International Publishing AG
The registered company address is: Gewerbestrasse 11, 6330 Cham, Switzerland

Preface

This monograph focuses on the applications of the integral equations method (IEM), particularly with regard to the form of the boundary element method (BEM), for modeling the electrical resistivity tomography (ERT) method in geophysics. This book is written by two authors with different scientific backgrounds: Igor Modin is a geophysicist, and Balgaisha Mukanova conducts research on computational mathematics and inverse problems. This monograph reflects the theoretical and practical research of the authors over the past decade and the results of their collaboration since 2013.

We consider the applications of the IEM and BEM to the study of geological media using direct current (DC). Both the IEM and the BEM allow for the solution of direct sounding problems using the resistivity method for a medium model with a piecewise-constant electrical conductivity distribution. Such a conductivity distribution simulates many practically important distributions of electrical properties. At the same time, currently available interpretation programs provide a smooth distribution of the electrical properties of a medium. As a rule, geophysicists replace these smooth distributions with a piecewise-constant conductivity distribution during the geological interpretation. In this situation, the solution of the direct problem with a piecewise-constant conductivity function provides an important auxiliary tool for refining the interpretation results. In addition, an essential part of the design of an electrical survey is a simulation to determine the capabilities of the method for solving geological tasks of varying complexities.

In contrast to finite difference methods (FDMs) and finite element methods (FEMs), the BEM has a number of advantages, including higher accuracy, more economical approach, and lack of artificial boundary conditions at the boundaries of the computational domain. The main advantage of the BEM is that the solution of the problem in the whole domain is reduced to a problem stated for the boundaries only. This fact significantly decreases the computational cost and simultaneously increases the accuracy of the calculations associated with the application.

Compared with the use of FEMs to solve partial differential equations (PDEs), the use of the BEM to solve integral equations can be restricted to the simplest finite elements of the first or zero order. The reason for this is that there is no need to find the derivatives and formulate the problem in a weak sense, as is common when solving PDEs through an FEM. Then, we do not consider any theoretical aspects of finite element theory. Additional information on the contemporary use of the BEM is available on the Internet. Corresponding references and links can be found, for instance, in http://www.boundary-element-method.com/.

This monograph is organized as follows. Chapter 1 presents a review of the literature and a brief introduction to resistivity sounding methods and ERT. For the convenience of the reader, the main material in Chap. 2 is preceded by a preliminary section from a course in mathematical physics. Chapter 2 also describes some of the mathematical facts and theorems that we refer to thereafter.

Chapter 3 describes equipment, recommendations for field measurements, and mathematical models. This chapter can be used independently as an introduction to geophysical and mathematical methods for the resistivity surveying of subsurface media. This chapter contains the mathematical models commonly used for electromagnetic surveys, the analytical solutions for layered media, and an introduction to the IEM. The material concludes with a discussion of resistivity filter coefficients that are computed and used in practice. The statements of direct and inverse problems are formulated in Sects. 3.3, 3.4 and 3.6, and the methods used to solve inverse problems are outlined.

Chapters 4 and 5 present the applications of the IEM and BEM for solving different types of direct problems. In Chap. 4, the theorems and mathematical expressions for the methods are formulated, as they are required to have a strong mathematical basis for the numerical simulations. However, those sections can be omitted by specialists in the field of geophysics. The BEM and adaptive mesh generation algorithms for forward DC sounding problems in 2D and 3D media with a piecewise-constant resistivity distribution are also presented. The integral equations for various 2D media models, namely, media with piecewise-linear contact boundaries, media with immersed local inhomogeneities, and media with buried relief, are derived and solved numerically. In the abovementioned models, the earth's surface is assumed to be flat.

Chapter 5 focuses on the new results obtained by authors during application of the BEM to the modeling of ERT data above a medium with ground surface relief. For 2D and 3D conductivity distributions, the influence of the relief on the interpretation results is shown. Each solution of the direct problem is compared using appropriate interpretation results based on different inversion programs. The possible inaccuracies and errors that can arise during the interpretation processes associated with the relief are discussed. Finally, some numerical data obtained for different model parameters are presented.

We would like to use this opportunity to thank our colleagues and students in the Geology faculty at Moscow State University and in the Information Technologies faculty at the Eurasian National University. A former PhD student, T. Mirgalikyzy, helped provide some numerical tests and plot the results in an admissible form. Our current PhD student, K. Baranchuk, provided her results of physical modeling for a comparison with our numerical simulations, and A. Skobelev ran some simulations using the interpretation programs Res2Inv and Zond2Dres. Another former student, M. Tussupova, adapted our programs for parallel computing technology. We are also grateful to D. Azimova for help with the editing of pictures.

The work on this book has been partially supported by a grant from a Ministry of the Republic of Kazakhstan entitled “Luchshiy prepodavatel' vuza - 2016”.

The authors are also grateful for the support of the project team working on the Innovation and Discovery in Russian Science and Engineering series of books, especially Prof. Carlos Brebbia.

Astana, Kazakhstan Balgaisha Mukanova
Moscow, Russia Igor Modin

Contents

List of Accepted Abbreviations and Symbols

BEM – Boundary element method
CIP – Coefficient inverse problem
ERT – Electrical resistivity tomography
IEM – Integral equations method
ODE – Ordinary differential equation
PDE – Partial differential equation
SLAE – System of linear algebraic equations
VES – Vertical electrical sounding
VP – Vertical profiling

We primarily use Cartesian coordinates and denote points by (x_1, x_2, x_3) or (x, y, z).

$\boldsymbol{R}^n$ is a Euclidean space of dimension n.

Vectors are denoted with a straight, bold font. Individual points at $\boldsymbol{R}^3$ are also written in capital letters such as A, B, M, N, P, and Q.

The position $\mathbf{x}$ or $\mathbf{r}$ of the point in the three-dimensional space $\boldsymbol{R}^3$ is defined in terms of the radius vector, and the notation depends on the context and convenience of use. r denotes the modulus of the vector $\mathbf{r}$.

The terms $d\Gamma_P$ or $d\Gamma_M$ under integrals denote the elements of the surface Γ, where the coordinates of the points P or M are the integrating variables.

$\mathbf{n_M}$ or $\mathbf{n_P}$ denote the unit vectors normal to a surface computed at the points M and P, respectively.

$\mathbf{l}_x$, $\mathbf{l}_y$, and $\mathbf{l}_z$ denote the unit vectors of the Cartesian coordinate system (x, y, z).

MP is a vector directed from the point M toward the point P.

$|MP|$ is a module of the vector directed from point M to point P, or vice versa.

$G(M,P)$ is the potential created at the point P from a point source located at the point M of the medium (the Green's function); in the case of a homogeneous medium, $G(M,P) = -1/(4\pi|MP|)$.

The notation σ with various indices is used for the specific conductivities of the media, and $\rho = 1/\sigma$ is the electrical resistivity of the medium.

Δ denotes Laplace's operator.

$L_2(\Gamma)$ is a linear space of real-valued measurable functions defined on the set $\Gamma \subset \boldsymbol{R}^n$, where the following integral $\|f(M)\|_2 \equiv \int\limits_{\Gamma} |f(M)|^2 d\Gamma$ exists.

$C(\Gamma)$ is a linear space of real-valued continuous functions defined on the set $\Gamma \subset \boldsymbol{R}^2$, where the following inequality holds:

$\|f(M)\|_C \equiv \sup\limits_{\Gamma} (|f(M)|) < \infty,\ M \in \Gamma.$

$C^2(\Gamma)$ is a linear space of real-valued, twice continuously differentiable functions defined on the set $\Gamma \subset R^2$, where the following estimation holds:

$\|f(M)\|_{C^2} \equiv \sup\left(\|f\|_C \|f_x\|_C, \|f_y\|_C, \|f_{xx}\|_C, \|f_{xy}\|_C, \|f_{yy}\|_C\right) < \infty.$

Chapter 1
Introduction

The method of electrical prospecting has been developing for approximately 100 years. The method was first introduced during successful field experiments conducted by the Schlumberger brothers following the first mathematical attempts to solve the interpretation problem (Langer 1933; Slihter 1933; Stefanescu and Shlumberger 1930; Stevenson 1934). Electrical prospecting represents an industrial method used to create and observe an electric field in order to retrieve information on the structure of a geological section. This method is being utilized by vast numbers of scientists and engineers for engineering geology, hydrogeology, ecology, and geotechnical and archaeological problems to search for ancient settlements, defense constructions, kurgans, and burial grounds. Ore geophysicists use this method to prospect for deposits of polymetallic substances in addition to copper, gold, and lead ores (Yerohin 2012; Yerokhin et al. 2011). Resistivity methods are extensively used to survey the upper sections of geological media because they provide greater surveying depths than other electrical sounding techniques and because the mathematical methods for interpreting the results are more developed.

Electrical resistivity tomography (ERT) includes numerous aspects: special measurement methods (i.e., for gathering field data) based on the principle of electrical sounding; digital equipment for automatically injecting direct current into the medium and recording the signals acquired by measuring electrodes; and special programs to visualize, process, interpret, and ultimately image the obtained data in the form of a geoelectric cross-section. The maturity of the electrical tomography method is progressing as a result of improvements in the equipment and automation of the measurement process.

Various publications influenced the origin of the electric tomography method, including those by Edwards (1977), Barker (1981, 1992), Griffits and Turnbill (1985), Zohdy (1989), Dahlin (1993, 1996), Loke and Barker (1996), and Bobachyev et al. (1995, 1996, 2006).

Two special features of ERT are its two-dimensional (2D) inversion performance and a high density of observations (Dahlin 1993, 1996, 2001; Dahlin and Zhou

B. Mukanova, I. Modin, *The Boundary Element Method in Geophysical Survey*,
Innovation and Discovery in Russian Science and Engineering,
https://doi.org/10.1007/978-3-319-72908-4_1

2004; Dahlin et al. 2007; Loke 2000; Loke and Barker 1996; Loke and Dahlin 1997). The main peculiarity of the 2D inversion process that makes it attractive for thousands of geophysics around the world is its ability to draw geological sections, which can be used immediately to indicate geological content.

The automation of measurement acquisition allows the accumulation of large amounts of data that must be numerically processed. As a consequence, the roles of mathematical models and algorithms for data interpretation problems are increasing.

Geophysical problems are divided into direct and inverse problems according to their mathematical classification. Direct problems indicate that it is necessary to determine the observed electric field and apparent resistivity for a given set of geometric and electrical properties of the medium.

Inverse problems require the distribution of the specific electrical conductivity to be recovered from the observed data. However, measured data are available only at the surface of the medium and within boreholes. These problems are currently being addressed through various inversion programs. In other words, interpretation programs are necessary for solving inverse problems. Mathematically, inverse geophysical problems belong to the class of coefficient inverse problems (CIP), which are severely ill-posed. This means that the exact solution of such an inverse problem either does not exist or is non-unique; thus, the results are unstable with respect to the input data. In practice, the ill-posedness of an inverse problem is expressed in terms of equivalence principles, based upon which the inversion results for similar pseudosections can be substantially different. In other words, geophysical inverse problems do not satisfy the stability condition with respect to the measured data. The choice of an appropriate solution depends on the experience of the interpreter and additional information. Mathematical modeling represents an auxiliary tool for refining the results of such inversion scenarios.

Currently, several methods can be used to solve direct geophysical problems, including the radio-technical analysis method (i.e., the transmission surface method; Madden 1971); the integral equations method (IEM) (Alpine 1947; Hohmann 1975; Khmelevskii and Shevnin 1988; Modin et al. 1988; Bobachyev 2002); the finite difference method (FDM) (Mufti 1976; Dey and Morrison 1979); the finite element method (FEM) (Coggon 1971); and the boundary elements method (BEM) (Xu et al. 1998; Xu 2001). The most influential research in this field includes the work of several authors (Inman et al. 1973; Lehrnann 1995; LaBrecque et al. 1996; Ellis and Oldenburg 1994; Lesur et al. 1999; Maurer et al. 1998; Menke 1984; Loke and Dahlin 1997). In addition, a few analytical solutions for direct problems exist and are commonly used for software testing purposes (Skalskaya 1948; Veshev 1959; Koefoed 1979; Tarkhov 1980).

FDMs and FEMs are useful for a variety of practical aims, but they have several particular disadvantages: (1) The methods have a low computational accuracy for the first derivatives of potential fields and for the computational results of the apparent resistivity in a coarse mesh, requiring high computational costs to refine the mesh. (2) Problems occur during construction of the grid, which must be adapted to the structure of the complicated computational domain. (3) Problems exist along the artificial boundary conditions at the boundaries of the computational domain. There are also problems associated with singularities, that is, difficulties in describing the field near the heterogeneous surface. These problems are related to the source function and description of the field near the corner points of the relief boundaries; namely, the field goes to infinity near the bottom of convex upward forms of the surface, but goes to zero near the top of convex downward surficial features. These disadvantages are even more important when sharp boundaries and sharp corners are apparent within the model, because even small smoothness changes significantly change the apparent resistivity field (Yerokhin et al. 2011; Yerohin 2012). Meanwhile, geophysics problems require high accuracy and fast field computations. The IEM and BEM satisfy both of these requirements and thus constitute alternative methods for solving direct problems (Alpine 1947; Bobachyev 2002; Bobachyev et al. 2006; Mirgalikyzy et al. 2015; Mukanova et al. 2017; Orunkhanov et al. 2004a, b, 2005; Orunkhanov and Mukanova 2006); this is the main topic of the present monograph.

Multiple complicated algorithms are utilized in the background of an inversion program needed to solve either direct or inverse problems. However, as the ERT method is relatively new and constantly developing, the associated 2D inversion algorithms can be improved.

Currently available interpretation programs are based on the successive solutions of a sequence of direct problems that are used to find a solution that most closely fits the measured data, for example, Res2DInv (Loke 2000) and ZondRes2D (A. E. Kaminskiy; last updated on 4 October 2013). These programs are expected to solve an inverse problem automatically within the framework of a 2D inversion of the electric field without human intervention, which includes the entering of additional, prior information. Because of the influence of the principle of equivalence, a formal approximation of an experimental or theoretically calculated field leads to an increase in the contrast within the considered section, which changes the geometry of the acquired cross-section. In most 2D inversion programs, the solution of the inverse problem is performed with a minimal contrast of the electric properties of the medium. As a result, the solution appears smooth with blurred boundaries, which do not usually exist in a real geological section. Therefore, 2D inversion schemes are not ideal for interpreting a real geological section from electric field data. Most authors call such a transformation a “controlled transformation.” Most authors in American publications refer to the ERT method as “electrical imaging” or “resistivity imaging” (Barker 1992; Dahlin and Zhou 2004), which suggests a distant likeness between real sections and inversion sections.

Furthermore, as a rule, geophysicists replace these smooth distributions with a piecewise-constant conductivity distribution during the geological interpretation. In this situation, the solution of the direct problem with a piecewise-constant conductivity function provides an important auxiliary tool for refining the interpretation results. From this perspective, the BEM seems to be the most appropriate method for solving direct piecewise-constant conductivity problems.

It is well known that the observed distribution of an electric field in a medium depends on numerous factors, including the geometry of the relative positions of the source and the measuring electrodes, the distribution of the specific electric resistivity, $\rho(x, y, z)$, and the relief of the earth's surface. The last factor complicates the discovery and allocation of $\rho(x, y, z)$ via measurements of the electric field at the earth's surface.

Most 2D inversion programs use the topography of the earth's surface to solve the inverse problem as a part of the solution for the direct problem. The effects of heterogeneities in the section and the relief produce a complicated image of the resulting geoelectric pseudo-section. As long as the field of the evoked potentials (i.e., the induced polarization) depends on the enclosed geoelectric section, the determination of the geometry of an anomalously polarized object and its properties is the final result of a geophysical survey. Check drilling, which is conducted to confirm the results of geophysical surveying, is very expensive, and the absence of downhole ore objects forecasted by a geophysicist can have very negative consequences. Without special mathematical modeling of the systematization of sectional distortions caused by the influences of relief during a 2D or 3D inversion, it is impossible to achieve a final geoelectric section that is equivalent to the true geological section.

In practice, few results are associated with a dependence on the anomalies caused by relief polarization. Some of these results were obtained from physical models (Veshev 1959, 1980). Bobachyev (2003) estimated the influence of the relief using a 1D approach for a homogeneous external field. In other publications (Chanturishvili 1959; Veshev 1959), the relief anomalies were calculated for specific relief models, such as half-spherical recesses and valleys.

Various studies have been performed to examine the influence of surface relief on resistivity sounding data (Bobachyev 2002; Chanturishvili 1959, 1983; Fox et al. 1980; Mirgalikyzy et al. 2015; Mukanova et al. 2017; Holcombe and Jiracek 1984; Veshev 1980).

FEMs and FDMs are the most commonly used numerical methods for solving direct and inverse problems (Coggon 1971; Demirci et al. 2012; LaBrecque et al. 1996; Loke 2000). Several approaches exist that consider the topography (Demirci et al. 2012; Erdogan et al. 2008; Fox et al. 1980; Tsourlos et al. 1999; Gunther et al. 2006; Gunther and Rucker 2013; Penz et al. 2013). The influence of the 2D topography was also considered using "full-air" and "half-air" approximations (Demirci et al. 2012; Erdogan et al. 2008). Such approaches are based on the use of rectangular and triangular finite elements near the surface–air boundary. An "FE distorted-mesh" approach was presented by Holcombe and Jiracek (1984) and Loke (2000) that was based on modification of the grid in the vicinity of the boundary.

Previous studies (Mirgalikyzy et al. 2015; Mukanova et al. 2017; Orunkhanov and Mukanova 2006; Orunkhanov et al. 2004a, b, 2005) showed that the formulation of a mathematical model using an IEM can provide an efficient and accurate solution for direct vertical electrical sounding (VES) problems. The IEM method is based on the theory of fundamental solutions. The field is represented in the form of simple layer potentials distributed along the inner and outer boundaries. In some cases, the IEM can be reduced to the BEM.

The presence of relief complicates the formulation of BEM problems relative to cases when the surface is flat, because a reflection method can be used for plain earth–air boundaries, thereby resulting in a relatively simple type of integral equation or system of integral equations. When a surface with relief separates the sounding medium from complicated internal boundaries, the corresponding mathematical model should be constructed as a system of integral equations. Until recently, there were no examples of numerical solutions for such problems using the IEM, even in the case of a system with at least two integral equations. This problem was first addressed using mathematical modeling through the BEM by the authors of this monograph (Mukanova et al. 2017).

During the first steps of our approach, we consider the case when the earth–air contact is flat with an assumed local inclusion or buried relief within the structure of the sounding medium (Orunkhanov and Mukanova 2006). The discretization pattern of the transition boundaries significantly influences the quality of the field computations. This introduces an auxiliary problem associated with the development of algorithms to construct a grid that can adapt to the geometries of the transition surfaces and the array of measuring electrodes.

While performing the system of integral equations, it is also necessary to develop a sustainable numerical method to solve it. The system of integral equations in its discrete form represents a system of linear algebraic equations (SLAE) with a dense matrix. The size of such a matrix depends on the geometry of the medium and is proportional to the square of the number of mesh points along the inner and outer boundaries. The corresponding size may be large, and the resulting matrix may require several gigabytes of computational short-term memory. The inversion of large, dense matrixes is computationally time consuming, which is why we must increase the computational performance through parallel computing technologies. Based on our experience with solving an SLAE containing dense matrixes, the most efficient increase in the computational performance is available through a parallel system with shared memory, whereas a cluster system is relatively ineffective because of the time required for communication among nodes.

As mentioned above, the method of potentials is the main technique used for field modeling in this monograph. The contact boundaries and heterogeneous inclusions within the geoelectric section act as secondary sources of the electric field. The corresponding problem is reduced to a system of integral equations considering the densities of the secondary sources and induction along the contact surfaces of conductive media and along the surface of the medium. Peculiarly, most of the resulting integral equations are defined in an infinite domain with singularities in their kernels. The kernel function in the integral operator belongs neither to the space $C(\boldsymbol{R}^2)$ nor the space $L_2(\boldsymbol{R}^2)$. This makes the direct application of classical Fredholm's theory impossible. In Chaps. 4 and 5, we prove some mathematical theorems to verify the solvability of the obtained equations.

Let us recall that the advantages of the BEM include a decrease in the dimension of the problem from 3D to 2D and the presence of a unified (i.e., one-for-all) approach for the complicated configuration of the transition boundaries. However, there are currently no systematic, numerical computational models for ERT based on the BEM for nonhomogeneous media with relief along the outer boundary. In this book, we fill this gap to some extent by presenting numerical analyses for media characterized by piecewise-constant conductivity and ground surface relief.

References

L.M. Alpine, Istochniki polya v teorii electricheskoirazvedki. Prikladnaya Geophizika **3**, 56–200 (1947)

R.D. Barker, The offset system of electrical resistivity sounding and its use with a multicore cable. Geophys. Prospect. **29**(1), 128–143 (1981)

R.D. Barker, A simple algorithm for electrical imaging of the subsurface. First Break **10**(2), 53–62 (1992)

A.A. Bobachyev, *Resheniye pryamykh i obratnykh zadach elektrorazvedki metodom soprotivleniy dlya slozhno-postroyennykh sred,* Dissertation, Moscow, MSU, 95 p, 2003

A.A. Bobachyev, Programmnoye obespecheniye dlya odnomernoy interpretatsii krivykh VEZ, VEZ-VP i MTZ, in *Voprosy teorii i praktiki geologichekoy geologicheskoy interpretatsii gravitatsionnykh, magnitnykh i elektricheskikh poley, Part 1: Proceedings of the 29th session of the International Seminar*, 28 Jan–2 Feb 2002 (UGGA, Yekaterinburg, 2002)

A.A. Bobachyev, M.N. Marchenko, I.N. Modin, E.V. Pervago, A.V. Urusova, V.A. Shevnin, Novye podkhody k elektricheskim zondirovaniyam gorizontal'no-neodnorodnykh sred. Physika Zemli **12**, 79–90 (1995)

A.A. Bobachyev, I.N. Modin, E.V. Pervago, V.A. Shevnin, Mnogoelektrodnyye elektricheskiye zondirovaniya v usloviyakh gorizontal'no-neodnorodnykh sred (Review), in *Razvedochnaya geofizika*, vol. 2 (JCS 'Geoinformmark', Moscow, 1996)

A.A. Bobachyev, A.A. Gorbunov, I.N. Modin, V.A. Shevnin, Elektrotomografiya metodom soprotivleniy i vyzvannoy polyarizatsii. Pribory i systemy razvedochnoi geophisiki **2**, 14–17 (2006)

L.S. Chanturishvili, *Electro Investigation for the Design of Roads in Rough Terrain* (Avtotransizdat, Moscow, 1959)

L.S. Chanturishvili, *Spetsial'nyye Zadachi Elektrorazvedki Pri Proyektirovanii Dorog* (Transport, Moscow, 1983)

J.H. Coggon, Electromagnetic and electrical modeling by the finite element method. Geophysics **36**, 132–155 (1971)

T. Dahlin, *On the automation of 2D resistivity surveying for engineering and environmental applications*, PhD thesis, Lund University, 1993

T. Dahlin, 2D resistivity surveying for environmental and engineering applications. First Break **14**, 275–283 (1996)

T. Dahlin, The development of DC resistivity imaging techniques. Comput. Geosci. **27**, 1019–1029 (2001)

T. Dahlin, B. Zhou, A numerical comparison of 2D resistivity imaging with 10 electrode arrays. Geophys. Prospect. **52**, 379–398 (2004)

T. Dahlin, R. Wisen, D. Zhang, 3D Effects on 2D resistivity imaging modelling and field surveying results. In *13th European Meeting of Environmental and Engineering Geophysics, Session: Electrical and Electromagnetic Methods,* vol. 1 (2007)

I. Demirci, E. Erdogan, M.E. Candasayar, Two-dimensional inversion of direct current resistivity data incorporating topography by using finite difference techniques with triangle cells: investigation of Kera fault zone in western Crete. Geophysics **77**(1), 67–75 (2012)

A. Dey, H.F. Morrison, Resistivity modeling for arbitrary shaped two-dimensional structures. Geophys. Prospect. **27**, 106–136 (1979)

L.S. Edwards, A modified pseudosection for resistivity and IP. Geophysics **42**, 1020–1036 (1977)

R.G. Ellis, D.W. Oldenburg, The pole-pole 3-D DC-resistivity inverse problem: a conjugate-gradient approach. Geophys. J. Int. **119**, 187–194 (1994)

E. Erdogan, I. Demirci, M.E. Candasayar, Incorporating topography into 2D resistivity modeling using finite-element and finite-difference approaches. Geophysics **73**(3), 135–142 (2008)

R.C. Fox, G.W. Hohmann, T.J. Killpack, L. Rijo, Topographic effects in resistivity and induced-polarization surveys. Geophysics **45**, 75–93 (1980)

D.H. Griffits, J. Turnbill, A multi-electrode array for resistivity surveying. First Break **3**(7), 16–20 (1985)

T. Gunther, C. Rucker, Boundless electrical resistivity tomography: BERT 2—the user tutorial, Ver. 2.0. (Geophysical Inversion and Modelling Library, https://www.pygimli.org/, 2013)

T. Gunther, C. Rucker, K. Spitzer, Three-dimensional modelling and inversion of dc resistivity data incorporating topography—I. Modelling. Geophys. J. Int. **166**, 495–505 (2006)

G.W. Hohmann, Three-dimensional induced polarization and electromagnetic modeling. Geophysics **40**, 309–324 (1975)

H.T. Holcombe, G.R. Jiracek, Three-dimensional terrain corrections in resistivity surveys. Geophysics **49**, 439–452 (1984)

J.R. Inman, J. Ryu, S.H. Ward, Resistivity inversion. Geophysics **38**(6), 1088–1108 (1973)

V.K. Khmelevskii, V.A. Shevnin, *Geophyzicheskie Metody Issledoavnia* (Nedra, Moscow, 1988), 296 p

O. Koefoed, *Geosounding Principles: Resistivity Sounding Measurements* (Elsevier, Amsterdam, 1979)

D.J. LaBrecque, M. Miletto, W. Daily, A. Ramirez, E. Owen, The effect of noise on Occam's inversion of resistivity tomography data. Geophysics **61**(2), 538–548 (1996)

R.E. Langer, An inverse problem in differential equations. Am. Math. Soc. Bull. **39**, 814–820 (1933)

H. Lehrnann, Potential representation by independent configurations on a multielectrode array. Geophys. J. Int. **120**, 331–338 (1995)

V. Lesur, M. Cuer, A. Straub, 2-D and 3-D interpretation of electrical tomography measurements, part 2: the inverse problem. Geophysics **64**(2), 396–402 (1999)

M.H. Loke, in *Topographic modeling in electrical imaging inversion: 62nd conference and technical exhibition, EAGE, Extended Abstracts*, D-2 (2000)

M.H. Loke, R.D. Barker, Rapid least-squares inversion of apparent resistivity pseudosections using a quasi-Newton method. Geophys. Prospect. **44**, 131–152 (1996)

M.H. Loke, T. Dahlin, A combined Gauss-Newton and quasi-Newton inversion method for the interpretation of apparent resistivity pseudosections, Paper presented at the *3rd Meeting of the Environmental and Engineering Geophysics Society*—European Section, Sept 1997 (Aarhus, Denmark, 1997)

T.R. Madden, The resolving power of geoelectric measurements for delineating resistive zones within the crust. In *The stincture and physical properties of the earth's crust*, ed. By J.G. Heacock, Am. Geophys. Union, Geophys. Monogr., vol. 14.955105 (1971)

H. Maurer, K. Holliger, D.E. Boerner, Stochastic regularization: smoothness or similarity? Geophys. Res. Leu. **25**(15), 2889–2892 (1998)

W. Menke, *Geophysical Data Analysis: Discrete Inverse Theory* (Academic, Orlando, FL, 1984)

T. Mirgalikyzy, B. Mukanova, I. Modin, Method of integral equations for the problem of electrical tomography in a medium with ground surface relief. J. Appl. Math. **2015**, 207021 (2015). https://doi.org/10.1155/2015/207021

I.N.Modin, V.A. Shevnin, V.K. Khmelevskii, A.G. Yakovlev et al. In *Electricheskoye Zondirovanie Geologicheskoi Sredy. Part I* (MSU, Moscow, 1988), p. 176

I.R. Mufti, Finite-difference modeling for arbitrary-shaped two dimensional structures. Geophysics **41**(62) (1976)

B. Mukanova, T. Mirgalikyzy, D. Rakisheva, Modelling the influence of ground surface relief on electric sounding curves using the integral equations method. Math. Prob. En. **2017**, 9079475 (2017). https://doi.org/10.1155/2017/9079475

M. Orunkhanov, B. Mukanova, The integral equations method in problems of electrical sounding, in *Advances in High Performance Computing and Computational Sciences*, ed. by Y.I. Shokin, N. Danaev, M. Orunkhanov, N. Shokina (Eds), vol. 93, (Springer, Berlin, 2006), pp. 15–21

M.K. Orunkhanov, B.G. Mukanova, B.K. Sarbasova, Chislennaya realizacia metoda potencialov v zadache zondirovania nad naklonnym lpatom, in *Computational Technologies*, vol. 9, (Siberian Branch of Russian Academy of Sciences, Novosibirsk, 2004a), pp. 45–48

M.K. Orunkhanov, B.G. Mukanova, B.K. Sarbasova, Chislennoe modelirovanie zadach electricheskogo zondirovania. In *Computational Technologies*, Special Issue, part 3, vol. 9 - (Almaty-Novosibirsk, 2004b), pp. 259–263

M. Orunkhanov, B. Mukanova, B. Sarbasova, Convergence of the method of integral equations for quasi three-dimensional problem of electrical sounding, in *Computational Science and High Performance Computing II*, ed. by E. Krause, Y. Shokin, M. Resch, N. Shokina (Eds), (Springer, Berlin, 2005), pp. 175–180

S. Penz, H. Chauris, D. Donno, C. Mehl, Resistivity modeling with topography. Geophys. J. Int. **194**(3), 1486–1497 (2013)

I.P. Skalskaya, Pole tochechnogo istochnika toka, raspolozhennogo na poverkhnosti Zemli nad naklonnym plastom. J. Tech. Phys. **18**(10), 1243–1254 (1948)

L.B. Slihter, The interpretation of resistivity prospecting method for horizontal structures. Physics **4**, 307–322 (1933)

S.S. Stefanescu, C. Shlumberger, Sur la distribution electrique potencielle dans une terrain a couches horizontals, homogenes et isotropes. J. Phys. Radium **7**, 132–141 (1930)

A.F. Stevenson, On the theoretical determination of earth resistance from surface potencial measurements. Physics **5**, 114–124 (1934)

A. G. Tarkhov (ed.), *Electrorazvedka, Sparvochnik Geophizika* (Nedra, Moscow, 1980)

P.I. Tsourlos, J.E. Szymanski, G.N. Tsokas, The effect of topography on commonly used resistivity arrays. Geophysics **64**(5), 1357–1363 (1999)

A.V. Veshev, Vliyaniye rel'yefa na rezul'taty rabot kombinirovannym elektroprofilirovaniyem, in *Uchenye Zapiski LGU*, vol. 278, (LSU, Leningrad, 1959)

A.V. Veshev, In *Electroprofilirovanie na Postoyannom I Peremennom Toke*, 2nd ed. (Nedra, Leningrad, 1980). (in Russian)

S.Z. Xu, *The Boundary Element Method in Geophysics, Geophysical Monograph Series (Issue 9)* (SEG Books, 2001)

S.Z. Xu, S. Zhao, Y. Ni, A boundary element method for 2-D dc resistivity modeling with a point current source. Geophysics **63**, 399–404 (1998)

S.A.Yerokhin, Primeneniye elektrotomografii pri resheniya rudnykh, inzhenernykh i arkheologicheskikh zadach, Dissertation, Moscow State University, Moscow, 2012

S.A. Yerokhin, I.N. Modin, V.P. Novikov, A.M. Pavlova, Vozmozhnosti Elektricheskoy Tomografii Pri Izuchenii Karstovo-Suffozionnykh Voronok, in *Ingenernye Izyskania*, vol. 11, (Geomarketing, Moscow, 2011)

A.A.R. Zohdy, A new method for the automatic interpretation of Schlumberger and Wenner sounding curves. Geophysics **54**(2), 245–253 (1989)

Chapter 2
Mathematical Background

2.1 Elements of Potential Theory for Laplace's Equation

In the classical theory of potentials for the Laplace equation, the solution is expressed in terms of simple- or double-layer potentials. The functions that describe the densities of the simple or double layers depend on either a single variable (Tikhonov and Samarskii 1963) or on several variables that are defined in a bounded domain (Gunther 1934; Tricomi 1957). In this section, we consider functions defined in two dimensions (2D), possibly unbounded surfaces in a three-dimensional (3D) space. We restrict the class of surfaces to the following conditions, known as the Lyapunov conditions (Tikhonov and Samarskii 1963):

1. A normal vector and a tangent plane are defined at each point on the surface.
2. Let θ be the angle between two normal vectors at the points P and Q. For any pair of points P and Q on the surface, there exist constants $0 < \alpha \leq 1$ and C such that the angle θ satisfies the condition

   $$|\theta| \leq C|PQ|^{\alpha}.$$

3. There exists a number $d > 0$ for all points on the surface at which the lines parallel to the normal vector at the point M have only one intersection with the surface inside the sphere with radius d and center at the point M.

These conditions allow us to introduce a local parameterization of the surface near the point M in both spherical and cylindrical coordinates with a center at the point M. Consequently, we can uniquely map the vicinity of the point M to a circle of radius that does not exceed d. These spheres are known as Lyapunov spheres.

If the surface forms the boundary of some spatial domain Ω, then the side of the surface facing the domain Ω is called the "inner" side and the opposite side is called the "outer" side.

B. Mukanova, I. Modin, *The Boundary Element Method in Geophysical Survey*,
Innovation and Discovery in Russian Science and Engineering,
https://doi.org/10.1007/978-3-319-72908-4_2

Surfaces satisfying conditions 1–3 are called Lyapunov surfaces. Let Γ be a surface satisfying conditions 1–3. Suppose that the function $\nu(P)$ is defined on this surface and is bounded. The following function is known as the potential of a simple layer with a density $\nu(P)$:

$$u(M) = \iint\limits_{\Gamma} \frac{\mu(P)d\Gamma_P}{|MP|}. \tag{2.1}$$

In some cases, it is convenient to apply an alternative definition of the potential of a simple layer in the form

$$u(M) = \frac{1}{2\pi} \iint\limits_{\Gamma} \frac{\nu(P)d\Gamma_P}{|MP|}. \tag{2.2}$$

Here, $M \in R^3$. In the definition above, the density of a simple layer $\nu(P)$ is related to the function $\mu(P)$ in the representation (2.1) by the following formula:

$$\nu(P) = 2\pi\mu(P). \tag{2.3}$$

If the domain Ω is bounded, then the function $u(M)$ has a number of remarkable properties:

1. The function $u(M)$ is defined for all points $M \in R^3$ of the space and is bounded and continuous.
2. The function $u(M)$ satisfies Laplace's equation everywhere except for the points on the surface Γ:

$$\Delta u = 0 \tag{2.4}$$

3. There exist normal derivatives of the function $u(M)$ on both sides of the surface that have a discontinuity at the surface Γ.

Let

$$\left.\frac{\partial u}{\partial n}\right|_{+}, \left.\frac{\partial u}{\partial n}\right|_{-}$$

be the derivatives of the potential $u(M)$ along the direction of the outer normal **n** taken from the outer and inner sides of the surface at the point M. The derivatives from the different sides are calculated by passing through the surface Γ from the inside and outside of the domain Ω; these values are respectively defined by the following equalities:

$$\begin{aligned}\left(\frac{\partial u}{\partial n}\right)_{-}(M) &= 2\pi\mu(M) + \iint\limits_{\Gamma} \mu(P)\frac{\partial}{\partial n}\left(\frac{1}{|MP|}\right)d\Gamma_P \\ \left(\frac{\partial u}{\partial n}\right)_{+}(M) &= -2\pi\mu(M) + \iint\limits_{\Gamma} \mu(P)\frac{\partial}{\partial n}\left(\frac{1}{|MP|}\right)d\Gamma_P,\end{aligned} \tag{2.5}$$

They can be alternatively written in terms of the density $\nu(P)$:

$$\begin{aligned}\left(\frac{\partial u}{\partial n}\right)_{-}(M) &= \nu(M) + \frac{1}{2\pi}\iint\limits_{\Gamma} \nu(P)\frac{\partial}{\partial n}\left(\frac{1}{|MP|}\right)d\Gamma_P \\ \left(\frac{\partial u}{\partial n}\right)_{+}(M) &= -\nu(M) + \frac{1}{2\pi}\iint\limits_{\Gamma} \nu(P)\frac{\partial}{\partial n}\left(\frac{1}{|MP|}\right)d\Gamma_P.\end{aligned} \tag{2.6}$$

Equalities (2.5) and (2.6) are also valid for an unbounded surface Γ under the existence of improper integrals in (2.5) and (2.6). The following expression is known as the direct value of the normal derivative of the potential of a simple layer at the point M:

$$w(M) = \iint\limits_{\Gamma} \mu(P)\frac{\partial}{\partial n_M}\left(\frac{1}{|MP|}\right)d\Gamma_P \tag{2.7}$$

We note here that the derivative is taken along the normal at a fixed point M and that the integration is conducted along the coordinates of the point P.

The proof of the properties of the function $u(M)$ is well known and is given in textbooks on the equations of mathematical physics (Tikhonov and Samarskii 1963; Vladimirov 1971); consequently, it is omitted here.

The function $\frac{\partial}{\partial n_M}\left(\frac{1}{|MP|}\right)$ in the expression (2.7) has the following singularity when P approaches the point M for a Lyapunov surface:

$$\frac{\partial}{\partial n_M}\left(\frac{1}{|MP|}\right) \sim \frac{1}{|MP|^{2-\alpha}},$$

where α is an exponent in condition 2.

We can now introduce the function $v(M)$, which is defined by the following formula:

$$v(M) = \iint\limits_{\Gamma} \mu(P)\frac{\partial}{\partial n_P}\left(\frac{-1}{|MP|}\right)d\Gamma_P \tag{2.8}$$

Unlike the function (2.7), the normal derivative in (2.8) is taken at the variable integration point P, and the point M is an arbitrary point in the 3D space. The function (2.8) defines the potential of a double layer. The properties of these functions are also described in the abovementioned textbooks. For further consideration, we require the following property.

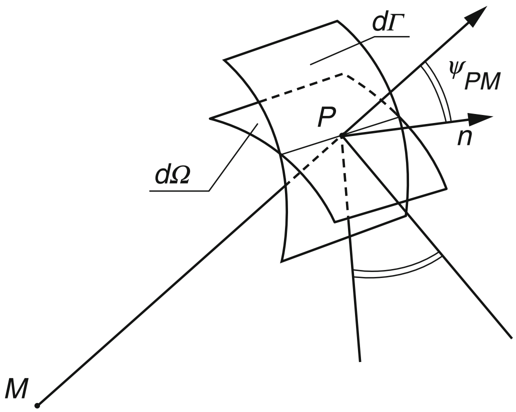

Fig. 2.1 The surface element $d\Gamma$, the normal **n** with respect to it, and its projection $d\Omega$

Proposition 2.1 *Let* Γ *be a surface with normal vectors defined at each point* P. *If the point* M *does not belong to* Γ*, then the modulus of the function* v(M*), where the density is constant and equal to the unit density* μ(P*)* = *1, is equal to the solid angle at which the surface* Γ *is visible from the point* M *(Tikhonov and Samarskii 1963).*

The proof of this property originates from the consideration of Fig. 2.1. Let $d\Gamma$ be a small element on the surface Γ. The derivative along the normal of the function $-1/|MP|$ is equal to the scalar product of the gradient of that function and the normal taken at the point P. It is not difficult to verify that the gradient of the function is directed along the vector MP. Let ψ_{PM} be the angle between the direction of MP and the direction of the normal $\mathbf{n}_\mathrm{P}$ at the point P. Let $d\Omega$ be the projection of $d\Gamma$ at the point P onto the plane perpendicular to the vector MP. Then, the angle between this plane and the plane tangent to $d\Gamma$ at the point P is equal to the angle between the normal $\mathbf{n}_\mathrm{P}$ and the vector MP. Therefore, the product of $d\Gamma_\mathrm{P}$ with the cosine of this angle is equal to the element of the area $d\Omega$ on a sphere of radius MP centered at point M; then, the ratio of the area of this element to the square of the distance $|PM|^2$ is the solid angle element, under which the element $d\Gamma$ is visible from the point P:

$$d\Theta = \frac{d\Omega}{|MP|^2}.$$

Then, the function (2.8) for $\mu = 1$ can be rewritten as follows:

$$\begin{aligned} v(M) &= \iint\limits_{\Gamma} \left(\nabla \frac{-1}{|\,MP\,|}, \mathbf{n}_\mathbf{P} \right) d\Gamma_P = \iint\limits_{\Gamma} \frac{\left(\vec{MP}, \mathbf{n}_\mathbf{P}\right)}{|MP|^3} d\Gamma_P \\ &= \iint\limits_{\Gamma} \frac{\cos\psi_{PM}}{|MP|^2} d\Gamma_P = \iint\limits_{\Gamma} \frac{d\Omega}{|MP|^2} = \iint\limits_{\Gamma} d\Theta = \Theta. \end{aligned} \tag{2.9}$$

Thus, the integral (2.8) is equal to the solid angle at which a part of the surface Γ can be seen from the point M. The sign in (2.9) depends on which side of the surface the point M is located. A "+" sign is used if the point is on the side from which the normal is directed, and a "−" sign is used otherwise.

2.2 Elements of Integral Equation Theory

A number of electrical sounding problems are reduced to a Fredholm integral equation of the second kind, with a symmetric kernel. Here, we provide several facts of this theory that we shall rely upon during the subsequent presentation (Petrovskii 1965; Tikhonov and Samarskii 1963; Tricomi 1957).

Let a function $K(P,M)$ be defined in the bounded domain $\Omega \subset R^2 \times R^2$, $\Omega = \Gamma \times \Gamma$, $\Gamma \subset R^2$. Suppose the two following conditions hold:

(a) The function $K(P, M) \in L_2(\Omega)$; that is, the following integral exists:

$$\int_{\Omega} K^2(P, M) d\Omega < \infty \tag{2.10}$$

Then, by the Fubini theorem, the following integrals exist for almost all $P \in \Gamma$ and $M \in \Gamma$:

$P(M) = \int_{\Gamma} K^2(P, M) d\Gamma_P < \infty, Q(M) = \int_{\Gamma} K^2(P, M) d\Gamma_M < \infty,$

where

$\int_{\Gamma}\int_{\Gamma} K^2(P, M) d\Gamma_P d\Gamma_M = \int_{\Gamma}\int_{\Gamma} K^2(P, M) d\Gamma_P d\Gamma_M = \int_{\Gamma} K^2(P, M) d\Omega.$

(b) The function $K(P,M)$ is symmetric with respect to the variables P and M:

$$K(P, M) = K(M, P), \forall P \in \Gamma, \forall M \in \Gamma. \tag{2.11}$$

Let us define the integral operator for an arbitrary function $f(M) \in L_2(\Gamma)$ defined on Γ as follows:

$$Af(M) = \int_{\Gamma} K(M, P) f(P) d\Gamma_P. \tag{2.12}$$

Through the assumptions about the functions $K(M, P)$ and $f(M)$, the operator (2.12) can be defined, the result of which is a function $Af(M) \in L_2(\Gamma)$. The following integral equation is known as a Fredholm integral equation of the second kind:

$$f(M) = \lambda Af(M) + g(M), \quad \lambda \in R, \quad g(M) \in L_2(\Gamma)$$

or

$$f(M) = \lambda \int_{\Gamma} K(M, P) f(P) d\Gamma_P + g(M) \tag{2.13}$$

Next, we formulate a number of theorems that we shall refer to thereafter.

Theorem 2.1 (the Fredholm alternative). *For every non-zero fixed complex number* λ, *either (2.14) has a non-trivial solution* f(M) ∈ $L_2(\Gamma)$ *or the non-homogeneous (2.13) has a solution for all* g(M)*:*

$$f(M) = \lambda A f(M) \tag{2.14}$$

The functions satisfying (2.14) are called eigenfunctions of the integral equation (2.14) or are sometimes known as the eigenfunctions of the kernel $K(M, P)$.

For symmetric kernels, the following properties are valid: Eigenfunctions that are not identically equal to zero can exist; the eigenvalues for symmetric kernels are real; the functions corresponding to different eigenvalues are orthogonal to each other; only a finite number of eigenfunctions can correspond to the same eigenvalue; and the set of eigenvalues does not have finite limit points. If the number of eigenfunctions is infinite, they can be normalized and ordered so that the corresponding eigenvalues increase:

$$\lim |\lambda_i| = \infty \quad \text{as} \quad i \to \infty.$$

The number of eigenfunctions is at most countable. The number of eigenvalues is finite if and only if the kernel is degenerate. Otherwise, the number of eigenvalues is infinite.

The problem with the construction of eigenfunctions and eigenvalues of (2.14) is rather complicated and goes beyond the scope of this monograph.

The following theorems also hold:

Theorem 2.2 *Let* $\Gamma \subset R^2$ *be a bounded measurable set,* $\Omega = \Gamma \times \Gamma$, $\Gamma \subset R^2$. *If* $K(M, P) \in L_2(\Omega)$*, then (2.12) with sufficiently small* λ *will have a unique solution for any* $g(M) \in L_2(\Gamma)$*.*

The proof of this theorem follows immediately from the properties of the eigenvalues of (2.13) with symmetric kernels and from the Fredholm alternative. It is sufficient to define $|\lambda| < \min_i |\lambda_i|$.

Theorem 2.3 *The solution of the inhomogeneous equation (2.13) exists if and only if the right-hand side of that equation is orthogonal to any eigenfunction of (2.14):*

$$\int_\Gamma g(M)h(M)d\Gamma_M = 0, \quad \forall h(M) : h(M) = \lambda \int_\Gamma K(M,P)h(P)d\Gamma_P.$$

From a practical perspective, Theorems (2.1) through (2.3) are significant because it is always possible to numerically solve (2.13) by using direct calculations to verify the stability of the obtained solution with respect to small perturbations in the input parameters of the equation. The instability of the numerical procedure for some input parameters can indirectly indicate that the parameter λ in the equation is an eigenvalue. In this case, an acceptable practice is to consider the problem with other input data or to ensure that the solution is within the spectrum. In geophysical practice, changes in the input parameters represent changes in the positions of the source electrodes or changes in the hypothesis about the media model.

Furthermore, we are interested in integral equations with a singularity of the following form:

$$K(P,M) = k(P,M)/|PM|^{\alpha}, \tag{2.15}$$

where

$M = (x,y) \in \Gamma, \quad P = (x_P, y_P) \in \Gamma, \quad \Gamma \subset R^2, \quad 1 \le \alpha < 2.$

Here, Γ is a bounded set, and the function $k(P,M)$ is bounded, continuous and symmetric with respect to the variables M and P. In this case, the kernels of (2.15) do not belong to $L_2(\Gamma)$, since the function of the order $1/|PM|^{-2\alpha}$ is not integrable in the small vicinity of the point M at the surface Γ with respect to variable point P. This means that the conditions of Theorem 2.1 are not satisfied.

However, according to (Petrovskii 1965), the integral equation (2.13) with a kernel of the form (2.15) and $\alpha < 2$ can be reduced to an integral equation with an iterated second-order kernel $K_2(P, M)$ for which all of the Fredholm theorems are valid. We recall that an iterated kernel of order n is defined as follows:

$$\begin{aligned} K_1(P,M) &= K(P,M), \\ K_n(P,M) &= \int_{\Gamma} K(P,Q)K_{n-1}(Q,M)d\Gamma. \end{aligned}$$

To obtain an integral equation with an iterated second-order kernel, it is sufficient to substitute the operator of the integral equation into (2.13) and change the order of integration:

$$f(M) = \lambda^2 \iint_{\Gamma} K_2(P,M)f(P)d\Gamma_M + \Sigma_2(M). \tag{2.16}$$

The right-hand side of (2.16) is defined as

$$\Sigma_2(M) = g(M) + \lambda \iint_{\Gamma} K(P,M)g(P)d\Gamma_P.$$

After the integration in (2.16), the order of the singularity in the kernel $K_2(P, M)$ decreases to

$$K_2(P,M) \le \frac{K(P,M)}{|PM|^{2\alpha-2}}.$$

Remark 2.1 Under our assumption that $\alpha \ge 1$, the singularity in the kernel of (2.16) disappears, and thus, (2.16) becomes an equation with a continuous bounded kernel. Thus, Theorems (2.1) through (2.3) for (2.16) remain valid.

Remark 2.2 The results formulated above are obtained for a bounded domain Γ. However, according to remarks of (Petrovskii 1965), Theorems (2.1) through (2.3) also hold on unbounded domains under the condition of compactness of the integral operator.

In most of the mathematical models considered here, the integration regions are unlimited. Chapters 4 and 5 describe the application of this theory to the case of infinite domains.

2.3 Fourier and Hankel Transforms

2.3.1 The Fourier Transform

As shown in Driver's functional analysis course (Driver 2003), it is possible to define the concept of a scalar product, as well as a related norm and an orthonormal basis, in a functional space similar to $\boldsymbol{R}^n$.

In the space $L_2(\Gamma)$, the inner (scalar) product is defined by the following formula:

$$(f, g) = \int_{\Gamma} f(x) g(x) d\Gamma. \tag{2.17}$$

This formula generates the corresponding norm:

$$\|f\|_2 = \int_{\Gamma} |f(x)|^2 d\Gamma \tag{2.18}$$

The concept of orthogonality in a functional space is generalized in the following manner:

Definition. Two functions of $L_2(\Gamma)$ are orthogonal if their scalar product is zero.

During the course of functional analysis, it is proven that the space $L_2(\Gamma)$ is complete; that is, the limit of any fundamental sequence that converges in the norm (2.18) belongs to $L_2(\Gamma)$. In addition, in $L_2(\Gamma)$, there exist many countable orthonormal bases such that any element of $L_2(\Gamma)$ is represented as a functional series as follows:

$$f(x) = \sum_{i=1}^{\infty} f_i \varphi_i(x), \tag{2.19}$$

where $\varphi_i(x)$, $i = 1, 2, \ldots$ are basis functions. The convergence of the series in (2.19) is understood in the sense of convergence in the norm of L_2; that is, the series (2.19) converges if and only if

$$\lim_{N\to\infty} \parallel \sum_{1}^{N} f_i\varphi_i(x) - f(x) \parallel_2 = 0$$

The following Perceval equality holds for Fourier coefficients:

$$\|f(x)\|_2 = \sqrt{\sum_{i=1}^{\infty} f_i^2}$$

The representation (2.19) is known as the Fourier expansion of the function *f(x)* on the basis $\varphi_i(x)$, and the expansion coefficients f_i define the Fourier coefficients. These coefficients are calculated in terms of the scalar product of the function by the corresponding basis function and are defined by the following formula:

$$f_i = (f(x), \varphi_i(x))$$

The choice of the basis functions depends on the specific nature of the problem that is being solved each time; it is independently determined by the researcher.

Representation (2.19) means that any function $f(x)$ in $L_2(\Gamma)$ can be approximated as a finite linear combination of the basis functions. The accuracy of this approximation depends on the number of functions involved in the approximation and the properties of the function $f(x)$.

Let the finite-dimensional space S_N be a set of functions that can be represented as a finite linear combination of the first N basis functions:

$$f(x) = \sum_{i=1}^{N} f_i\varphi_i(x), \quad f_i \in R, \quad i = 1, 2, \ldots, N. \tag{2.20}$$

This sum lies within the space S_N. Since the functions in S_N are determined by their Fourier coefficients f_i, this space can be identified within the space $\boldsymbol{R}^{\mathrm{n}}$. The norm of the functions in S_N is determined similarly to the norm of the vectors of $\boldsymbol{R}^{\mathrm{n}}$ via the root of the sum of the squares of the coordinates. This norm coincides with the norm of the function in L_2. It is also obvious that a chain of embeddings of a lower dimensional space into a larger one is fulfilled:

$$S_N \subset S_{N+1} \subset S_{N+2} \subset \ldots \subset L_2([0,1]). \tag{2.21}$$

In mathematical modeling, it is sometimes useful to replace complex-defined functions with a finite sum of their Fourier expansions, since this greatly simplifies the computations.

The mathematical models in many geophysical sounding methods can be reduced to solutions of the Laplace equation. In many applications, it is convenient to express the solution in terms of the eigenfunctions of the Laplace operator. It is obvious that trigonometric functions are eigenfunctions of the Laplace operator defined in Cartesian coordinates:

$$\Delta = \left(\frac{\partial^2 u}{\partial x^2} + \frac{\partial^2 u}{\partial y^2} + \frac{\partial^2 u}{\partial z^2}\right),$$

$$\begin{aligned}&\Delta(\cos\,(kx+\alpha)\,\cos\,(ly+\beta)\,\cos\,(mz+\gamma))\\&= -\left(k^2+l^2+m^2\right)\cos\,(kx+\alpha)\,\cos\,(ly+\beta)\,\cos\,(mz+\gamma),\\&\alpha,\beta,\gamma\in R,\quad k,l,m = 0,1,2,\,\ldots\end{aligned}$$

For a bounded domain of rectangular form, the basis is often formed from trigonometric functions. However, if the domain of the defined variables is not bounded, then trigonometric functions are not square-integrable and, therefore, cannot form a basis in the space. Nevertheless, it is possible to represent the function through trigonometric functions based on a Fourier transform. Let there be an absolutely integrable function of three variables (x, y, z) in Cartesian coordinates. A partial Fourier transform with respect to x is

$$\tilde{f}(k_x, y, z) = \int\limits_{-\infty}^{\infty} f(x,y,z)\exp\left(-ik_x x\right)dx. \tag{2.22}$$

The following inversion formula holds:

$$f(x,y,z) = \frac{1}{2\pi}\cdot\int\limits_{-\infty}^{\infty}\tilde{f}(k_x,y,z)\exp\left(ik_x x\right)dk_x. \tag{2.23}$$

Partial transforms with respect to other variables are defined similarly. Throughout this book, we apply the transform with respect to the variable y as follows:

$$\tilde{f}\left(x,k_y,z\right) = \int\limits_{-\infty}^{\infty} f(x,y,z)\exp\left(-ik_y y\right)dy. \tag{2.24}$$

Moreover, we consider functions that are even with respect to the variable y. In this case, the Fourier transform (2.23) can be written in the form of a cosine transform:

$$\tilde{f}\left(x,k_y,z\right) = 2\int\limits_{0}^{\infty} f(x,y,z)\,\cos\,\left(k_y y\right)dy. \tag{2.25}$$

For even functions, the imaginary part of the Fourier transform vanishes. In this case, the inversion formula (2.23) is reduced to

$$f(x,y,z) = \frac{1}{\pi}\cdot\int\limits_{0}^{\infty}\tilde{f}(k_x,y,z)\cdot\,\cos\,(k_x x)dk_x. \tag{2.26}$$

The Fourier transform is often called the spectrum or spectral representation of the function. Fourier transforms have the following important property. Suppose that the functions $f(x, y, z)$ and $g(x, y, z)$ are given in R^3. A convolution of the functions $(f * g)$ (x, y, z) with respect to the variable x is the following function:

$$f^{*}g(x,y,z) = \int\limits_{-\infty}^{\infty} f(x',y,z)\cdot g(x-x',y,z)dx'.$$

If there exists a Fourier transform of the functions $f(x, y, z)$ and $g(x, y, z)$, there must exist a Fourier transform of the convolution

$$h(x,y,z) = f^{*}g(x,y,z),$$

and the following formula holds:

$$\tilde{h}\,(k_x,y,z) = \tilde{f}\,(k_x,y,z)\cdot\tilde{g}\,(k_x,y,z). \tag{2.27}$$

2.3.2 The Hankel Transform

We now write the Laplace operator in cylindrical coordinates:

$$\frac{1}{r}\frac{\partial}{\partial r}\left(r\frac{\partial u}{\partial r}\right)+\frac{1}{r^2}\frac{\partial^2 u}{\partial\varphi^2}+\frac{\partial^2 u}{\partial z^2}=0,\quad (r>0,\ \ z\in R,\ \ 0<\varphi\leq 2\pi).$$

We introduce the following notation for the radial part of the Laplace operator:

$$\Lambda_r u \equiv \frac{1}{r}\frac{\partial}{\partial r}\left(r\frac{\partial u}{\partial r}\right).$$

The zero-order Bessel function of the first kind is an eigenfunction of the Laplace operator defined in cylindrical coordinates. Indeed, suppose that some function $R_\lambda(r)$ is an eigenfunction of the operator Λ_r:

$$\Lambda_r R_\lambda(r) \equiv \frac{1}{r}\frac{d}{dr}\left(r\frac{dR_\lambda}{dr}\right) = -\lambda^2 R_\lambda.$$

Then, this function satisfies the following equation:

$$(rR')' + \lambda^2 rR = 0 \Rightarrow R'' + \frac{1}{r}R' + \lambda^2 R = 0. \tag{2.28}$$

Then, we perform a change of variables $x = \lambda r$ and obtain

$$R_\lambda(r) = R(x/\lambda) = y(x), \quad R' = \lambda y', \quad R'' = \lambda^2 y'' \Rightarrow$$
$$\lambda^2 y'' + \frac{\lambda^2}{x} y' + \lambda^2 y = 0.$$

It follows from the above that the function $y(x) = R(x/\lambda)$ is precisely the zero-order Bessel function of the first kind, $y(x) = J_0(x), \quad R_\lambda(r) = J_0(\lambda r)$.

Thus, we have

$$\Lambda_r J_0(\lambda r) \equiv \frac{1}{r}\frac{d}{dr}\left(r\frac{dJ_0(\lambda r)}{dr}\right) = -\lambda^2 J_0(\lambda r). \tag{2.29}$$

Similar to the definition of the Fourier transform with trigonometric functions, it is possible to define a Fourier transform with Bessel functions. This transformation is known as a Hankel transform, sometimes also called a Bessel–Fourier transform.

We denote the Hankel transform of the function $U(r, z)$ with respect to the variable r by $\Phi U(\lambda, r)$ with the Bessel function $J_0(\lambda r)$:

$$\Phi U(\lambda, z) = \int_0^\infty U(r, z) J_0(\lambda r) r dr. \tag{2.30}$$

It is known that this transformation is an inverse of itself:

$$U(r, z) = \int_0^\infty (\Phi U)(\lambda, z) J_0(\lambda r) \lambda d\lambda.$$

Let $V(\lambda, r)$ be the Hankel transform ΦU. Suppose that the function $U(r, z)$ tends to zero at infinity and that the function $\partial U(r, z)/\partial r$ decreases at infinity faster than $1/r$. Let us derive a formula for the Hankel transform of the Laplace operator applied to the function $U(r, z)$:

$$\Phi\Lambda_r U = \int_0^\infty \Lambda_r U(r, z) J_0(\lambda r) r dr = \int_0^\infty \frac{1}{r}\frac{\partial}{\partial r}\left(r\frac{\partial U(r, z)}{\partial r}\right) J_0(\lambda r) r dr =$$
$$= r J_0(\lambda r) \frac{\partial U(r,z)}{\partial r}\bigg|_{r=0}^{r=\infty} - \int_0^\infty \frac{\partial U(r, z)}{\partial r} \cdot \frac{\partial J_0(\lambda r)}{\partial r} r dr.$$

Considering that the function $U(r, z)$ decreases at infinity, integrating by parts gives

$$\Phi\Lambda_r U = -r U(r, z) \frac{\partial J_0(\lambda r)}{\partial r}\bigg|_{r=0}^{r=\infty} + \int_0^\infty U(r, z) \frac{\partial}{\partial r}\left(r\frac{\partial J_0(\lambda r)}{\partial r}\right) dr.$$

Now, we consider property (2.29) of the function $J_0(\lambda r)$ and the condition of the decrease of the function $U(r, z)$ at infinity:

$$
\begin{aligned}
(\Phi\Lambda_r U)(\lambda,z) &= \int\limits_0^\infty U(r,z)\frac{1}{r}\frac{\partial}{\partial r}\left(r\frac{\partial J_0(\lambda r)}{\partial r}\right) r dr - rU(r,z)\frac{\partial J_0(\lambda r)}{\partial r}\Bigg|_{r=0}^{r=\infty} \\
&= -\lambda^2 \int\limits_0^\infty U(r,z)J_0(\lambda r) r dr = -\lambda^2 \Phi U(\lambda,z).
\end{aligned} \tag{2.31}
$$

Thus, the Hankel transform (2.30) of the radial part of the Laplace operator of the function $U(r, z)$ is equal to the product of the Hankel transform of the same function by the number $-\lambda^2$.

References

B.K. Driver, Compact and Fredholm operators and the spectral theorem. In *Analysis Tools with Applications*, Chapter 35 (Springer, Berlin, 2003), pp. 579–600

N.M. Gunther, *La théorie Du Potentiel et Ses Applications Aux problèmes Fondamentaux de la Physique Mathématique* (Gauthier-Villars, Paris, 1934)

I.G. Petrovskii, *Lekcii po teorii integral'nykh uravneniy* (Nauka, Moscow, 1965)

A.N. Tikhonov, A.A. Samarskii, *Equations of Mathematical Physics. (Translation from Russian)* (Pergamon, 1963)

F.G. Tricomi, *Integral Equations* (Interscience, New York, 1957)

V.S. Vladimirov, *Equations of Mathematical Physics* (Marcel Dekker, New York, 1971)

Chapter 3
Electrical Survey Technique and Mathematical Models

3.1 Electrical Arrays, Field Measurements, and the Electrical Resistivity Tomography Method

Electrical exploration is a component of exploration geophysics that is used to study the structure of the earth by exploiting electromagnetic fields to search for minerals, solve numerous near-surface tasks, and provide constraints for the design and construction of buildings. Electrical exploration is based on the differences in the electromagnetic properties of rocks, primarily with regard to the electrical resistivity ρ. From the perspective of physical fundamentals, electrical prospecting methods can be divided into high-frequency methods of electrical exploration (e.g., ground-penetrating radar (GPR) and radio transmission methods), low-frequency methods (e.g., magnetotelluric sounding (MTS) and time-domain electromagnetic (TEM) methods), and DC methods. The major component of such techniques is the resistivity method. This monograph is devoted to the resistivity method in the modification of electrical resistivity tomography (ERT).

The resistivity method includes different modifications of electrical surveying techniques, the theory of which is based on the study of the distribution of the electric field generated by artificial sources with known parameters in conducting geological media (Khmelevskoi 1984; Yakubovskii 1980).

The resistivity method is based on a dependence of the electric field observed at the earth's surface on the distribution of the resistivity throughout the medium. The electric field is created by the current $I_{\mathrm{A}\boxed{?}}$ flowing from an electrode A to an electrode B. The electric field strength is measured by receiving electrodes M and N. For small MN separations, the potential difference ΔU_{MN} is proportional to the component of the electric field strength in the direction of the line MN:

$$\Delta U_{\mathrm{MN}} \approx (\mathbf{E} \cdot \mathbf{MN}).$$

B. Mukanova, I. Modin, *The Boundary Element Method in Geophysical Survey*,
Innovation and Discovery in Russian Science and Engineering,
https://doi.org/10.1007/978-3-319-72908-4_3

A specific arrangement of four source and measuring electrodes is known as an electric survey installation or array. There are many types of arrays. The measurement results for each particular array depend on the configuration of the array and on the distribution of the resistivity in a region of the geoelectric section through which the electric current actually penetrates.

To estimate the approximate dimensions of this region, the distribution of the following derivative is used:

$$\mathrm{Sens}\,(x,z) = \frac{\partial\rho_\kappa(x_a,x_b,x_m,x_n)}{\partial\rho(x,z)}.$$

This derivative is calculated for an array located on the earth's surface, for which the receiving and feeding electrodes are located at four arbitrary points. This derivative is known as the sensitivity (Sens) of the array.

The sensitivity represents how a change in the resistivity at a point (x, z) affects the measured signal within the receiving dipole MN for an initially homogeneous half-space. Examples of the sensitivity sections for the three-electrode MNB array are shown in Fig. 3.1. A comparison of these sections demonstrates that the size of the area of influence, including the depth, depends on the geometry of the array. The installation is primarily sensitive to the distance between the source and measuring electrodes. This distance is called the spacing of array.

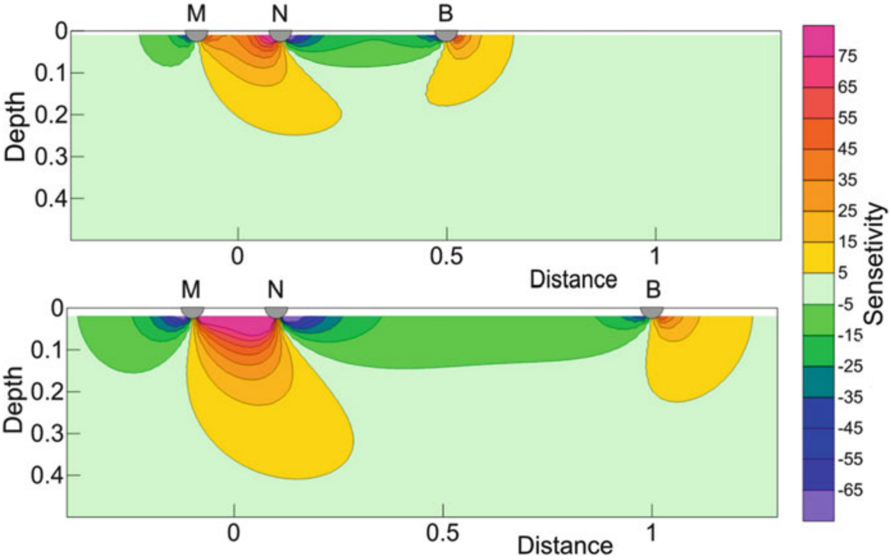

Fig. 3.1 Sensitivity sections in conventional units for a Pole-Dipole array, with two OB values and the same MN lines in relative units

By increasing or decreasing the spacing, we can accordingly increase or decrease the depth of the investigation. This makes it possible to study geoelectric sections at various depths based only on measurements from the earth's surface.

3.1.1 Types of Arrays

In the field, measurements are performed using the resistivity method with either one or two point sources or with a dipole source. The main types of electric survey arrays are shown in Fig. 3.2.

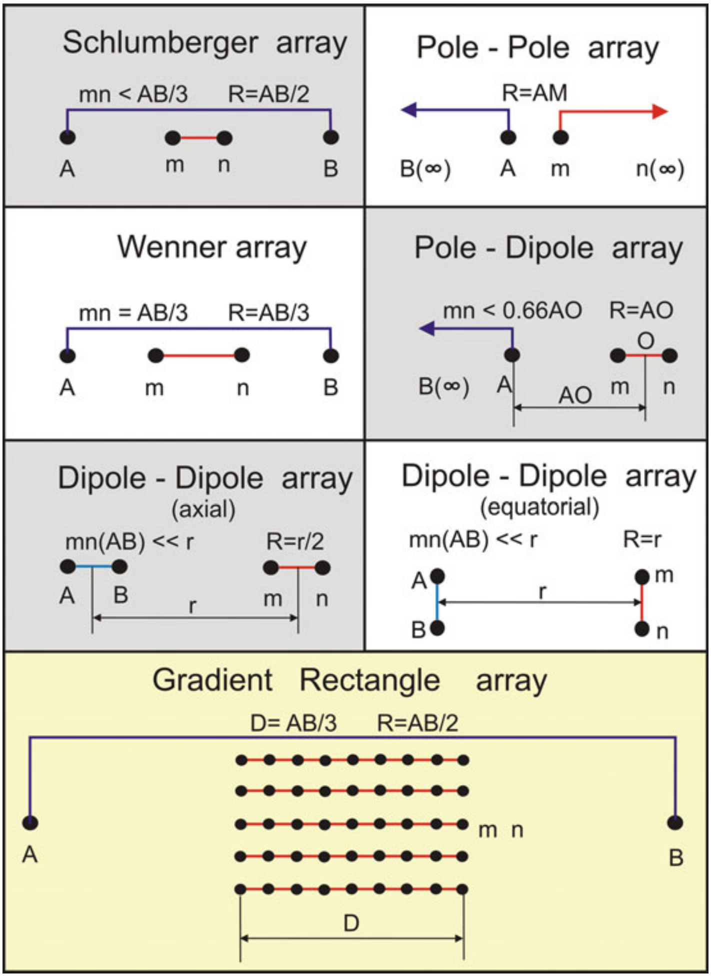

Fig. 3.2 Main types of electric survey installations electrical survey arrays for the resistivity method (*R* is a separation)

3.1.2 Apparent Resistivity

The concept of the apparent resistivity was introduced for convenience within the analysis and interpretation of the observed electric field. The apparent resistivity represents the observed electric field normalized by the parameters of the array in such a way that, within a homogeneous half-space, the apparent resistivity coincides with the true resistivity. The value of the apparent resistivity for a surface array is calculated using the following formula:

$$\rho_\mathrm{a} = K\frac{\Delta U_\mathrm{MN}}{I_\mathrm{AB}}, \quad K = 2\pi \Big/ \left(\frac{1}{\mathrm{AM}} - \frac{1}{\mathrm{AN}} - \frac{1}{\mathrm{BM}} + \frac{1}{\mathrm{BN}}\right), \tag{3.1}$$

where ΔU_MN is the measured potential difference between the receiving electrodes M and N, I_AB is the current along the line AB, and K is the geometric factor of the array.

In a generalized case, the apparent resistivity exhibits a complex dependency on the resistivity distribution throughout the sounding medium. For a horizontally layered medium, the apparent resistivity is approximately equal to the specific resistance of the layers averaged over a certain volume. For horizontally inhomogeneous media, the apparent resistivity may be greater than the maximum resistivity of a particular object within a section or less than the minimum resistivity of that same object. The size of the spatial region affecting the observation results depends on the separation and geometry of the array. As the spacing of array increases, deeper layers can be imaged within this region (Fig. 3.1).

3.1.3 Different Types of Resistivity Methods

Within the framework of the resistivity method, various research methods have been developed to solve particular types of problems (Fig. 3.3). Traditionally, there are three main types of resistivity technologies.

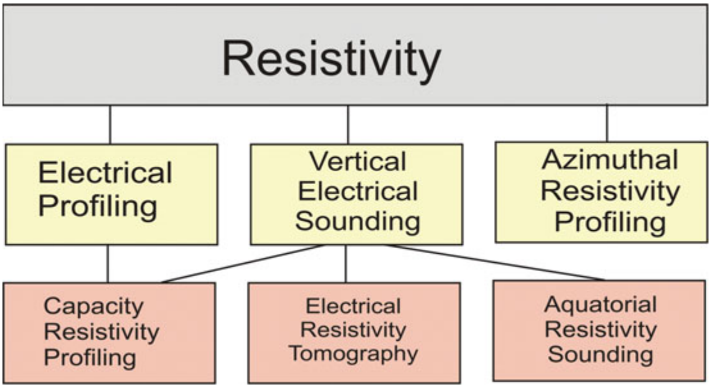

Fig. 3.3 Basic modifications of the resistivity method

3.1.4 Electroprofiling

For electroprofiling (EP) methods, the array is moved along the profile without changing the configuration. Since the geometry of the installation does not change, the depth of the investigation remains approximately constant. This technique was designed to map horizontal heterogeneities within a geoelectric section.

3.1.5 Electrical Sounding

At each observation point, measurements are taken while increasing the spacing within the array. With the help of electrical sounding data, the depth distribution of the resistivity of the medium can be investigated.

3.1.6 Circular (Azimuthal) Measurements (Profiling and Sounding)

At each point, measurements are collected along different directions of the axis of the installation (i.e., the azimuth of the array). This special technique is used to study media with azimuthal resistivity anisotropy.

3.1.7 Electrical Resistivity Tomography

Real geological media are often heterogeneous in both the horizontal and the vertical directions. To study such media, two-dimensional (2D) electrotomography methods have been used in recent years by combining probing and profiling techniques. A feature of this technique is the use of an automatic 2D inversion during the interpretation. Such interpretations are conducted using automatic 2D or 3D inversion programs. Automatic inversion techniques require a high observation density and a specific survey implementation. Modern high-performance equipment provides the requisite measurement speed for field observations. There are both surface and well-surface installations for electrotomography methods. In addition, some electrotomographic installations are performed in motion both on land (e.g., using an OhmMapper) and in aquatic environments (e.g., narrow-azimuth continuous aquatic sounding). Currently, 3D modifications of electrotomography techniques are in development. The resolution (i.e., the number of the smallest objects in the geoelectric section that can be stably detected in the electric field) and the corresponding quality of the electrotomography data interpretation are closely related to the number and density of measurements within the profile. The number of measurements usually reaches 1000 and, thus, the speed of the acquisition of field measurements is of fundamental importance and largely determines the practical applicability of this method. Special equipment with the programmable ability to switch electrodes automatically is used to achieve maximum efficiency during fieldwork (Griffiths and Barker 1993; Bobachyev et al. 1996; Dahlin 2001). For the sake of brevity, we use the term "multi-electrode equipment" hereafter.

Multi-electrode equipment sets constitute numerous electrodes (usually ranging from 48 to 128 pieces) connected by an electrical multiwire cable. In this case, each electrode can be used not only as a receiving electrode but also as a supply electrode (Fig. 3.1). Thus, once the array of electrodes has been installed and connected, the entire process of profiling measurements can be conducted.

Multi-electrode equipment sets were first developed during the beginning of the 1990s. Then, multi-channel and multi-electrode systems were introduced at the beginning of the twenty-first century. Such equipment is able to communicate with the given electrodes with a generator and a meter, and the equipment also allows parallel measurements along several receiving lines (Fig. 3.4). This approach provides a significant increase in the measurement speed, which essentially reduces the measurement time, allowing one station to finish acquiring data in 10–15 min.

The most globally recognized devices for ERT are manufactured by Iris Instruments (Syscal Pro, developed by both France and Japan), ABEM (Terrameter, LUND Imaging System, Sweden), and AGIUSA (Supersting, USA). In Russia, there are several developers of similar systems, namely, OMEGA-48 (Logis, Moscow), SGD-ETT (SibGeofizPribor, Krasnoyarsk), SKALA-64 (AA Trofimuk Institute of Oil and Gas Geology and Geophysics, Novosibirsk), and ERA-MULTIMAX (SPC ERA, S.Peterburg).

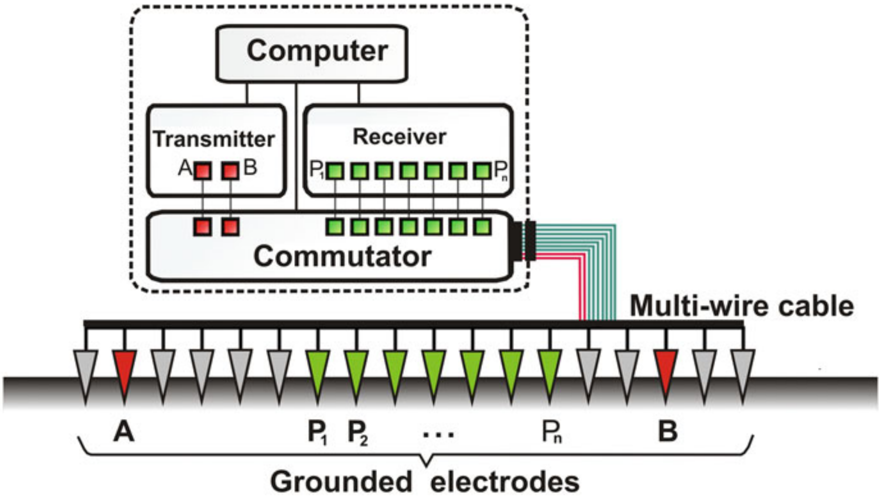

Fig. 3.4 Multi-electrode and multichannel system

The measurement procedure with multi-electrode equipment consists of switching the roles of the electrodes (i.e., either providing or measuring the current) without moving the electrode system. This process is described within a so-called measurement sequence, which comprises a list of all of the planned measurements without changing the position of the cables along the observed profile. This distinguishes the electrotomography method from the vertical electrical sounding (VES) method, where it is sufficient to determine the electrode interval along the profile and the spacing of the grid.

Typically, measurement sequences are generated using one of four traditional electrical survey arrays, namely, the Wenner, Schlumberger, dipole axial, and Pole-Dipole array. A set of such measurements can be represented by electrical probes with frequent intervals or by multipurpose profiling. Thus, we can obtain a data set in which both deep and surface objects are imaged. The depth of the survey section and the details of the study area can be assessed from the images generated using the VES and electrical profiling (EP) methods. For example, the depth for the Schlumberger array is estimated as one-third to one-tenth of the spacing of AB, and the detail of the section is comparable to the electrode interval along the profile. Using classical settings allows one to represent the results of the measurements in a standard manner, including pseudo-sections, sounding curves, and profile graphs. To optimize the measurement speed and inversion reliability, non-traditional arrays (for example, multigradient arrays and Dahlin array) have been developed. As a rule, ERT equipment is programmed with a set of predefined measurement sequences. However, this does not exclude the possibility of using sequences prepared or edited by the user and optimized for specific tasks.

Note that the results of ERT depend on the type of multi-electrode equipment employed, as they have different depths and resolving abilities in addition to other unique features.

ERT has a wide range of applications. At present, ERT is used to map complex geological structures with limited dimensions, spatially varying properties, and steep incidence angles. ERT applications include prospecting primarily for ore deposits of different minerals, solving engineering and geological problems for the designs of buildings and structures, solving hydrogeological problems, and mapping permafrost. ERT is also used to map pollution and search for archaeological objects. Usually, electrotomography is utilized for detailed surveys at a scale of 1:5000 or larger. ERT has been successfully used to confidently identify and study objects at depths of 30–50 m (sometimes 100–150 m or more). At the same time, as with all geophysical methods, objects at depths that are comparable with the transverse length of the profile cannot be reliably detected.

It follows from Table 3.1 that the most effective array is a combined three-electrode installation. A symmetrical four-electrode Schlumberger array also possesses good qualities. By virtue of the reciprocity theorem, the Schlumberger inverse array M_AB_N is theoretically equivalent to the traditional Schlumberger array. This array therefore allows for the implementation of multichannel measurements. The Dipole-Dipole axial array also has satisfactory qualities. However, in a conventional Dipole-Dipole axial array, one position of a measuring electrode corresponds to only

Table 3.1 Comparison of electroprospecting arrays in relation to electrotomography

Arrays	DI	ΔU_{mn}	S	Nch	$\mathrm{k_m}$	Inf
A_M	High	High	Low	Yes	Large	Two lines
A_M_N_B	Medium	High	Low	No	Small	No
A_MN_B	Medium	Medium	Medium	Yes	Medium	No
AB_MN	Low	Low	High	Yes	Small	No
A_MN + MN_B	High	Medium	High	Yes	Large	One line

A_M Pole-Pole array, *A_M_N_B* Wenner array, *A_MN_B* Schlumberger array, *AB_MN* Dipole-Dipole axial array, *A_MN* + *MN_B* two Pole-Dipole arrays, *DI* depth of the investigation, ΔU_{mn} level of the measured signal, *S* resolution, *Nch* possibility of multichannel measurements, k_m number of measurements within a single cycle of observations, *Inf* the need to set the line to "infinity"

one position of a current electrode; in the inverse array, a plurality of measuring electrode positions can correspond to the current array. The Wenner and Pole-Pole arrays are rarely used in practice. The Wenner array is not convenient because it is cumbersome to install, lacks the ability to provide multichannel measurements, and provides only a small number of independent physical measurements. The Pole-Pole array is also not commonly used because of the need to create two lines at "infinity."

The primary parameters of ERT methods are all geometric parameters:

1. The number of applied electrodes, which depends on the equipment
2. The distance interval between the electrodes, which depends on the cable length
3. The type of electrical survey array (i.e., measurement sequence)
4. The range of the spacing used (specified by the measurement sequence)
5. The length of the dipoles (determined by the measurement sequence)
6. The interval of the shifted alignment when working with long profiles

All of these parameters are described in the log files; it is recommended that these files be stored together with the measurement results.

In addition to the geometric parameters of the survey, the following dynamic parameters should also be considered:

1. The signal shape, namely, whether it is meandering, meandering with a pause, or sinusoidal
2. The signal duration when the current is flowing into the current dipole or the period of the harmonic signal
3. The amount of stored data

The duration of the current pulse or the operating frequency can directly affect the measurement speed. In addition, measurements with large pulse widths (or low operating frequencies) are usually less distorted by induction and industrial noise. When using ERT, a 0.5-s pulse is used, whereas a 0.25-s pulse is employed in favorable conditions. For harmonic signals, operating frequencies ranging from 5 to 10 Hz (i.e., periods of 0.2–0.1 s) are usually selected. For successful measurements using the vertical profiling (VP) method, the pulse length should range from 1 to 2 s.

A meander with a pause is usually used only for measurements of induced polarization parameters.

Field measurements with multi-electrode equipment are performed in several stages:

1. The first stage consists of deployment of the electrical equipment, grounding of electrodes, and connection of the measuring electrodes to the spit. The distance between the electrodes is determined either directly along the cable or along a measuring tape. In the presence of sharp relief, the distances are measured along the relief. The spit is located along a straight line as much as possible. To accomplish this, the intended profile of the survey is preliminarily marked on the terrain. Smooth turns of the cables are allowed, but sharp breaks or abrupt turns in the spit position are unacceptable. The depth and quality of the grounding of the electrodes determines the transient resistance, which is verified using special measurements before the survey is initiated (see point 3).
2. For a Pole-Dipole array, the "infinity" placement must be organized; its position depends on the terrain conditions and the operational methodology. The correct location on the ground is verified and recorded using a GPS receiver. To reduce transient resistance, several electrodes can be grounded at infinity. Usually, the maximum number of measurements from one position of infinity must be determined.
3. The measurement process begins with verifying the grounding of each electrode. For this purpose, a special operating mode is provided for all multi-electrode stations. In this mode, the resistance of a grounded electrode is determined in pairs or with respect to a reference electrode. The value of the transient resistance depends on the operating conditions and the parameters of the equipment. As a rule, the transient resistance should be less than 5–10 kOhm and should be similar for all electrodes located in the same type of ground. If the resistance of an individual electrode is high, a new hole is dug or the existing hole is either deepened or wetted with salt water. Sometimes, additional electrodes must be used and attached to the system.
4. The transmitter parameters must be established. Before initiating the measurement process, it is necessary to set the abovementioned operating parameters, namely, the measurement sequence and the duration and shape of the pulse. In addition, the output voltage of the generator (e.g., 400 V) or the amplitude of the current in the supply line (depending on the type of equipment used) must also be set. The optimal parameters are determined by the experimental method. A higher current within the supply line leads to better signal-to-noise ratios. However, if the signal level is too high (i.e., the first voltage), the analog-to-digital converter (ADC) of the measurement instrument may restart. In unfavorable conditions, it is necessary to break the measurement sequence into two sections for small and large spacing and operate the system with different output parameters for the generator.
5. The parameters of the measurement instrument must be established. One way to improve the quality of the measurements is to accumulate a useful signal

through repeated measurements. The number of accumulations depends on the level of interference and, as a rule, is equal to 2–6 accumulations.

6. The measurements are usually conducted in automatic mode and, at a high measurement speed, it is almost impossible to control the process. The operator usually monitors the level of the measured signal, the current strength in the line, and the voltage of the battery.
7. A height-planned anchor of the profile is necessary for the correct processing and interpretation of the ERT data. Usually, this step is performed in parallel with the measurement process. For this step, it is desirable to note the position of each electrode and store it within a GPS receiver. Because the accuracy of the GPS altitude reference is poor, an additional definition of the profile relief is performed using a tachometer or a high-precision GPS measurement device.
8. The qualities of the measurements are checked immediately after the observations are acquired through primary data processing and the construction of pseudo-sections of the apparent resistivity. High-density observations lead to smooth pseudo-sections without separate anomalous measurements. If the quality of the data obtained is doubtful, the measurements are repeated with an increase in the data accumulation number and an increased generator voltage. If abnormal measurements are observed at the same electrodes, then the grounding of those electrodes is checked and improved.
9. After performing measurements with a single electrode system, a part of the electrode array is physically moved for a long profile. After completing the measurement acquisition for one allocation, the first segment of the line is shifted by moving it to the end of the alignment along the observation profile (i.e., the “roll-along” technique). To accelerate movement of the array, connectors are located on both sides of the segments and the electrodes are connected to the same lines of the cable, thereby allowing one segment to remain stationary (Fig. 3.5). In this case, there is no sense in repeating the measurements in which only half of the electrodes are used. Therefore, it is recommended to apply the measurement sequence in which these measurements are already excluded. It is possible to move the array along a distance that is one-quarter of the whole line. This is convenient when working with lines that are divided into four segments. At the same time, the labor productivity is slightly reduced; however, with this disaggregation, the refinement of the work increases.
10. The result of the fieldwork is a set of pseudo-sections of apparent resistivities (Fig. 3.6). The qualities of the materials can be assessed directly in the field after the experiment. To quantify their quality, measurement errors are calculated. For ERT, these errors are calculated using the following formula:

$$\sigma = \frac{1}{N}\sum_{i}^{N}\frac{\left|\rho_i^{\mathrm{o}} - \rho_i^{\mathrm{c}}\right|}{\rho_i^{\mathrm{o}} + \rho_i^{\mathrm{c}}}\cdot 100\%,$$

where σ is the percentage error in the measurements using the ERT method, ρ_i^{o} is a measurement at the i-th common point, ρ_i^{c} is a control measurement at the i-th

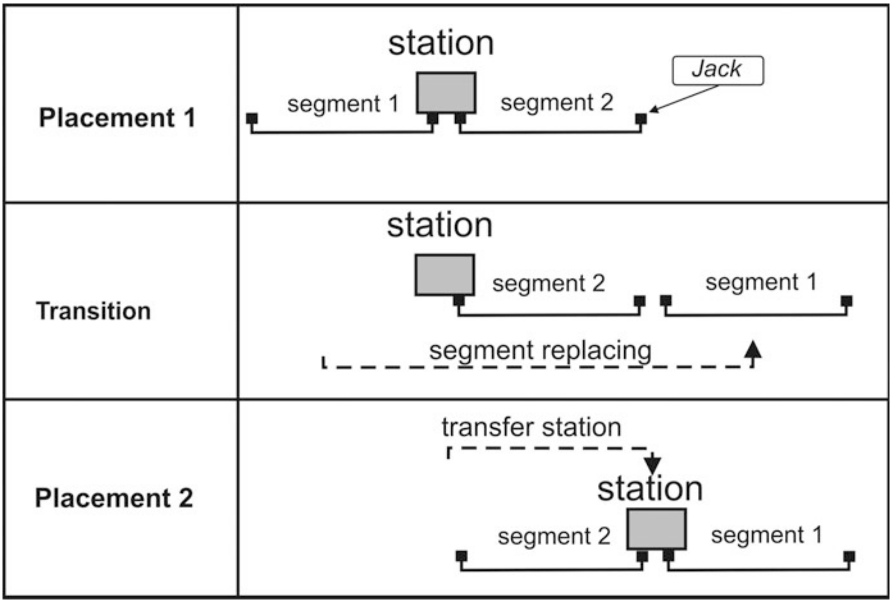

Fig. 3.5 Scheme of cable moving by technology roll-along

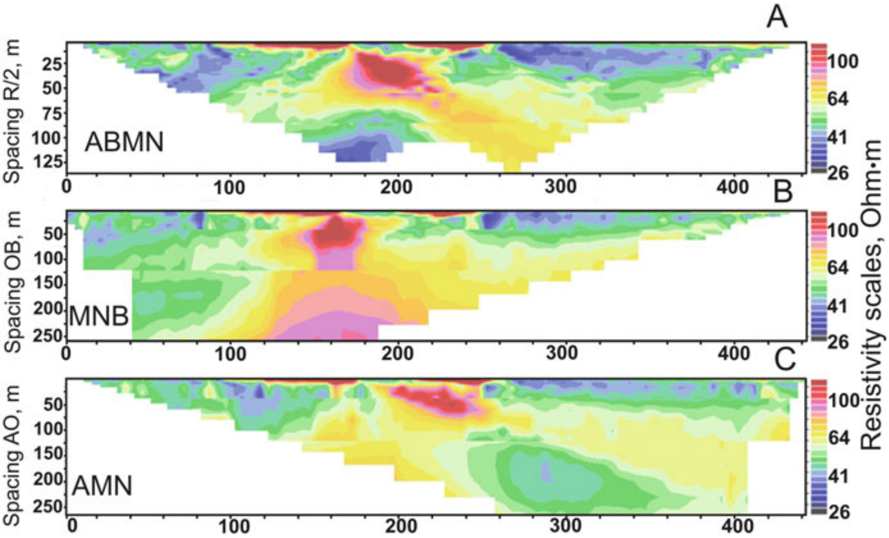

Fig. 3.6 Examples of pseudo-sections of apparent resistivities: (**a**) Dipole-Dipole array ABMN, (**b**) Pole-Dipole array MNB, and (**c**) Pole-Dipole array AMN

ordinary point, and N is the number of control points. As a rule, the obtained average value of the measurement error should not exceed 1–3% for each study site. An error of more than 5–7% indicates large interference, which can worsen the signal-to-noise ratio. It is therefore necessary to check for errors, especially for large distances where the useful signal can have a small amplitude. Large measurement errors can significantly affect the quality of the interpretation in future steps.

3.2 Mathematical Model of the Resistivity Method

One of the reasons for the popularity of the ERT method is that the mathematical methods for interpreting the measurement data are more developed. Maxwell's equations are the basic model for describing the electromagnetic field in a medium. Let us write the Maxwell equations in the SI system for the electromagnetic field in a medium:

$$\begin{aligned} \operatorname{rot}\mathbf{H} &= \mathbf{j} + \frac{\partial \mathbf{D}}{\partial t}, \\ \operatorname{rot}\mathbf{E} &= -\frac{\partial \mathbf{B}}{\partial t}, \\ \operatorname{div}\mathbf{B} &= 0, \\ \operatorname{div}\mathbf{D} &= q. \end{aligned} \tag{3.2}$$

Here, $\mathbf{H}$ is the magnetic field strength, $\mathbf{E}$ is the electric field strength, $\mathbf{B}$ is the magnetic induction, $\mathbf{D}$ is the electric induction and q is the bulk density of electric charge.

The system (3.2) is not yet closed. To close it, characteristics of the medium such as the coefficients of the dielectric constant, magnetic permeability, and specific electrical conductivity (or specific electrical resistance) are introduced. In the general case of an anisotropic medium, these coefficients form tensors. However, here we only consider isotropic media. In this case, each of these coefficients is a scalar.

The vectors of magnetic and electric induction are connected to the electric and magnetic field strengths by the following material equations:

$$\mathbf{D} = \varepsilon_0\varepsilon\mathbf{E}, \ \ \mathbf{B} = \mu_0\mu\mathbf{H}, \ \ \mathbf{j} = \sigma\mathbf{E}. \tag{3.3}$$

Here, ε and μ are the coefficients of the relative electric and magnetic permeabilities of the medium, σ is the coefficient of specific electrical conductivity, $\varepsilon_0 = 1/(\mu_0 c^2) = 8.854187 \times 10^{-12}$ F/m and $\mu_0 = 4\pi \times 10^{-7}$ H/m are the dielectric and magnetic constants, respectively, and $c = 299{,}792{,}458$ m/s is the speed of light in a vacuum.

Considering the material equations (3.3), Maxwell's equations are rewritten as follows:

$$\begin{aligned}
&\operatorname{rot}\mathbf{H} = \sigma\mathbf{E} + \varepsilon\varepsilon_0 \frac{\partial \mathbf{E}}{\partial t},\\
&\operatorname{rot}\mathbf{E} = -\mu\mu_0 \frac{\partial \mathbf{H}}{\partial t},\\
&\operatorname{div}(\mu\mu_0\mathbf{H}) = 0,\\
&\operatorname{div}(\varepsilon\varepsilon_0\mathbf{E}) = q.
\end{aligned} \tag{3.4}$$

In this monograph, we consider media with a piecewise constant distribution of electrical conductivity. However, the divergence operation in (3.4) does not make sense in the regions of conductivity jump. In this case, we must start from a more general, integral formulation of the Maxwell equations:

$$\begin{aligned}
&\oint\limits_{\partial S} \mathbf{H}\cdot\mathbf{dl} = \iint\limits_{S} \sigma E_n dS + \varepsilon_0 \frac{d}{dt} \iint\limits_{S} \varepsilon E_n dS\\
&\oint\limits_{\partial S} \mathbf{E}\cdot\mathbf{dl} = -\mu_0 \frac{d}{dt} \iint\limits_{S} \mu H_n dS,\\
&\oint\!\!\!\oint\limits_{S} \mu\mu_0 H_n dS = 0,\\
&\oint\!\!\!\oint\limits_{S} \varepsilon\varepsilon_0 E_n dS = Q.
\end{aligned} \tag{3.5}$$

Here, Q is the total charge inside the surface S. First, let us simplify the model for the case of ERT. In practice, for the vast majority of media, the coefficient of relative permeability μ can be assumed to be constant and equal to unity. In an electric tomography survey, the internal charges that create an electric field inside the medium are absent, and the current in the medium flows due to external sources only. Therefore, we can set $q = 0$ in (3.4). Let H_0, E_0, T, and X be the characteristic scales of the magnetic field strength, electric field, time, and spatial length, respectively. Now, introduce the relative (dimensionless) variables into (3.4):

$$\mathbf{H}' = \mathbf{H}/H_0, \quad \mathbf{E}' = \mathbf{E}/E_0, \quad t' = t/T, \quad \mathbf{r}' = \mathbf{r}/X. \tag{3.6}$$

Substituting (3.6) into (3.4), we obtain the equations with dimensionless variables:

$$
\begin{aligned}
&\operatorname{rot}\mathbf{H}' = \sigma\frac{E_0X}{H_0}\mathbf{E}' + \varepsilon\varepsilon_0\frac{E_0X}{TH_0}\frac{\partial\mathbf{E}'}{\partial t'},\\
&\operatorname{rot}\mathbf{E}' = -\mu\mu_0\frac{H_0X}{TE_0}\frac{\partial\mathbf{H}'}{\partial t'},\\
&\operatorname{div}(\mathbf{H}') = 0,\\
&\operatorname{div}(\varepsilon\varepsilon_0\mathbf{E}') = 0.
\end{aligned}
\tag{3.7}
$$

The system (3.7) contains more equations than unknowns (eight equations and six unknowns). However, the last two scalar relations express the conditions that the electric and magnetic fields must satisfy at the initial moment. It can be shown that if the last equations are satisfied at the initial time, then they are satisfied at each subsequent time. Therefore, assuming that at the initial moment these conditions are valid, we exclude the last two equations from consideration. Further simplification of the system (3.7) depends on the ratio of the physical quantities σ and $\varepsilon\varepsilon_0/T$. If the value of $\varepsilon\varepsilon_0/T$ in (3.7) is significantly less than the conductivity σ, then the second term in the first equation can be neglected. Therefore, the bias current is smaller than the conduction current. This result is possible if the source field has a low frequency or the magnitude of the characteristic time scale T is relatively large.

In this case, the second term on the right-hand side of the first equation, which is responsible for the bias current and is associated with the variable nature of the magnetic field, is negligible. Similarly, we can omit the right-hand side of the second equation. Instruments that are used for sounding in electrical tomography operate in the low-frequency range, up to 20 Hz, which allows the application of the direct current (DC) model (i.e., neglecting the dependence of the quantities in the equation on time). However, at higher frequencies, it is necessary to consider the omitted values. Depending on the frequency of the sounding signal and the values of the material constants, we can obtain other mathematical models, such as quasi-stationary and wave models.

Based on the above considerations, and returning to the dimensional variables, we obtain a DC model. This model is a theoretical basis for sounding by the ERT method:

$$
\begin{aligned}
&\operatorname{rot}\mathbf{H} = \sigma\mathbf{E},\\
&\operatorname{rot}\mathbf{E} = 0.
\end{aligned}
\tag{3.8}
$$

We now apply the divergence operation to the first equation of the model (3.8). Considering that $\operatorname{div}(\operatorname{rot}\mathbf{H}) = 0$, we obtain:

$$
\operatorname{div}(\sigma\mathbf{E}) = 0. \tag{3.9}
$$

The second equation in (3.8) shows that the electric field has an irrotational character; therefore, we can introduce the potential of the electric field, which is denoted by the function U:

$$\mathbf{E} = \mathrm{grad} U. \tag{3.10}$$

This relation identically satisfies the equation $\mathrm{rot}\mathbf{E} = 0$. By substituting (3.10) for (3.9), we obtain an equation for the potential function:

$$\mathrm{div}\,(\sigma\,\mathrm{grad}\,U) = \nabla \cdot (\sigma \nabla U) = 0. \tag{3.11}$$

In the case of an electrically homogeneous medium, the coefficient of (3.11) is constant, and we obtain the Laplace equation for the electric field potential:

$$\nabla \cdot \nabla U \equiv \Delta U = 0 \tag{3.12}$$

However, (3.12) holds for a constant conductivity coefficient. In the case of discontinuity in the conductivity, we must start from the integral form of the law of conservation of charge (3.9) that is written through the potential U. To this end, we integrate (3.9) with respect to an arbitrary volume V:

$$\iiint\limits_{V} \mathrm{div}\,(\sigma \nabla U) dV = \iint\limits_{\partial V} \sigma \nabla U \cdot \mathbf{dS} = \iint\limits_{\partial V} \sigma \frac{\partial U}{\partial n} dS = 0 \tag{3.13}$$

Let dV be the small element of the volume that is in the vicinity of some smooth surface on which the conductivity is discontinuous and has the values of $\sigma +$ and $\sigma -$ from different sides. Let the volume dV contain the element dΓ inside it. If the volume is contracted to the surface dΓ from two sides, from (3.13) we obtain:

$$\sigma_{+} \frac{\partial U}{\partial n}\bigg|_{+} = \sigma_{-} \frac{\partial U}{\partial n}\bigg|_{-}. \tag{3.14}$$

Relation (3.14) expresses the equality of the normal current from two sides of surface Γ. The potential function completely determines the electric field in the medium. To determine the current density at any point in the medium, we apply Ohm's law and obtain:

$$j = \sigma \nabla U = \frac{1}{\rho} \nabla U.$$

3.3 Direct and Inverse Problems in the Resistivity Method

In this section, we provide some examples of the formulation of direct and inverse problems for the mathematical models of ERT. Maxwell's equations are linear, which allows us to use the principle of the superposition of electric fields. Therefore, the resulting field in the medium, which is induced by different sources, is equal to the vector sum of the fields from each source. When the current is ejected in the medium, two poles (positive and negative) are necessarily present; they can change their polarity with a given frequency. However, the time in which the ERT devices are reading the data from electrodes is so small that the current in this interval can be regarded as constant; as shown in Sect. 3.2, an approximation of the DC theory is sufficient at low frequencies. Furthermore, according to the principle of superposition, in numerical modeling, we consider problems in which an electric field is excited by a single source (sink). In the presence of several sources (sinks), the potentials (electric fields and currents) from all sources can be algebraically combined. Therefore, in most of the mathematical models that are considered here, we consider the case of a single point source.

Let us consider the simplest model of a source with a current I that is placed at the origin in a homogeneous conducting half-space $z > 0$ with specific conductivity σ (and resistivity $\rho = 1/\sigma$). In this case, the potential is given by the function

$$U = -\frac{I}{2\pi\sigma r} = -\frac{I\rho}{2\pi r}. \tag{3.15}$$

Here, r is the distance to the source. It is easy to check that the function (3.15) satisfies Laplace's equation. The electric field strength for a point source has the form:

$$\mathbf{E} = \nabla U = \frac{I}{2\pi\sigma r^2}\frac{\mathbf{r}}{r}, \tag{3.16}$$

and the current density at each point of the medium is given by the following formula:

$$\mathbf{j} = \sigma\mathbf{E} = \frac{I}{2\pi r^3}\mathbf{r}.$$

Due to the spherical symmetry of the source function, at all points of the surface of the medium (formed by the plane $z = 0$), the component of the electric field $E_{\mathrm{n}} = 0$ is normal to the surface. Therefore, at all points of the surface of the medium, except the origin, the current is equal to zero. By the definition of the potential (3.15), the total current that is flowing into the medium is equal to I. Indeed, integrating over a hemisphere of radius R with the center at the origin, we obtain the total current from Ohm's law:

$$\int_0^{\pi}\int_0^{\pi/2} j_n d\Gamma = \int_0^{\pi}\int_0^{\pi/2} \sigma E_n R^2 \sin d\theta d\varphi = \frac{I}{2\pi}\int_0^{2\pi}\int_0^{\pi/2} \sin d\theta d\varphi = I.$$

The representation (3.15) is convenient if the size of the electrode through which the current flows into the medium is negligible compared with the step between the measuring electrodes. As a rule, this condition is satisfied in practice. Let us use the definition of the Dirac delta function and write the boundary condition in symbolic form. If a current source is placed at the origin, then the current density that is directed along the normal to the boundary is

$$\frac{\partial U}{\partial n} = \frac{I}{\sigma R_0^2} \cdot \delta(r). \tag{3.17}$$

Here, $\delta(r)$ is a cylindrically symmetric delta function such that the integral over any circle that encloses the origin is unity. The multiplier corresponds to the dimension of the current density, because the delta function is a dimensionless abstract mathematical object. We now consider the case of an inhomogeneous medium in which the conductivity coefficient $\sigma(x, y, z)$ depends on the coordinates of the points. Let the medium occupy the half-space $z > 0$. In this case, the field potential satisfies the following equation and boundary conditions:

$$\begin{cases} \nabla \cdot (\sigma \nabla U) = 0, \quad z > 0 \\ \sigma \dfrac{\partial U}{\partial z}(x, y, 0) = \dfrac{I}{R_0^2} \cdot \delta(r), \quad r = |\mathbf{r}| = \sqrt{x^2 + y^2 + z^2} \\ \lim\limits_{r \to \infty} U = 0. \end{cases} \tag{3.18}$$

If the function $\sigma(x, y, z)$ is defined at all points of the medium, then the problem (3.18) is a direct problem. To solve a direct problem, it is necessary to find a distribution of the electric field in a medium $U(x, y, z)$ that satisfies the conditions (3.18). In a general case, the problem (3.18) is solved numerically; analytic solutions are known only for certain simple cases. The solution to the direct problem determines the value of the field on a surface of the medium $U(x, y, 0)$. If the conductivity distribution $\sigma(x, y, z)$ is known, then the results of the numerical calculation of the function $U(x, y, 0)$ should be close to the measured values. Such situations are realized under the conditions of physical modeling, when the researcher artificially forms a medium with known properties and conducts measurements on it. Then, a numerical simulation is performed, and the results are compared with the measured data. Such modeling allows, for example, the errors of a mathematical model to be estimated.

However, in practice, the goal of the survey is to obtain the distribution of the resistivity, (i.e., it is a priori unknown). Therefore, the data to solve a direct problem are insufficient. However, we can measure the potential difference on the surface and calculate the apparent resistivities of the medium. These data give additional information for determining the conductivity of the medium, which is how the inverse problem arises; in geophysics, this problem is called the data interpretation problem. However, based on additional data, the researcher can make assumptions regarding the nature of the distribution $\rho(x, y, z)$ in the medium. Depending on these assumptions, different formulations of inverse problems are possible. For example, if the medium is vertically nonuniform, then the resistivity function depends only on the depth z. As shown above, in ERT, the current electrodes are placed in different positions. However, if the distribution of resistivities in the medium depends only on the depth z, then the measurement results remain the same when moving the array along the profile. This observation provides a basis for solving the problem of interpretation within the framework of a one-dimensional (1D) medium model. In this case, considering the superposition principle, it is sufficient to consider only one position of the current electrode. Because of the cylindrical symmetry of the field, the equations of the direct problem are written in a cylindrical coordinate system (r, φ, z) in this case. Because of the cylindrical symmetry, the dependence on the azimuth angle φ is omitted, and the direct problem has the following form:

$$\begin{aligned}
&\frac{\partial}{\partial z}\left(\sigma(z)\frac{\partial U}{\partial z}\right)+\frac{\sigma(z)}{r}\frac{\partial}{\partial r}\left(r\frac{\partial U}{\partial r}\right)=0, \quad z>0, \quad r>0\\
&\sigma(0)\frac{\partial U}{\partial z}(r,0)=\frac{I}{R_0^2}\cdot\delta(r),\\
&\lim_{z\to\infty}U(r,z)=0, \quad \lim_{r\to\infty}U(r,z)=0.
\end{aligned}$$

Note that by setting the scales for the quantities $U(r, z)$, then $\sigma(z)$, r, and z are $I/(\sigma(0)\, R_0)$, $\sigma(0)$, and R_0, respectively. Then the direct problem in the dimensionless variables has the following form:

$$\begin{aligned}
&\frac{\partial}{\partial z}\left(\sigma(z)\frac{\partial U}{\partial z}\right)+\frac{\sigma(z)}{r}\frac{\partial}{\partial r}\left(r\frac{\partial U}{\partial r}\right)=0, \quad z>0, \quad r>0\\
&\frac{\partial U}{\partial z}(r,0)=\delta(r),\\
&\lim_{z\to\infty}U(r,z)=0, \quad \lim_{r\to\infty}U(r,z)=0.
\end{aligned} \tag{3.19}$$

The inverse problem is posed as follows: find the distribution $\sigma(z)$ from the measurements of the potential on the surface with

$$\frac{\partial U}{\partial r}(r,0)=\psi(r), \quad 0<r<\infty \tag{3.20}$$

In geophysics, inverse problems are often called data interpretation problems, and the solution procedure is called “inversion.” Examples of numerical algorithms to solve the inverse problem (3.19) with the data (3.20) are provided in the literature (Mukanova and Orunkhanov 2010; Mukanova 2013a, b). Formulations of the direct and inverse problems for the mathematical model (3.19) can be modified if we introduce a medium with piecewise constant resistivity that depends on the coordinate z. In this case, we arrive at the classic model of a horizontally layered medium. The distribution of the function $\sigma(z)$ is described by a finite number of parameters, such as the depths of the layers and their resistivities (see, for instance, Sect. 3.4). Some ideas for the approximate solution to the inverse problem for this model of the medium are described (Koefoed 1979). The solution to the problem in an interactive mode, with the active participation of the user, is realized in several software packages, for example, in the program IPI2Win (http://geophys.geol.msu.ru/ipi2win.htm), co-authored by I. N. Modin.

The requirements for the correct statement of a mathematical problem were first formulated by French mathematician and mechanic Jacques Hadamard. According to Hadamard, a problem is posed correctly (well-posed) and it makes sense to solve it if and only if the problem satisfies the following three conditions:

1. A solution to the problem exists
2. The solution is unique
3. The solution depends continuously on the input data

A problem that meets these requirements is called a *direct problem*. The classical problems of mathematical physics are stated in such a way that these requirements are satisfied. However, in practice, not all problems are well-posed. The main reason for this is a lack of information. The main feature of inverse problems is that they do not satisfy Hadamard's conditions.

Definition. A problem where the necessary data for the statement of a direct problem are insufficient, but some additional information about the solution is available, is called an *inverse problem*.

Definition. Inverse problems in which the unknown data are the coefficients of the equations are called *coefficient inverse problems* (CIPs).

Note that CIPs are characterized by large instability with respect to the input data (i.e., they are ill-posed). Nonetheless, they have the greatest practical interest because the coefficients of the mathematical model usually contain information about the properties of the medium, such as the thermal conductivity, electrical permeability, elasticity, and speed of sound in the medium. In many practical applications, these coefficients must be determined on the basis of some indirect measurements and other available additional information. However, when we have more additional information, the inverse problem can be solved more accurately.

In practice, ERT often assumes that the distribution of the resistivity has a two-dimensional (2D) character. In this case, the measured data are obtained by moving the current electrodes along the profile. It is also possible to formulate the inverse problem for a three-dimensional (3D) conductivity distribution. In this case, a survey is performed on the 2D surface to obtain the measured data. Let us construct a possible formulation of the inverse problem for the 2D resistivity distribution. Let the surface of the medium coincide with the plane $z = 0$, the abscissa axis be directed along the profile, and a a parameter that describes the position of the supply electrode along the profile $a = (a, 0, 0)$. Then, the potential that is created by a point source depends on the coordinates (x, y, z) and the parameter a: $U = U(x, y, z, a)$. In the inverse problem statement, it is necessary to find the distribution of the electrical resistivity $\rho(x, z)$ of the medium from the measured data on the surface:

$$U(x,y,0,a) = \psi(x,a), \quad 0 < x < L, \quad 0 < a < L. \tag{3.21}$$

where the function $U(x, y, z, a)$ is a solution to the following boundary value problem:

$$
\begin{aligned}
&\frac{\partial}{\partial x}\left(\sigma(x,z)\frac{\partial U}{\partial x}\right)+\sigma(x,z)\frac{\partial^2 U}{\partial y^2}+\frac{\partial}{\partial z}\left(\sigma(x,z)\frac{\partial U}{\partial z}\right)=0, \quad z>0\\
&\sigma(x,0)\frac{\partial U}{\partial z}(x,y,0,a)=\delta(\mathbf{r}-\mathbf{a}),\\
&\lim_{r\to\infty} U(x,y,z,a)=0, \quad r=\sqrt{x^2+y^2+z^2}.
\end{aligned}
\tag{3.22}
$$

Thus, according to the sounding data, which form a function of two variables $\psi(x, a)$, it is also necessary to determine the function of two variables $\rho(x, z)$ for the values of $0 < x < L$ and $0 < z < L$. This problem is currently being solved by using 2D inversion programs, which convert the measured data into a geoelectric profile $\rho(x, z)$ (http://www.geotomosoft.com/downloads.php; http://zond-geo.ru/english/zond-software/ert-and-ves/zondres2d/).

The formulation of the inverse problem that is presented above is adapted to the theory of CIPs. In this formulation, it is assumed that the potential can be measured at each point of the profile and for an arbitrary position of the current electrode. However, in ERT practice, the values of the potential differences are measured at certain points along the profile. Through these potential differences, the apparent resistivity is calculated, relative to the points at the center of each segment of MN. This discrete set of apparent resistivity values forms a geoelectrical pseudo-section. Then, it is entered into an inversion program. The inversion program, in turn, generates a geoelectric section.

The present inversion programs provide a solution in the form of a smooth function. However, for geologists and geophysicists, it is usually required in practice to provide the sounding results with the sharply defined boundaries of different media. This is necessary, for example, to assess the amounts of the reserves of materials. Therefore, the result of the interpretation is transformed into a geoelectric section with a piecewise constant resistivity distribution. After this step, it makes sense to simulate the constructed section with a piecewise constant resistivity function, which allows us to determine how accurately the obtained model fits the measured data. The most accurate and efficient method for modeling such media is the method of integral equations. The method of boundary finite element represents a special case of the integral equations method (IEM) and has many applications. This method is discussed in later chapters. To check the correctness of the numerical algorithms and determine the admissible numerical parameters, it is useful to conduct test calculations on known analytical solutions.

3.4 The Electric Field of a Point Source Above a Horizontally Layered Medium

The material in this chapter has a reference nature and is partly written based on the known solutions and techniques that are described in the literature. The algorithm for calculating the apparent resistivity that is described in this section is further used in testing the numerical methods that are described in Chaps. 4 and 5.

3.4.1 Introduction

For geological reasons, sedimentary rocks, which in most cases form the upper part of the section, accumulate in the form of layered strata. At the same time, the horizontal boundaries of the layers can extend over very long distances: for continental deposits, this distance can be tens or hundreds of meters, and for marine sedimentary rocks, these boundaries can extend many kilometers or tens of kilometers. Such strata can consist of dozens of layers of considerable thickness that differ significantly in their lithology and that can therefore have different electrical properties. In the first approximation, the properties of a single layer in the horizontal direction change insignificantly. If the array is placed completely within the boundaries of this layered medium, then the most suitable mathematical model of the section under investigation is a horizontally layered stratum; at each point, the electric resistivity varies only vertically. The model of a horizontally layered medium is the first and a very important approximation of the geological structure of the earth. This model was completely dominant in electrical exploration until the early 1990s, when a more complex model of a horizontally inhomogeneous 2D medium appeared. Such a transition is natural due to the development of technical capabilities, the theory of electrical exploration, and the use of personal computers at all stages of geophysical survey.

The model of the medium is shown in Fig. 3.7. The model under consideration is divided into two half-spaces: an upper half-space, which has a very high resistivity of air, and a lower half-space, which consists of *n* layers. Suppose that at point *A* on the surface of the earth, where the origin of the coordinates is located, there is a

Fig. 3.7 Model of horizontally inhomogeneous layered medium

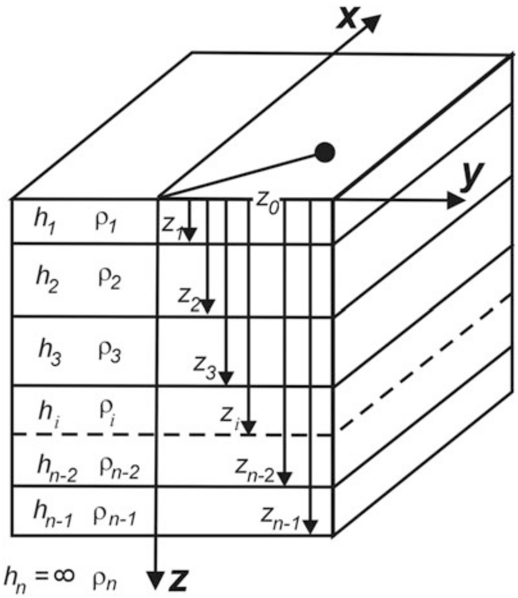

current electrode A ($z_A = 0$). The layers have resistivities of $\rho_1, \rho_2, \ldots, \rho_i, \ldots, \rho_{n-1}$ and thicknesses of h_1, $h_2, \ldots$, $h_i, \ldots$, h_{n-1}, respectively. The lowest layer has an infinitely large thickness, and our arrays "do not feel" its base. The soles of the layers (the depths of the lower boundaries) are located at the marks d_1, $d_2, \ldots$ $d_i, \ldots$ d_{n-1}. The problem is stated as follows: find a component of the electric field on the earth's surface for $z = 0$ that is directed radially from the point source at a distance r.

3.4.2 *Statement of the Problem and Its Solution in General Form*

1. It is necessary to find the solution to Laplace's equation $\Delta U = 0$ in each of the layers. We write the Laplace equation (3.11) in cylindrical coordinates:

$$\frac{1}{r^2}\frac{\partial^2 U}{\partial \phi^2} + \frac{\partial^2 U}{\partial r^2} + \frac{1}{r}\frac{\partial U}{\partial r} + \frac{\partial^2 U}{\partial z^2} = 0.$$

   The electric field and its potential have axial symmetry, giving $\frac{\partial U}{\partial \varphi} = 0$. Therefore, the Laplace equation takes a simpler form:

$$\frac{\partial^2 U}{\partial r^2} + \frac{1}{r}\frac{\partial U}{\partial r} + \frac{\partial^2 U}{\partial z^2} = 0.$$

2. At the contact of the layers, we state the boundary conditions that correspond to the equality of the potentials, the equality of the normal components of the current density, and the absence of a vertical component of the current density on the earth's surface:

$$U_i = U_{i+1}\big|_{z=z_i}; \quad \frac{1}{\rho_i}\frac{\partial U_i}{\partial z} = \frac{1}{\rho_{i+1}}\frac{\partial U_{i+1}}{\partial z}\bigg|_{z=z_i}; \quad \frac{\partial U_1}{\partial z} = 0\bigg|_{z=0}.$$

3. The potential near the source in the first layer comprises the potential of the primary current source itself and the anomalous potential $U'_1(r, z)$, which originates from the reflections of the electric field from the upper and lower boundaries of the first layer:

$$U_1 = \frac{I\rho_1}{2\pi}\frac{1}{\sqrt{r^2 + z^2}} + U'_1(r, z).$$

   For brevity, we use the notation $q = \frac{I\rho_1}{2\pi}$.
4. The physical condition for the damping of the field at infinity must be satisfied. At a considerable distance from the source, all functions $U_1 \ldots U_n \to 0$, as $r, z \to \infty$.
5. We determine the solution to the Laplace equation $\Delta U = 0$ by separating the variables in the form

$$U = u(r) \cdot v(z).$$

$$\frac{1}{u(r)} \frac{d^2u(r)}{dr^2} + \frac{1}{ru(r)} \frac{du(r)}{dr} + \frac{1}{\nu(z)} \frac{d^2v(z)}{dz^2} = 0.$$

This equation has two terms: the first term depends only on r, the second term depends only on z, and their sum is zero. Therefore, each term is equal to a constant, such that the two constants have different signs. Therefore, each of these parts of the equation constitutes a new equation. In particular, we can write the equation for $u(r)$ in the following form:

$$\frac{1}{u} \frac{d^2u}{dr^2} + \frac{1}{ru} \frac{du}{dr} = -m^2.$$

The last expression is the Bessel equation, whose solutions are the Bessel functions of the first type of zero order $c_1J_0(mr)$. Here, c_1 is an arbitrary constant.

The second equation is the Helmholtz equation

$$\frac{1}{v} \frac{d^2v}{dz^2} = m^2,$$

whose solution is the exponential function

$$c_2e^{mz} + c_3e^{-mz}.$$

A particular solution can be represented in the form

$$(c_2e^{mz} + c_3e^{-mz})c_1J_0(mr) = (c_1c_2e^{mz} + c_1c_3e^{-mz})J_0(mr) = (Ae^{mz} + Be^{-mz})J_0(mr).$$

A general fundamental solution for each layer and for all m can be represented in integral form through exponential and cylindrical functions:

$$U_i = \int\limits_0^\infty (A_ie^{-mz} + B_ie^{mz})J_0(mr)dm$$

Here, A_i and B_i are functions that depend on the geological section's parameters in each layer. We note an interesting feature of the last formula. We use the well-known Fourier transform formula

$$U(x, y, z) = \frac{1}{2\pi} \int\limits_{-\infty}^{\infty} \int \widetilde{U}\left(\sqrt{k_x^2 + k_y^2}, z\right) e^{-i\left(k_xx+k_yy\right)} dk_xdk_y,$$

which is related to the Hankel transform as follows:

$$U(x,y,z) = \int_{-\infty}^{\infty} \widetilde{U}(mz)J_0(mr)mdm.$$

From the structures of the last expressions, the integrand function $\widetilde{U}$ is the same in the Fourier and Hankel transforms. Therefore, this function is henceforth called the spectral potential. We note one more feature that follows from the Hankel transform: the integration variable m, which was introduced purely formally, physically represents an infinite set of spatial frequencies that describe the structure of the electric potential of a point source for a given medium structure. In addition, it is easy to show that the boundary conditions are satisfied for the spectral potential and its derivatives.

6. In the first layer, the potential comprises the potential of the primary source itself and the anomalous potential that is associated with the influence of the earth's surface and the base of the first layer:

$$U_1 = \frac{q}{\sqrt{r^2+z^2}} + \int_0^{\infty} (A_1 e^{-mz} + B_1 e^{mz}) J_0(mr)\, dm;$$

$$\frac{\partial U_1}{\partial z} = 0|_{z=0}$$

The equality of the first derivative of the potential on the surface of the earth corresponds to the physical condition of the absence of a vertical current from the earth to air. It cannot penetrate upwards, because air has very high resistivity. The vertical component of the current density from each primary source is equal to zero, since an imaginary reflection occurs in the form of an imaginary source. This reflection completely compensates for the action of the primary source at the boundary. In addition, the aggregate of secondary sources generates a zero for the vertical current density on the surface of the earth, which can be written formally as

$$-mA_1 e^{-mz} + mB_1 e^{mz}|_{z=0} = 0; \qquad \Rightarrow A_1 = B_1.$$

The first term in the equation for the potential in the first layer can be represented according to the Weber–Lipschitz formula in the form of an integral:

$$\frac{1}{\sqrt{r^2+z^2}} = \int_0^{\infty} e^{-mz} J_0(mr) dm.$$

Then, the integrand for the spectral potential can be written in the following form:

$$\widetilde{U}_1 = qe^{-mz} + B_1(e^{-mz} + e^{mz}).$$

For $z = 0$, all the exponentials tend to unity, and the expression for the potential in the first layer acquires a relatively simple form:

$$U_1(r) = \int\limits_0^\infty (q + 2B_1)J_0(mr)dm. \tag{3.23}$$

Thus, the coefficient B_1 must be found for the integral in (3.23) to be calculated, and it depends on the parameters of the geoelectric section

7. In the last layer, $B_n\exp(mz) \to \infty$ as $z \to \infty$ and, consequently, does not satisfy the physical condition of damping the potential. We equate B_n to zero because this term is responsible for the field from the lower edge of the layer. Indeed, when the measurement point approaches the lower edge inside the layer, this component of the field grows with depth as we approach the secondary charges at the lower edge of the layer. The last layer has no bottom edge, and there are no sources of this component. Consequently,

$$\begin{aligned} &B_n \equiv 0 \\ &\widetilde{U}_n = A_n e^{-mz}. \end{aligned}$$

Now, we can write out all the equations for the spectral potential for all layers:

$$\begin{aligned} &\widetilde{U}_1 = qe^{-mz} + B_1(e^{-mz} + e^{mz}); \\ &\widetilde{U}_2 = A_2e^{-mz} + B_2e^{mz}; \\ &\ldots\ldots\ldots\ldots\ldots\ldots\ldots\ldots\ldots \\ &\widetilde{U}_i = A_ie^{-mz} + B_ie^{mz}; \\ &\ldots\ldots\ldots\ldots\ldots\ldots\ldots\ldots\ldots \\ &\widetilde{U}_{n-1} = A_{n-1}e^{-mz} + B_{n-1}e^{mz}; \\ &\widetilde{U}_n = A_ne^{-mz}. \end{aligned}$$

The boundary conditions for the spectral potential are written similar to the boundary conditions for the ordinary potential:

$$\widetilde{U}_i = \widetilde{U}_{i+1}|_{z=z_i}; \quad \frac{1}{\rho_i}\frac{\partial \widetilde{U}_i}{\partial z} = \frac{1}{\rho_{i+1}}\frac{\partial \widetilde{U}_{i+1}}{\partial z}|_{z=z_i}.$$

Then, the equalities for the base of the first layer at $z = z_1$, for the internal boundaries $z = z_i$, and for the last boundary on the roof of the lower layer can be written as a system of equations:

$$\left.\begin{array}{l}
B_1(e^{-mz_1}+e^{mz_1}) = A_2e^{-mz_1}+B_2e^{mz_1};\\
\frac{1}{\rho_1}[B_1(e^{-mz_1}-e^{mz_1})] = \frac{1}{\rho_2}[A_2e^{-mz_1}-B_2e^{mz_1}];\\
\bullet\bullet\bullet\\
A_ie^{-mz_i}+B_ie^{mz_i} = A_{i+1}e^{-mz_i}+B_{i+1}e^{mz_i};\\
\frac{1}{\rho_i}[A_ie^{-mz_i}-B_ie^{mz_i}] = \frac{1}{\rho_{i+1}}[A_{i+1}e^{-mz_i}-B_{i+1}me^{mz_i}];\\
\bullet\bullet\bullet\\
A_{n-1}e^{-mz_{n-1}}+B_{n-1}e^{mz_{n-1}} = A_ne^{-mz_{n-1}};\\
\frac{1}{\rho_{n-1}}[A_{n-1}e^{-mz_{n-1}}-B_{n-1}e^{mz_{n-1}}] = \frac{1}{\rho_n}A_ne^{-mz_{n-1}}.
\end{array}\right\}$$

It is easy to verify that this system contains n equations and n unknown quantities. For example, for a three-layered medium, we have four independent equations (two boundary conditions on the roof and two boundary conditions on the base of the second layer) and four unknowns, namely, B_1, A_2, B_2, and A_3.

8. We aim to find an electric field on the surface of the earth. That is, we aim to determine the coefficient B_1. The resulting system can be solved in a usual way by excluding the variables. In this case, the unknowns are obtained through rather cumbersome calculations. It is more convenient to solve the system by using an algorithm that implements the sweep method.

Divide the left-hand side of the first equation by the left-hand side of the second equation, and, correspondingly, divide the right-hand side of the first equation by the right-hand side of the second equation:

$$\frac{\frac{A_i}{B_i}e^{-mz_i}+e^{mz_i}}{\frac{A_i}{B_i}e^{-mz_i}-e^{mz_i}} = \frac{\rho_{i+1}}{\rho_i}\frac{\frac{A_{i+1}}{B_{i+1}}e^{-mz_i}+e^{mz_i}}{\frac{A_{i+1}}{B_{i+1}}e^{-mz_i}-e^{mz_i}}$$

Denote

$$R_i(z_i) = \frac{\frac{A_i}{B_i}e^{-mz_i}+e^{mz_i}}{\frac{A_i}{B_i}e^{-mz_i}-e^{mz_i}}, \quad R_{i+1}(z_i) = \frac{\frac{A_i}{B_i}e^{-mz_i}+e^{mz_i}}{\frac{A_i}{B_i}e^{-mz_i}-e^{mz_i}}.$$

Then,

$$R_i(z_i) = \frac{\rho_{i+1}}{\rho_i}R_{i+1}(z_i).$$

Elementary algebraic transformations give

$$\frac{A_i}{B_i} = e^{\left(\frac{1}{2}\ln\frac{A_i}{B_i}+\frac{1}{2}\ln\frac{A_i}{B_i}\right)}; \quad 1 = e^{\left(\frac{1}{2}\ln\frac{A_i}{B_i}-\frac{1}{2}\ln\frac{A_i}{B_i}\right)}.$$

Substitute the formulas above into the expression for $R_i(z_i)$, and obtain the simple expression of the hyperbolic cosine:

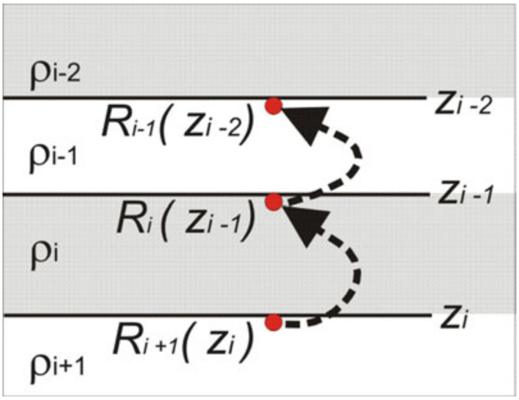

Fig. 3.8 The bottom-up sweep algorithm in the R_i calculation

$$R_i(z_i) = \frac{e^{\frac{1}{2}\ln\frac{A_i}{B_i}}\left[e^{\left(\frac{1}{2}\ln\frac{A_i}{B_i}-mz_i\right)} + e^{-\left(\frac{1}{2}\ln\frac{A_i}{B_i}-mz_i\right)}\right]}{e^{\frac{1}{2}\ln\frac{A_i}{B_i}}\left[e^{\left(\frac{1}{2}\ln\frac{A_i}{B_i}-mz_i\right)} - e^{-\left(\frac{1}{2}\ln\frac{A_i}{B_i}-mz_i\right)}\right]} = \mathrm{cth}\left(\frac{1}{2}\ln\frac{A_i}{B_i} - mz_i\right).$$

It is not difficult to derive an expression for $R_i(z_{i-1})$ in terms of $R_{i+1}(z_i)$:

$$R_i(z_{i-1}) = \mathrm{cth}\left(arcth\frac{\rho_{i+1}}{\rho_i}R_{i+1}(z_i) + mh_i\right).$$

Figure 3.8 shows a scheme of the transition from bottom to top in computing R_i. At each subsequent step, we move to the top of the next upper layer and calculate $R_{i-1}(z_{i-2})$. Finally, we find R_1 at the earth's surface:

$$R_1(0)|_{z=0} = \mathrm{cth}\left[mh_1 + arcth\frac{\rho_1}{\rho_2}R_2(h_1)\right].$$

On the top of the last lower layer, $R_n = 1$ because $B_n = 0$:

$$R_n = \frac{A_n e^{-mz_{n-1}} + 0 \cdot e^{mz_{n-1}}}{A_n e^{-mz_{n-1}} - 0 \cdot e^{mz_{n-1}}} \equiv 1.$$

Therefore, we can start from the $(n-1)$th layer:

$$R_{n-1}(z_{n-2}) = \mathrm{cth}\left[mh_{n-1} + arcth\frac{\rho_n}{\rho_{n-1}}\right].$$

At the first layer, formally, R_1 is equal to

$$R_1(0) = \frac{B_1 e^{-mz} + B_1 e^{mz} + q e^{-mz}}{B_1 e^{-mz} - B_1 e^{mz} + q e^{-mz}}\Big|_{z=0}$$
$$= \frac{2B_1 + q}{q}\Big|_{z=0}.$$

By the expression $2B_1 + q = qR_1(0)$ and (3.23), we have

$$U_1 = \frac{I\rho}{2\pi} \int\limits_0^\infty R_1(m,0) J_0(mr) dm.$$

Note that

$$\frac{\partial J_0(mr)}{\partial r} = -mJ_1(mr),$$

where J_1 is a Bessel function of the first type and first order.

Now, we can formally write the solution to the problem and calculate the apparent resistivity, which, with Ohm's law, can be written in the form of a Hankel integral:

$$\rho_\kappa = \frac{E}{j_0} = \frac{2\pi r^2}{I}\left(-\frac{\partial U}{\partial r}\right) = \rho_1 r^2 \int\limits_0^\infty R_1(0) J_1(mr)\, m\, dm. \tag{3.24}$$

The integral (3.24) for apparent resistivity was obtained by mathematicians in the 1930s. It seems that only simple tasks remain, namely, to calculate the integral in formula (3.24) and determine the apparent resistivity value. However, from a practical point of view, implementation of the algorithm encounters an intractable obstacle in the form of a Bessel function, which has a quasiperiodic character and decays very slowly with increasing argument. Direct computations of the Hankel integral (3.24) are extremely inefficient, even on modern computers. For a long time, there was no way to solve this problem effectively. To solve the inverse problems for the VES method practically, mathematicians and geophysicists used to apply many interpretation charts that made it possible to obtain estimates with very low accuracy in terms of the parameters of the geoelectric section.

Finally, in the 1970s, a theoretical approach to the solution to this problem was created, and in the mid-1980s, numerical methods to solve the integral (3.24) were developed. These new methods allow one to obtain the solution to a direct problem with high accuracy and rapid calculation (practically in real time). With the advent of personal computers, highly advanced interpreting programs were written, and these algorithms are still used to solve the inverse problem in the VES method. Let us briefly discuss the essence of numerically computing the integral (3.24).

3.4.3 Algorithm of Linear Filtration

Introduce the new variables $x = \ln r$ and $y = \ln(1/m)$ into formula (3.24). Then, $r = e^x$, $m = e^{-y}$, and $dm = -e^{-y}dy$. The limits of integration are $y = \infty$ for $m = 0$ and $y = -\infty$ for $m = \infty$. Then, we have

$$\rho_\kappa = \rho_1 e^{2x} \int_{\infty}^{-\infty} R_1(e^y) J_1(e^{-y} e^x) e^{-y}(-e^{-y}) dy = \rho_1 \int_{-\infty}^{\infty} R_1(e^y) J_1\left(e^{(x-y)}\right) e^{(2x-2y)} dy.$$

The last integral is a convolution:

$$\rho_\kappa = \rho_1 \int_{-\infty}^{\infty} R(y) g(x-y) dy = \rho_1 \int_{-\infty}^{\infty} R(x-y) g(y) dy.$$

It is important that the function $g(y)$ does not depend on the parameters of the medium. Only the function $R(y)$ is related to the geoelectrical section, and $R(y)$ contains all the information of the section. Then, its discrete form can be written as a linear filter. The formula of the linear filter is quite simple:

$$\rho_a(r_j) = \rho_1 \cdot \sum_{k=1}^{n} R(x_{k+j-1}) \cdot g(k),$$

where R is a function that depends on the geological section parameters and the abscissa value x, which has the physical meaning of the length of the spatial wave; $g(k)$ denotes the coefficients of the filter of which there are n; r is the separation ($AB/2$); and j is its index. In the literature, the formula of a linear filter is often given in a slightly different form: when R depends on m, where $m = 1/X$, then the index for m has the form $(j - k)$, and the coefficients g are specified in inverse order. However, the use of X instead of m is more convenient, because it is easier to work with indices. In addition, with increasing X, the values of R correspond to the greater depth of the study, which is analogous to the behavior of ρ_a with increasing r.

The principle of linear filtration can be explained with the help of Fig. 3.9: the top line is the axis of spacing r on a logarithmic scale. Below it, also on a logarithmic scale, is the $X = 1/m$ axis. To compute the value of ρ_a for one spacing of r, it is necessary to calculate the n values of the function R for a grid of values of X_i that increase in a geometric progression with a coefficient q. The difference between the values of r and the central point X_C is called the shift α (where $\alpha = X_C/r$). Based on the number of coefficients to the left of the center (M), one can calculate the position of the first point X with respect to r:

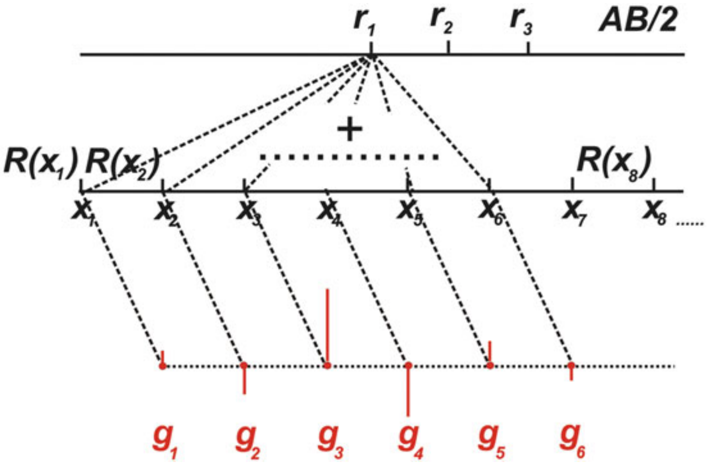

Fig. 3.9 Diagram of the linear filtration algorithm

$$X_1 = r \cdot \alpha / q^{\mathrm{M}}. \tag{3.25}$$

To calculate ρ_{a} for the following values of r, which increase with the same factor q as the X values, we can use all the values of R (except the first) that were calculated for the previous spacing of r.

At the third lower level (see Fig. 3.9), a set of filter coefficients is schematically shown. The value of each coefficient can be either positive or negative; the coefficients with the largest modulus are found in the middle part of the filter, and they decrease toward the edges. The sum of all the filter coefficients must be equal to 1. For example, we can cite the filter parameters that were computed by V. A. Shevnin for a symmetric Schlumberger array (S-16). The number of filter coefficients n is equal to 15, the number of points per decade equals 7, $\alpha = 1.005$, and $M = 9$. The values of the filter coefficients are −0.015821, 0.203596, −1.222006, 3.856356, −5.567616, 2.414293, −0.758876, 2.122195, −0.671525, 0.783732, −0.290884, 0.169452, −0.031227, 0.003612, and 0.004705. The sum of all coefficients is equal to 0.99998610.

The VES curve of type Q is shown in Fig. 3.10. The calculation is most difficult for this type of apparent resistivity curve because the anomalous field with large spacing should almost completely compensate for the primary field, and the remaining difference field must be calculated with very high accuracy. The quality of the calculated VES curve can be estimated from the right asymptote, which exactly corresponds to 1. In this case, the calculation speed is several milliseconds, and the resistivity contrast between the first and second layer is 0.001, which is practically unattainable with most of the existing algorithms. For many years, V. A. Shevnin's filters have been successfully used in the program of interactive interpretation of electrical soundings IPI2Win, which was developed by the team at the Moscow Electrotechnical Laboratory and has been widely used in Russia and other countries.

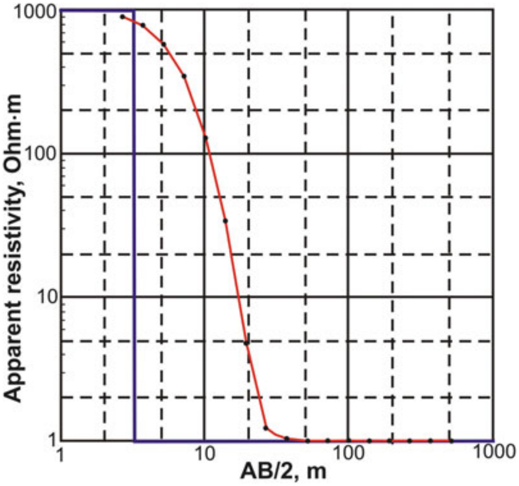

Fig. 3.10 The VES curve $\rho_2/\rho_1 = 0.001$

3.5 Introduction to the Integral Equations Method and the Boundary Element Method

The few medium models that yield analytical solutions to direct problems are usually characterized by a piecewise constant resistivity distribution. If the solution cannot be constructed analytically, the most convenient method for applications is the method of integral equations and its modified form the boundary element method (BEM). To facilitate an understanding of the material in subsequent chapters, and as an introduction to the method, let us consider the solution to the electrical sounding problem above an inclined plane. Based on this example, we demonstrate application of the reflection method and the derivation of the integral equation and provide some recommendations for the numerical solution to the problem. All of these techniques are later generalized to more complicated models of media.

Thus, consider the problem of determining the field and its derivatives for a point source that is located above an inclined plane. Suppose that the half-space $\{z \geq 0\}$ corresponds to the earth and is divided by an inclined plane into regions with different resistivities ρ_1 and ρ_2 (Fig. 3.11).

The potential of a stationary current source in a medium with constant conductivity satisfies Laplace's equation,

$$\Delta U = 0. \tag{3.26}$$

Equation (3.26) holds everywhere in $\Omega = \{(x, y, z)|z > 0\}$ except the geoelectrical boundary $\Gamma = \{(x, y, z) \in \Omega, |z = \tan(\alpha)x, \ \ \alpha < \pi/2\}$.

The conditions of continuity of the potential and the current density in the normal direction with respect to the boundary Γ are written as follows:

$$U|_{-} = U|_{+}, \tag{3.27}$$

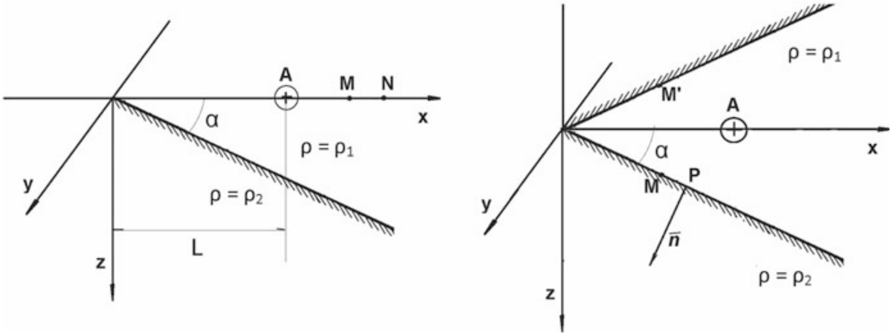

Fig. 3.11 Sounding scheme above an inclined plane (left) and reflection into upper half-space (right)

$$\frac{1}{\rho_1}\frac{\partial U}{\partial n}\bigg|_{-} = \frac{1}{\rho_2}\frac{\partial U}{\partial n}\bigg|_{+}. \tag{3.28}$$

The signs "+" and "−" mean that the normal derivative is taken from the corresponding side of the boundary Γ. The positive direction of the normal corresponds to the + sign and is directed from a medium with resistivity ρ_1 to a medium with resistivity ρ_2. The condition of vanishing at infinity and the boundary condition on the earth's surface must also be satisfied:

$$\begin{aligned} &U(\infty) = 0 \\ &\frac{\partial U}{\partial z}\bigg|_{z=0} = \frac{I\rho_1}{R_0^2}\cdot\delta\left(\vec{r} - \overrightarrow{OA}\right). \end{aligned} \tag{3.29}$$

Here, R_0 is some scale of length. The function $\delta(\boldsymbol{r})$ is the generalized Dirac delta function such that the integral over the surface of the ball that surrounds point A is equal to one and at all other points, is equal to zero. In this case, condition (3.29) simulates a point current source, and the delta function symbolically describes the current that is flowing into the medium. The multiplier $I/R_0{}^2$ (3.29) reflects the dimensional nature of the current density, since the delta function is introduced as a dimensionless abstract mathematical object. According to Ohm's law, the normal derivative of the potential is proportional to the current density by the formula (3.29),

$$\frac{\partial U}{\partial n} = \rho_1 \cdot j_n.$$

This yields the representation of the boundary condition (3.29).

We pass to the dimensionless variables by taking as units of the potential and length scale the quantities of $I/(\rho_1 R_0)$ and R_0, respectively. Then, we seek the potential $U(P)$ in the problem (3.26,. 3.27, 3.28, and 3.29) in the form of

$$U(P) = \frac{I\rho_1}{R_0}(U_0(P) + u(P)), \tag{3.30}$$

where $P = (x,\ y,\ z)$, $U_0(P) = -\left(2\pi\sqrt{x^2 + y^2 + z^2}\right)^{-1}$ is a known solution to the potential of a point source in a homogeneous half-space, and $u(P)$ is an addendum to the solution due to the presence of a geoelectric boundary Γ. The representation (3.30) allows us to eliminate the singularity in the boundary condition (3.29) and write the condition for the function $u(P)$ as follows:

$$\left.\frac{\partial u}{\partial z}\right|_{z=0} = 0. \tag{3.31}$$

The representation (3.30) is known in geophysics as an expression of the field as a sum of a "normal" and an "anomalous" field. Accordingly, the field consists of a field without inhomogeneity, plus some additive term that is related to this inhomogeneity. In this case, the normal field corresponds to a homogeneous half-space, and the anomalous field is associated with the presence of an inclined plane. This representation means that we interpret the inhomogeneities of the medium as certain secondary sources of the field, which introduce distortions into the field in a homogeneous medium. The problem of calculating the field and apparent resistivity was first stated in an article by Tikhonov (1946), and it is shown that the problem reduces to an integral equation. Here, we derive this equation, because fragments of this reasoning are used in the following chapters for more complicated medium models.

In this example, we demonstrate the application of the reflection method, which is often used to solve the direct problems of VES, where the ground surface of the medium is assumed to be flat. The condition (3.31) can be treated as a symmetry condition for the extension of the function $u(x,\ y,\ z)$ to the entire space. This condition is easily satisfied if the lower half-space is symmetrically reflected into the upper half-space so that the medium occupies the entire space (Fig. 3.11). Next, introduce the secondary current sources with a certain density $\nu(M)$ that are distributed on the boundary Γ and that are symmetrically distributed on its reflection in the upper half-space Γ'. We now seek the function $u(P)$ in the form of the potential of the sources that are distributed on the surfaces Γ and Γ':

$$\begin{aligned} u(P) &= \frac{1}{2\pi}\iint\limits_{\Gamma}\frac{\nu(M)}{|PM|}\mathrm{d}\Gamma(M) + \frac{1}{2\pi}\iint\limits_{\Gamma'}\frac{\nu(M')}{|PM'|}\mathrm{d}\Gamma'(M) \\ &= \frac{1}{2\pi}\iint\limits_{\Gamma}\nu(M)\left(\frac{1}{|PM|} + \frac{1}{|PM'|}\right)\mathrm{d}\Gamma(M). \end{aligned} \tag{3.32}$$

Here, point M' is a point that is symmetrical to M with respect to the plane $z = 0$. The function $\nu(M)$ is a function of two variables that are defined at the plane Γ. According to the materials in Chap. 2 (Sect. 2.2), this function *u(P)* satisfies Laplace's equation on $\Omega\backslash\Gamma$ and is continuous and symmetrical with respect to the plane $z = 0$. This result guarantees the fulfillment of the boundary conditions (3.31) and (3.27). The conditions (3.29) are satisfied because of the function $U_0(P)$ and because the simple-layer potential $u(P)$ decreases at infinity. Now, it is necessary for the function $\nu(M)$ to satisfy the condition (3.28). The condition (3.28) is expressed in terms of the function $u(P)$ as follows:

$$\frac{1}{\rho_2}\frac{\partial u}{\partial n}\bigg|_{\Gamma_+} - \frac{1}{\rho_1}\frac{\partial u}{\partial n}\bigg|_{\Gamma_-} = \left(\frac{1}{\rho_1} - \frac{1}{\rho_2}\right)\frac{\partial U_0}{\partial n}(P). \tag{3.33}$$

In (3.33), we consider that the function $\partial U_0/\partial n$ is continuous on Γ; therefore, its derivatives on both sides of the surface coincide with and are equal to $\partial U_0/\partial n(P)$.

We use the formula (2.6) from Chap. 2 for the values of the normal derivative of the potential of a simple layer from two sides of the surface:

$$\left(\frac{\partial u}{\partial n}\right)_-(P) = \nu(P) + \frac{1}{2\pi}\iint_\Gamma \nu(M)\frac{\partial}{\partial n_P}\left(\frac{1}{|PM|} + \frac{1}{|PM'|}\right)\mathrm{d}\Gamma$$

$$\left(\frac{\partial u}{\partial n}\right)_+(P) = -\nu(P) + \frac{1}{2\pi}\iint_\Gamma \nu(M)\frac{\partial}{\partial n_P}\left(\frac{1}{|PM|} + \frac{1}{|PM'|}\right)\mathrm{d}\Gamma.$$

Substitute these expressions in the formula (3.33):

$$\frac{1}{\rho_2}\left(-\nu(P) + \frac{1}{2\pi}\iint\limits_\Gamma \nu(M)\frac{\partial}{\partial n_P}\left(\frac{1}{|PM|} + \frac{1}{|PM'|}\right)d\Gamma(M)\right) -$$
$$\frac{1}{\rho_1}\left(\nu(P) + \frac{1}{2\pi}\iint\limits_\Gamma \nu(M)\frac{\partial}{\partial n_P}\left(\frac{1}{|PM|} + \frac{1}{|PM'|}\right)d\Gamma(M)\right) = \left(\frac{1}{\rho_1} - \frac{1}{\rho_2}\right)\frac{\partial U_0}{\partial n}(P). \tag{3.34}$$

Remark 3.1 The gradient vector of the function $1/|PM|$ at point P is always directed from point M to point P (i.e., it lies in the plane Γ); simultaneously, the direction of the normal **n** at any point is always orthogonal to the plane Γ. Therefore, the angle between the normal **n** and the gradient is always equal to $\pi/2$. Hence, the normal derivative is equal to zero:

$$\frac{\partial}{\partial n_P}\left(\frac{1}{|PM|}\right) \equiv 0 \tag{3.35}$$

for all points $M \in \Gamma$. This method provides an advantage to the geoelectric model with flat boundaries: the singularity in the kernel of the integral equation vanishes due to (3.35) as $M \to P$. The reflection coefficient is denoted by $\kappa = (\rho_1 - \rho_2)/(\rho_1 + \rho_2)$. After obvious transformations, we obtain from (3.34) and (3.35) the integral equation for the density function of the simple layer $\nu(P)$:

$$\nu(P) = \frac{\kappa}{2\pi} \iint\limits_{\Gamma} \nu(P) \frac{\partial}{\partial \mathbf{n_P}} \left(\frac{1}{|PM'|} \right) \mathrm{d}\Gamma(M) + \kappa \frac{\partial U_0}{\partial \mathbf{n}_P}(P) \tag{3.36}$$

The potential is calculated through the function $\nu(P)$ in the form

$$u(P) = \frac{I\rho_1}{2\pi R} \iint\limits_{\Gamma} \nu(M) \left(\frac{1}{r_{PM}} + \frac{1}{r_{PM'}} \right) \mathrm{d}\Gamma_M \tag{3.37}$$

Equation (3.36) is one of the simplest integral equations in geophysical models and can be solved by the BEM. Tikhonov (1946) showed that the integral operator in (3.36) is contractive, the solution to the integral equation exists, and the iterative process converges to this solution for all κ.

For the BEM application, we must approximate (3.36) by using its discrete form. For a numerical implementation of the method, we restrict the boundary Γ to some finite domain G. Therefore, the integrals over the outer part of this region are neglected or we assume that the density of the secondary charges is negligible far from the current source. This approach is physically justified: if the primary field decreases with increasing distance from the source, then the secondary field that is generated by it must also decrease at infinity. Stricter estimates of the nature of the decrease in the density of secondary sources are obtained in Chap. 4.

Moreover, in the computational domain G, a grid is constructed. This grid divides G into cells. Because of the symmetry with respect to the $y = 0$ axis, it is sufficient to search for the unknown function in the half of the computational domain in which $y > 0$.

There are different options for mesh construction. Because our computational area is flat, the simplest version of the sampling is obtained on a uniform rectangular mesh. Figure 3.12 shows possible meshes.

Let us introduce a coordinate system (ξ, η) on the computational area (Fig. 3.12). Let the boundaries of the grid cells be given by the formulas $\xi_i = i \cdot h$, $\eta_j = j \cdot h$, $i, j = 0, N$. The mesh step is equal to $h = L/N$, where L is the width of the calculated area, and h is a sampling step.

Denote the cell of the computational area by $S_{ij} = \{(\xi, \eta) | \xi_i < \xi_i \le \xi_{i+1}, \eta_j < \eta_j \le \eta_{j+1}\}$. Let us consider various ways of approximating unknown functions through their discrete values on a grid. We have a function of two variables that is defined on a 2D rectangular grid domain. It can be assumed that, within a single cell, the density of secondary sources $\nu(P)$ is constant. Such a sampling corresponds to the simplest type of approximation through a finite-element function that is constant within each cell.

It is known that a finite-element function is a finite function with bounded support that represents a polynomial of degree n. A finite element of degree zero ${\varphi_{ij}}^0(x, y)$ is a function that is equal to one within a single grid cell (i, j) and is equal to zero in all other cells. Then, an arbitrary function, which is defined by its values in the grid cells, can be approximated by a linear combination of finite elements:

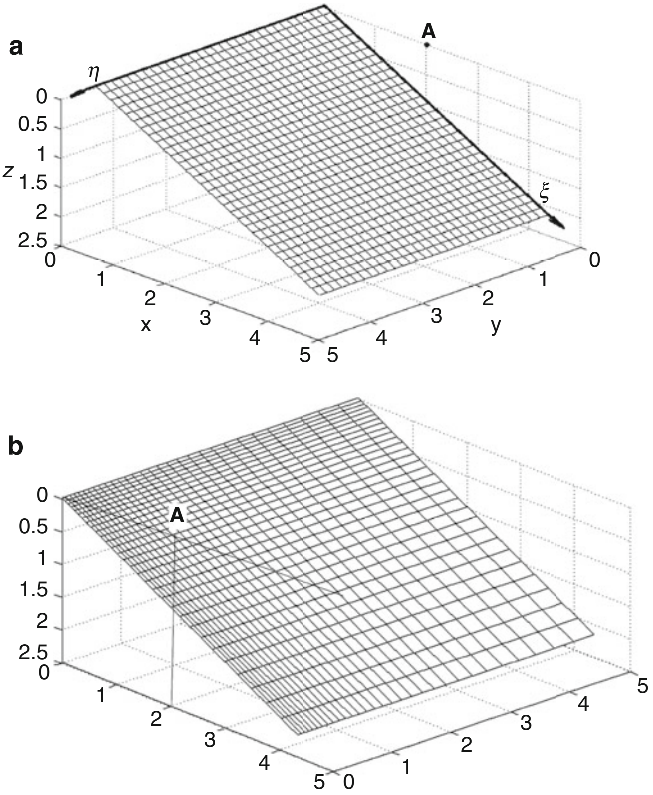

Fig. 3.12 Uniform grid on coordinate system (ξ, η) on the computational area (**a**) and corresponding non-uniform grid on Cartesian coordinates (**b**)

$$\nu(\xi,\eta) = \sum_{k,\,l=1}^{N} \nu_{kl}\varphi_{kl}^{0}(\xi,\eta). \tag{3.38}$$

We denote by the indices (i, j) the constant values of the functions within the cell S_{ij}. In this approximation, integration by the rectangle formula yields a natural approximation of the integral in (3.36). Then, (3.36) can be written in the following approximate discrete form:

$$\nu_{ij} = \sum_{k,\,l}^{N} K_{ij,kl}\nu_{kl} + b_{ij}, \quad i = \overline{1,N}, \quad j = \overline{1,N} \tag{3.39}$$

Here, the coefficients of (3.39) are defined by the following formulae:

$$K_{ij,kl} = \frac{\kappa}{2\pi}\frac{\partial}{\partial n_P}\left(\frac{1}{\mid P_{ij}M_{kl}{}' \mid}\right)S_{kl}, \quad b_{ij} = \kappa\frac{\partial U_0}{\partial n_P}\left(P_{ij}\right), \tag{3.40}$$

where point P_{ij} is the center of the cell (i, j), point $M_{kl}{}'$ is the center of the cell (k, l) that is reflected in the upper half-space, and S_{kl} is the area of the cell (k, l).

The potential (3.37) can be computed similarly through a discrete approximation of the integral over the boundary Γ. The method of boundary finite elements is a method in which the approximation of unknown functions is conducted with the help of finite elements that are defined on the boundary surfaces (see, for instance, Brebbia 2012).

However, the rectangle formula has the lowest accuracy among the formulae of numerical integration. To improve the accuracy of numerical integration, it is necessary to use higher-order numerical integration formulae. These formulae are based on the approximation of a function on the grid cells through their values at grid nodes by higher-order polynomials or by higher-order boundary elements. In particular, linear finite elements that depend on two variables can be defined on triangles. Therefore, for the application of linear elements, triangulation of the computational domain is necessary. The application of linear boundary elements and triangulation algorithms is described in Chap. 5. We note that the trapezoid formula corresponds to the integration of the functions that are approximated by finite linear elements. It is possible to use finite elements of a higher order; however, this use is relevant only to problems that are formulated in terms of differential equations. In our case, we reduce all problems to integral equations; therefore, for the purposes of our research, smoothness of the finite elements is not required to be higher than linear.

Let ν_{ij} be the value of an unknown function at grid node (i, j). To improve the accuracy of the calculations, we approximate the integral in (3.36) by using the Simpson cubature formula, which has fourth-order accuracy on a rectangular grid. In this case, the equation again reduces to the form (3.39). However, such an approximation is not a realization of a certain finite elemental representation because, in this case, we do not write out an explicit formula for a finite element of the second order, which would constitute a basis for representing the function in a form that is analogous to (3.38).

In this sense, BEM can be treated as a particular case of the IEM. In this section, in the numerical examples, we calculate the integrals by using the cubature formula of Simpson.

Using the obtained solution $\nu(M)$, it is possible to calculate the potential function and construct the apparent resistivity curves for different positions of the measuring line with respect to the slope of the inclined plane. This method is implemented numerically on the basis of the following iterative scheme:

$$\begin{aligned} \nu_0(M) &= \kappa \frac{\partial U_0}{\partial n}(M), \\ v(M) &\approx \sum_0^n \kappa^k v_k(M), \end{aligned} \tag{3.41}$$

$$\nu_k(M) = \frac{1}{2\pi} \iint\limits_{\Gamma} \nu_{k-1}(M_1) \frac{\partial}{\partial n_1} \left(\frac{1}{r_{MM_1'}} \right) d\Gamma(M_1), \tag{3.42}$$

The potential $u(P)$ is approximately calculated by formula (3.37) through $\nu_n(M)$. For different positions of the measuring line concerning the slope of the formation, different values of the slope angle, and the conductivity ratios of the layers, it is possible to calculate the apparent resistivity curves from the potential values.

The algorithm was tested by comparing the apparent resistivity curves for a small angle of inclination of 5° with the apparent resistivity curves for a two-layer medium. The curves for a two-layer medium were built based on the solution that was constructed in Sect. 3.4. At a sufficiently small angle of inclination of the boundary (5°), similar curves of apparent resistivity are obtained at different positions of the measuring line, namely, 0°, 90°, and 180°. The relative difference between the theoretical curve for horizontally layered medium and computed curves for inclination angle of 5° did not exceed 4%. The apparent resistivity was calculated by the theoretical limit formula:

$$\rho_a = \frac{2\pi s^2}{I\sigma_1} \frac{du}{ds}, \tag{3.43}$$

where the parameter s is measured along the profile. The use of the theoretical curve (3.43) makes it possible to compare the solution to the available analytical solution for the field potential and apparent resistivity and to verify the quality of the numerical solution.

To test the method, the calculation results were compared with the solution that is was obtained by Skalskaya (1948) for an inclination angle of π/4, which is given in the form of the 2D convolutions of the Bessel function with a known function. The solution, which is constructed according to the formula (Skalskaya 1948) for an angle of inclination of 45°, was compared with the data obtained in the numerical solution to the integral equation. This method achieves good accuracy in computing the apparent resistivity along the slope direction of the second layer and a measuring line that is parallel to the line of the intersection of the second layer with the earth's surface. Table 3.2 shows the comparison of results for this case. Here, L is the size of the calculation area that is shown in Fig. 3.12 along the axes (ξ, η) on which the density of a single layer was calculated. As a length scale, the vertical distance from the source to the boundary of G was taken. The case of high media contrast was the

Table 3.2 Comparison of the numerical solution with the analytical solution for an inclined plane with $\alpha = \pi/4$ on a uniform grid

Grid size	L (domain size)	Contrast ρ_2/ρ_1	Relative error Δ_u (%)
60 × 60	16	5	1.2
60 × 60	16	9	2.2
60 × 60	16	79	3.6
60 × 60	11	79	3.2
100 × 100	11	79	2.6

least favorable for the convergence of iterations and the accuracy of the calculation. Maximum error is achieved when the contrast of the media is increased; however, this error decreases with the refinement of the mesh. In the vicinity of the intersection of G with the earth's surface, the accuracy of the calculation drops sharply and, in the worst conditions, with a high contrast ($\sigma_2/\sigma_1 = 1/80$) and coarse mesh (60×60), reaches 18%.

The 3D distribution of the potential at inclination angles, which is necessary to consider in practice (for angles that exceed 10°), is calculated on a grid of size 50×50 in 10–20 iterations.

This problem and all other problems that are considered here have the following peculiarity: to increase the accuracy of the calculation, it is necessary to both increase the size of the calculation area and refine the mesh. These requirements lead to a situation in which expansion of the computational domain with an unchanged number of grid points causes low accuracy in the domains in which the gradient of the unknown function is large.

Note that the solution changes little for the points that are far from the current source, and there is thus no reason to use the same mesh density that is in the vicinity of the current source. The idea of constructing an adaptive mesh has long been used in numerical solutions to the problems of mathematical physics. We can also implement it in solving the integral equation. However, we do not want to lose the fourth-order accuracy of Simpson's formula for numerical integration on a uniform grid. To combine these two requirements, it is necessary to construct a mesh that is dense in the areas in which the gradient of the solution is large and uniform with some changes in the variables. For instance, a uniform grid that is constructed with a logarithmic variable scale satisfies these two requirements. This grid can be constructed by the following changes in the variables:

$$p(\xi,\eta) = \ln(1+\xi), q(\xi,\eta) = \ln(1+\eta). \tag{3.44}$$

For the conductivity ratio $\sigma_1/\sigma_2 = 79$ on a 60×60 mesh with calculated area $L = 11$, the relative accuracy of the potential near the surface line on a uniform grid is above 18% and for a nonuniform grid is equal to 6%; for the ratio $\sigma_1/\sigma_2 = 5$, these values are 6% for a uniform grid and 3% for a nonuniform grid, with 15 iterations.

Computational accuracy can be improved by further refinement of the mesh. Figure 3.13 shows the distribution of the densities of a simple layer on a uniform and logarithmic grid; the higher degree of detail of the data for the logarithmic grid is evident. Systematic calculations of apparent resistivity for multiple conductivity ratios and slope angles yield the following acceptable calculation parameters: the size of the domain in two coordinates is $[-5, 5] \times [5, 5]$; the size of the logarithmic grid is 32×32; and numerical integration is conducted by using the 2D Simpson formula. With these parameters, the maximum deviation from the exact solution for the slope angle $\pi/4$ does not exceed 6%.

Now, we derive the equations for the case of several parallel inclined layers. Let Γ_0 be the earth's surface and Γ_i be the slope boundary between two media with the

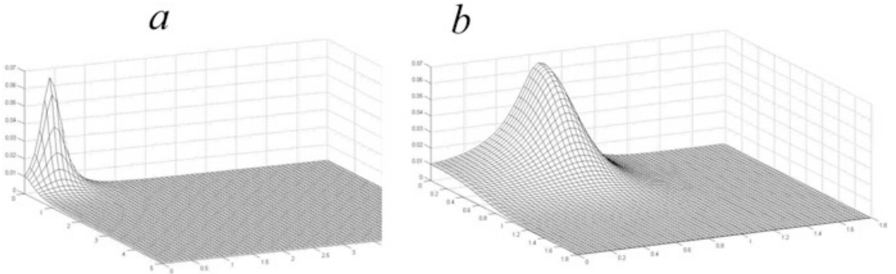

Fig. 3.13 The densities of a simple layer on (**a**) uniform and (**b**) logarithmic grids. The slope of the geoelectric boundary is 30°, and $\sigma_2/\sigma_1 = 1.5$

conductivities σ_i and σ_{i+1} for $i = 1,\ldots, n$. We seek the potential of the pointwise current source over several inclined layers in the form

$$U = \frac{I}{R\sigma_1}\left(-\frac{1}{2\pi r} + u\right) \tag{3.45}$$

Here, r is the dimensionless distance to the source. The function u satisfies Laplace's equation, the boundary conditions at infinity, and the boundary conditions on the contact surfaces of the media:

$$\left.\frac{\partial u}{\partial n}\right|_{\Gamma_0} = 0, \quad u|_{\Gamma_i^-} = u|_{\Gamma_i^+},$$

$$\sigma_i \left.\frac{\partial u}{\partial n}\right|_{i^-} - \sigma_{i+1}\left.\frac{\partial u}{\partial n}\right|_{i^+} = -\left[(\sigma_i - \sigma_{i+1})\left.\frac{\partial U_0}{\partial n}\right|_i\right] \tag{3.46}$$

The function $U_0 = -1/(2\pi r)$ is a potential of a point source in the dimensionless variables.

Similar to the method above, we symmetrically reflect the lower half-space to the upper half-space and search for the solution u in the form of the potential of several simple layers that are distributed on the angled contact boundaries and their reflections in the upper half-space:

$$u(M) = \frac{1}{2\pi}\sum_{i=1}^{n}\left(\iint\limits_{\Gamma_i} \nu_i(M_i)\frac{d\Gamma_i}{|MM_i|} + \iint\limits_{\Gamma_i} \nu_i(M_i')\frac{d\Gamma_i'}{|MM_i'|}\right) \tag{3.47}$$

From formulae (2.6) for the derivative of the potential of a single layer, which is taken from the different sides of the boundary Γ_i, we obtain:

$$\left(\frac{\partial u}{\partial \mathbf{n}}\right)_{i^-}(M) = \nu_i(M) + \frac{1}{2\pi}\iint\limits_{\Gamma_i} \nu_i(M_i)\frac{\cos\left(\mathbf{n}, MM_i'\right)}{|MM_i'|^2}\mathrm{d}\Gamma_i + \\ \frac{1}{2\pi}\frac{\partial}{\partial \mathbf{n}_i}\left[\sum_{i\neq j}\iint\limits_{\Gamma_j}\nu_j(M_j)\left(\frac{1}{|MM_j|}+\frac{1}{|MM_j'|}\right)\mathrm{d}\Gamma_j\right], \tag{3.48}$$

$$\left(\frac{\partial u}{\partial \mathbf{n}}\right)_{i^+}(M) = -\nu_i(M) + \frac{1}{2\pi}\iint\limits_{\Gamma_i} \nu_i(M_i)\frac{\cos\left(\mathbf{n}, MM_i'\right)}{MM_i'2}\mathrm{d}\Gamma_i + \\ \frac{1}{2\pi}\frac{\partial}{\partial \mathbf{n}_i}\left[\sum_{i\neq j}\iint\limits_{\Gamma_j}\nu_j(M_j)\left(\frac{1}{|MM_j|}+\frac{1}{|MM_J'|}\right)\mathrm{d}\Gamma_j\right], M\in\Gamma_i. \tag{3.49}$$

The conditions (3.46) imply that the function $u(M)$ must be satisfied on the boundaries between the layers. Substituting the expressions (3.48) and (3.49) into (3.46), we obtain a system of n integral equations that determine the unknown densities ν_i for $i = 1,..,n$:

$$\nu_i(M) = \frac{\kappa_i}{2\pi}\left[\iint\limits_{\Gamma_i}\nu_i\frac{\cos\left(\mathbf{n}, MM_i'\right)}{\left|MM_i'\right|^2}\mathrm{d}\Gamma_i + \frac{\partial}{\partial \mathbf{n}_i}\left(\sum_{i\neq j}\iint\limits_{\Gamma_j}\nu_j\left(\frac{1}{|MM_j|}+\frac{1}{\left|MM_j'\right|}\right)\mathrm{d}\Gamma_j\right)\right] \\ + \kappa_i\frac{\partial U_0}{\partial \mathbf{n}_i}(M). \tag{3.50}$$

Here, $\kappa_i = (\sigma_{\mathrm{i}+1} - \sigma_{\mathrm{i}})/(\sigma_{\mathrm{i}+1} + \sigma_{\mathrm{i}})$.

Another widely known method for solving direct problems is the finite difference method (FDM). FDM is described in sufficient detail in textbooks; therefore, we do not describe it here. Note that in the case of a gradient medium in which the resistivity is a smooth function of the coordinates of the point in the medium, this method is a natural choice for solving the direct problem. Currently, there are software packages that implement the solution to multidimensional Maxwell equations with the FDM, such as the MEEP package, which is available on the Massachusetts Institute of Technology (MIT) website:

(https://meep.readthedocs.io/en/latest/).

However, geophysical objects do not always have continuous distributions of electrical properties. For example, in the case of a discontinuous conductivity coefficient, (3.11) generally does not make sense, and the solution to the problem should be understood in the weak sense. Nevertheless, in this case, it is also possible to construct a difference scheme by using the finite volume method. To construct a divergent difference scheme and to accord with the definition of a weak solution, we must start from the more general integral form of (3.13). In the finite volume method, the difference scheme is constructed based on an approximation of the integral conservation law that is written for each elementary volume of the grid, such as the finite-difference time-domain (FTDT) method. The disadvantage of this method is its implementation on a grid with a constant step and the need to discretize the entire 3D domain of the solution. An example of a solution to the VES direct problem for a medium that contains a cylindrically symmetric inclusion was discussed in by Orunkhanov et al. (2004a, b). Our experience has shown that computing the apparent resistivity based on the difference method is inefficient because it produces large errors as a result of numerical differentiation on the mesh; in addition, the influence of artificial boundary conditions, which are required by the difference scheme, is significant. To avoid these issues, it is necessary to expand the computing area greatly. Based on an analysis of the results of the application of the IEM to the inclined plane problem and the results of modeling from the finite volume method (Orunkhanov et al. 2004a, b), we prefer the IEM in its modified BEM form. The most important advantage of this method is that only the boundary of the computational domain is subject to discretization, which considerably reduces the amount of computation. The results of applying this method are presented in Chaps. 4 and 5.

Next, we list the reasons for choosing IEM and BEM for media with sharply expressed geoelectric boundaries:

(a) The distribution of the potential is 3D, but the sought-after distribution of a single layer is a function of two spatial variables; thus, the computational costs are comparable to the computational costs of 2D problems.
(b) Compared with the FDM, apparent resistivities are calculated more accurately.
(c) The numerical realization is simpler than the method of finite volumes in the 3D case.
(d) A natural scheme for parallelizing computations is allowed.
(e) The method admits a natural generalization to several inhomogeneities, which may be the subject of further research.
(f) Constructing an adaptive mesh is simpler in the 2D case than in the 3D case.

3.6 Methods of Solving Inverse Problems

The regularization method and minimization of the residual functional are widely used to solve inverse problems. To introduce these concepts, we first define the inverse problem operator.

The operator of the inverse problem and a set of well-posedness. All the problems that were mentioned in Sect. 3.3 can be presented in a mapping form that compares the required missing functions and measured data. Thus, an *inverse problem operator* can be determined for each inverse problem. Considering that, in ERT, we are mostly interested in recovering the conductivity σ, let σ denote the input data for this operator. To formulate the direct problem correctly, this operator associates the data that are missing with some additional information or measured data (ψ):

$$\Lambda\sigma = \psi \tag{3.51}$$

Then, the inverse problem solution is reduced to the inversion of the operator (3.51): the existence of a unique solution to the inverse problem is equivalent to the existence of the inverse operator Λ^{-1}.

Let us consider the problems (3.19) and (3.20). It is practically possible to create a physical model with predetermined properties and perform measurements on it. Then, for the same model, one can solve a direct problem. The experimental data always differ from the solution to the direct problem that is obtained numerically using model (3.19). These differences between the model and the observed data occur because the measured data are always contaminated with many errors, including errors of the mathematical model, measurement errors, and other noises. Therefore, it is only possible to satisfy (3.20) approximately.

The problem of the continuous dependence on input data is reduced to the question of the continuity of the inverse operator Λ^{-1}. In many practically important cases, the operator Λ does not have a continuous inverse operator in its domain of definition. For instance, in the CIP (3.19) and (3.20), the output data are measured data $\psi(r)$, and the solution to the CIP is the function $\sigma(z)$.

In geophysics, there are principles of equivalence that state that similar measured data can correspond to geoelectric sections that are very different from one another. Therefore, the functions $\sigma(z)$ that are far from one another can yield similar curves of apparent resistivity. This finding obviously violates the stability requirement regarding the solution to the inverse problem, because very distant functions $\sigma(z)$ can correspond to the same input data $\psi(r)$ within the admissible measurement error. However, the uniqueness condition for the solution can nevertheless be satisfied (see, for example, Tikhonov 1949). Examples of how these features of interpretation problems are expressed in 1D problems are provided, for instance, by Koefoed (1979).

Usually, the question of the existence of a solution for each measured function remains open, and the inverse problem is replaced by some other problem that is solvable. This method is discussed next.

Let us define a misfit functional as follows:

$$J(\sigma) = \|\Lambda\sigma - \psi\|_2^2 \tag{3.52}$$

This functional represents the difference between the data $\Lambda\sigma$ that we obtain if the given function σ is substituted into the direct problem, and the measured data ψ. Then, the inverse problem is reduced to the minimization problem of the functional (3.52). This problem again raises questions concerning the existence of a minimum of this functional in the set of possible functions $\sigma \in \Sigma$. However, in many practically important cases, the problem of minimizing $J(\sigma)$ can be solved by applying the Tikhonov regularization method (Ivanov 1962; Tikhonov and Arsenin 1977). First, we should restrict the operator Λ to some compact subset S of Σ (Tikhonov and Arsenin 1977). In numerical simulations, this subset is bounded and belongs to some finite dimensional space; the minimization problem can thus be reduced to a problem in finite dimensional space. Moreover, a quasi-solution to the inverse problem is sought as a minimizer of the regularized misfit functional, which has the form

$$J_\alpha(\sigma) = J(\sigma) + R_\alpha(\sigma) = \|\Lambda\sigma - \psi\|_2^2 + \alpha\|\sigma - \sigma_0\|_S^2 \to \min_S . \qquad (3.53)$$

Here, the norm $\|\cdot\|_S$ defines some admissible norm in S, the parameter $\alpha > 0$ is a small real number, and the function σ_0 is given a priori. Minimizing the functional (3.53) instead of (3.52) has several advantages. First, if we know a priori that the solution is close to the known function σ_0, then this information can be included in (3.53). If such information is unavailable, then we can set $\sigma_0 = 0$. Second, because the measured data always contain noise of some level δ, for a sufficiently small parameter $\alpha \sim \delta$, the addition of an auxiliary term R_α does not affect the accuracy of the functional, but the regularization parameter α improves the properties of the functional $J(\sigma)$. For instance, in many practically important cases of linear inverse problems, the minimization problem (3.53) has a unique minimizer on the compact set S. The choice of the parameter α depends on the noise level δ of the measured data. It is natural to choose this parameter so that $\alpha \to 0$ as $\delta \to 0$. The problem of minimizing the residual functional can generally be solved by the methods of variational and extreme problems (Bruaset and Survey 1995). However, in several simple cases, it is sometimes possible to explicitly solve for the relations that determine the minimum of the residual functional (Mukanova 2013a, b).

What are the best practices for selecting the parameter α and the finite dimensional set S? To check whether the selected parameters are suitable for solving the inverse problem, the quasi-solution method is first tested on the so-called synthetic measurement data.

Definition. Data ψ that are obtained by solving a direct problem with known input data σ are called *synthetic measurement data*.

Next, we solve the inverse problem, for example, by minimizing the regularized misfit functional. In this case, we obtain an approximate solution σ_α. Because the solution σ to the problem is known in advance, we can compare the solution σ_α to the exact function σ. Thus, the use of synthetic measurement data allows one to test a numerical method for solving the inverse problem on a large amount of synthetic data and many parameters. Then, based on numerical experiments, an acceptable set of parameters and the class S of unknown functions σ is established for which a solution can be successfully constructed. These data represent *noise-free* synthetic data. However, to work fully with synthetic data, we should include the noise (i.e., the distortions of the data) in the calculation and perform simulations for different noise levels.

Unfortunately, the gradient method has a disadvantage that is associated with local minima. To succeed, we must provide a good initial guess with the input data σ; otherwise, the solution could be unrealistic.

In several cases, the new globally convergent method can be applied to solve CIP (Beilina and Klibanov 2012). However, to the best of our knowledge, no application has been published of this method in geophysical practice for ERT.

In some cases, inverse problems may turn out to be linear, which means that the input and output data are linearly mapped to one another. For such problems, the solution methods are well developed and find applications in practice (Mueller and Siltanen 2012). However, as a rule, the inverse problems of geophysics are not linear. For example, in problems (3.19) and (3.20), the input and output data are not linearly dependent, which can easily be verified directly. In addition, the solutions to the inverse problems are unstable concerning the input data. Therefore, the solutions are ambiguous. However, in some cases, the problem can be reduced to a linear problem (Mukanova and Romanov 2016).

Consider an example. Suppose that the internal structure and construction material of a newly constructed artificial object (e.g., a dam) are known. Let us now imagine that because of some external factors, such as water leakage and the influence of weather conditions, some changes have gradually occurred in the material of the dam. If these changes are small compared with the initial state of the dam, we can linearize the problem in the following way. For simplicity, let us consider the 2D case and assume that the apparent resistivity measurements are conducted along the boundary part of the dam's cross-section by the ERT method. Let the section of the dam occupy the 2D region Ω. Let Γ be a part of the boundary of the region $\partial\Omega$ on which the measurements are taken; for example, suppose that this is the boundary with the atmosphere (i.e., the boundary of the region into which the electric field penetrates), which is expressed as $\partial\Omega = \mathit{\Gamma}\ U\ \mathit{\Gamma}_1$. For each of the possible positions **a** of the current electrodes, we can write the following mathematical model:

$$\begin{gathered}
\frac{\partial}{\partial x}\left(\sigma(x,z)\frac{\partial U}{\partial x}\right)+\frac{\partial}{\partial z}\left(\sigma(x,z)\frac{\partial U}{\partial z}\right)=0,\,(x,z)\in\Omega\\
\sigma(x,z)\frac{\partial U}{\partial \mathbf{n}}(x,z,\mathbf{a})\Big|_{\Gamma}=\delta(\mathbf{r}-\mathbf{a}),\\
\lim_{r\to\infty}U(x,z,\mathbf{a})=0,r=\sqrt{x^2+z^2}.
\end{gathered}\tag{3.54}$$

Note that to formulate a direct problem correctly, the conditions (3.54) must be supplemented with some additional physically justified conditions on the remaining part of the boundary Γ_1. Suppose that the measurements are taken for the different positions of the current electrodes in the section of the dam that is defined by the plane $y = a$, then

$$U(x,z,\mathbf{a})=\psi(x,z,\mathbf{a}),\quad (x,z),(a_x,a_z)\in\Gamma.\tag{3.55}$$

Here, the vector $\mathbf{a} = (a_x, a_z)$ determines the current position of the source electrode. Suppose that, at the beginning of the operation of the dam, we know the distribution of electrical conductivity $\sigma_0(x, z)$ and the measurements of $\psi_0(x, z, \mathbf{a})$. Let the solution be represented in the form $U(P) = U_0(P) + u(P)$, where the solution $U_0(P)$ is the solution at the beginning of the dam's operation. To determine the function $U_0(P)$, we can apply one of the methods to solve a direct problem: the IEM or its modification in the form of a BEM, or FDM. For application, we need to set some boundary conditions on the inaccessible part of the boundary. As shown in Sect. 3.5, in the case of application of the IEM, one can consider a problem in an infinite domain and impose the condition that the potential decreases to zero at infinity. Suppose that, compared with the initial state of the dam, the change in the specific electrical conductivity is small and has the form $\sigma(x, z) = \sigma_0(x, z) + \sigma_1(x, z)$. Then, we can linearize the problem as follows:

$$\begin{aligned}&\frac{\partial}{\partial x}\left((\sigma_0(x,z)+\sigma_1(x,z))\frac{\partial(U_0+u)}{\partial x}\right)+\frac{\partial}{\partial z}\left((\sigma_0(x,z)+\sigma_1(x,z))\frac{\partial(U_0+u)}{\partial z}\right)=0,\ (x,z)\in\Omega\\&(\sigma_0(x,z)+\sigma_1(x,z))\ \frac{\partial(U_0+u)}{\partial\mathbf{n}}(x,z,\mathbf{a})\Big|_{\Gamma}=\delta(\mathbf{r}-\mathbf{a}).\end{aligned}$$

Considering that the function $U_0(x, z)$ is a solution to the problem for the known coefficient $\sigma_0(x, z)$, we obtain the following formulation of the direct problem for the unknown function $u(x, z)$:

$$\begin{aligned}&\frac{\partial}{\partial x}\left(\sigma_0(x,z)\frac{\partial u}{\partial x}\right)+\frac{\partial}{\partial z}\left(\sigma_0(x,z)\frac{\partial u}{\partial z}\right)=F(x,z),\quad (x,z)\in\Omega\\&F(x,z)=-\frac{\partial}{\partial x}\left(\sigma_1(x,z)\frac{\partial U_0}{\partial x}\right)-\frac{\partial}{\partial z}\left(\sigma_1(x,z)\frac{\partial U_0}{\partial z}\right),\\&\frac{\partial u}{\partial\mathbf{n}}(x,z,a)\Big|_{\Gamma}=0,\quad u(x,z,a)|_{\Gamma_1}=0.\end{aligned}\tag{3.56}$$

Assume that the values of $u(x, z)$ on Γ are measured for each of the possible positions $\mathbf{a}_j$ of the current electrode. Then, the measured data are rewritten as

$$\begin{aligned}&u(x,z,\mathbf{a_j})=\psi_1(x,z,\mathbf{a}_j)\equiv\psi(x,z,\mathbf{a}_j)-\psi_0(x,z,\mathbf{a}_j),\\&(x,z)\in\Gamma,\mathbf{a}_j=\left(a_x^{(j)},a_z^{(j)}\right)\in\Gamma,j=\overline{1,K}.\end{aligned}\tag{3.57}$$

In the formulation of the inverse problem (3.56) and (3.57), it is necessary to recover the function $F(x, z)$. Then, from these values, we must solve the first-order partial differential equation with respect to the function $\sigma_1(x, z)$:

$$\begin{aligned}&\frac{\partial}{\partial x}\left(\sigma_1(x,z)\frac{\partial U_0}{\partial x}\right)+\frac{\partial}{\partial z}\left(\sigma_1(x,z)\frac{\partial U_0}{\partial z}\right)=-F(x,z),\\&\sigma_1(x,z)|_{\Gamma}=g(x,z).\end{aligned}\tag{3.58}$$

with boundary conditions on the boundary of the domain Γ.

Remark 3.2: Because the boundary of the region Γ is accessible for measurement, we can assume that the values of $\sigma_1(x, z)$ at this boundary are known. Methods for solving first-order partial differential equations (3.58) are described in the handbook by Kamke (1959). The main difficulty in solving the problem (3.56) and (3.57) is in the definition of the function $F(x, z)$.

However, the linearization that was performed above substantially simplifies the recovery of the function $F(x, z)$. Suppose that this function is representable as a linear combination of finite elements of the zero or first order that are defined on a certain mesh. In the case of zero-order elements, it is convenient to use a regular rectangular grid; in the case of first-order elements, the triangulation of the computational domain is convenient. Thus, we can write

$$F(x,z) = \sum_{i=1}^{N} C_i \varphi_i(x,z). \tag{3.59}$$

Then, we can solve many direct problems in which there are finite-element functions on the right-hand side:

$$\begin{aligned} &\frac{\partial}{\partial x}\left(\sigma_0(x,z)\frac{\partial u_{ij}}{\partial x}\right) + \frac{\partial}{\partial z}\left(\sigma_0(x,z)\frac{\partial u_{ij}}{\partial z}\right) = \varphi_i(x,z), \quad (x,z)\in\Omega \\ &\frac{\partial u_{ij}}{\partial \mathbf{n}}\left(x,z;\mathbf{a}_j\right)\bigg|_{\Gamma} = 0, u_{ij}\left(x,z;\mathbf{a}_j\right)\big|_{\partial\Omega\backslash\Gamma} = 0. \end{aligned} \tag{3.60}$$

Here, we added additional boundary conditions for the inaccessible part of the boundary $\partial\Omega\backslash\Gamma$ so that the direct problem could be solved correctly. However, the statement of physically justified direct problems for each right-hand side of $\varphi_i(x, z)$ deserves a separate study. Note that the problems (3.60) can be solved in advance for some reasonable choice of the functions $\varphi_i(x, z)$, $i = 1,\ldots, N$ and for a certain set of positions of the supply electrode $\mathbf{a}_j$.

Then, the solution to the direct problem with the right-hand side $F(x, z)$ can be represented in the form

$$u_j(x,z) = \sum_{i=1}^{N} C_i u_{ij}(x,z;\mathbf{a}_j), \quad j = \overline{1,K}. \tag{3.61}$$

The corresponding synthetic measurement data are calculated by using the values of the functions (3.61) at the boundary Γ.

Now, it remains to select the coefficients C_i of the linear combination (3.59) such that they best approximate the measured data in the sense of the root-mean-square deviation. Thus, the problem is reduced to the problem of minimizing the residual functional with respect to the coefficients $(C_1, C_2,\ldots, C_N)$:

$$J(C_1,C_2,\ldots,C_N) = \sum_{j=1}^{K}\int_{\Gamma}\left(\sum_{i=1}^{N} C_i u_{ij}\left(x,z;\mathbf{a}_j\right) - \psi\left(x,z;\mathbf{a}_j\right)\right)^2 d\Gamma + \alpha\sum_{i=1}^{N} C_i^2 \tag{3.62}$$

Here, the function $\psi(x, z; \mathbf{a}_j)$ is the measured data.

Upon closer examination, we see that the functional (3.62) is a positively defined quadratic form with respect to the variables $(C_1, C_2,\ldots, C_N)$. In this case, the condition that is satisfied by a minimum of the functional can be written explicitly and expresses the vanishing of the first derivatives regarding C_k, where $k = 1,.., N$. Differentiating the functional (3.62) with respect the variable C_k yields

$$\frac{\partial J(\mathrm{C}_1, \mathrm{C}_2, \ldots \mathrm{C}_N)}{\partial C_k} = 2\sum_{j=1}^{K} \int_{\Gamma} \left(\sum_{i=1}^{N} C_i u_i\left(x, z; \mathbf{a}_j\right) - \psi\left(x, z; \mathbf{a}_j\right) \right) u_k(x, z; \mathbf{a}_j) \mathrm{d}\Gamma$$
$$= 2 \sum_{j=1,\, i=1}^{K,N} C_i \int_{\Gamma} u_i(x, z; \mathbf{a}_j) u_k(x, z; \mathbf{a}_j) d\Gamma - 2\sum_{j=1}^{K} \int_{\Gamma} \psi(x, z; \mathbf{a}_j) u_k(x, z; \mathbf{a}_j) \mathrm{d}\Gamma + 2\alpha C_k,$$
$$k = 1, 2, \ldots, N. \tag{3.63}$$

Let us introduce a matrix **A** and a vector **B** through the following definitions:

$$\mathbf{A}_{ik} = \sum_{j=1}^{K} \int_{\Gamma} u_i(x, z; \mathbf{a}_j) u_k(x, z; \mathbf{a}_j) \mathrm{d}\Gamma$$

$$\mathbf{B}_k = \sum_{j=1}^{K} \int_{\Gamma} \psi(x, z; \mathbf{a}_j) u_k(x, z; \mathbf{a}_j) \mathrm{d}\Gamma.$$

Matrix A forms a so-called stiffness matrix for the FEM. Now, we equate the derivatives (3.63) to zero:

$$(\alpha \mathbf{I} + \mathbf{A})\mathbf{C} = \mathbf{B}$$

Here, **I** denotes the identity matrix. Finally, we obtain a system of linear equations in the unknown (C_1, C_2,. . ., C_N) with a matrix (α**I** + **A**). This is the general approach for solving a linear inverse problem. However, in each specific case, we must always perform complicated studies to obtain an appropriate solution to the inverse problem being considered.

References

L. Beilina, M.V. Klibanov, *Approximate Global Convergence and Adaptivity for Coefficient Inverse Problems* (Springer, New York, 2012)

A.A. Bobachyev, I.N. Modin, E.V. Pervago, V.A. Shevnin, Mnogoelektrodnyye elektricheskiye zondirovaniya v usloviyakh gorizontal'no-neodnorodnykh sred (Review), *Razvedochnaya geofizika*, 2, JCS 'Geoinformmark', Moscow, 1996

C.A. Brebbia, J.C.F. Telles, L. Wrobel, *Boundary Element Techniques. Theory and Applications in Engineering* (Springer, Berlin, 2012)

A.M. Bruaset, *A Survey of Preconditioned Iterative Methods. Research Notes in Mathematics Series, 328* (Addison-Wesley, New York, 1995), pp. 63–75

T. Dahlin, The development of DC resistivity imaging techniques. Comput. Geosci. **27**, 1019–1029 (2001)

D.H. Griffiths, R.D. Barker, Two-dimensional resistivity imaging and modelling in areas of complex geology. J. Appl. Geophys. **29**, 211–226 (1993)

V.K. Ivanov, O lineynykh nekorrektnykh zadachakh. Doklady USSR Acad. Sci. **145**(2), 270–272 (1962)

Von E. Kamke, *Partielle Differential Gleichungen Erster Ordnung für Eine Gesuchte Funktion* (Leipzig, 1959)

V.K. Khmelevskoi, *Electrorazvedka* (MSU, Moscow, 1984)

O. Koefoed, *Geosounding Principles: Resistivity Sounding Measurements* (Elsevier, Amsterdam, 1979)

J.L. Mueller, S. Siltanen, *Linear and Nonlinear Inverse Problems with Practical Applications* (SIAM, 2012)

B. Mukanova, Numerical reconstruction of unknown boundary data in the Cauchy problem for Laplace's equation. Inverse Probl. Sci. Eng. **21**(8), 1255–1267 (2013a)

B. Mukanova, A numerical solution to the well resistivity-sounding problem in the axisymmetric case. Inverse Probl. Sci. Eng. **21**(5), 767–780 (2013b)

B.G. Mukanova, M.K. Orunkhanov, Inverse resistivity problem: geoelectric uncertainty principle and numerical reconstruction method. Math. Comput. Simul. **80**, 2091–2108 (2010)

B. Mukanova, V.G. Romanov, Inverse source problem for wave equation and GPR data interpretation problem. Eurasian J. Math. Comput. Appl. **4**(3), 15–28 (2016)

M.K. Orunkhanov, B.G. Mukanova, B.K. Sarbasova, Chislennaya realizacia metoda potencialov v zadache zondirovania nad naklonnym lpatom, in *Computational Technologies*, vol. 9. (Siberian Branch of Russian Academy of Sciences, Novosibirsk, 2004a), pp. 45–48

M.K. Orunkhanov, B.G. Mukanova, B.K. Sarbasova, Chislennoe modelirovanie zadach electricheskogo zondirovania, in *Computational Technologies*, Special Issue, part 3, 9 (Almaty-Novosibirsk, 2004b), pp. 259–263

I.P. Skalskaya, Pole tochechnogo istochnika toka, raspolozhennogo na poverkhnosti Zemli nad naklonnym plastom. J. Tech. Phys. **18**(10), 1243–1254 (1948)

A.N. Tikhonov, Ob electrozondirovanii nad naklonnym plastom. Trudy Instituta Teoreticheskoi Pisiki **1**, 116–136 (1946)

A.N. Tikhonov, Ob edinsvennosti reshenia zadachi electrorazvedki. Doklady USSR Acad. Sci. **69** (6), 797–800 (1949.) (in Russian)

A.N. Tikhonov, V.Y. Arsenin, *Solutions of Ill-Posed Problems* (Winston and Sons, Washington, DC, 1977)

Y.V. Yakubovskii, *Electrorazvedka* (Nedra, Moscow, 1980)

Chapter 4
The Boundary Element Method in ERT Direct and Inverse Problems

4.1 The Integral Equations Method for Solving Direct Electrical Sounding Problems Above a 2D Medium with Piecewise-Linear Contact Boundaries

Due to the fundamental laws of the propagation of electromagnetic fields expressed in Maxwell's equations, heterogeneities within a geoelectric section act as secondary sources of the electric field. Replacing the heterogeneities in the geoelectric section with a system of secondary sources is the basic principle of the integral equations method (IEM). The intensities of the secondary sources in an inhomogeneous medium are determined by the gradient of the electrical conductivity and the strength of the electric field at a given point in space. In this case, the electric field **E** is the sum of the primary field generated by the external sources $\mathbf{E}_0$ (i.e., the field of the current electrodes or other sources generating the electric current) and the electric fields $\mathbf{E}_S$ generated by all of the secondary sources. Thus, the intensity of a secondary source depends on the intensity of all other secondary sources, and they are simultaneously affected by their electric fields. This is the essence of the mechanism of interaction between the causative agents of the secondary field. A mathematical description of this phenomenon leads to integral equations (which are, as a rule, are Fredholm equations of the second kind). Subsequently, these equations are discretized into systems of linear algebraic equations (SLAE), which are solved using either direct or iterative methods.

In the abovementioned case, we obtain a solution following a finite number of arithmetic operations ($2/3n^3$) operations using the Gaussian method, where n is the dimension of the SLAE). Direct methods exhibit a significantly higher computational efficiency during the calculation of fields at several external source positions. Meanwhile, iteration methods are employed to obtain a series of approximate solutions and require substantially fewer operations to achieve an acceptable accuracy. The disadvantage of an iterative method is the uncertainty in the rate of its

B. Mukanova, I. Modin, *The Boundary Element Method in Geophysical Survey*,
Innovation and Discovery in Russian Science and Engineering,
https://doi.org/10.1007/978-3-319-72908-4_4

convergence. At the physical level, the principle of the iterative approach can be explained through an example of the perturbation method. In the first stage of calculations in this method, it is assumed that the electric field near an inhomogeneity is equal to the primary field, based upon which the intensities of the secondary sources are calculated. Then, the secondary fields are calculated and added to the primary field, after which the intensities of the secondary sources are again calculated. This process is repeated until the intensities of the secondary sources are stable. The replacement of inhomogeneities with secondary sources can be performed in different ways, leading to different modifications of the IEM. In gradient media, we derive volumetric integral equations in which the charges or dipoles act as secondary sources. In piecewise-homogeneous media, simple layers are used as secondary sources, leading to surface integral equations. In the case of a finite-element approximation of an integrand, we employ a BEM that is, generally speaking, a particular case of the IEM.

Integral equations can be written for both the intensities of the secondary sources and the values of the potentials. By solving these integral equations, we obtain either the distribution of the secondary sources or the potentials within the inhomogeneities. We can then calculate the field at any point, including those within inhomogeneities, at the secondary current source or charge level. When describing secondary sources, both their charges and currents can be utilized because there is a connection between them within the conducting medium. For example, in the unit time interval, $I = Q/(\varepsilon\rho)$, where I is a flowing current, and Q is the total charge of the source. In differential form, an analogous equation can be written in the following form: $\mathrm{d}I/\mathrm{d}V = q/(\varepsilon\rho)$**,** where $\mathrm{d}I/\mathrm{d}V$ is the current density flowing out of the volume $\mathrm{d}V$, and q is the bulk charge density. Similar to the case involving primary sources, it is more convenient from the author's perspective to measure the intensities of secondary sources through the current rather than the charge when using the IEM.

This concept involving both normal and anomalous parts of a geoelectric section is an important component of the IEM. In the IEM computational process, geoelectric models with algorithms that are effective for calculating the Green's function can be used as a normal section. Recall that the Green's function $G(P, M)$ represents the potential at the point M of a single pointwise source of electric current located at the point P within a given geoelectric section.

Separating the electrical field of a geoelectric section into normal and anomalous components is very important. When solving direct electrical exploration problems using the IEM, this differentiation allows us to exclude secondary sources related to inhomogeneities in the normal section. The effect of the normal section is considered through the Green's function. Such an approach makes it possible to reduce the dimensionality of a SLAE following the discretization of the problem. From this perspective, it is preferable that the normal section contains as many inhomogeneities within the investigated medium as possible. However, the complexity of calculation of the corresponding Green's function increases. Therefore, separating the geoelectric section into normal and anomalous components should be conducted in such a way that the total computational costs in calculating the Green's function and in the subsequent solution of the integral equation are minimal. In many cases, a homogeneous half-space model or the contact between two half-space models is used as a normal section in the IEM.

4.1.1 2D Statement of Resistivity Method Problems

The mathematical algorithm and the program used to solve flat two-dimensional (2D) problems were developed by the author subsequent to the three-dimensional (3D) modeling program in 1988. This program, known as IE2DL, was developed in collaboration with E. V. Pervago, who is also an author of the data preparation program VCOORD. Despite its apparent lack of physical representation, IE2DL is now employed for numerous applications. The basic properties of a transversely polarized electric field within a geological section for a flat problem are exactly the same as those in a quasi-3D case. When using the method of the median gradient, the differences between their corresponding algorithms completely disappear. The main advantage of IE2DL is its potential to create highly sophisticated 2D models and calculate the electric fields for models similar to real geoelectric sections. In addition, all the calculations in IE2DL are performed for specific lengths of the current and measuring electrodes. The program provides a wide variety of electroprospecting arrays, thereby allowing the modeling of fields for a variety of practical situations. An important feature of the program is that the current electrodes can be located within the inhomogeneities, and the inhomogeneities themselves can intersect the surface of the earth. The electric field is calculated at any point along the half-surface.

For the sake of clarity, it should be noted that the second physical model modeled in the framework of this program is a 2D medium that is infinitely extended along the axis Oy. The excitation of this medium is produced by infinitely long lines placed along the y-axis. The detection of an electric field is performed via infinitely long reception lines. As demonstrated later, this problem corresponds to the first zero spatial harmonic of a quasi-3D problem. Later, based on the program IE2DL, A. A. Bobachev developed an algorithm and a program for constructing current lines in a 2D section (A. A. Bobachev 2003). We briefly dwell on the features of this mathematical algorithm and, at the end of this section, provide an example of a calculation for this problem.

Figure 4.1 shows a generalized model of the geoelectric section for which the algorithm was developed. We consider a pure 2D model in which the electric current propagates only along the flat cross-section of the medium. This problem corresponds to the physical modeling of electrically conductive paper. The difference between this problem and its physical analog is the unlimited space of the modeling domain. Therefore, the electric current flows freely along the plane section. In physical modeling, one must always remember that the edges of electrically conductive paper completely reflect the electric current. Inclusions with a piecewise-constant distribution of the resistivity $\rho_i(x, y)$ ($i = 1, 2, 3, \ldots, N$) are placed within

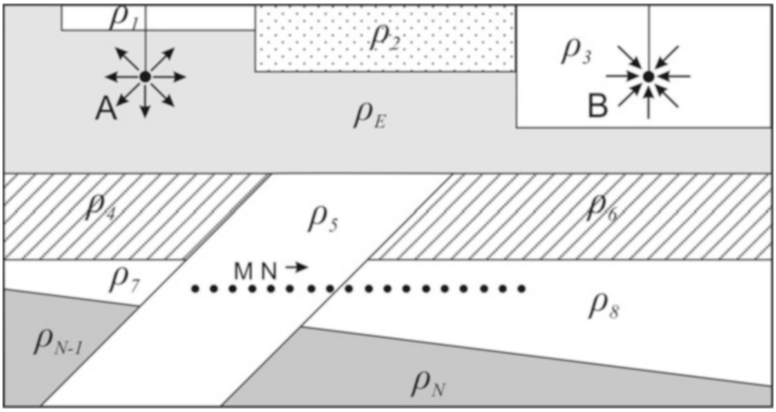

Fig. 4.1 Model of a 2D geoelectric section

the lower half-plane. The heterogeneities can have almost arbitrary shapes, and they can touch each other and intersect the surface of the earth. The boundaries of the inhomogeneities Γ are characterized by the external normal $\mathbf{n}(x, y)$ at each point. The thesis of A. A. Bobachyev describes how a high-density charge can accumulate along the intersecting model boundaries in the case of an external field acting along acute angles, but the charge itself is integrated; as a result, its action can be considered through additional refinements of the mesh at the boundaries. The model is excited by one or more DC sources. In such a piecewise-homogeneous medium, the electric field potential satisfies the Laplace equation at all points that do not belong to the interfaces and at which there are no external sources. In addition, the conditions are satisfied at infinity and at the sources. The conditions also hold for the conjugation of the potential along the interfaces of media with different electrical conductivities.

It is possible to derive equations for secondary surface sources located along both the outer and inner surfaces of inhomogeneities. In this case, the solution of the problem in terms of the surface sources makes it possible to analyze the physical mechanism more efficiently regarding formation of the anomalous field.

The electric field in this model is the sum of the normal field of the current electrodes $\mathbf{E}^0(M)$ and anomalous field $\boldsymbol{E}^{\mathrm{an}}(M)$ that is induced by secondary surface sources:

$$\mathbf{E}(M) = \mathbf{E}^0(M) - \int_\Gamma \nabla_M G(P, M) \cdot I(P) \cdot d\Gamma_P, \tag{4.1}$$

where $\{I_L(P) \cdot \mathrm{d}\Gamma_P\}$ denotes the intensity of a secondary surface source located at the point P, $G(P, M)$ is the Green's function for a half-space, and $I_L(P)$ is numerically equal to the density of the electric current flowing from the boundary element $\mathrm{d}\Gamma_P$, which is located at a point P.

To calculate the electric field or its potential according to the above formulae, it is necessary to find the distribution of the source densities for the anomalous field

$I_L(P)$. Together with the primary sources in the homogeneous medium, the anomalous field should create such a field that would otherwise be created only by the primary sources in an inhomogeneous medium. Consider a small element dΓ of the surface Γ. The resistivity of the enclosing half-space is ρ_E. The surface density of the source I_L within a small element of the boundary dΓ can be regarded as constant, and the element itself is flat. Then, near the boundary element dΓ, we obtain the following through the differential form of Ohm's law:

$$E_n^{\mathrm{e}} = E_n^{\mathrm{ex}} + \frac{I_L \rho_E}{2}, \quad E_n^{\mathrm{i}} = E_n^{\mathrm{ex}} - \frac{I_L \rho_E}{2}, \tag{4.2}$$

where $E_n{}^{\mathrm{i}}$ and $E_n{}^{\mathrm{e}}$ are the normal components of the total field **E** inside and outside, respectively, the inhomogeneity near the boundary Γ. The external field E^{ex} denotes the sum of the fields at the point M produced by the primary and secondary sources located outside of dΓ in the geoelectric section. Therefore, $E_n{}^{\mathrm{ex}}$ is the projection of the external field onto the normal to dΓ. Equation (4.2) has a simple physical meaning. The current I_L that is excited on the surface of the element dΓ flows from the surface along two mirror-wise reflection directions. In the first case, the current flows along the normal; thus, the component of the anomalous field of the element dΓ has a positive value. In the second case, the current flows against the normal inside the body; thus, the component of the anomalous field has a negative value. In both cases, the resistivity is equal to the resistivity of the enclosing medium in which the given element of the boundary is located. The value of 2 in the denominator of (4.2) means that half of the field flows along the normal to the external environment while the other half flows inside the body (see Fig. 4.2).

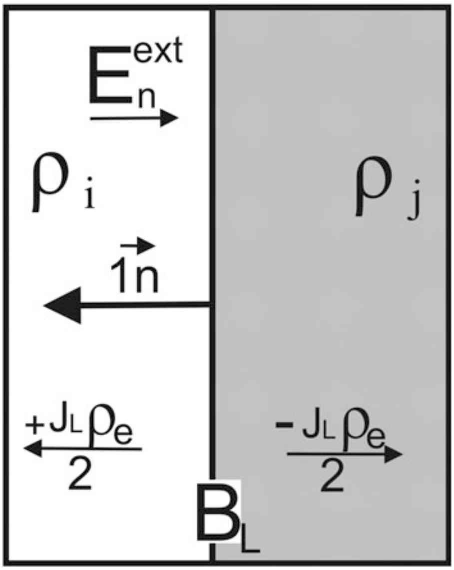

Fig. 4.2 The element dΓ of the boundary Γ

Using the boundary condition for the equality of the normal current density at the inhomogeneity boundary $E_n{}^{\mathrm{E}}/\rho_i{}^{\mathrm{E}} = E_n{}^{\mathrm{I}}/\rho_j$ and (4.2), we obtain the following:

$$I_L = \frac{2}{\rho_e}\frac{\rho_j - \rho_i}{\rho_i + \rho_j}E_n^{\mathrm{ex}}.$$

Substituting the expression of the normal component of the electric field (4.1) into the previous formula, we obtain the Fredholm integral equation of the second kind with respect to I_L:

$$I_L(M) = K\left[E_n^0(M) - \int\limits_{\Gamma} \frac{\partial G(P,M)}{\partial n}\cdot I_L(P)\cdot d\Gamma_P\right],$$

where $E_n{}^0$ is the component of the normal field, which is perpendicular to the surface Γ, **n** is the normal to Γ at the point M, and the coefficient K depends on the contrast of the inclusion with respect to the surrounding medium, where $K = \frac{2}{\rho_e}\cdot\frac{\rho_j - \rho_i}{\rho_i + \rho_j}$.

By solving the integral equation (4.2), we can define the distribution of the densities of secondary current sources within the simulation domain. After this, the potential and electric field are computed at the required points, after which it is possible to calculate the apparent resistivity.

Below, we give a calculation example for the model shown in Fig. 4.3. This calculation is meant to demonstrate the possibilities of the program IE2DL developed by the author. In this model, the inhomogeneities intersect the earth's surface, the supply electrodes and line MN are below the ground surface and inside different inhomogeneities, and the line MN crosses the contact.

4.1.2 *Quasi-3D Modeling: Transverse Polarization*

The mathematical algorithm described below for the solution of a quasi-3D problem was developed by the author in 1987 in collaboration with A. G. Yakovlev, V. A. Shevnin, and S. A. Berezina (Rogova) (Modin et al. 1988). Later, using the basic principles of this algorithm, the author managed to implement this algorithm in the form of the program IE2DR1, which was created in 1991. Its prototype was the program PRIZT, which was developed by A. G. Yakovlev, V. A. Shevnin, and S. A. Berezina. The PRIZT program was meant purely for research purposes; the model included a single rectangular body placed in a homogeneous half-space, and only two arrays (the median gradient and the VES) were used. The IE2DR1 program possesses advanced capabilities for calculating electric fields in real media. In particular, its advantages include the following:

1. An almost complete set of the 17 most common installations
2. A large number of inclusions that can intersect each other and cross the surface of the earth

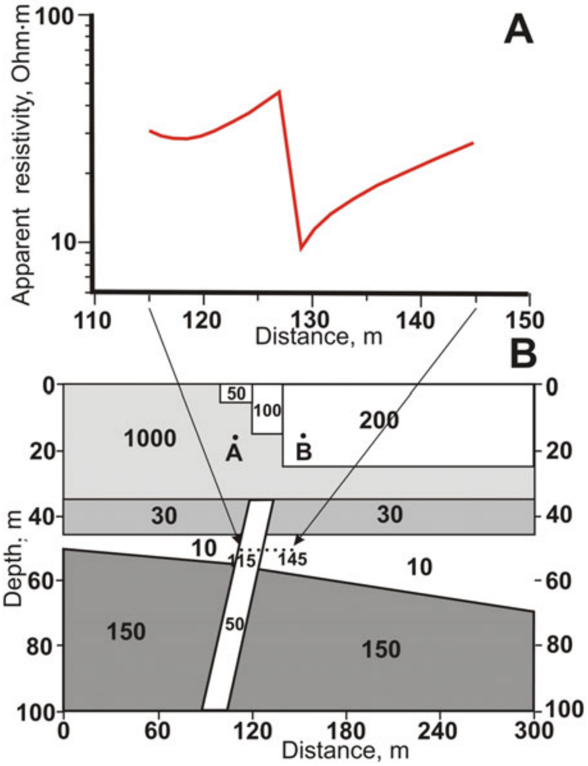

Fig. 4.3 The results of modeling using the IE2DL program. The depth of the MN lines is 50 m, the current electrodes A and B are located at a depth of 15 m. The step along the profile (conditionally in the horizontal drift) is 1 m. The number of observation points is 31. The length of the line MN is 1 m. (**a**) Plot of apparent resistivity versus distance.(**b**) 2D geoelectric section

3. The current and measuring electrodes can be located within the heterogeneity
4. Soundings can be performed at the required depth

The given problem of the field of a pointwise source placed on the surface of a conducting half-space with a 2D inhomogeneity is 2D with respect to the object. However, the problem is also 3D with respect to the field. Formally, the solution of a direct problem in such media can be obtained using 3D modeling methods. The computational costs are of the same or a higher order as the simulation of the electric field in the presence of 3D inhomogeneities. A more effective approach is based on the expansion of the field into components that harmonically vary in the lengthwise direction of the structures. In this way, the quasi-3D problem reduces to a series of 2D problems in the spectral domain for the corresponding set of spatial frequencies. After solving the problem at the spectrum level, the electric field in the real space is calculated with the help of an inverse Fourier transform. This approach allows us to reduce the calculation time for an electric field of a pointwise source in a 2D medium by several orders of magnitude.

Let us examine the possibilities of the IEM for solving quasi-3D problems using the simple model shown in Fig. 4.4. In this model, an inclusion with a resistivity ρ^{I} is infinitely elongated along the y-axis (i.e., a horizontal cylindrical body) and is placed inside a homogeneous half-space with a resistivity ρ^{E}. The current electrode is

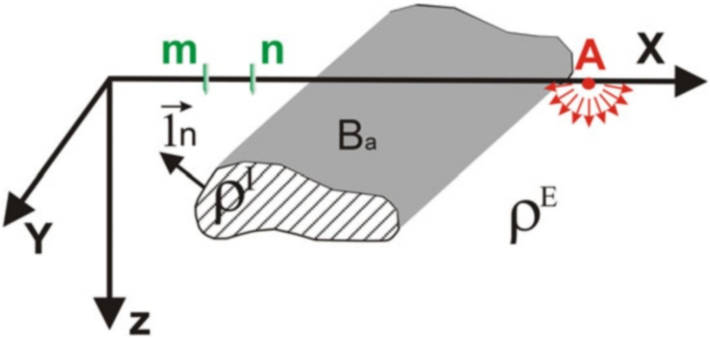

Fig. 4.4 Model of a 2D inhomogeneity inside a homogeneous half-space

located at a point A with coordinates (x_A, 0, 0). In the IEM, the electric field is the sum of the primary field of the source electrode in a homogeneous half-space and the field generated by the secondary sources located along the boundary of the heterogeneity. The surface density of the secondary sources can be found from the following equation:

$$I_{\rm S}(M) = K\left[E_n^0(M) - \iint\limits_{\Gamma} \frac{\partial G(P,M)}{\partial n} I_{\rm S}(P)d\Gamma_P\right], \tag{4.3}$$

where

$$K = \frac{2}{\rho^{\rm E}}\frac{\rho^{\rm E}-\rho^{\rm I}}{\rho^{\rm E}+\rho^{\rm I}}, \quad P\in\Gamma, \quad M\in\Gamma.$$

After computing the intensities of the secondary sources, the electric field at the required points is calculated by the formula

$$E(M) = E_n^0(M) - \int\limits_{\Gamma} \frac{\partial G(P,M)}{\partial n} I_{\rm S}(P)d\Gamma_P.$$

Let the points M and P have coordinates (x, y, z), and (x', y', z'), respectively. The Green's function $G(P, M)$ depends on the arguments (x, x', y, y', z, z'). In (4.3), the Green's function is differentiated in the direction of the normal at the point M. For a 2D body elongated along the y-axis, the direction of the normal depends only on the coordinates x and z of the point M. Consequently, the derivative of the Green's function depends on (x, x', y, y', z, z').

We note that the integration over the surface Γ can be represented as a sequential integration along a line directed along the y-axis and then along the contour L, which is the cross-section of the surface of the horizontal cylinder Γ transected by the plane xOz. Thus, (4.3) can be rewritten in the following form:

$$I_S(x,y,z) = K\left[E_n^0(x,y,z) - \int\limits_L \int\limits_{-\infty}^{\infty} \frac{\partial G}{\partial n}(x,x',y-y',z,z') \cdot I_S(x',y',z')\ dy'dL\right]. \tag{4.4}$$

The inner integral is the convolution integral of the functions $\partial G/\partial n$ and I_s with respect to the y coordinate.

Now, we enter the spectral domain. Since the quantities I_S, $E^0{}_n$, and $\partial G/\partial n$ are even functions with respect to the variable y, we can apply the cosine Fourier transform (2.25):

$$\tilde{I}_S\left(x,k_y,z\right) = 2\int\limits_0^{\infty} I_S(x,y,z)\cos\left(k_y y\right)dy,$$

$$\tilde{E}_n^0\left(x,k_y,z\right) = 2\int\limits_0^{\infty} E_n^0(x,y,z)\ \cos\left(k_y y\right)dy,$$

$$\frac{\partial \tilde{G}}{\partial n}\left(x,x',k_y,z,z'\right) = 2\int\limits_0^{\infty} \frac{\partial G}{\partial n}(x,x',y,z,z')\cos\left(k_y y\right)dy.$$

Because of the 2D geometry of the medium, the normal **n** does not depend on the y coordinate; thus, the Fourier transform and the differentiation commute. The spectra of I_S, E_n, and $\partial G/\partial n$ are the amplitudes of the spatial harmonics with a frequency k_y. We apply a direct Fourier transform to the left and right sides of (4.4):

$$\tilde{I}_S\left(x,k_y,z\right)$$
$$= K\left\{\tilde{E}_n^0\left(x,k_y,z\right) - \int\limits_L\int\limits_0^{\infty}\left[\int\limits_{-\infty}^{\infty}\frac{\partial G}{\partial n}(x,x',y-y',z,z')\cdot I_S(x',y',z')dy'\right]\times\cos\left(k_y y\right)dy\,dL\right\}.$$

According to property (2.27), the convolution spectrum is the product of the spectra of the convoluted functions. Consequently,

$$\tilde{I}_S\left(x,k_y,z\right) = K\left[\tilde{E}_n^0\left(x,k_y,z\right) - \int\limits_L \frac{\partial \tilde{G}}{\partial n}\left(x,x',k_y,z,z'\right)\cdot \tilde{I}_S\left(x',k_y,z'\right)dL'\right]. \tag{4.5}$$

The integral equation (4.5) for the spectra of the secondary sources at the frequency k_y is written over the contour L rather than the surface Γ, as shown in the original equation (4.4). Thus, the Fourier transform reduces the dimensionality of the solved equation. For a homogeneous half-space, we have the following:

$$E_n^0(x,y,z) = \frac{\rho^E}{2\pi r^3}\mathbf{r}\cdot\mathbf{n},$$

$$\frac{\partial G}{\partial n}(x,x',y-y',z,z') = \frac{\rho^E}{4\pi}\left(\frac{\mathbf{r}}{r^3}+\frac{\mathbf{r}_*}{r_*^3}\right)\cdot\mathbf{n},$$

$$\mathbf{r}_A = (x - x_A) \cdot \mathbf{l}_x + y \cdot \mathbf{l}_y + z \cdot \mathbf{l}_z,$$
$$\mathbf{r} = (x - x') \cdot \mathbf{l}_x + (y - y') \cdot \mathbf{l}_y + (z - z') \cdot \mathbf{l}_z,$$
$$\mathbf{r}_* = (x - x') \cdot \mathbf{l}_x + (y - y') \cdot \mathbf{l}_y + (z + z') \cdot \mathbf{l}_z,$$

where $\mathbf{n}$ is the unit vector of the outer normal to the surface Γ at the point (x, y, z). Considering that $(\mathbf{1}_y, \mathbf{n}) = 0$, we obtain the following expressions for the spectra of $E_n{}^0$ and $\partial G/\partial n$:

$$\tilde{E}_n^0\left(x, k_y, z\right) = \frac{\rho^E}{2\pi}\left[(x - x_A) \cdot (\mathbf{l}_x \cdot \mathbf{n}) + z \cdot (\mathbf{l}_z \cdot \mathbf{n})\right] \cdot \int\limits_0^\infty \frac{\cos\left(k_y \cdot y\right)}{\left(R_A^2 + y^2\right)^{3/2}} dy, \tag{4.6}$$

$$\begin{aligned} &\frac{\partial G}{\partial n}\left(x, x', k_y, z, z'\right) \\ &= \frac{\rho^E}{2\pi}\left\{\left[(x - x') \cdot (\mathbf{l}_x \cdot \mathbf{n}) + (z - z') \cdot (\mathbf{l}_z \cdot \mathbf{n})\right] \cdot \int\limits_0^\infty \frac{\cos\left(k_y \cdot y\right)}{\left(R^2 + y^2\right)^{3/2}} dy + \right. \\ &\left. + \left[(x - x') \cdot (\mathbf{l}_x \cdot \mathbf{n}) + (z + z') \cdot (\mathbf{l}_z \cdot \mathbf{n})\right] \cdot \int\limits_0^\infty \frac{\cos\left(k_y \cdot y\right)}{\left(R_*^2 + y^2\right)^{3/2}} dy \right\} \end{aligned} \tag{4.7}$$

where $R_A{}^2 = (x - x_A)^2 + z^2$, $R^2 = (x - x')^2 + (z - z')^2$, and $R_*{}^2 = (x - x')^2 + (z + z')^2$. The parameters R_A, R, and R_* are the projections of the vectors $\mathbf{r}_a$, $\mathbf{r}$, and $\mathbf{r}^*$, respectively, onto the xOz plane. There is a cosine transform from functions of the form $I/(a^2 + y^2)^{3/2}$ in (4.6) and (4.7), where a is a constant. For this transformation, we have the following:

$$S\left(k_y, a\right) = \int\limits_0^\infty \frac{\cos\left(k_y \cdot y\right)}{\left(a^2 + y^2\right)^{3/2}} dy = \frac{k_y}{2a} K_1 \cdot \left(a \cdot k_y\right),$$

where $K_1(x)$ is the MacDonald function (modified Bessel function of the second kind) of the first order. In the numerical solution of the integral equation (4.5), we use the tabulated values of the function $K_1(x)$ to calculate $E_n{}^0$ and $\partial G/\partial n$ in a homogeneous half-space. To reduce (4.5) in the SLAE, the contour L is divided into the elements Δl, within which I_S is supposed to be constant. After calculation of the spectral densities I_S of the secondary sources, the electric fields and their potentials are calculated at the required points. The spectral potential is calculated using the following formula:

$$\tilde{U}\left(x, k_y, z\right) + \int\limits_{La} \tilde{G}\left(x - x', k_y, z, z'\right) \cdot I_S\left(x', k_y, z'\right) dl.$$

The potentials and the components of the field can be represented in terms of an inverse Fourier transform:

$$U(x,y,z)=\frac{1}{\pi}\cdot\int\limits_{0}\tilde{U}\left(x,k_y,z\right)\cdot\cos\left(k_y\cdot y\right)dk_y,$$

$$E_x(x,y,z)=-\frac{1}{\pi}\cdot\int\limits_{0}^{\infty}\frac{\partial\tilde{U}}{\partial x}\left(x,k_y,z\right)\cdot\cos\left(k_y\cdot y\right)dk_y=E_x^0(x,y,z)-$$

$$\frac{1}{\pi}\cdot\int\limits_{0}^{\infty}\left[\int\limits_{La}\frac{\partial G}{\partial x}\left(x-x',k_y,z,z'\right)\cdot\tilde{I}_S\left(x',k_y,z'\right)dl\right]\cos\left(k_y\cdot y\right)dk_y.$$

To compute the cosine transform, it is useful to apply an approach similar to that used in the Hankel transform. The expression for E_x can then be written in the following form:

$$\begin{aligned}&E_x(x,y,z)=E_x^0(x,y,z)+\frac{1}{\pi}\cdot\int\limits_{0}^{\infty}\tilde{E}_x^{\text{ан}}\left(x,k_y,z\right)\cdot\cos\left(k_y\cdot y\right)dk_y,\\&\text{где}\quad\tilde{E}_x^{\text{ан}}\left(x,k_y,z\right)=-\int\limits_{La}\frac{\partial G}{\partial x}\left(x-x',k_y,z,z'\right)\cdot I_S\left(x',k_y,z'\right)dl'.\end{aligned}\tag{4.8}$$

The anomalous field in (4.8) can be represented by

$$E_x^{\text{ан}}(y)=\int\limits_{0}^{\infty}f\left(k_y\right)\cdot\cos\left(k_y\cdot y\right)dk_y.$$

We introduce the notation $s=\ln(x)$ and $t=\ln(1/k_y)$. Then, $y=e^s$, $k_y=e^{-t}$, and $\mathrm{d}k_y=-e^{-t}\mathrm{d}t$, and the limits of integration in (4.8) are changed such that the limits of t and k_y are ∞ and $-\infty$, respectively, when $k_y=0$.

Hence, we have

$$E_x^{\text{ан}}(y)=\int\limits_{-\infty}^{\infty}f(e^{-t})\cdot\cos\left(e^{-t}\cdot e^{S}\right)\cdot(-e^{-t})dt=\int\limits_{-\infty}^{\infty}f'(t)\cdot f''(s-t)dt,\tag{4.9}$$

where $f'(t)=f(e^{-t})e^{-t}$ and $f''(s-t)=\cos(e^{s-t})$. The last integral is the convolution of the function $f'(t)$, which depends on the geoelectric model; the function $f''(s-t)$ is related to the type of the integral transformation. In a discrete form, the integral equation (4.9) can be represented as

$$\left(E_x^{\text{ан}}\right)_j=\sum_{i=-k}^{n}C_i(f')_{j-i},$$

Fig. 4.5 Calculation example on the surface of the 2D inhomogeneous half-space (program IE2DP1): (**a**) VES curves at certain points; (**b**) model of the geoelectric section

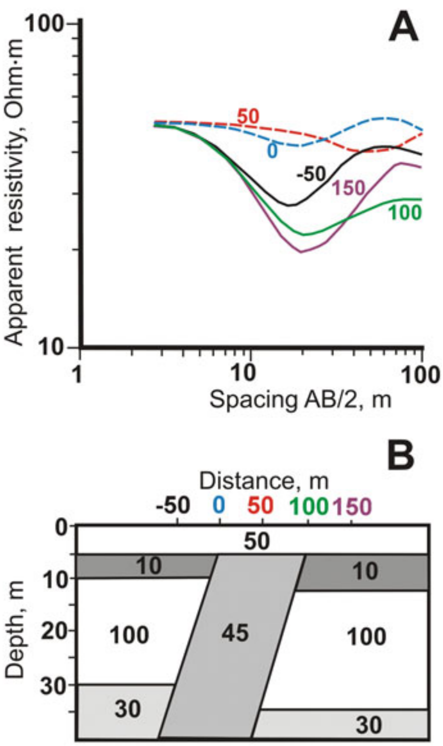

where C_i is the set of pre-computed coefficients. In the particular case where the electrical survey array is placed on the earth's surface and is oriented across the inhomogeneity ($y = 0$, $z = 0$), we have $E_z = 0$ (because $j_z = 0$ for $z = 0$) and $E_y = 0$ (due to the symmetry of the transverse polarization of the field). Because $\cos(k_y y) = 1$ for $y = 0$, the cosine transform is reduced to the ordinary integral

$$E_x(x,0,0) = E_x^0(x,0,0) - \frac{1}{\pi} \cdot \int_0^\infty \left[\int_{La} \frac{\partial \tilde{G}}{\partial x} \left(x - x', k_y, 0, z'\right) \cdot I_S\left(x', k_y, z'\right) dl' \right] dk_y.$$

We present an example calculation using the program IE2DP1 for the model shown in Fig. 4.5. The model of the geoelectric section corresponds to a low-amplitude tectonic disturbance zone (a fairly typical situation for the Donetsk region). To simulate a zone of alteration within the rocks, an inhomogeneity is placed at the center of the model. The left side of the anomaly is elevated and inclined to the right. The curves at the pickets −50 m and 150 m practically correspond to the horizontally layered VES curves. Substantially strong distortions of the VES curves are located within the contact zone that, during a formal layer-by-layer interpretation, can lead to false geological conclusions. In particular, the curve at the picket 0 m appears to be a four-layer curve, whereas the locally normal curve at this point should be a two-layer curve.

4.1.3 Quasi-3D Modeling: Longitudinal Polarization

A mathematical algorithm for longitudinal polarization over 2D objects was also developed within the framework of the joint project to solve quasi-3D problems, led by I. N. Modin, A. G. Yakovlev, V. A. Shevnin, and S. A. Berezina (Rogova) (Modin et al. 1988). From a mathematical perspective, the algorithms for both longitudinal and transversal polarization have very similar solutions. However, during a concrete implementation of the numerical algorithm, we encountered considerable difficulties. In 1993, the author independently developed a personal computer program (IE2DP2) purely for research on longitudinal polarization with capabilities closely analogous to those of the program PRIZT. Much later, in 2004, A. A. Bobachyev developed another version of the program IE2DP2 because of increasing numbers of personal requests. This program is universal and permits the use of almost any array, as the geoelectric sections can be virtually arbitrary. Most importantly, however, the program can work with any physical relief regardless of its complexity. This version of IE2DP2 represents the pinnacle of the programming of DC problems both in terms of its ability to solve complex problems and its potential for modeling electric fields in horizontally inhomogeneous media.

In geological and engineering practice, forced action arrays are mostly used for longitudinal polarization problems. Several situations then require the use of a longitudinal array: (1) river crossings (VES pickets are located along the profile and must span the river; thus, the river stream is perpendicular to the profile); (2) dams and bunds (the only possible installation location is along the body of such a bulk structure); and (3) across large and active transport highways (when the use of a physical line with cables and electrodes across such a road is dangerous). In addition, strong distortions of the VES curves may be observed in the third scenario as a result of the intersection of the current and measuring electrodes with underground communication lines and the body of the embankment itself. More than approximately 10–15% of such cases are encountered during electrical exploration applications. However, these cases are extremely important and cannot be ignored.

Thus, we must solve the problem regarding the field of a pointwise current source on the surface of a conducting half-space, with a 2D piecewise-constant distribution of the resistivity $\rho(x, z)$ (Fig. 4.6). Thus, both the problem under consideration and the previous problem have 2D geometries and 3D electrical fields. The principle difference is that the entire array is deployed perpendicularly to the cross-section of Γ. In this problem, as in the calculation of the field in a layered medium, there is no fundamental difference between the Schlumberger four-electrode installation and the three-electrode installation, because the second electrode does not create distortions and specific anomalies of the electric field; instead, the second electrode only doubles the field. For the sake of brevity, it should be noted from a practical perspective that the two-dimensionality of the cross-section in the framework of the longitudinal polarization problem is more challenging than that in the transverse polarization problem. The main physical requirement is that the entire array must be placed completely within a block exhibiting a generally 2D structure. In a number of

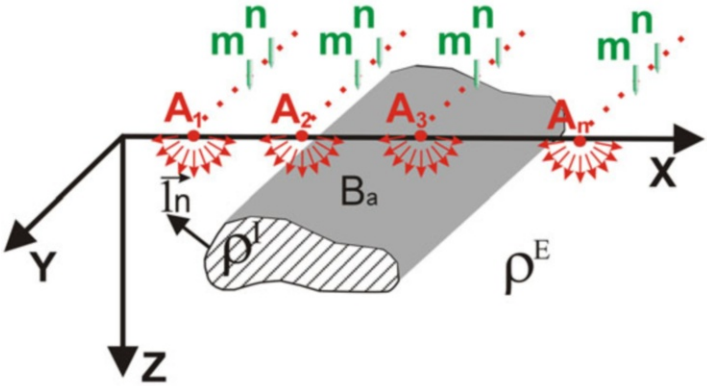

Fig. 4.6 The model of a 2D section and a sounding installation in the case of longitudinal polarization

cases, this requirement is physically impossible due to the complex structures of both natural and artificial objects. In addition, each application of a longitudinal installation should be performed following a thorough examination of the whole study area, which increases the cost of the survey. Therefore, the decision to use a longitudinal array should be scrutinized.

The formal solution of the direct problem completely coincides with the solution presented in the previous section, except for the final formulas. Therefore, the surface density of the secondary sources can be found from the following equation:

$$I_S(M) = K\left[E_n^0(M) - \int\limits_{\Gamma} \frac{\partial G(P,M)}{\partial n} \cdot I_S(P)\,d\Gamma_p\right].$$

Then, bypassing all the intermediate conclusions for the y component of the field, we can write the inverse Fourier transform:

$$\begin{aligned} Ey(x,0,0) &= Ey^0(x,0,0) \\ &\quad - \frac{1}{\pi}\int\limits_0^{\infty}\int\limits_{L_a} \tilde{G}\left(x-x', k_y, z, z'\right)\tilde{I}s\left(x', k_y, z'\right)dl' k_y \sin\left(k_y y\right)dk_y. \end{aligned}$$

To find the electric field, the calculations are performed according to the following algorithm. The potential is initially transferred to the spectral region with respect to the spatial frequencies k_y. In the program, the potential spectra are calculated for the intervals of the necessary distances x for the different depths of the sources z' and receivers z. Then, for each frequency, a 3D matrix of values $\tilde{G}_{k_y}(\Delta x, z, z')$ is computed, following which it is easy to interpolate the results for the required points. Furthermore, the SLAE is solved in the spectral domain, and the spectral density of

Fig. 4.7 Example of calculations using the programs IE2DP2 and IE2DP1 with longitudinal, transverse, and locally normal VES curves (**a**) and a geoelectric section model (**b**)

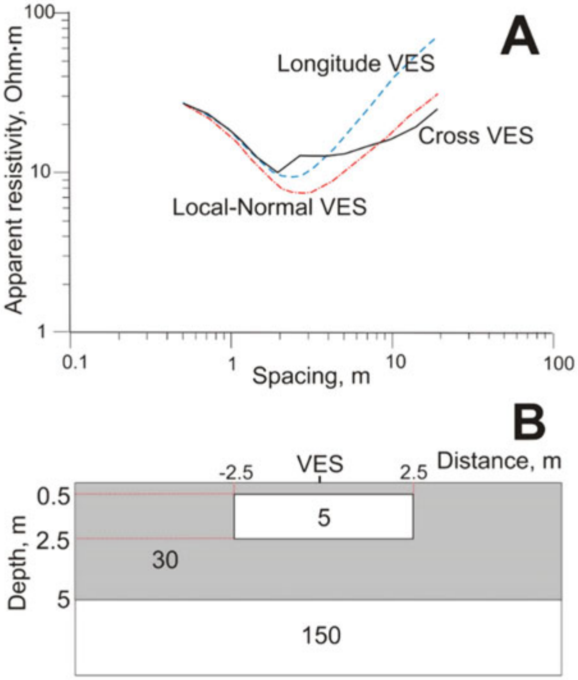

the secondary sources $\tilde{I}s(k_y)$ is defined for each frequency. The next step is to integrate over all the internal and external circuits L_a and obtain the spectrum of the anomalous electric field $\tilde{E}_y{}^{аном}(k_y)$. The last step is integration of the electric field spectra over all frequencies at the required points:

$$E_y(x,0,0) = E_y{}^0(x,0,0) + \frac{1}{\pi}\int\limits_0^\infty \tilde{E}_y{}^{аном}(x,k_y)k_y \sin\left(k_y y\right)dk_y.$$

As the previous expression cannot be numerically obtained via ordinary integration, the integral is converted to a convolution integral and then calculated.

In the relatively simple example below, we demonstrate the difference between the VES curves for longitudinally polarized and transversely polarized fields. The results of the calculations using the programs IE2DP1 and IE2DP2 are shown in Fig. 4.7. The geoelectric model consists of a two-layered medium and a conducting inclusion. This example demonstrates the fundamental differences between three VES curves calculated at one point. The locally normal curve corresponds to a four-layer section of type HA at picket 0 ($\rho_1 = 30, \rho_2 = 5, \rho_3 = 30$, and $\rho_4 = 150$ Ohm m; $h_1 = 0.5$, $h_2 = 2$, and $h_3 = 2.5$ m). The transverse curve of the VES exhibits a distortion when the current electrodes intersect the horizontal boundaries of the inhomogeneity, and the curve then descends to a locally normal curve and runs parallel to it at large spacings. As shown below, this behavior of the curve is completely natural and obeys the distortion from the so-called *P*-effect. In contrast to the transverse VES curve, the longitudinal VES curve is smooth, because no electrode of this installation intersects the horizontal boundaries. However, after reaching a minimum, a strong rise in the curve steeper than 45° can be observed. This rise is caused by the effect of the current concentration within the conductors.

4.2 The BEM for Solving Direct Sounding Problems Above a Medium with an Immersed Local Inhomogeneity

In the previous section, we considered 2D mathematical models for media with rectilinear contact boundaries. We also considered Fourier transformation method, which were used to reduce the 3D problem into a 2D problem. In this section, we consider the theoretical and computational aspects of solving direct problems using the BEM in a 3D formulation for media with sufficiently smooth boundaries.

4.2.1 Statement of the Problem and the Mathematical Model

Here, we consider the mathematical aspects and describe a numerical solution algorithm of the problem considered in Sect. 4.1.2 for a 3D formulation or, more precisely, for a 2.5D formulation. Let the medium contain a local 2D inhomogeneity (Fig. 4.8). Suppose that the medium has a 2D piecewise-constant conductivity distribution. Let a current electrode be placed at a point A on a planar surface of the medium that coincides with the plane $z = 0$ in Cartesian coordinates. A schematic model of the medium is shown in Fig. 4.8. Let the containing layer have a constant

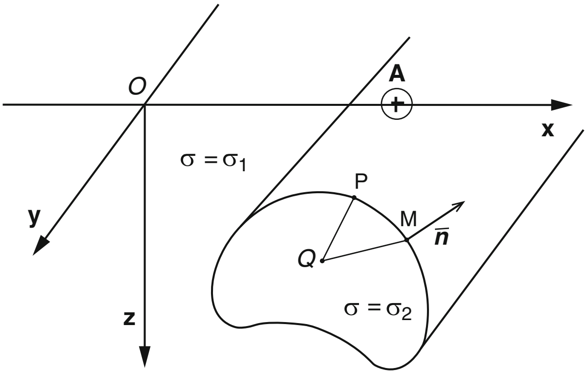

Fig. 4.8 Model of the medium with a 2D local inclusion

resistivity ρ_1 (conductivity $\sigma_1 = 1/\rho_1$), and let the local inclusion have the resistivity ρ_2 (conductivity $\sigma_2 = 1/\rho_2$).

Concerning the geometry of the inclusion, we make the following assumptions:

(a) The Cartesian *x*–*y* plane coincides with the earth's surface, and the conductivity distribution does not depend on the *y* coordinate.
(b) The intersection of the medium with the *y* plane (which is a constant) forms a stellar closed curve in the *x*–*z* plane (Fig. 4.8).
(c) There exists a parameterization $\rho = r(\theta)$ of the inclusion surface Γ in cylindrical coordinates (ρ, θ, ζ) with a center at some point $Q(x_Q, z_Q)$ and an axis ζ parallel to the axis *Oy* of the Cartesian coordinate system (Fig. 4.8). Let the function $\rho = r(\theta)$ satisfy the following conditions:

$$\begin{aligned} &r(\theta)\in C^2([0,2\pi]), \quad 0 < R_1 \le r(\theta) \le R_2, \quad \max(|r'(\theta)|,|r''(\theta)|) \le K, \\ &m = R_1 - 2\pi K > 0, \quad \theta\in[0,2\pi). \end{aligned} \tag{4.10}$$

(d) The smallest distance from the surface *Oxy* to the inhomogeneity is $d_\Gamma > 0$.

Let us now derive an integral equation. In contrast to the derivation given in Sect. 4.1, we obtain this equation based on the potential theory described in Chap. 2 (Sect. 2.1). Based on the mathematical model of the direct current, the potential of a stationary field satisfies the Laplace equation

$$\Delta U = 0. \tag{4.11}$$

The conditions of continuity for the potential and the normal component of the current are satisfied on the surface Γ:

$$U|_+ = U|_-, \quad \sigma_1 \frac{\partial U}{\partial n}\bigg|_+ = \sigma_2 \frac{\partial U}{\partial n}\bigg|_- . \tag{4.12}$$

Here, the signs "+" and "−" correspond to the derivatives in the direction of the normal **n** taken on different sides of the surface Γ (Fig. 4.8). Let R_0 be a specified length scale. We can write the conditions for the decrease of the potential at infinity and the boundary condition at the earth's surface:

$$\begin{aligned} &\frac{\partial U}{\partial z}\bigg|_{z=0} = \frac{I}{R_0^2\sigma_1}\delta(\mathbf{r} - \mathbf{OA}), \\ &U(\infty) = 0. \end{aligned} \tag{4.13}$$

Here, **OA** is the radius vector of a point source of direct current, and *I* is the current of the source electrode. We then represent the solution of the problem given in (4.11) through (4.13) at the point *M* in the form of a sum of the potentials of a point source in a homogeneous half-space and an unknown regular additive:

$$U(M) = \frac{I}{R_0\sigma_1}(U_0(M) + u(M)) = \frac{I}{R_0\sigma_1}\left(-\frac{1}{2\pi \mid AM \mid} + u(M)\right). \tag{4.14}$$

Here, the multiplier $I/R_0\sigma_1$ forms the scale of the potential measurement. The function $u(M)$ must also satisfy the Laplace equation everywhere except for the boundary Γ. The boundary conditions can be rewritten as follows:

$$\sigma_1 \frac{\partial u}{\partial n}\bigg|_{\Gamma_+} - \sigma_2 \frac{\partial u}{\partial n}\bigg|_{\Gamma_-} = -\left(\sigma_1 \frac{\partial U_0}{\partial n}\bigg|_{\Gamma_+} - \sigma_2 \frac{\partial U_0}{\partial n}\bigg|_{\Gamma_-}\right), \tag{4.15}$$

$$\frac{\partial u}{\partial z}\bigg|_{z=0} = 0 \tag{4.16}$$

Similar to the sounding problem over an inclined plane described in Chap. 3 (Sect. 3.5), we seek a solution $u(M)$ in the form of a simple layer potential created by secondary sources distributed over the geoelectric boundary Γ and its reflection in the upper half-space:

$$u(M) = \frac{1}{2\pi}\iint\limits_{\Gamma} \nu(P)\frac{1}{\mid MP \mid} d\Gamma_P + \frac{1}{2\pi}\iint\limits_{\Gamma} \nu(P)\frac{1}{|MP|'} d\Gamma_P, \tag{4.17}$$

where the point $P(x, y, z) \in \Gamma$, $P'(x, y, -z) \in \Gamma'$, and Γ' is a symmetric reflection of the surface Γ in the half-space $z < 0$. A symmetric reflection ensures that condition (4.16) is satisfied at the surface of the earth. The quantities $|MP|$, $|MP'|$ denote the distances from the point M to the points P and P', respectively. Now, we can derive the integral equation via the unknown function $\nu(M)$ $M \in \Gamma$ in a way similar to that presented in Chap. 3 (Sect. 3.5).

According to (2.6), the normal derivative of the first term of the potential (4.17) on the surface Γ has a discontinuity, and its values on different sides of the surface are expressed through the following formulae:

$$\begin{aligned}
\left(\frac{\partial u}{\partial n}\right)_{\Gamma-}(M) &= \nu(M) + \frac{1}{2\pi}\iint\limits_{\Gamma} \nu(P)\frac{\partial}{\partial n}\frac{1}{\mid MP \mid}d\Gamma + \frac{1}{2\pi}\iint\limits_{\Gamma} \nu(P)\frac{\partial}{\partial n}\frac{1}{|MP|'}d\Gamma \\
\left(\frac{\partial u}{\partial n}\right)_{\Gamma+}(M) &= -\nu(M) + \frac{1}{2\pi}\iint\limits_{\Gamma} \nu(P)\frac{\partial}{\partial n}\frac{1}{\mid MP \mid}d\Gamma + \frac{1}{2\pi}\iint\limits_{\Gamma} \nu(P)\frac{\partial}{\partial n}\frac{1}{|MP|'}d\Gamma.
\end{aligned} \tag{4.18}$$

Here, the sign "+" corresponds to the side of the surface with a conductivity σ_1, and the sign "−" corresponds to the side facing the inside of the inclusion. The normal **n** is the outer normal to the inclusion boundary.

Substituting the expressions in (4.18) into the boundary conditions of (4.15), we obtain the following:

$$\nu(M) = \frac{(\sigma_1 - \sigma_2)}{2\pi(\sigma_1 + \sigma_2)} \times \iint\limits_{\Gamma_i} \nu(P) \frac{\partial}{\partial n}\left(\frac{1}{\mid MP \mid} + \frac{1}{\mid MP' \mid}\right) d\Gamma + \frac{(\sigma_1 - \sigma_2)}{(\sigma_1 + \sigma_2)} \frac{\partial U_0}{\partial n}\bigg|_{\Gamma}. \tag{4.19}$$

We let κ be the reflection coefficient:

$$\kappa = \frac{(\rho_2 - \rho_1)}{(\rho_2 + \rho_{12})} = \frac{(\sigma_1 - \sigma_2)}{(\sigma_1 + \sigma_2)}.$$

Now, we can rewrite (4.19) in the following form:

$$\nu(M) = \frac{\kappa}{2\pi} \iint\limits_{\Gamma} \nu(P) \frac{\partial}{\partial n_M}\left(\frac{1}{r_{MP}} + \frac{1}{r_{MP'}}\right) d\Gamma_P + \kappa F_0(M), \tag{4.20}$$

where $F_0(M) = \partial U_0 / \partial n, \quad \mathrm{M} \in \Gamma$

Equation (4.20) is similar to the equation for an inclined plane problem (3.36), but it contains the additional term

$$\frac{\partial}{\partial n_M}\left(\frac{1}{r_{MP}}\right).$$

This term has an integrable singularity when the integration point M tends toward the point P. This circumstance considerably complicates the computational aspect of the problem in comparison with the example of sounding above an inclined plane.

4.2.2 Solvability of the Integral Equation

This section may be of particular interest to mathematicians and specialists in the field of numerical methods; thus, a reader who is interested only in the applied aspects of this method can skip this section.

Equation (4.20) can be written in the following operator form:

$$\nu = A\nu + f, \tag{4.21}$$

where the integral operator is defined as follows:

$$A\nu(M(\theta, \varsigma)) \equiv \int\limits_{0}^{2\pi} \int\limits_{-\infty}^{\infty} \nu(\theta_1, z_1) \frac{\partial}{\partial n_M}\left(\frac{1}{\mid MP \mid} + \frac{1}{\mid MP' \mid}\right) I(\theta_1, \varsigma_1) d\theta_1 d\varsigma_1. \tag{4.22}$$

Here, $I(\theta, \varsigma)$ is the Jacobian of the transformation from Cartesian coordinates to the parameterization of the surface. Suppose that the defined area of the operator A is the set of continuous bounded functions $\nu(M) \in C(\Gamma)$, $\|\nu\|_C < \infty$, $M \in \Gamma$. The order of decrease of that function at infinity is established in Lemma 4.1. Assume that the surface Γ is parameterized in accordance with the conditions of (4.10) so that the points on the surfaces $M(\theta, \varsigma)$ and $P(\theta_1, \varsigma_1)$ are given by the cylindrical coordinates $(r(\theta), \theta, \varsigma)$ and $(r(\theta_1), \theta_1, \varsigma_1)$, respectively.

We cannot apply the Fredholm theory directly to the integral equation (4.20) for the following reasons. First, for $P \to M$, the kernel of the equation has a singularity at $|MP|^{-1}$: thus, neither the theory for continuous kernels nor the theory for quadratically summable kernels can be applied. Fortunately, this difficulty is easily overcome by transition to an iterated second-order kernel. However, to consider an equation with an iterated kernel in the class $L_2(\Gamma)$, we must verify that the right-hand side of (4.20) and the right-hand side of the equation with an iterated kernel also belong to $L_2(\Gamma)$. Second, we must verify the compactness of the integral operator with an iterated second-order kernel in the space $L_2(\Gamma)$. The differences between (4.20) and the classical problems of potential theory (Gunther 1934; Petrovskii 1965; Tricomi 1957) are expressed in the fact that simple layers are considered defined on a bounded surface in the classical formulation. In other words, classical problems are posed in such a way that the domain in which the desired solution of the integral equation is defined is bounded. In our formulation, simple layers are considered defined on an unbounded surface. Therefore, to justify the numerical method for solving the integral (4.20), we must investigate the properties of the integral operator in (4.20). However, in the case involving a low media contrast, there is no need to use an iterated kernel (Mukanova 2010). We show this below based on the following lemma.

Lemma 4.1 The operator of the integral equation (4.20) is continuous on the set of bounded functions $\nu \in C(\Omega)$, $\Omega = [0, 2\pi] \times (-\infty, \infty)$ and is contractive for sufficiently small $|\kappa|$.

Proof. It is easy to verify that the derivative with respect to some direction $\mathbf{n}$ at the point M is

$$\frac{\partial}{\partial n}\left(\frac{1}{|MP|} + \frac{1}{|MP'|}\right) = \frac{\cos\psi}{|MP|^2} + \frac{\cos\psi'}{|MP'|^2}, \tag{4.23}$$

where the angles ψ and ψ' are formed by the vector $\mathbf{n}$ and the directions MP and MP', respectively.

Let us first prove the continuity of the operator. Consider two functions $\nu_1(M)$, $\nu_2(M) \in C(\Gamma)$. We estimate the norm of the difference between the values of the operator A:

$$\begin{aligned} \|A\nu_1 - A\nu_2\|_C &\le \|\nu_1 - \nu_2\|_C \cdot \frac{|\kappa|}{2\pi} \iint\limits_{\Gamma} \left(\frac{|\cos\psi|}{|MP|^2} + \frac{|\cos\psi'|}{|MP'|^2} \right) d\Gamma_P \\ &\equiv \|\nu_1 - \nu_2\|_C \cdot \frac{|\kappa|}{2\pi} (I_1(M) + I_2(M)). \end{aligned} \tag{4.24}$$

Now, we uniformly estimate the right-hand side in (4.24) with respect to the point M. Consider the parameterization of the surface Γ according to conditions (4.10). Let points M and P have cylindrical coordinates $(\rho, \theta, \varsigma)$ and $(\rho_1, \theta_1, \varsigma_1)$, respectively. The following equalities then hold:

$$\begin{aligned} I_1(M) &= \iint\limits_{\Gamma} \frac{|\cos\psi|}{|MP|^2} d\Gamma = \int\limits_0^{2\pi} \int\limits_{-\infty}^{\infty} \frac{|(MP, \mathbf{n})| \sqrt{r(\theta_1)^2 + r'^2(\theta_1)} d\varsigma_1 d\theta_1}{|PM|^3}, \quad \left(r'(\theta) = \frac{dr}{d\theta} \right) \\ I_2(M) &= \iint\limits_{\Gamma} \frac{|\cos\psi'|}{|MP'|^2} d\Gamma = \int\limits_0^{2\pi} \int\limits_{-\infty}^{\infty} \frac{|(MP', \mathbf{n})| \sqrt{r(\theta_1)^2 + r'^2(\theta_1)} d\varsigma_1 d\theta_1}{|P'M|^3}. \end{aligned} \tag{4.25}$$

In terms of the chosen parameterization, we have

$$|MP|^2 = \rho^2 - 2\rho_1\rho \cos(\theta - \theta_1) + \rho_1^2 + (\varsigma - \varsigma_1)^2.$$

The Cartesian coordinates of the vectors PM and $P'M$ are expressed in terms of cylindrical coordinates:

$$\begin{aligned} PM &= (\rho \cos\theta - \rho_1 \cos\theta_1, \varsigma - \varsigma_1, \rho \sin\theta - \rho_1 \sin\theta_1), \\ P'M &= \left(\rho \cos\theta - \rho_1 \cos\theta_1, \varsigma - \varsigma_1, \rho_1 \sin\theta_1 + \rho \sin\theta + 2\varsigma_Q\right), \\ \vec{n} &= \frac{1}{\sqrt{\rho^2 + r'^2(\theta)}} ((r'(\theta)\sin\theta + \rho\cos\theta), 0, \rho\sin\theta - r'(\theta)\cos\theta). \end{aligned} \tag{4.26}$$

Here, ς_Q is the depth of occurrence of the center of the polar coordinate system associated with the inclusion.

To calculate the integral I_1 in expressions (4.25), we consider the cylindrical coordinate system with an axis ς_1 passing through the center of the polar coordinate system parallel to the axis Oy of the initial Cartesian system (Fig. 4.8) and rotate the polar axis θ_1 in the θ direction. Then, the coordinates of the points M and P are ($\rho = r(0)$, 0, ς) and ($\rho_1 = r(\theta_1)$, $\theta_1 - \theta$, ζ_1), respectively. We then substitute the expressions of (4.26) into the expressions of (4.25) and change the integration variables such that $z = \zeta_1 - \zeta$. We can then obtain the following:

$$
\begin{aligned}
I_1 &= \frac{1}{\sqrt{\rho^2 + r'^2(\theta)}} \int\limits_0^{2\pi} \int\limits_{-\infty}^{\infty} \frac{\left|\rho^2 - \rho\rho_1 \cos\theta' - r'(0)\rho_1 \sin\theta'\right|}{\left(\rho^2 + \rho_1{}^2 - 2\rho\rho_1 \cos\theta' + z'^2\right)^{3/2}} \sqrt{r(\theta')^2 + r'^2(\theta)}\, dz'\, d\theta' \\
&\leq \frac{\sqrt{R_2^2 + K^2}}{R_1} \int\limits_0^{2\pi} \int\limits_{-\infty}^{\infty} \frac{\left|\rho^2 - \rho\rho_1 \cos\theta' - r'(0)\rho_1 \sin\theta'\right|}{(\rho^2 + \rho_1{}^2 - 2\rho\rho_1 \cos\theta' + z'^2)^{3/2}} dz'\, d\theta'.
\end{aligned}
\tag{4.27}
$$

The improper integral with respect to z' in the expressions of (4.27) can be taken explicitly; therefore, integrating with respect to the variable z', we obtain

$$
I_1 \leq \frac{2\sqrt{R_2^2 + K^2}}{R_1} \int\limits_0^{2\pi} \frac{\left|\rho^2 - \rho\rho_1 \cos\theta' - r'(0)\rho_1 \sin\theta'\right|}{\rho^2 + \rho_1{}^2 - 2\rho\rho_1 \cos\theta'} d\theta'. \tag{4.28}
$$

We can represent the values of the function $\rho = r(\theta)$ in terms of $\rho_1 = r(\theta_1)$ as follows:

$$
\rho = r(\theta_1) + (\theta - \theta_1) \int\limits_{0_1}^{1} \frac{dr}{d\theta}(\theta_1 + t(\theta - \theta_1))dt \equiv \rho_1 + L(\theta')\theta'. \tag{4.29}
$$

Then, considering the direction of the polar axis and the definition of θ, we have

$$
\rho_1 = r(\theta) - \theta' \frac{dr}{d\theta}(0) + \frac{\theta'^2}{2} \int\limits_0^1 \int\limits_{0_1}^1 \frac{d^2 r}{d\theta'^2}(ts\theta')dtds \equiv \rho - r'(0)\theta' + L_1(\theta')\frac{\theta'^2}{2}, \tag{4.30}
$$

By virtue of (4.10), the functions satisfy inequalities $|L(\theta')| \leq K$, $|L_1(\theta')| \leq K$ and are both bounded and continuous. Now, we estimate the integrand in (4.28). Expressing ρ_1 with (4.30) and substituting it into the numerator of the fraction in (4.28), we obtain the following (the prime notation for θ is omitted):

$$
\begin{aligned}
&\rho^2 - \rho\rho_1 \cos\theta - r'(0)\rho_1 \sin\theta = 2\rho^2 \sin^2(\theta/2) + r'(0)\rho(\theta\cos\theta - \sin\theta) + \\
&+ r'^2(0)\theta' \sin\theta - L_1\theta^2(\rho\cos\theta + r'(0)\sin\theta)/2 \leq 2R_2{}^2 \sin^2(\theta/2) + \\
&0.5KR_2\theta^2 + K^2\theta^2 + 0.5K(R_2 + K)\theta^2 \leq \left(0.5R_2^2 + KR_2 + 1.5K^2\right)\theta^2.
\end{aligned}
\tag{4.31}
$$

Here, we use the estimate $|\theta\cos(\theta) - \sin(\theta)| \leq 0.5\theta^2$ which is obtained by expanding the function in a Taylor series and estimating the remainder term on the interval $[0, 2\pi]$. Substituting (4.29) into the denominator of the integrand in (4.28), we obtain the following:

$$\rho^2 + {\rho_1}^2 - 2\rho\rho_1 \cos\theta' = 4{\rho_1}^2 \sin^2(\theta'/2) + 4\rho_1 L(\theta') \sin^2(\theta'/2) + L^2\theta'^2 \geq \\ \geq \left(4R_1 m \sin^2(\theta'/2) + K^2\theta'^2\right). \tag{4.32}$$

Substituting the estimates of the expressions in (4.31) and (4.32) into inequality (4.28), we have

$$I_1 \leq \frac{\sqrt{R_2^2 + K^2}\left(R_2^2 + 2KR_2 + 3K^2\right)}{R_1} \int_0^{2\pi} \frac{\theta^2 d\theta}{K^2\theta^2 + 4R_1 m \sin^2(\theta/2)} \leq C_1 \\ = \text{const.} \tag{4.33}$$

We can now estimate the integral I_2. If the value d_Γ is the depth of occurrence of the inhomogeneity, then

$|MP'| \geq \sqrt{4d_\Gamma^2 + z'^2}$, and the following inequality hold for I_2:

$$I_2 = \int_0^{2\pi} \int_{-\infty}^{\infty} \frac{|\cos(\psi'|)}{|MP'|^2} \sqrt{r^2(\theta) + {r'}^2(\theta)} dz d\theta \\ \leq \int_0^{2\pi} \sqrt{r^2(\theta) + {r'}^2(\theta)} \int_{-\infty}^{\infty} \frac{dz}{4d_\Gamma^2 + z'^2} d\theta = \frac{C\pi}{2d_\Gamma}, \tag{4.34}$$

where C is the length of the contour of the cross-section of the surface Γ. Then, from estimates (4.24), (4.33), and (4.34), we obtain

$$\|A\nu_1 - A\nu_2\|_C \leq \|\nu_1 - \nu_2\|_C \cdot \frac{|\kappa|}{2\pi}\left(C_1 + \frac{C\pi}{2d_\Gamma}\right). \tag{4.35}$$

This implies the continuity of the operator A.

It follows from inequality (4.35) that the operator A is contractive for sufficiently small values of $|\kappa|$ corresponding to small media contrasts. The lemma is proven.

Remark. For the particular case when the inhomogeneity cross-section is a circle of radius R, direct calculations using (4.27) and (4.34) yield $C_1 = 2\pi$, $C = 2\pi R$, and

$$\|A\nu_1 - A\nu_2\|_C \leq \|\nu_1 - \nu_2\|_C \cdot |\kappa|\left(1 + \frac{R}{2d_\Gamma}\right).$$

Let us consider the iterative scheme for the solution of (4.20). We define an initial approximation of the function $\nu_0(M) \in C(\Gamma)$. Each subsequent approximation $\nu_{m+1}(M)$ is calculated using (4.20) by substituting $\nu_m(P)$ for $\nu(P)$ in the right-hand side:

$$\nu_{m+1}(M) = \frac{\kappa}{2\pi} \iint\limits_{\Gamma} \nu_m(P) \frac{\partial}{\partial n} \left(\frac{1}{|MP|} + \frac{1}{|MP'|} \right) d\Gamma_P + \kappa F_0(M), \quad m = 0, 1, 2, \ldots \tag{4.36}$$

Theorem 4.1. *Under the abovementioned assumptions (a) through (d) and for sufficiently small values of* $|\kappa|$, *the iterative process in (4.36) converges on* Γ *to a unique solution of the integral equation (4.20) for any initial* $\nu_0(M)$ *satisfying the conditions of the lemma.*

Proof. We estimate the uniform norm of the difference between two successive approximations. The estimate (4.35) of the lemma implies

$$\|\nu_{m+1} - \nu_m\|_C \leq \|\nu_m - \nu_{m-1}\|_C \cdot \frac{|\kappa|}{2\pi} \left(C_1 + \frac{C\pi}{2d_\Gamma} \right).$$

Then, for sufficiently small $|\kappa|$ values such that

$$|\kappa| \leq 2\pi \left(C_1 + \frac{C\pi}{2d_\Gamma} \right)^{-1} = \frac{4\pi d}{2C_1 d_\Gamma + C\pi} = \frac{4\pi}{2C_1 + C\pi/d_\Gamma}, \tag{4.37}$$

it follows that the iterative process (4.36) converges as a geometric progression with the denominator $|\kappa|(C_1 + C\pi/2d_\Gamma)/2\pi$. The uniqueness of the solution follows from the properties of a contractive operator.

It also follows from (4.37) that cases with a small ratio of the length of the contour C to the depth d_Γ are favorable for the speedy convergence of the iterative process.

Remark 4.1 The estimates of the Lemma 4.1 and the results of Theorem 4.1 can be easily generalized to the case of several local inclusions placed along the direction of the axis *Oy*.

4.3 The BEM for Solving Direct Sounding Problems Above a Medium with Buried Relief, with Numerical Examples

In this section, we consider the mathematical aspects of the 2.5D and 3D solutions of electrical sounding problems above buried relief. In this case, the domain of the definition of an unknown function in the integral equation is infinite in both variables. This requires some additional research to justify the numerical method.

4.3.1 Statement of the Direct Problem and Solvability of the Integral Equation

Let us formulate the mathematical statement of the VES problem over a medium with buried 2D relief. Concerning the geometry of the medium, we assume the following:

(a) Let the Cartesian x–y plane coincide with the earth's surface, and assume that the conductivity distribution does not depend on the y coordinate.
(b) The medium consists of two layers; the boundary Γ between them allows for a parameterization of the form $z = f(x)$, where the function $f(x)$ (Fig. 4.9) satisfies the following conditions:

$$\begin{aligned} & f(x) \in C^2(R), \quad f(x) \equiv h, \qquad |\, x \,| \geq a, \\ & \max(|f'(x)|, \quad |f''(x)|) \leq K, \quad 0 < m_f \leq |\, f(x) \,| \leq M_f < \infty. \end{aligned} \tag{4.38}$$

(c) The distribution of the conductivity is piecewise constant and 2D in the domain $z > 0$: $\sigma(x, z) = \sigma_1$, if $z < f(x)$ and $\sigma(x, z) = \sigma_2$, if $z \geq f(x)$ for all $\{(x, y, z) | z > 0\}$.

Let the origin of the coordinate system coincide with the point location of the current source. We remain within the framework of the mathematical model described in Chap. 3 (Sect. 3.2):

$$\begin{aligned} & \Delta U = 0, \quad (x, y, z) \in \{z > 0\} \backslash \Gamma, \\ & \left.\frac{\partial U}{\partial z}\right|_{z=0} = \frac{I}{R_0^2 \sigma_1} \delta(\mathbf{r}), \\ & \sigma_1 \left.\frac{\partial U}{\partial n}\right|_{\Gamma+} = \sigma_2 \left.\frac{\partial U}{\partial n}\right|_{\Gamma-} \\ & U(\infty) = 0. \end{aligned} \tag{4.39}$$

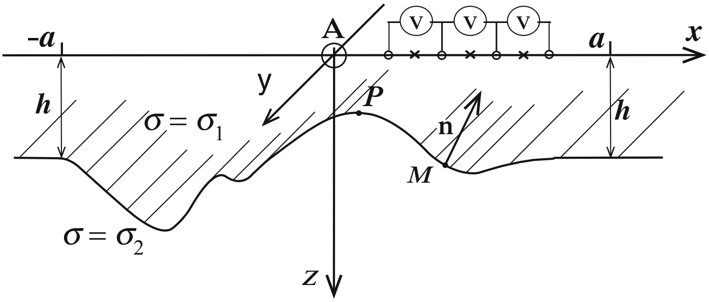

Fig. 4.9 The sounding scheme over a model with buried 2D relief and the model of the medium

Additionally, as in Sect. 4.2, we represent the solution of the problem at an arbitrary point M in the form of a sum of potentials:

$$U(M) = \frac{I}{R_0\sigma_1}(U_0(M) + u(M)),$$

where I is the current strength, and R_0 is a given length scale.

In the numerical simulation, it is convenient to take the function $U_0(M)$ in the form of a solution for a two-layered medium with conductivities of σ_2 (if $z > h$) and σ_1 (if $z \leq h$). As shown in Chap. 3 (Sect. 3.4), this solution is expressed in terms of Bessel functions of the first kind and zero order and has the form

$$\begin{aligned} U_0(r,z) &= \frac{\rho_1 I}{2\pi}\int\limits_0^\infty K(\lambda)J_0(\lambda r)rdr \\ &= \frac{I}{2\pi\sigma_1}\int\limits_0^\infty (1 + 2\theta_1(\lambda)\cos h\,(\lambda z))J_0(\lambda r)rdr, \end{aligned} \tag{4.40}$$

if $z \leq h$, and is equal to

$$U_0(r,y) = \frac{I}{2\pi\sigma_1}\int\limits_0^\infty (1 + \theta_2(\lambda)\exp{(-\lambda z)})J_0(\lambda r)rdr, \tag{4.41}$$

if $z > h$.

The functions $\theta_1(\lambda)$ and $\theta_2(\lambda)$ are given by the following expressions:

$$\begin{aligned} \theta_1(\lambda) &= \frac{\kappa\exp(-2\lambda h)}{1-\exp(-2\lambda h)}, \quad \kappa = \frac{\sigma_1 - \sigma_2}{\sigma_1 + \sigma_2}, \\ \theta_2(\lambda) &= (1+\exp(2\lambda h))\theta_1(\lambda) = \frac{\kappa(1+\exp(-2\lambda h))}{(1-\exp(-2\lambda h))}. \end{aligned} \tag{4.42}$$

Here, $r = \sqrt{x^2 + y^2}$ is the distance from a point to the Oz axis. Then, the function $u(M)$ is a solution of the boundary value problem:

$$\begin{aligned} &\Delta u = 0, \quad (x,y,z) \in \{\{z > 0\}\backslash\Gamma\}, \\ &\left.\frac{\partial u}{\partial z}\right|_{z=0} = 0, \\ &\sigma_1\left.\frac{\partial u}{\partial u}\right|_{\Gamma+} - \sigma_2\left.\frac{\partial u}{\partial n}\right|_{\Gamma-} = -\sigma_1\left.\frac{\partial U_0}{\partial u}\right|_{\Gamma+} + \sigma_2\left.\frac{\partial U_0}{\partial n}\right|_{\Gamma-} \\ &u(\infty) = 0. \end{aligned} \tag{4.43}$$

Additionally, as in Sect. 4.2, we represent the solution $u(M)$ in the form of a simple layer potential generated by secondary sources distributed along the geoelectric boundary Γ and its reflection in the half-space $\{z < 0\}$:

$$u(M) = \frac{1}{2\pi} \iint_{\Gamma} \nu(P) \left(\frac{1}{| MP |} + \frac{1}{|MP|'} \right) d\Gamma_P. \tag{4.44}$$

Repeating the arguments of Sect. 4.2, we know that the function $\nu(M)$ satisfies an integral equation of the form of (4.20), but the function $\nu(M)$ is defined in $\boldsymbol{R}^2$:

$$\nu(M) = \frac{\kappa}{2\pi} \iint_{\Gamma} \nu(P) \frac{\partial}{\partial n} \left(\frac{1}{| MP |} + \frac{1}{| MP' |} \right) d\Gamma_P + \kappa F_0(M), \tag{4.45}$$

where $F_0(M) = \partial U_0 / \partial n, \quad \mathrm{M} \in \Gamma$.

Here, the points M and P belong to the integration surface Γ, and the point P' belongs to its reflection in the half-space $\{z < 0\}$.

Let us consider the solvability of (4.45). Again, we cannot directly apply the classical results of Chap. 2 (Sect. 2.2) because the domain of Γ is unbounded. However, in this case, the iteration procedure can also be justified for small media contrasts (Mukanova 2010).

Lemma 4.2. *Suppose that the abovementioned conditions (a) through (c) hold and that the function ν(x, y), defined on the surface Γ, is both bounded and continuous, and satisfies the descending condition at infinity:*

$$|\nu(x, y)| \leq \frac{C_\nu \parallel \nu \|_C}{| x |}, \tag{4.46}$$

where C_ν is a constant. Then, the functions

$$\mu(x, y) = \iint_{\Gamma} \nu(x_1, y_1) \frac{\partial}{\partial n} \left(\frac{1}{|MP|} \right) d\Gamma(x_1, y_1),$$

$$\mu_1(x, y) = \iint_{\Gamma} \nu(x_1, y_1) \frac{\partial}{\partial n} \left(\frac{1}{|MP'|} \right) d\Gamma(x_1, y_1),$$

where

$$M = (x, y, f(x)), P = (x_1, y_1, f(x_1)) \in \Gamma, P' = (x_1, y_1, -f(x_1))$$

satisfy the estimates

$$\mu(x, z) \leq C_1(K, a, C_\nu) \sup_{\Gamma} |\nu(x, z)|, \quad \mu_1(x, z) \leq C_2(K, a, C_\nu) \sup_{\Gamma} |\nu(x, z)| \tag{4.47}$$

and the decreasing conditions at infinity:

$$\mu(x, z), \quad \mu_1(x, z) \sim O(1/|x|) \quad \text{as} \quad |x| \to \infty.$$

Proof. The derivative with respect to the direction **n** is

$$\partial/\partial\mathbf{n}(1/|MP| + 1/|MP'|) = \cos\psi/|MP|^2 + \cos\psi'/|MP'|^2, \tag{4.48}$$

where the angles ψ and ψ' are formed by the vector **n** and the directions MP and MP', respectively.

Considering (4.48), we transform the expressions for $\mu(x, z)$ and $\mu_1(x, z)$ and consider the parameterization of Γ according to condition (b):

$$\begin{aligned} \mu(x,z) &= \iint\limits_{\Gamma} \nu(x_1,y_1)\left(\frac{\cos\psi}{|MP|^2}\right)\sqrt{1+f'(x_1)}dx_1dy_1 \\ \mu_1(x,z) &= \iint\limits_{\Gamma} \nu(x_1,y_1)\left(\frac{\cos\psi'}{|MP|^2}\right)\sqrt{1+f'(x_1)}dx_1dy_1. \end{aligned} \tag{4.49}$$

With regard to the parameterization of Γ, the vectors MP, MP', and **n** have the following components:

$$MP = (x_1 - x, y_1 - y, f(x_1) - f(x)), \quad MP' = (x_1 - x, y_1 - y, f(x_1) + f(x)),$$

$$\mathbf{n} = \frac{1}{\sqrt{1+f'(x)}}(f'(x), 0, -1),$$

Therefore, the expressions of (4.49) can be rewritten as

$$\begin{aligned} \mu(x,y) &= \frac{1}{\sqrt{1+f'^2(x)}}\int\limits_{-\infty}^{\infty}\int\limits_{-\infty}^{\infty}\frac{\nu(x_1,y_1)(f(x)-f(x_1)-f'(x)(x-x_1))}{|MP|^3}\sqrt{1+f'^2(x_1)}dx_1dy_1, \\ \mu_1(x,y) &= \frac{1}{\sqrt{1+f'^2(x)}}\iint\limits_{\Gamma}\frac{\nu(x_1,y_1)(-f(x_1)-f(x)-f'(x)(x-x_1))}{|MP'|^3}\sqrt{1+f'^2(x_1)}dx_1dy_1. \end{aligned} \tag{4.50}$$

We first prove the assertion of the lemma for the function $\mu(M)$. Let us take some $b > 2a$. Consider two cases: (1) the point $M(x, z)$ is such that $|x| > b$, and (2) the point $M(x, z)$ is such that $|x| \le b$.

Then, the function $\mu(M)$ from the expressions of (4.50) is equal to

$$\begin{aligned} \mu(M) = \frac{1}{\sqrt{1+f'(x)^2}}\Bigg[&\int\limits_{|x_1|>a}\int\limits_{-\infty}^{\infty}\frac{\nu(x_1,y_1)\cos\psi}{|MP|^2}\sqrt{1+f'(x_1)^2}dx_1dy_1 \\ &+\int\limits_{-a}^{a}\int\limits_{-\infty}^{\infty}\frac{\nu(x_1,y_1)\cos\psi}{|MP'|^2}\sqrt{1+f'(x_1)^2}dx_1dy_1\Bigg]. \end{aligned}$$

By the assumptions implied for the function $f(x)$, the first term is zero for $|x| > b$ and for $|x_1| > a$; hence,

$$\begin{aligned}
|\mu(M)| &\leq \|\nu\|_C \int\limits_{|x_1|\leq a} \int\limits_{-\infty}^{\infty} \frac{\sqrt{1+K^2}}{(x-x_1)^2+(y-y_1)^2}\,dx_1 dy_1 \\
&= \|\nu\|_C \sqrt{1+K^2}\pi \int\limits_{-a}^{a} \frac{dx_1}{|x-x_1|} \leq \|\nu\|_C \sqrt{1+K^2}\pi \ln\left|\frac{x+a}{x-a}\right| \\
&\leq \|\nu\|_C \sqrt{1+K^2}\pi \ln\left|\frac{3a}{a}\right| = \sqrt{1+K^2}\pi\ \ln 3\|\nu\|_C.
\end{aligned} \tag{4.51}$$

Considering the asymptote of the function $\ln|(x+a)/(x-a)|$ as $x \to \infty$, we also know that for $|x| \to \infty$: $\mu(M) \sim O(1/|x|)$. Thus, the assertion of the lemma for the function $\mu(M)$ for $|x| > b$ is proven.

For $x \leq b$, it suffices to obtain an estimate for the modulus of the function $\mu(M)$. Considering the representation of an increment in the function with a remainder term in Lagrangian form, we have

$$|f(x) - f(x_1) - f'(x)(x-x_1)| \leq K(x-x_1)^2. \tag{4.52}$$

We divide the regions of integration with respect to x_1 in the equations of (4.50) into two parts and consider the inequality (4.52) and the conditions of the lemma, after which we have

$$\begin{aligned}
|\mu(x,z)| \leq \frac{(1+K^2)K}{2}\|\nu\|_C \int\limits_{-b}^{b} (x-x_1)^2 \int\limits_{-\infty}^{\infty} \frac{dy_1}{\sqrt{(x-x_1)^2+(y-y_1)^2}^{\,3}}\,dx_1 + \\
(1+K^2)\|\nu\|_C \int\limits_{|x_1|>b} \int\limits_{-\infty}^{+\infty} \frac{C_\nu dy_1 dx_1}{|x_1|\left[(x-x_1)^2+(y-y_1)^2\right]}.
\end{aligned}$$

Now, we calculate the elementary integrals and, using the asymptotic behavior of the function $\nu(P)$, substitute the estimate $|\nu(P)| \leq C\nu/|x_1|$. Then, we consider the boundedness of a function of the form $\ln(b \pm x)/x$ for all x, including $x \to 0$, and obtain the following:

$$\begin{aligned}
|\mu(M)| &\leq 2(1+K^2)Kb\|\nu\|_C + C_\nu\|\nu\|_C(1+K^2)\pi \int\limits_{|x_1|>b} \frac{dx_1}{|x_1||\ x-x_1|,} \\
|\mu(x,z)| &\leq 2K(1+K^2)b\|\nu\|_C + C_\nu\|\nu\|_C \frac{\pi}{x}\ \ln\frac{b+x}{b-x} \\
&\leq (1+K^2)(2Kb + 3\pi C_\nu/b)\|\nu\|_C.
\end{aligned} \tag{4.53}$$

Combining (4.51) and (4.53), we obtain the assertion of the lemma with respect to the function $\mu(M)$:

$$\mu(M) \leq \left[\pi\sqrt{1+K^2}\ln 3 + \left(1+K^2\right)\left(2Kb + 3\pi C_\nu/b\right)\right]\|\nu\|_C = C_1\|\nu\|_C.$$

Now, we are going to prove the lemma for the function $\mu_1(M)$. Suppose that $x > a$. It follows from the expressions of (4.50) and the conditions on the function $f(x)$ that

$$\mu_1(x,y) = (1+K^2)\int\limits_{|x_1|>a}\int\limits_{-\infty}^{\infty}\frac{2H\nu(x_1,y_1)}{((x_1-x)^2+4H^2+(y_1-y)^2)^{3/2}}dx_1dy_1+$$

$$+(1+K^2)\int\limits_{|x_1|<a}\int\limits_{-\infty}^{\infty}\frac{\nu(x_1,y_1)\Big(H+f(x_1)\Big)}{((x_1-x)^2+\Big(H+f(x_1)\Big)^2+(y_1-y)^2)^{3/2}}dx_1dy_1 \leq 4H(1+K^2)\|\nu\|_C\times$$

$$\int\limits_{|x_1|>a}\frac{C_\nu dx_1}{|\,x_1\,|\,((x_1-x)^2+4H^2)}+2(H+M_f)(1+K^2)\|\nu\|_C\int\limits_{|x_1|<a}\frac{dx_1}{(x_1-x)^2+4m_f^2}.$$

Calculating the elementary integrals, we obtain the following:

$$|\,\mu_1(x,y)\,| \leq \frac{4C_\nu H\left(1+K^2\right)\|\nu\|_C}{x^2+4H^2}\left(\ln\frac{\sqrt{4H^2+(a-x)^2}\sqrt{4H^2+(a+x)^2}}{a^2}+\right.$$

$$\left.x\left(\arctan\frac{a+x}{2H}-\arctan\frac{a-x}{2H}\right)\right)+\frac{\left(H+M_f\right)\left(1+K^2\right)\|\nu\|_C}{m_f}\left(\arctan\frac{x+a}{2m_f}-\right.$$

$$\left.\arctan\frac{x-a}{2m_f}\right) \leq C\left(C_\nu, H, m_f, M_f, a\right)\|\nu\|_C.$$

Analyzing the asymptote of the formula above for $|x| \to \infty$, we can see that $\mu_1(x, z) \sim O(\ln(x)/x^2) + O(1/x^2) \sim O(\ln(x)/x^2)$.

If $x \leq a$, then

$$|\mu_1(x,y)| \leq \left(1+K^2\right)\left|\int\limits_{|x_1|<a}\int\limits_{-\infty}^{\infty}\frac{(f(x_1)+f(x)-f'(x)(x_1-x))\nu(x_1,y_1)}{\left((x_1-x)^2+(f(x)+f(x_1))^2+(y_1-y)^2\right)^{3/2}}dx_1dy_1+\right.$$

$$\left.\int\limits_{|x_1|>a}\int\limits_{-\infty}^{\infty}\frac{\nu(x_1,y_1)(H+f(x))}{\left((x_1-x)^2+(f(x)+y_0)^2+(y_1-y)^2\right)^{3/2}}dx_1dy_1\right| \leq 2\left(M_f+Ka\right)\left(1+K^2\right)\|\nu\|_C\times$$

$$\int\limits_{|x_1|<a}\frac{dx_1}{(x_1-x)^2+4{m_f}^2}+2\left(H+M_f\right)\left(1+K^2\right)\|\nu\|_C\int\limits_{|x_1|>a}\frac{dx_1}{(x_1-x)^2+4{m_f}^2}.$$

Integrating with respect to x_1, we obtain the following:

$$\mu_1(x,z) \le \frac{\pi\left(1+K^2\right)}{m_f} \|\nu\|_C \cdot \max\left(M_f + Ka, M_f + H\right).$$

The lemma is thus proven.

Let us consider an iterative scheme to solve (4.45). We define an initial approximation of the function $\nu_0(M)$ satisfying the conditions of the lemma. Each subsequent approximation $\nu_{j+1}(M)$ is calculated using the iterative scheme similar to (4.36):

$$\nu_{j+1}(M) = \frac{\kappa}{2\pi} \iint\limits_{\Gamma} \nu_j(P) \frac{\partial}{\partial n}\left(\frac{1}{|\,MP\,|} + \frac{1}{|\,MP'\,|}\right) d\Gamma_P + \kappa F_0(M), \quad j = 0, 1, 2, \ldots \tag{4.54}$$

Theorem 4.2. *Under the abovementioned assumptions (a) through (c) and for sufficiently small values of* $|\kappa|$, *the iterative process in (4.54) converges uniformly on* Γ *to the solution of the integral equation (4.45) for any initial* $\nu_0(M)$ *satisfying the conditions of the lemma.*

Proof. Let us estimate the uniform norm of the difference between two successive approximations. It follows from (4.54) that

$$\left\|\nu_{j+1} - \nu_j\right\|_C \le \frac{|\kappa|}{2\pi} \iint\limits_{\Gamma} \left|\nu_j - \nu_{j-1}\right| \left|\frac{\partial}{\partial n}\left(\frac{1}{|\,MP\,|} + \frac{1}{|\,MP'\,|}\right)\right| d\Gamma_P, \quad j = 0, 1, \ldots \tag{4.55}$$

Estimating the integrals based on the lemma, we obtain

$$\left\|\nu_{j+1} - \nu_j\right\|_C \le \frac{|\kappa|}{2\pi}\Big(C_1(K,a,C_\nu) + C_2(K,a,C_\nu)\Big)\left\|\nu_j - \nu_{j-1}\right\|_C.$$

Hence, it follows that for sufficiently small values of $|\kappa|$, the iterative process in (4.54) converges uniformly on Γ to some function $\nu(M)$ as a geometric progression with a denominator of

$$q = \kappa(C_1(K,a,C_\nu) + C_2(K,a,C_\nu))/2\pi.$$

Considering the limit in (4.54) as $j \to \infty$, the function $\nu(M)$ satisfies the integral equation (4.45). The transition to the limit under the integral in this case is correct with the existence of integrals and the uniform convergence of the integrands. The improper integral with respect to x_1 and z_1 also converges uniformly by virtue of the properties of a Newtonian potential with a polar kernel defined on a Lyapunov surface.

4.3.2 Solvability of the Integral Equation in the 3D Case

In this section, we justify a numerical method for the purpose of solving the integral equation to calculate the field in a medium with an immersed 3D relief. Let us formulate the mathematical formulation of the problem.

The assumptions concerning the geometry of the inhomogeneity are as follows:

(a) Let the Cartesian x–y plane coincide with the surface of the earth, and let axis Oz be directed inward.
(b) The distribution of the conductivity is piecewise constant: $\sigma(x, y, z) = \sigma_2$, if $z \geq f(x, y)$ and $\sigma(x, y, z) = \sigma_,$ if $0 < z < f(x, y)$ for any point $M = \{(x, y, z) | z \geq 0\}$.
(c) There exists a parameterization of the internal geoelectric boundary Γ of the form $z = f(x, y)$ (Fig. 4.10) with the function $z = f(x, y)$.
(d) The surface Γ can be represented as a finite union of the surfaces Γ_i on which the cosine of the angle between the normal to the surface and the direction of AM is constant: $\Gamma = \cup_{i=1}^{I} \Gamma_i$.

For the 3D geometry of the buried relief, the integral equation has the same form (4.45), where the function U_0 can be obtained from (4.40) or (4.14).

In this case, the problem again reduces to an integral equation similar to (4.45):

$$\nu(M) = \frac{\kappa}{2\pi} \iint_{\Gamma} \nu(P) \frac{\partial}{\partial n} \left(\frac{1}{|MP|} + \frac{1}{|MP'|} \right) d\Gamma_P + \kappa F_0(M), \tag{4.56}$$

where the right-hand side is equal to the derivative of the “normal” field $U_0(M)$ in the direction **n**:

$$F_0(M) = \partial U_0 / \partial n \quad \mathrm{M} \in \Gamma.$$

Let us formulate the following lemma without proof (Mukanova 2010).

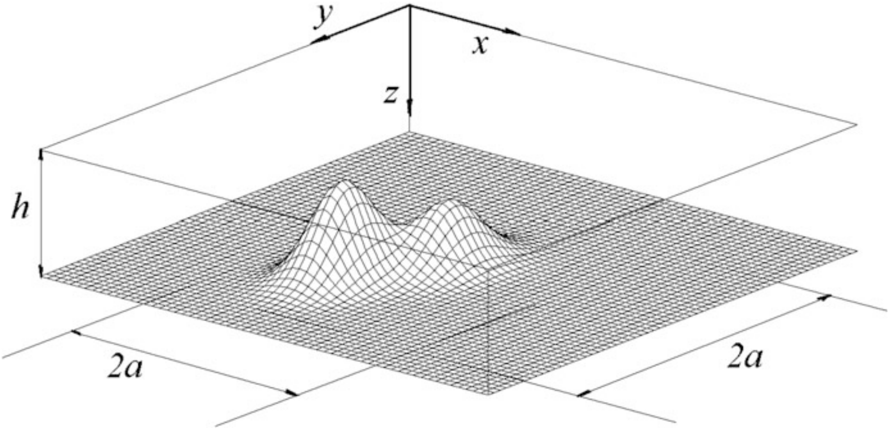

Fig. 4.10 The sounding scheme over a model with buried 3D relief and the model of the medium

Lemma 4.3. *Suppose that the abovementioned conditions (a) through (c) hold and that the function ν(M) for* M = *(*x, y, z*)* ∈ S *is bounded and continuous on* S *and satisfies the decreasing condition of the form*

$$|\nu(M)| \leq \frac{C_\nu \|\nu\|_C}{r}, \text{ for } r = \sqrt{x^2 + y^2} > a_f, C_\nu = \text{const.}$$

Then, the functions

$$\mu(M) = \iint\limits_S \nu(M_1)\frac{\partial}{\partial n}\left(\frac{1}{|MP|}\right)d\Gamma_P, \quad \mu_1(M) = \iint\limits_S \nu(M_1)\frac{\partial}{\partial n}\left(\frac{1}{|PM'|}\right)d\Gamma_P$$

satisfy the following estimates:

$$\mu(M) \leq C_1 f(K, C_\nu, a)\|\nu\|_{C(\Gamma)}, \quad \mu_1(M) \leq C_2\big(K, m_f, M_f, C_\nu, a\big)\|\nu\|_{C(\Gamma)},$$
$$\mu(\mathrm{M}) = O(1/r), \quad \mu_1(\mathrm{M}) = O(1/r) \text{ as } r \to \infty.$$

The main steps in the proof of the above lemma differ slightly from the proof of Lemma 4.3 and contain a large number of cumbersome calculations; therefore, we omit them here.

Based on Lemma 4.3, we can prove the following theorem similar to Theorem 4.2.

Theorem 4.3. *Under assumptions (a) through (c) for sufficiently small* $\kappa = |\sigma_2 - \sigma_1|/(\sigma_2 + \sigma_1)$*, the iterative process in (4.54) converges uniformly on Γ to the solution of the integral equation (4.56) for any initial* $\nu_0(\mathrm{M})$ *satisfying the conditions of Lemma 4.3.*

A distinctive feature of the theorems proven herein is that the desired functions are not required to belong to $L_2(\Gamma)$. The solution can be obtained in the class of continuous functions that satisfy the relatively weak conditions of decreasing on infinity.

We now consider the solvability of the integral equation (4.56) in the class of continuous and quadratically summable functions in $\boldsymbol{R}^2$. Let the dimensionless scales of the length, conductivity, and potential be R_0, σ_1, and $I/(\sigma_1 R_0)$, respectively. We formulate the results of this section in dimensionless variables. Without the loss of generality, we can assume that the center of the Cartesian coordinate system coincides with the point *A* (i.e., with the position of the point source).

Let us prove the following lemma.

Lemma 4.4. *Let* $\mathrm{U}_0 = -1/(2\pi|\mathrm{AM}|)$ *be a solution corresponding to a homogeneous medium with a conductivity* $\sigma_1 = 1$*. We introduce the notation* $\mathrm{F}_0(\mathrm{M}) = \partial \mathrm{U}_0/\partial \mathrm{n}$*,* $M \in \Gamma$*. Then, the function defined as*

$$F_1(M) = \frac{\kappa}{2\pi} \iint\limits_{\Gamma} F_0(P) \frac{\partial}{\partial n} \left(\frac{1}{|MP|} + \frac{1}{|MP'|} \right) d\Gamma_P + \kappa F_0(M), \quad M \in \Gamma \tag{4.57}$$

is continuous and quadratically summable on the surface Γ.

Proof. First, we prove that the function $F_0(M)$ is bounded, continuous, and quadratically summable on $\boldsymbol{R}^2$, after which we prove the lemma.

The normal to the surface and the vector AM in the parameterization defined by condition (b) are given by the following formulae:

$$\begin{aligned} \mathbf{n} &= \left(f_x, f_y, -1\right) / \sqrt{1 + f_x^2 + f_y^2}, \\ \mathbf{AM} &= \{x, y, f(x, y)\}. \end{aligned}$$

For $R_M = \sqrt{x^2 + y^2} > 2a_f$, the function $F_0(M) = \partial U_0 / \partial n$ is written as follows:

$$F_0(M) = \frac{z}{|AM|^3} = \frac{f(x, y)}{|AM|^3}, \quad x^2 + y^2 > 2a_f. \tag{4.58}$$

Then, under assumptions (a) through (c) of this subsection, the following estimates hold:

$$|F_0(M)| \le \frac{M_f}{|AM|^3} \le \frac{M_f}{\left(x^2 + y^2 + m_f^2\right)^{3/2}} \le \frac{M_f}{R^3}, \quad R = x^2 + y^2. \tag{4.59}$$

On the other hand, this function is bounded inside the circle of radius $2a_f$:

$$\begin{aligned} |F_0(M)| &= \frac{\left|f_x(x, y)x + f_y(x, y)y - f(x, y)\right|}{\sqrt{x^2 + y^2 + f^2(x, y)}^3} \le \frac{K(x^2 + y^2)}{\left(x^2 + y^2 + m_f^2\right)^{3/2}} \\ &\le \frac{K}{\sqrt{x^2 + y^2 + m_f^2}} \le \frac{K}{m_f}. \end{aligned} \tag{4.60}$$

The estimates (4.59) and (4.60) guarantee the boundedness of the function $F_0(M)$ and the summability of the improper integral of ${F_0}^2(M)$, that is, $F_0(M) \in L_2(\Gamma)$.

Suppose now that the function $F(M)$ is continuous, bounded on Γ, and satisfies the estimate

$$|F(M)| \le \frac{C_F}{R^{1+\gamma}}, \quad R = \sqrt{x^2 + y^2}, \quad \gamma > 0. \tag{4.61}$$

Let us study the asymptotic behavior of the operator of the integral equation applied to the function $F(M)$ as $R \to \infty$:

$$
\begin{aligned}
&Q(M) = \iint\limits_{\Gamma} F(P)\frac{\partial}{\partial n}\left(\frac{1}{|MP|} + \frac{1}{|MP'|}\right) d\Gamma_P = \iint\limits_{\Gamma} F(P)\tilde{K}(M,P) d\Gamma_P,\\
&\tilde{K}(M,P) \triangleq \frac{\partial}{\partial n}\left(\frac{1}{|MP|} + \frac{1}{|MP'|}\right), \quad M = (x_M, y_M) \in \mathrm{R}^2.
\end{aligned}
\tag{4.62}
$$

Let M be such a point that $R = \sqrt{x_M^2 + y_M^2} > 2a_f$. We consider the parameterization of Γ with respect to the variables x and y in the expression (4.62) and split the integral (4.62) into two terms: the integral over the interior of a circle of radius $R/2$ with the center at the point M and the integral over the outer part of the circle:

$$
\begin{aligned}
Q(M) &= \iint\limits_{K_{R/2}} F(P)\tilde{K}(M,P)J(P)dx'dy' + \iint\limits_{R^2/K_{R/2}} F(P)\tilde{K}(M,P)J(P)dx'dy'\\
&\equiv I_1 + I_2.
\end{aligned}
\tag{4.63}
$$

Here, $P = (x, y)$ and $J(P)$ is the Jacobian of the transformation to the surface parameterization with respect to the coordinates (x, y).

We estimate each term in the integral equation (4.63) separately. By virtue of condition (c), the Jacobian can be estimated as

$$
J(P) = \sqrt{1 + f_x^2 + f_y^2} \leq \sqrt{1 + 2K^2}.
$$

Since the point M is located at a distance R from the origin, the points on the circle $K_{R/2}$, whose center is at the point M, are placed at a distance of no less than $R/2$ from the origin. Therefore, considering the asymptotic behavior of the function $F(M)$, we can write the following:

$$
I_1 \leq C(K, C_F) \iint\limits_{K_{R/2}} \left|\tilde{K}(M,P)\right| \frac{dxdy}{|AM|^{1+\gamma}} \leq \frac{C_1(K, C_F)}{(R)^{1+\gamma}} \iint\limits_{K_{R/2}} \left|\tilde{K}(M,P)\right| dxdy. \tag{4.64}
$$

We now consider the polar coordinates in the last integral with a center at the point M. According to the surface properties, the integral in a neighborhood with a radius equal to the Lyapunov sphere radius d does not depend on the choice of points P and M on the surface, and the integral is bounded by some constant $C_2(d)$ depending only on d. We exclude this neighborhood from the circle $K_{R/2}$ and estimate the integral of the kernel:

$$
\iint\limits_{K_{R/2}} \frac{|\cos\psi_{PM}|}{|PM|^2} d\Gamma(M) = I_d + \int\limits_0^{2\pi} \int\limits_d^{R/2} \frac{1}{\rho^2}\rho d\rho d\varphi = 2\pi(\ln(R/2) - \ln d) + C_2(d).
\tag{4.65}
$$

$$\iint\limits_{K_{R/2}} \frac{|\cos\psi_{PM}|}{|MP'|^2} d\Gamma(M) \le \int\limits_0^{2\pi}\int\limits_d^{R/2} \frac{1}{\left(\rho^2+4m_f^2\right)} \rho d\rho d\varphi + \int\limits_0^{2\pi}\int\limits_0^{d} \frac{1}{\left(\rho^2+4m_f^2\right)} \rho d\rho d\varphi \le$$
$$\int\limits_0^{2\pi}\int\limits_d^{R/2} \frac{1}{\rho^2} \rho d\rho d\varphi + \int\limits_0^{2\pi}\int\limits_0^{d} \frac{1}{m_f^2} \rho d\rho d\varphi \le 2\pi(\ln(R/2) - \ln d) + C_3\left(d, m_f\right).$$

From the inequalities above and from (4.64) we obtain the following for some exponent $\eta < \gamma$:

$$\begin{aligned} I_1 &\le \frac{C_1(K, C_F)}{R^{1+\gamma}} \left[4\pi(\ln(R/2) - \ln d) + C_2(d) + C_3\left(d, m_f\right)\right] \\ &\le \frac{C_4(K, C_F, d)}{R^{1+\eta}} \end{aligned} \tag{4.66}$$

In the case of the function $F(M) = F_0(M)$, we have $\gamma = 2$, and then

$$I_1 \le \frac{C_2(K, C_F, d)}{R^{2+\eta_1}}, \quad 0 < \eta_1 < 1.$$

Here, we have considered that the logarithm increases slower than any power, that is,

$$\lim_{R\to\infty} \frac{\ln R}{R^\eta} = 0, \quad \text{for} \quad \forall\eta > 0.$$

Now, we can estimate the second term in (4.64). Note that the kernel of the equation satisfies the following inequality for $|MP| > R/2$:

$$\left|\tilde{K}(M, P)\right| \le \frac{1}{|MP|^2} + \frac{1}{|MP'|^2} \le \frac{4}{R^2} + \frac{1}{|MP|^2 + |PP'|^2} \le \frac{8}{R^2}. \tag{4.67}$$

Then, for the integral I_2, the following estimate holds:

$$I_2 \le \frac{8}{R^2} \int\limits_0^{2\pi} \int\limits_{R/2}^{\infty} |F_0(P)| J(P) d\rho d\varphi \le \frac{8}{R^2} \iint\limits_{R^2/K_{R/2}} |F_0(P)| d\Gamma_P. \tag{4.68}$$

The function $F_0(P)$ has the form $\frac{\partial}{\partial n}\left(-\frac{1}{2\pi|AP|}\right)$, where the normal $\mathbf{n}$ to the surface Γ is computed at the point P. Therefore, the estimate (4.68) can be computed as follows:

$$I_2 \leq \frac{8}{R^2} \iint\limits_{\boldsymbol{R}^2/K_{R/2}} |F_0(P)| d\Gamma_P = \frac{4}{\pi R^2} \iint\limits_{\boldsymbol{R}^2/K_{R/2}} \frac{|\cos \psi_{PA}|}{|AP|^2} d\Gamma_P. \tag{4.69}$$

Here, $\cos\psi_{PA}$ is the cosine of the angle between the normal to the surface Γ at the point P and the direction PA. Let us represent the integral in (4.69) as the sum of integrals over the surfaces Γ_i where the cosine signs are constant. Then, according to condition (d), we can estimate each term separately. Then, from Proposition 2.1 (see Chap. 2), we know that (4.69) is estimated using the sum of the solid angles, under which each part Γ_i of the surface Γ is visible from point A (i.e., the integral is bounded). Therefore, the following estimate holds:

$$I_2 \leq \frac{C_5}{R^2},$$

where some constant C_5 depends on the surface Γ.

Estimates (4.66) and (4.69) show that the asymptotic behavior of the function $Q(P)$ at infinity for the integral operator (4.62) is of the order $R^{-(2\,+\,\eta)}$, $\eta > 0$. This means that the functions of the form (4.57) are quadratically summable on the surface Γ. Since the function $F_0(M)$ satisfies (4.61), the lemma is proven.

Let $\nu(P)$ be a solution of (4.56). We substitute the expression of $\nu(P)$ from (4.56) instead of $\nu(M)$ and obtain

$$\nu(M) = \frac{\kappa}{2\pi} \iint\limits_{\Gamma} K(M,P) \left(\frac{\kappa}{2\pi} \iint\limits_{\Gamma} \nu(Q) K\big(P,Q\big) d\Gamma_Q + \kappa F_0(P) \right) d\Gamma_P + \kappa F_0(M).$$

According to the lemma, the integral of the second term exists, and it can be estimated via the Hölder inequality. Changing the order of integration in the first term (the order of integration can be changed by virtue of the existence and uniform convergence of the improper integrals according to (4.67)), we obtain the following:

$$\begin{aligned}\nu(M) &= \left(\frac{\kappa}{2\pi}\right)^2 \iint\limits_{\Gamma} \iint\limits_{\Gamma} \nu(Q) K(M,P) K(P,Q) d\Gamma_Q d\Gamma_P + \frac{\kappa^2}{2\pi} \iint\limits_{\Gamma} K(M,P) F_0(P) d\Gamma_P + \kappa F_0(M) \\ &= \frac{\kappa^2}{4\pi^2} \iint\limits_{\Gamma} \nu(Q) \left(\iint\limits_{\Gamma} K(M,P) K\big(P,Q\big) d\Gamma_P \right) d\Gamma_Q + \kappa \left(\frac{\kappa}{2\pi} \iint\limits_{\Gamma} K(M,P) F_0(P) d\Gamma_P + F_0(M) \right).\end{aligned}$$

Introducing the iterated second-order kernel

$$K_2(M,Q) = \iint\limits_{\Gamma} K(M,P) K(P,Q) d\Gamma_P, \tag{4.70}$$

we find that any solution of (4.56) is a solution of the integral equation

$$\nu(M) = \frac{\kappa}{2\pi} \iint\limits_{\Gamma} \nu(P) K_2(M,P) d\Gamma_P + \kappa F_1(M), \tag{4.71}$$

where the term $F_1(M)$ has the form of (4.57):

$$F_1(M) = \frac{\kappa}{2\pi} \iint\limits_{\Gamma} K(M,P) F_0(P) d\Gamma_P + F_0(M).$$

However, if the solution of (4.71) exists, and if we apply the transformations in the inverse order, we see that each solution of (4.71) is also a solution of (4.56). Therefore, (4.71) and (4.56) are equivalent.

Theorem 4.4. *The operator of the integral equation is compact in* $\mathrm{L}_2(\Gamma)$*, and there exists a unique solution of (4.71) for sufficiently small reflection coefficients* κ.

As follows from Lemma 4.4, the function $F_1(M)$ is quadratically summable; thus, (4.71) makes sense. However, as shown in the proof of Lemma 4.4 according to (4.67), the kernel

$$K(M,P) = \frac{\partial}{\partial n}\left(\frac{1}{\mid MP \mid} + \frac{1}{\mid MP' \mid}\right)$$

at infinity has a decreasing order of R^{-2}, which guarantees the quadratic summability of this function with respect to each of the variables on Γ. Then, the iterated kernel is also quadratically summable on the direct product $\Gamma \times \Gamma$ and, in accordance with Remark 2.1 (see Chap. 2), the singularity in the kernel vanishes (i.e., it becomes continuous and bounded).

The proof of the compactness of the operator $\boldsymbol{A}$ of the integral equation almost coincides with the proof of the compactness of the theorems by Petrovskii (1965). Without completely providing the proof from Petrovskii (1965), we outline only the basic steps of the proof:

1. Consider the set S of continuous functions uniformly bounded in the norm of $L_2(\Gamma)$.
2. Taking Hölder's inequality into account, show that the image $\boldsymbol{A}S$ of this set is uniformly bounded. Then, according to Lemma 4.4, the functions $\boldsymbol{A}S$ have the same order of decrease at infinity as $L_2(\Gamma)$.
3. Using an explicit expression for the kernel of the operator $\boldsymbol{A}$ similar to that used by Petrovskii (1965) and for the decrease of the functions at infinity, show that the image of S is a compact set in the space of continuous functions (i.e., it is uniformly bounded and equicontinuous).
4. According to Arzela's theorem, a uniformly convergent subsequence can be chosen from this set. By the nature of the decrease of this subsequence at infinity and the estimate of the norm in $L_2(\Gamma)$ via the norm of $C(\Gamma)$, show that this sequence also converges in $L_2(\Gamma)$. This completes the proof of the compactness of the operator of the equation.

Then, according to Remark 2.2, Theorems 2.1 through 2.3 hold (see Chap. 2, Sect. 2.2). This means that there exists a unique solution of (4.71) for sufficiently small values of κ. Thus, instead of (4.56), we can consider and solve (4.71), for which the above Fredholm theorems for equations of the second kind with a compact operator are valid.

4.3.3 Numerical Examples

In this subsection, we give two examples of the numerical solution of the ERT problem for a two-layer medium containing buried relief. We show examples of anomalies that arise in a numerical solution related to the buried relief. Preliminary test calculations for each case were performed to confirm that the result does not change for further grid refinement. The calculation algorithm was tested, comparing the results of calculations with known solutions for a two-layered medium as described in Chap. 5 (Sect. 5.2.2).

Here, we consider an example of the simplest forms of a buried relief, such as a shaft (Fig. 4.11).

The triangulation is constructed based on the algorithm described in detail in Chap. 5 (Sect. 5.1.2). Figure 4.11b shows the grid placed on the calculation area in Cartesian coordinates. The constructed triangulation allows us to approximate an unknown function using standard 2D linear finite elements. Then, the integral equation (4.45) is solved numerically based on an iterative procedure (4.54). The medium parameters are taken as follows: for the first example, $\rho_1 = 10$ and $\rho_2 = 1$ Ohm m; for the second example, $\rho_1 = 10$ and $\rho_2 = 100$ Ohm m. The shape of the buried relief is given by the following formula:

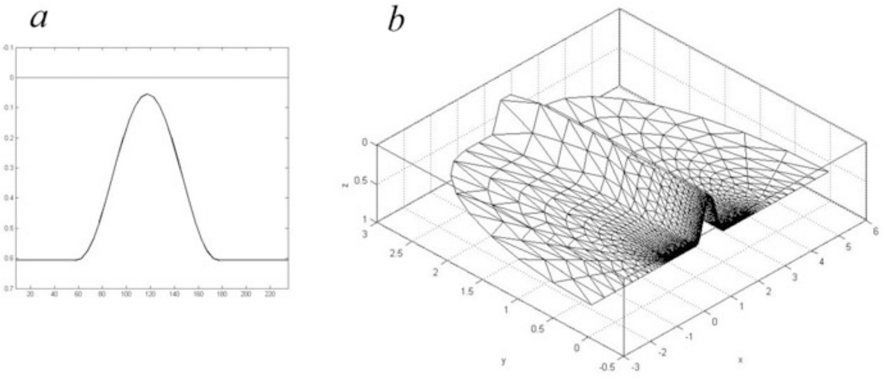

Fig. 4.11 (**a**) Cross-section of the buried relief and (**b**) triangulation of the computational domain

$$z = \begin{cases} d(\cos 2\pi(x - x_0) + 1.2) \\ 2.2d, \{x \le x_0\} \cup \{x \ge 1 + x_0\} \end{cases}.$$

Here the parameter d is determined through maximum inclination angle β of the relief. For instance, in the presented examples we use the inclination angle $\beta = \pi/3$. Then the corresponding parameters are the following: $AB = 235$ m, $MN = 5$ m, and $d = 21.6$ m.

Figure 4.12a, b show distributions of the $\nu(M)$ function over the relief surface shown in Fig. 4.11b. In Fig. 4.13a, b, apparent resistivity curves obtained numerically are shown in log–log scales. The curves are depicted for successive positions of the AMN installation, moving from left to right.

The upper parts of Fig. 4.13a, b show apparent resistivity curves. The corresponding relief shapes are depicted in the bottom of each picture. It is seen from Fig. 4.13 that the presence of the buried relief causes perturbation in the

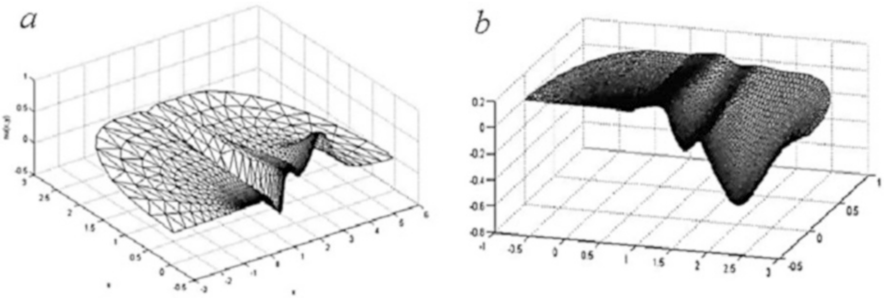

Fig. 4.12 Densities of secondary sources on the buried relief surface: (**a**) $\rho_1 = 10$ and $\rho_2 = 1$ Ohm m; (**b**) $\rho_1 = 10$ and $\rho_2 = 100$ Ohm m

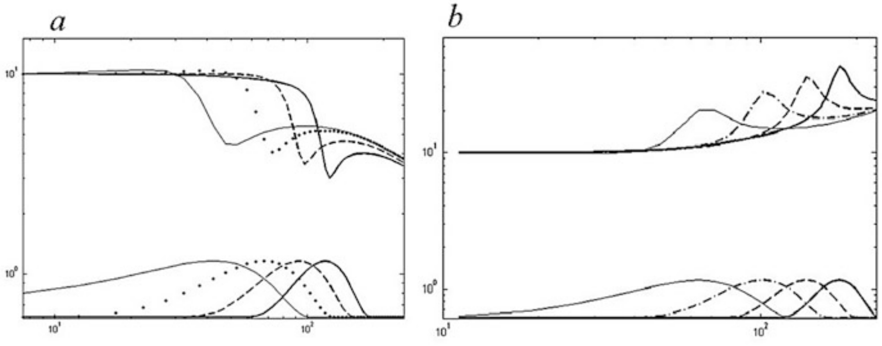

Fig. 4.13 Shape of the surface relief and the apparent resistivity curves in logarithmic scales for (**a**) medium with a low resistivity basis ($\rho_1 = 10$ and $\rho_2 = 1$ Ohm m) and (**b**) medium with a higher resistivity basis ($\rho_1 = 10$ and $\rho_2 = 100$ Ohm m)

double-layer resistivity curves. Simulations show that the amplitude of these distortions practically remains unchanged on a logarithmic scale for different positions of current electrode.

References

A.A. Bobachyev, Resheniye pryamykh i obratnykh zadach elektrorazvedki metodom soprotivleniy dlya slozhno-postroyennykh sred, thesis, Moscow, MSU, 95 p., 2003

N.M. Gunther, *La théorie du potentiel et ses applications aux problèmes fondamentaux de la Physique Mathématique* (Gauthier-Villars, Paris, 1934)

I.N. Modin, V.A. Shevnin, V.K. Khmelevskii, A.G. Yakovlev, et al., *Electricheskoye zondirovanie geologicheskoi sredy. Part I* (MSU, Moscow, 1988)

B.G. Mukanova, Komp'uternoe modelirovanie zadach electricheskogo zondirovania, Dissertation, Almaty, AlFarabi Kaz State University, 2010

I.G. Petrovskii, *Lekcii po teorii integral'nykh uravneniy* (Nauka, Moscow, 1965)

F.G. Tricomi, *Integral Equations* (Interscience, New York, 1957)

Chapter 5
The Boundary Element Method in the Sounding of Media with Ground Surface Relief

5.1 The BEM for a Homogeneous Medium with Surface Relief

In electric tomography, the current source produces an electric field that depends on the array geometry, geoelectric section, and the relief of the land surface. The influence of relief is expressed via anomalies in the distribution of the electric field, which can sometimes be incorrectly interpreted. In Chap. 4, in the case of a ground–air interface with a flat boundary, we applied a reflection method to derive the integral equation.

We start with the mathematical model of electrical resistivity tomography (ERT) above a homogeneous medium with ground surface relief to both identify the influence of relief on distortions of the field and obtain the apparent resistivity curves.

In the case of ground surface relief, we cannot apply a reflection method; however, as shown in Sect. 5.1 and 5.2, the resulting mathematical model can be formulated as either an integral equation or a system of integral equations. The authors of this monograph derived this integral equation for the first time (Mirgalikyzy et al. 2015). Some results of Sect. 5.1 have also been published (Mirgalikyzy et al. 2015); namely, Mirgalikyzy et al. (2015) considered the mathematical model with one source electrode, and performed numerical simulations on a regular rectangular mesh in cylindrical coordinates. The numerical results described here are obtained in an alternative way using the boundary element method (BEM) on a triangular mesh. The content of Sect. 5.2 is based on our collaborative work with the co-authors (Mukanova et al. 2017). Some of the numerical experiments were conducted by our former Ph.D. student T. Mirgalikyzy, and several simulations to choose acceptable mesh parameters through the use of parallelization technologies were conducted by our former bachelor student M. Tussupova. The material in Sect. 5.3 is new and published here for the first time.

B. Mukanova, I. Modin, *The Boundary Element Method in Geophysical Survey*,
Innovation and Discovery in Russian Science and Engineering,
https://doi.org/10.1007/978-3-319-72908-4_5

5.1.1 Mathematical Basics for 2D Relief

In this section, we derive the integral equation and then analyze the solvability of that equation. We make several assumptions regarding the geometry of the ground surface, as follows:

1. Assume that the studied medium occupies a part Ω of a space with some infinite smooth surface Γ. In this section, first we consider relief with 2D geometry.
2. Let the ground surface be formed by a cylindrical surface with generatrices parallel to axis *Oy* in Cartesian coordinates. In other words, the medium crossed by the planes $y = \text{const}$ remains invariable for all *y*. For convenience, we formulate conditions in the Cartesian system of coordinates *Oxyz*. Let the *Oz* axis be directed inside the medium, towards an increase in depth, the *Ox* axis be directed to the right, and the *Oy* axis be such that the system of coordinates is right (Fig. 5.1). Let the specific conductivity of the medium be equal to σ. Assume that the surface Γ satisfies Lyapunov's conditions (see Chap. 2, Sect. 2.1).

In addition to the conditions listed above, we impose some additional geometrical restrictions on the considered surfaces:

3. Let the current source be located at point *A* of the surface Γ; in the neighborhood of *A*, there is a strip of width $2a > 0$ whose surface is flat.
4. Assume that out of some strip of width *L*, the boundary of the medium turns into two half-planes. We choose the system of coordinates so that one of the two half-planes lies on the coordinate plane $z = 0$. Let there exist the parametrization of the surface Γ of the form

$$\Gamma = \left\{ (x, y, z) | -\infty < y < \infty,\ \ z = Z(x) = \left\{ \begin{matrix} f(x), & x \in [0, L], \\ 0, & x < 0. \\ kx + b, & x > L. \end{matrix} \right\} \right\} \tag{5.1}$$

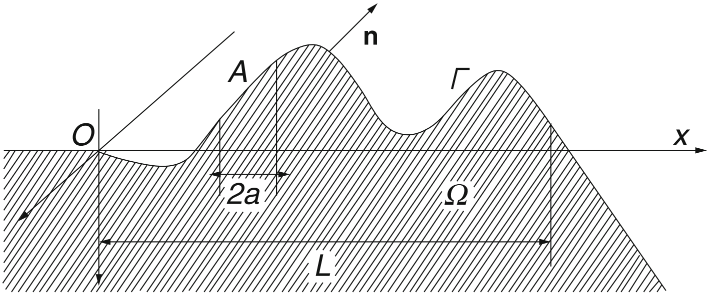

Fig. 5.1 Structure of a 2D model of a medium with a relief surface. See text for a description of the symbols used

The $Z(x)$ function defines a form of the relief in Cartesian coordinates. It is easy to see that external normal vectors to the surface are defined by the following formulae:

$$\mathbf{n} = \begin{cases} (f'(x), 0, -1)\Big/\sqrt{1+f'(x)^2}, & x \in [0, L], \\ (0, 0, -1), \quad x < 0. \\ (k, 0, -1)\Big/\sqrt{1+k^2}, & x > L. \end{cases} \tag{5.2}$$

The direction of a normal in (5.2) is defined in such a way that it is directed out of the medium; then, the medium is located in the region $z > Z(x, y)$.

5. The $f(x)$ function is uniformly limited together with its first derivative, so that $\|f(M)\|_{C^1} < \infty, \ M \in \boldsymbol{R}^2$.
6. Let Hölder's indicator for the normal vector in Lyapunov conditions be $\alpha > 0$ for the surface Γ.
7. Let the parts of a surface Γ_i, $i = 1,\ldots, N$ that are visible from any point P overlap each other a finite number of times; consequently the cosine of the angle under which points M of the surface Γ are visible from a point P changes the sign a finite number of times along Γ.

We consider the problem of the definition of an electric field in the domain Ω occupied by a medium of constant conductivity σ. The external current source is a current electrode placed on the ground surface. We transfer the source into the boundary condition; then, inside the domain Ω, we have Laplace's equation for the potential of the field. Thus, we are in the framework of the model (4.39) that is written for domain Ω as follows:

$$\begin{aligned} &\Delta U = 0, \quad (x, y, z) \in \Omega, \\ &\left.\frac{\partial U}{\partial n}\right|_{\Gamma} = \frac{I}{\sigma R_0^2}\delta(\mathbf{r} - OA), \quad \Gamma = \partial\Omega \\ &U(\infty) = 0. \end{aligned} \tag{5.3}$$

Here, A denotes the position of the source electrode, the point O designates the origin of a Cartesian coordinate system, and R_0 designates the length scale. We reduce the computation problem of the field potential to an integral equation. First, we present the solution of the problem (5.3) at an arbitrary point P in the form of the sum of the potentials of a pointwise source in a uniform half-space and the unknown potential of secondary sources. We pass to the dimensionless variables using R_0 as the scale of length and the relation $I/(R_0\sigma)$ as the scale of potential:

$$U(P) = U_0(P) + \frac{I}{R_0\sigma}u(P) = \frac{I}{R_0\sigma}\left(-\frac{1}{2\pi \mid AP \mid} + u(P)\right).$$

Substituting the function $U(P)$ in (5.3), we see that the $u(P)$ function for $P \in \Omega$ satisfies the following boundary value problem:

$$\begin{cases} \Delta u(M) = 0, \quad M \in \Omega \\ \left.\dfrac{\partial u}{\partial n}\right|_{\Gamma} = \dfrac{\partial}{\partial n} \left.\dfrac{1}{2\pi \mid AP \mid}\right|_{\Gamma} + \delta(\mathbf{r} - OA)\,. \\ \mathrm{u}(\infty) = 0 \end{cases} \tag{5.4}$$

We look for the function $u(P)$ in the form of a simple layer potential with a density $\mu(M)$ on the surface of the medium:

$$u(M) = \iint\limits_{\Gamma} \frac{\mu(P)}{\mid MP \mid} d\Gamma_P. \tag{5.5}$$

Representation (5.5) describes the polarization of a surface of the medium caused by a deviation of Γ from a plane surface. The capacity of the field induced on a surface by charges $\mu(M)$ compensates the external field of a pointwise source in such a way that the total current through the surface is equal to zero (except at point A).

The function expressed by (5.5) satisfies Laplace's equation out of the boundary surface Γ (see Chap. 2). At the surface, we state the boundary condition that ensures the following physical requirement: the current flowing into the medium through the surface at all points of the medium, excluding point A, must be equal to zero.

The current flowing into the medium is expressed in terms of the normal derivative of the potential from the inner side of the medium. According to the properties of the potential of a simple layer, the normal derivative of the potential has a discontinuity on surface Γ. According to (2.5), its value on the inner side of the surface is expressed as

$$\begin{aligned} \left(\frac{\partial u}{\partial n}\right)_{-}(M) &= 2\pi\mu(M) + \iint\limits_{\Gamma} \mu(P)\frac{\partial}{\partial n}\left(\frac{1}{\mid MP \mid}\right) d\Gamma_P \\ &= 2\pi\mu(M) + \iint\limits_{\Gamma} \mu(P)\,\frac{\cos\psi_{MP}}{|MP|^2}\, d\Gamma_P. \end{aligned} \tag{5.6}$$

Here, the angle ψ_{MP} is an angle between MP and the direction of normal at point M. Expression (5.6) allows one to derive an integral equation on the unknown function $\mu(M)$. Substituting (5.6) into the boundary condition (5.4), we have

$$2\pi\mu(M) + \iint\limits_{\Gamma} \mu(P)\,\frac{\cos\psi_{MP}}{|MP|^2}\, d\Gamma_P = \frac{\partial}{\partial n}\left.\left(\frac{1}{2\pi \mid AM \mid}\right)\right|_{\Gamma} + \delta(\mathbf{r} - OA)$$

or

$$\mu(M) = -\frac{1}{2\pi} \iint\limits_{\Gamma} \mu(P)\,\frac{\cos\psi_{MP}}{|MP|^2}\, d\Gamma_P + F_0(M), \tag{5.7}$$

where the function $F_0(M)$ is defined by the expression

$$F_0(M) = \frac{1}{2\pi}\left(\frac{\partial}{\partial n}\left(\frac{1}{2\pi \mid MA \mid}\right)\Bigg|_{\Gamma} + \delta(\mathbf{r} - OA)\right). \tag{5.8}$$

Consider the function (5.8). We notice that according to assumption (4) about a relief form, part of surface Γ is flat in the neighborhood of source point A; therefore, the following function vanishes:

$$\frac{\partial}{\partial n}\left(\frac{1}{2\pi \mid MA \mid}\right)|_{\Gamma} = \frac{\cos\psi_{MA}}{2\pi |MA|^2} = 0, \ \mid x - x_A \mid < a, \ \ M = (x, y, z) \in \Gamma \backslash \{A\}.$$

The reason for this is that the direction of normal on this flat part of a surface is orthogonal to the MA direction; therefore, in all points of that part of Γ, $\cos\psi_{MA} = 0$. However, the potential $1/(2\pi|AM|)$ at the point A exactly compensates the source created by the potential of $U_0(M) = -1/(2\pi|AM|)$. Therefore, if there is a flat area in the neighborhood of the source and the function $U_0(M) = -1/(2\pi|AM|)$ is considered the normal field, then the right side in the equation for the anomalous field $u(M)$ in this neighborhood vanishes. Let us show that the function $F_0(M)$ remains bounded outside of this area. Calculating the normal derivative of the function $U_0(P)$ and considering the surface equation and formula (5.2), we obtain

$$\mid F_0(M) \mid = \frac{1}{4\pi^2}\begin{cases} \dfrac{\mid z_A \mid}{|MA|^3}, & x < 0 \\ \dfrac{\mid f'(x)x - z + z_A \mid}{|MA|^3\sqrt{1 + f'^2(x)}}, & 0 \le x \le L \\ \dfrac{\mid -b + z_A \mid}{|MA|^3\sqrt{1 + k^2}}, & x > L \end{cases}.$$

Here, z_A is the z coordinate of the current source. As noted above, at the vicinity of point A and within its definition area, that function is bounded. Let us examine its behavior outside a circle of radius R. At sufficiently large R such that $|AM| > R$ for any point $M(x,y,z)$, we have

$$\mid F_0(M) \mid \le \frac{C(z_A, b, k)}{R^3}, \quad \text{for} \quad x \notin [0, L]$$

$$\mid F_0(M) \mid \le \frac{\mid f'(x)x - z + z_A \mid}{4\pi^2 R^3} \le \frac{C \mid x \mid + \mid z \mid + \mid z_A \mid}{4\pi^2 \sqrt{x^2 + y^2 + (z - z_A)^2}^3} \le$$

$$\text{Const}\frac{\mid x \mid}{\sqrt{x^2 + y^2}^3}, \ \text{for} \ 0 \le x \le L.$$

To determine whether that function is quadratically summable in R^2, it is necessary to show that the integral

$$I = \iint\limits_{\overline{K_R}} \frac{x^2 d\Gamma}{(x^2+y^2)^3} \tag{5.9}$$

taken over an external part of some circle of radius R is limited. Passing to parametrization (x, y) in the integral and using a uniform estimate of the Jacobian $J(x,y) = \sqrt{1+Z'^2(x)}$, we estimate integral (5.9) as follows:

$$I = \iint\limits_{\overline{K_R}} \frac{x^2 d\Gamma}{(x^2+y^2)^3} = \iint\limits_{\overline{K_R}} J(x,y) \frac{x^2 dxdy}{(x^2+y^2)^3}.$$

Furthermore, we pass to polar coordinates in the planes (x, y) and have

$$I \le C \int\limits_0^{2\pi} \int\limits_R^{\infty} \frac{r^2 \cos^2\varphi r dr d\varphi}{r^6} = C \int\limits_0^{2\pi} \int\limits_R^{\infty} \frac{\cos^2\varphi dr d\varphi}{r^3} = \frac{C\pi}{2R^2} \to 0, \quad \text{as} \quad R \to \infty.$$

We note that, by virtue of the obtained estimates, the decrease of the function $F_0(M)$ at infinity is of the order $\sim R^{-2}$.

Remark. It can be proven that if surface Γ has continuous curvature, then function $F_0(M)$ remains smooth and limited on Γ, even if the vicinity of source A is not flat.

Now, let us show that the function

$$F_1(M) = \frac{1}{2\pi} \iint\limits_{\Gamma} F_0(P) \frac{\cos\psi_{MP}}{|MP|^2} d\Gamma_P + F_0(M), \ M \in \Gamma \tag{5.10}$$

is also quadratically summable in $\boldsymbol{R}^2$. Let us study the behavior of the first term in (5.10), namely, the function

$$F_2(M) = \frac{1}{2\pi} \iint\limits_{\Gamma} F_0(P) \frac{\cos\psi_{MP}}{|MP|^2} d\Gamma_P, \ M \in \Gamma. \tag{5.11}$$

As point P tends to point M, kernel $K(P, M)$ of integral (5.11) has an integrable singularity of order $|PM|^{-1}$ and function $F_0(M)$ is bounded; therefore, for the existence of the integral, the order of decrease of the integrands in (5.11) at infinity is important. Let point M be located outside a circle of sufficiently large radius $R > 2L$. As shown above, function $F_0(M)$ is bounded by some constant C_F, is quadratically summable and has the following order of decreasing at infinity:

$$F_0(P) \le \frac{C_1}{r^2}, \quad r = \sqrt{x^2+y^2}.$$

We show first that integral (5.11) exists for each point of M lying on Γ. Pass in the integral (5.11) to parametrization of a surface on variables (x, y) and then represent the integral as a sum of two items: an integral over the circle of radius $R/2$ with the center at point M and over the external part of that circle:

$$F_2(M) = \frac{1}{2\pi} \iint\limits_{K_{R/2}} F_0(P) \frac{\cos\psi_{MP}}{|MP|^2} J(P)dxdy + \frac{1}{2\pi} \iint\limits_{R^2 \setminus K_{R/2}} F_0(P) \frac{\cos\psi_{MP}}{|MP|^2} J(P)dxdy$$
$$\equiv I_1 + I_2.$$

Here, $P = (x, y)$ and $J(P)$ is the Jacobian of the transition to coordinates (x, y). The Jacobian is estimated from the above by some constant.

Because point M is placed at distance R from the origin, then for points of the circle $K_{R/2}$, the center of which is at point M, the distance to the origin is not less than $R/2$. Then, taking into account an asymptotic of function $F_0(M)$, we have

$$I_1 \le C_2 \iint\limits_{K_{R/2}} \frac{|\cos\psi_{MP}|}{|MP|^2} \frac{dxdy}{|AM|^2} \le \frac{C_3}{R^2} \iint\limits_{K_{R/2}} \frac{|\cos\psi_{MP}|}{|MP|^2} dxdy. \tag{5.12}$$

The last integral is estimated in a similar manner to inequality (4.65) as the sum of the integral over a circle inside Lyapunov's sphere of radius d and the integral outside it:

$$\iint\limits_{K_{R/2}} \frac{|\cos\psi_{MP}|}{|PM|^2} dxdy = I_d + \int\limits_0^{2\pi} \int\limits_d^{R/2} \frac{1}{\rho^2} \rho d\rho d\varphi = 2\pi(\ln(R/2) - \ln d) + C_4(d). \tag{5.13}$$

Substituting (5.13) in inequality (5.12) and considering that the logarithm increases more slowly than any power function, we have

$$I_1 \le \frac{C_4}{R^{1+\eta}}, \quad 0 < \eta < 1. \tag{5.14}$$

Estimates for an external part of the circle of $K_{R/2}$ literally repeat the proof of the inequalities (4.68) and (4.69) and have the form

$$I_2 \le \frac{C_5}{R^{1+\alpha}}.$$

The last estimate guarantees that function $F_1(M)$ has an asymptotic on infinity of the order of $R^{-(1\,+\,\min(\alpha,\eta))}$ and that it is quadratically summable on Γ. Therefore, the integral equation with the second-order iterated kernel with the right-hand side of (5.10) makes sense. Applying Fredholm's theory in the same manner as in Chap. 4 (Sect. 4.3), Eq. (5.6) is reduced to the equation with the iterated kernel, similar to (4.71):

$$\mu(M) = \frac{1}{4\pi^2} \iint\limits_{\Gamma} \mu(P) K_2(M,P) d\Gamma_P + F_1(M), \tag{5.15}$$

where kernel $K_2(M, P)$ is defined by the formula

$$K_2(M,P) = \iint\limits_{\Gamma} \frac{\cos\psi_{MQ}}{|MQ|^2} \frac{\cos\psi_{QP}}{|QP|^2} d\Gamma_Q.$$

The above estimates for functions $F_0(P)$ and $F_1(P)$ allow us to organize the standard iterative procedure for (5.15), taking function $F_1(M)$ as an initial guess. However, for a numerical solution of the problem, it is possible to use the following iterative scheme:

$$\mu_{m+1}(M) = -\frac{1}{2\pi} \iint\limits_{\Gamma} \mu_m(P) \frac{\partial}{\partial n} \frac{1}{r_{MP}} d\Gamma(P) + F_0(M), \quad m = 0, 1, 2, \ldots \tag{5.16}$$

Remarks for the case of 3D buried relief. In the case of a 3D relief, we impose the requirements on surface geometry as in conditions (a), (c), and (d) in Chap. 4 (Sect. 4.3). Additionally, we assume only that the relief satisfies the condition that, in a neighborhood of source A, there is a circle of radius a on which surface Γ is planar.

The derivation of the integral equation in this case does not differ from the above. All the statements concerning application of the Fredholm theory to the equation with an iterated kernel remain valid. The proof of existence of improper integrals of a type of $F_1(M)$ of the previous section literally repeats the proof given in Chap. 4 (Sect. 4.3). The only additional requirement applied to function $F_0(M)$ is the condition of the existence of the small flat vicinity of the source.

5.1.2 Application of the BEM to Solve the Integral Equation

For the numerical solution of the integral equation, we must first construct a mesh on the computational domain. The ultimate goal of solving a direct problem is to compute the apparent resistivity curves. To calculate these curves, we must keep in mind the following:

(a) The distribution of the sought-after function $\mu(M)$ near the measuring line has the most influence on the potential distribution near the measuring line.
(b) The grid should be condensed near the source electrode.
(c) In numerical simulation, we must consider that in the ERT method, the electrodes are at equal distances and can change their roles; therefore, the mesh must be adapted to the location of the electrodes and condensed in the vicinity of any of them.
(d) The grid must be adapted to the shape of the ground surface.

To meet all the above requirements, we perform a triangulation of the computational domain, condensing to the measuring line and logarithmically expanding away from it. First, curvilinear coordinates (q, y) are introduced on the surface of the medium in such a way that coordinate q is measured along the line of the intersection of surface Γ with plane $y = \text{const}$. The transformation from (x, y) coordinates to (q, y) coordinates is conducted using the following formulae:

$$\begin{aligned} dq &= \sqrt{dx^2 + dz^2} = \sqrt{1 + Z'^2(x)}dx, \\ \frac{dx}{dq} &= \frac{1}{\sqrt{1 + Z'^2(x)}}, \quad x(0) = 0. \end{aligned} \tag{5.17}$$

The computational domain is taken in the form of an oval, and the triangulation of the surface is made in the plane of variables (q, y). The size of the computational area is defined by the axis length $L_q = AB$, which corresponds to the length of the measuring line of ERT installation; the height of the computing area along the axis Oy is taken as equal to the radius of the oval curving R_q (Fig. 5.2). The total width of the estimated area with respect to the variable q is $L_q + 2R_q$. Because of the symmetry of the problem with respect to the Oy axis, only triangles of the upper half of that oval are used. A typical example of a computational domain and a triangulation is depicted in Fig. 5.2. Calculation of the Cartesian coordinates of the triangles is conducted via the numerical solution of the ordinary differential equation (ODE) (5.17) using the fourth-order Runge–Kutta method.

It is convenient to calculate all functions in dimensionless quantities. In all the numerical examples described below, we use one-half of the length of measuring line AB as a scale of length. Therefore, in the given examples of triangulation, the length of that line is equal to $L_q = 2$. The triangulation is performed layer by layer, constructing concentric layers of triangles. Each layer of triangles has a height that is greater than that of the previous layer. The number of layers of triangles N is

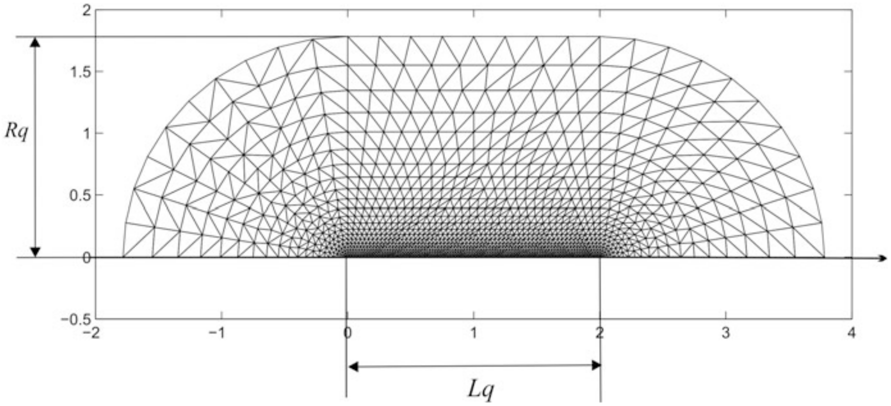

Fig. 5.2 Parameters of the computational domain and a typical triangulation mapped on the plane; R_q radius of the oval curving, L_q axis length

determined so that the thicknesses of the layers form a uniform grid in a logarithmic scale with the step $h_s = \log(1 + R_q\alpha)/N$. Here, α is a parameter of the non-uniformity of the grid. The larger α is, the greater the difference in the sizes of the smallest and largest triangles.

For modeling calculations when the form of a relief can be set analytically, it is convenient to set the computing area L_q, R_q, the parameter of non-uniformity α, and the number of layers of triangles N. These sizes determine a logarithmic step h_s along the radius, the height of the first layer $r_1 = h_1 = (\exp(h_s) - 1)/\alpha$, and a grid step on the measuring line $h_q = 2/\sqrt{3}h_1$.

For calculations for a real relief in the field, it is possible to control the density of the grid via two parameters: the number of electrodes K on the measuring line and the number of grid nodes N_{tr} between two consecutive electrodes. In this case, the triangulation is constructed in such a way that when the number of electrodes is given on the segment L_q, an integer number of triangles is located between two electrodes M and N. As a result, all the electrodes are placed at the vertices of triangles. In this way, the smallest step of a grid $h_q = L_q/N_{\text{tr}}/K$ is defined. It is equal to the edge of the smallest triangle. The sizes of the triangles increase in the following manner as we move away from the axis L_q: the logarithmic step of h_s is selected from the condition that the triangles on the first layer are equilateral; that is, their height is $h_1 = h_q\sqrt{3}/2$ or $r_1 = h_1 = (\exp(h_s) - 1)/\alpha$. From here, $h_s = \log(\alpha h_1 + 1)$ and the number of layers N of triangles is specified from the condition $N = \log(1 + R_q\alpha)/h_s$. In this way, the height of the i-th layer of triangles is defined as $r_i = (\exp(ih_s) - 1)/\alpha$.

The grid represented in Fig. 5.2 is constructed for the parameters $L_{\text{q}} = 2$, $R_q = 1$, $N = 20$, and $\alpha = 4.0$; the triangulation consists of 1464 nodes and 2803 triangles.

The constructed triangulation allows us to approximate an unknown function using standard 2D linear finite elements. Figure 5.3 shows the same grid as in Fig. 5.2, but placed on the calculation area in Cartesian coordinates.

To reduce the equation to a SLAE, the integral in (5.7) is approximated via the sum of integrals over triangles:

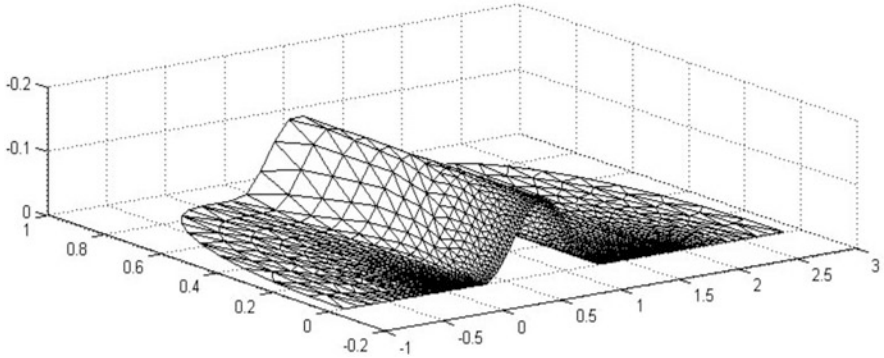

Fig. 5.3 Triangulation of the relief surface in Cartesian coordinates

$$\iint\limits_{\Gamma} \mu(P)\frac{\cos\psi_{MP}}{|MP|^2}d\Gamma_P \approx \sum_{l=1}^{N_\Delta}\iint\limits_{\Delta_l}\mu(P)\frac{\cos\psi_{MP}}{|MP|^2}d\Gamma_P$$

Because the integration formula over a triangle is approximately equal to the prism volume based on this triangle, the integral is approximately equal to the following sum:

$$\iint\limits_{\Delta_l}\mu(P)K(M,P)d\Gamma_P \approx \frac{1}{3}\left(\mu(P_i)K(M,P_i)+\mu(P_j)K(M,P_j)+\mu(P_k)K(M,P_k)\right)S_l.$$

Here, P_i, P_j, and P_k are the vertices of the triangle, and S_l is its area.

Then, Eq. (5.7) is written in a discrete form as follows:

$$\mu_i = \sum_{j=1}^{N_n} A_{ij}\mu_j + F_0^{(i)}, \quad i = \overline{1, N_n}, \tag{5.18}$$

where N_n is the number of nodes of a triangulation. Here, coefficients A_{ij} are formed by the sum on triangles having a common vertex at point P_j:

$$A_{ij} = \frac{1}{3}\sum_{l_j} K(M_i, P_j)S_{l_j}.$$

The system of equations in (5.18) can be solved by either iterative or direct methods. Our numerical experiments using compilers of Intel for the Fortran language show that the iterative method is several times faster because the iterative method allows use of embedded functions for operations with matrixes. In addition, our former student M. Tussupova found that, in the case of parallelization using OpenMP technology, it is possible to achieve an acceleration of the iterative process that is larger than the number of threads when working in parallel mode. For instance, using parallel operation on four threads, one would expect a fourfold acceleration, but the iterative process was accelerated nearly fivefold under these conditions. We explained this surprising circumstance by the fact that, in the parallel operation of threads, each thread can use the results of the new iterations that have been executed by other threads (i.e., any thread working on the mth iteration can take the results of the next iteration performed by another thread); this is impossible in the standard iterative procedure performed by a sequential program. Iterations were executed before achievement of a machine accuracy for variables with the accuracy of real (“float”) data types. Compared with a double-precision data type, we could reduce the volume of the random-access memory occupied by data by about 50%. Calculations show that the application of a double-precision variables data type has no practical influence on the results of the computation.

The goal of our calculations is computation of apparent resistivity. Therefore, after computing the density of a simple layer $\mu(M)$ in triangulation nodes, we calculate the potential $u(M)$ using (5.5). In dimensional variables, this formula is written as follows:

$$u(M) = \frac{2I}{\sigma L_{AB}} \iint\limits_{\Gamma} \frac{\mu(P)}{\mid MP \mid} d\Gamma_P \approx \frac{2I}{\sigma L_{AB}} \sum_{l=1}^{N_\Delta} \frac{\overline{\mu}_l S_l}{\mid M_i \bar{P}_l \mid}. \tag{5.19}$$

Here, $\overline{\mu}_l$ is the density averaged over the triangle with number l, and $\bar{P}_l$ is a center of gravity of that triangle. The averaged values are taken over the triangle vertices. For four-electrode array, it is necessary to compute the current potential for electrode B and then perform algebraic summation of the potentials for electrodes A and B.

After calculating the potential function, the apparent resistivity is calculated using formula (3.1), taking into account the representation of the field as a sum of the normal and anomalous fields:

$$\begin{aligned} \rho_a &= \frac{2\pi\Delta U_{MN}}{I_{AB}} \left(\frac{1}{AM} - \frac{1}{AN} - \frac{1}{BM} + \frac{1}{BN} \right)^{-1} \\ &= \frac{1}{\sigma} + \frac{2\pi\Delta u_{MN}}{I_{AB}} \left(\frac{1}{AM} - \frac{1}{AN} - \frac{1}{BM} + \frac{1}{BN} \right)^{-1}. \end{aligned}$$

Here, A and B are the positions of the current electrodes, and M and N are the positions of the measuring electrodes. The second term gives an anomalous deviation of the apparent resistivity from the resistivity of a homogeneous medium, which is only associated with the influence of the relief.

Before performing systematic calculations to identify possible anomalies, we must perform a series of tests of the numerical method. The first step is to check the convergence of the calculation results when changing and expanding the grid. Because the admissible grid parameters depend on the shape of the relief, it is desirable to conduct test calculations separately for each relief shape. In the calculations, the minimum grid step h_q, the non-uniformity parameter α, and the size of the computational domain R_q should vary.

For an inclination angle of relief of 20° and a half-width of the grid R_q varying in the interval from 1 to 2, the relative change in apparent resistivity is no more than 0.6%. However, the maximum relative deviation between the apparent resistivities calculated for $N = 20$ and $N = 101$ is 2.5% (Fig. 5.5). A change in N from 90 to 100 entails a change in ρ_a of not more than 0.5%. A change in α from 8 to 16 yields an average change in ρ_a of not more than 0.2%. Therefore, for this form of the relief and length of the measuring line, and a maximum inclination angle of 20°, the admissible computing parameters are $R_q = 1$, $\alpha = 8$, and $N = 20$. In the captions of Figs. 5.5, 5.6, 5.7, and 5.8, we denote the number of vertices and the number of triangles by f and k, respectively.

We then repeat the calculations for a triangular shape of the relief and an angle of inclination of 30°. When the width of the calculated region R_q varies from 10 to

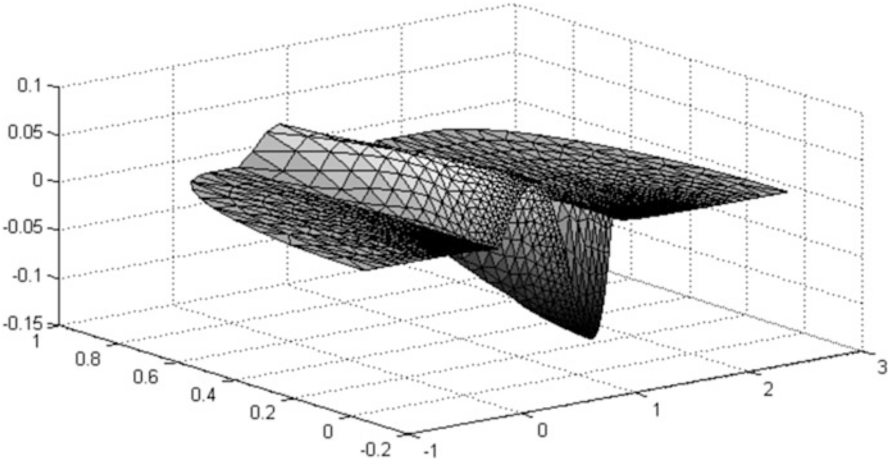

Fig. 5.4 Distribution of secondary sources on the surface of a relief in the form of a shaft

25, the relative change in apparent resistivity is no more than 1.5%. Figure 5.7 shows that grinding (i.e., subdividing) the mesh with a number of layers of triangles greater than $i = 30$ does not lead to any noticeable changes in the solution. Therefore, the value $N = 30$ is acceptable for most calculations. However, the maximum relative deviation between the apparent resistivity calculated for $N = 8$ and $N = 32$ is 3%. A change in N from 24 to 32 entails changes in ρ_a of not more than 2.03%. A change in α in the interval from 4 to 8 results an average change in ρ_a of no more than 2%. It follows that for the given relief shape and length of the measuring line at a slope angle of 30°, the calculation parameters $R_q = 10$, $\alpha = 8$, and $N = 32$ are acceptable.

One of the tests is to verify the principle of reciprocity for a four-electrode array. Another way of checking the algorithm is to load our simulation results into existing interpretation programs. If the interpretation program gives a homogeneous medium after the inversion of our computations, it provides an independent verification of our program. The results of such an experiment are discussed in Sect. 5.1.3.

Figure 5.4 shows the typical distribution of the $\mu(M)$ function over the relief surface shown in Fig. 5.3.

5.1.3 *The Influence of Different Relief Forms on the Results of Interpretation*

In this subsection, we discuss several examples of the numerical solution of the ERT problem for a homogeneous medium and for various forms of relief. We consider examples of anomalies that arise in a numerical solution related specifically to the relief. Preliminary test calculations for each form of the relief were performed to confirm that the result does not depend on the grid parameters. Here, we consider examples of the simplest typical forms of a relief, such as a shaft, a triangle valley, and a ledge. In the calculations, the geometric parameters of the relief, such as its angle of inclination and the height of the ledge, vary. For some of these options, examples of interpretation are given for the widely used interpretation programs Res2DInv and ZondRes2D. Numerical calculations have shown that the influence of the relief can lead to erroneous interpretation.

The apparent resistivity curves of VES for models of a relief with a negative triangular form for slope angles 10° and 20° are given in Fig. 5.6. It can be seen from the numerical results that the values of the maxima and minima of a curve of the apparent resistivity increase considerably with increase in angle.

Figures 5.5, 5.6, 5.7, 5.8, and 5.9 show the anomalies of the apparent resistivity for the relief forms listed above with angles of 10°, 20°, and 40°. The parameters of the grid were chosen for the most adverse case with a tilt angle of 40°. In this case, the level of anomalies is so great that it is necessary to use a rather small grid;

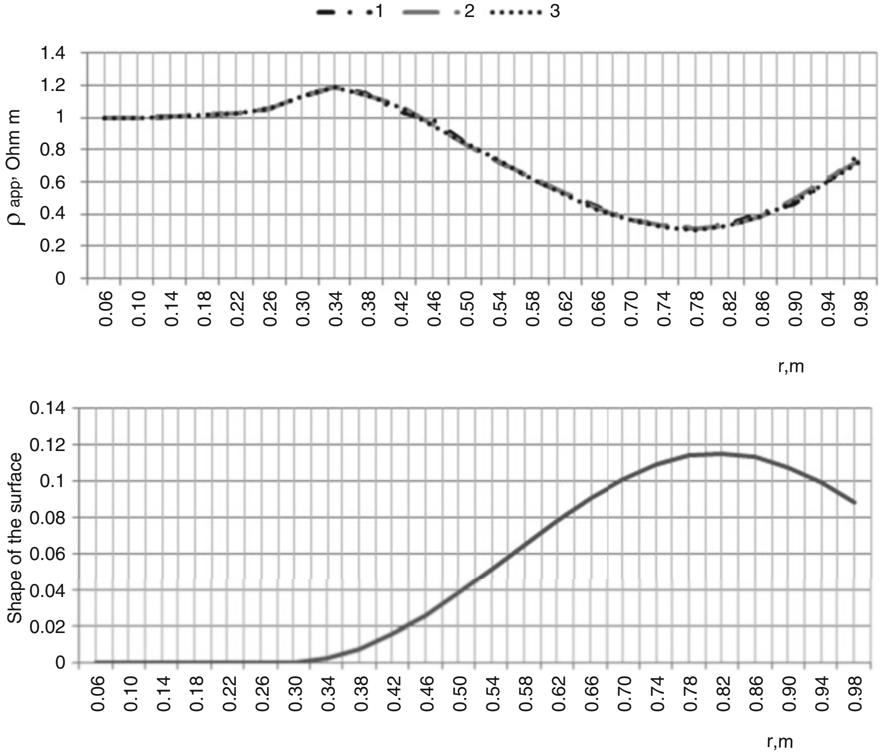

Fig. 5.5 Apparent resistivity curves and a relief form for different parameters: $N = 20$, $\alpha = 8.0$, $f = 993$, $k = 1844$ (*curve 1*); $N = 30$, $\alpha = 8.0$, $f = 2154$, $k = 4095$ (*curve 2*); and $N = 101$, $\alpha = 8.0$, $f = 23{,}103$, $k = 45{,}492$ (*curve 3*), where N is the number of layers of triangles, α is a parameter of the non-uniformity of the grid, f is the number of nodes, and k is the number of triangles

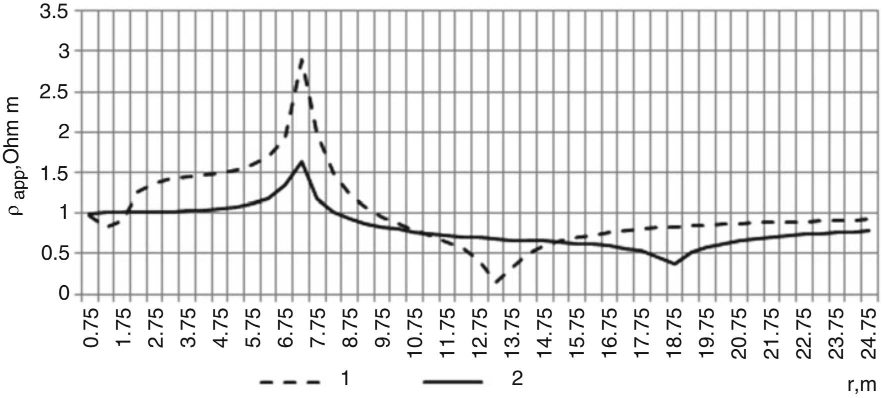

Fig. 5.6 Apparent resistivity curves for a three-electrode array where the model surface has negative shape of symmetrical triangle. The tilt slope angle is equal to 20° for *curve 1* and 10° for *curve 2*. The computational parameters are $N = 32$, $\alpha = 8.0$, and number of nodes $f = 12{,}366$

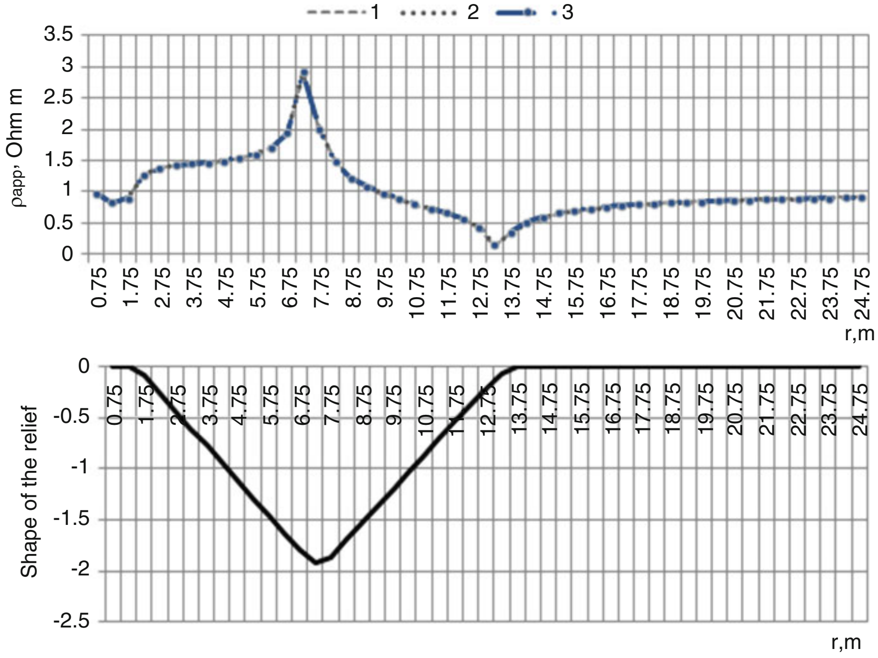

Fig. 5.7 A triangle form of a relief and apparent resistivity curves. The computational parameters for *curve 1* are $a = 10$, $N = 32$, $\alpha = 8.0$, number of nodes $f = 12{,}366$, number of triangles $k = 23{,}269$; for *curve 2*, $a = 15$, $N = 32$, $\alpha = 8.0$, $f = 10{,}580$, $k = 19{,}828$; and *curve 3*, $a = 25$, $N = 32$, $\alpha = 8.0$, $f = 8832$, $k = 16{,}465$

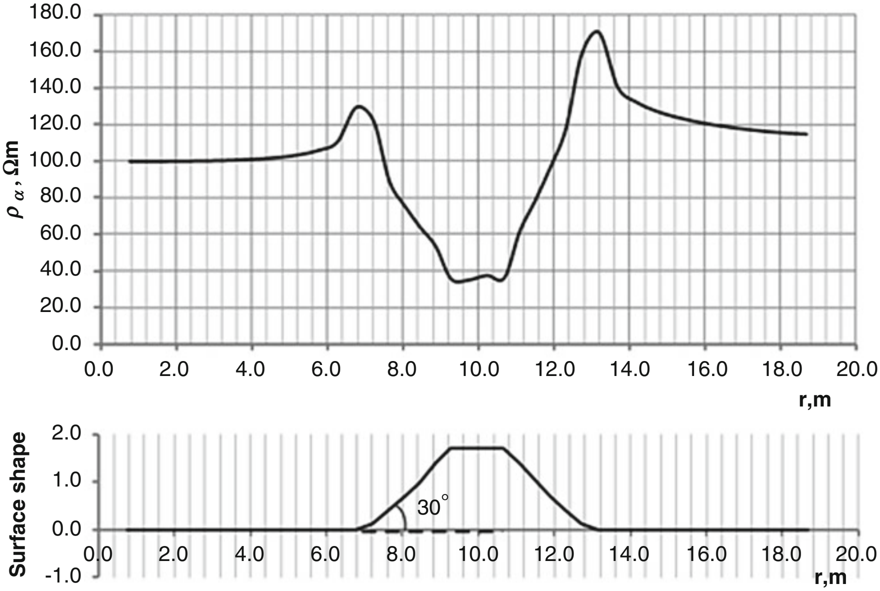

Fig. 5.8 Apparent resistivity curves and a relief form. The tilt slope angle is equal to 30°

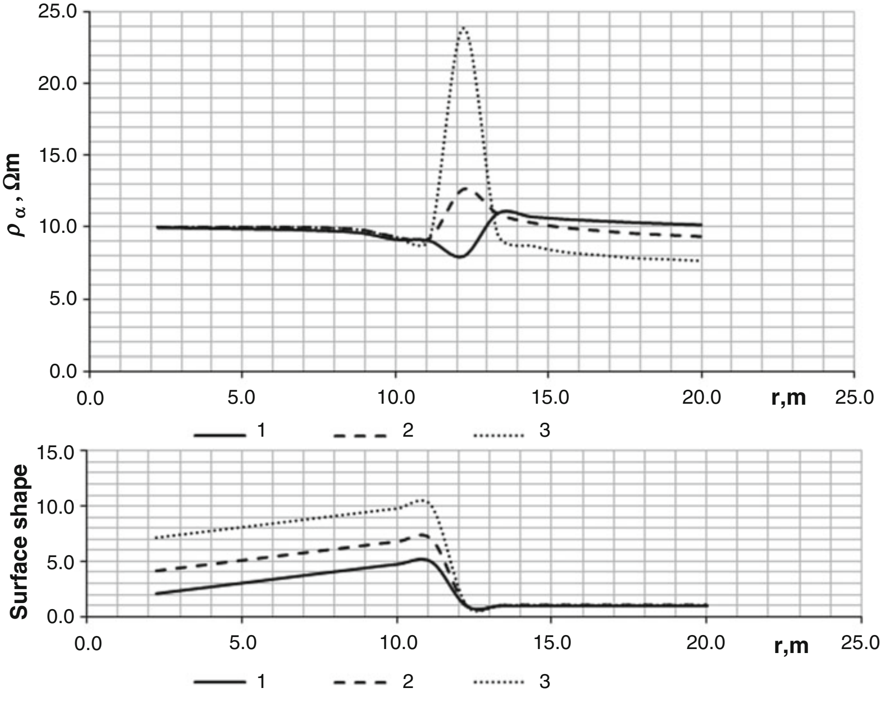

Fig. 5.9 Apparent resistivity curves and a relief form for tilt slope angles of 10° (*1*), 20° (*2*), and 40° (*3*)

otherwise, computing errors can result in wrong or negative values of the apparent resistivity curves.

After defining acceptable grid parameters, we performed numerous simulations; the obtained data were loaded into inversion programs. The influence of the shape of the relief on the interpretation can be seen from the results. Because the calculations were performed for a homogeneous relief, we expected that the result of the inversion would also show a homogeneous medium. In reality, different programs gave different results. Figure 5.10 shows a pseudo-section based on the simulation results for a homogeneous medium with a relief in the form of a shaft (Fig. 5.5).

Figure 5.11 shows an interpretation of the modeling of resistivity curves over the homogeneous medium executed by the Zon2DRes program for a relief with a slope angle of 20°. The results demonstrate that the interpretation was satisfactory only for small angles up to 20°; further increases in the angle caused artifacts that distorted the inversion result. The corresponding illustration is shown in Fig. 5.12. Note that this interpretation of the results of our calculations constitutes an additional test that verifies our algorithm. The most significant interpretation errors appeared when the interpretation was executed by the Res2DInv program (Fig. 5.13).

Both the Zon2DRes and the Res2DInv programs give satisfactory results for angles of less than 10°. Zon2DRes inverted the relief anomalies correctly up to a slope angle of 20°. The larger the angle is, the worse the interpretation results. The deviation from the uniform distribution of resistivity shown by the interpretation can be as great as 50% of the true value (even for the Zon2DRes program) when the slope angle of a relief reaches 40°.

Based on the numerical simulation, we arrived at the following conclusion: If the shape of the relief under consideration differs significantly from the forms that were checked in the numerical experiments, then for each relief form it is desirable to

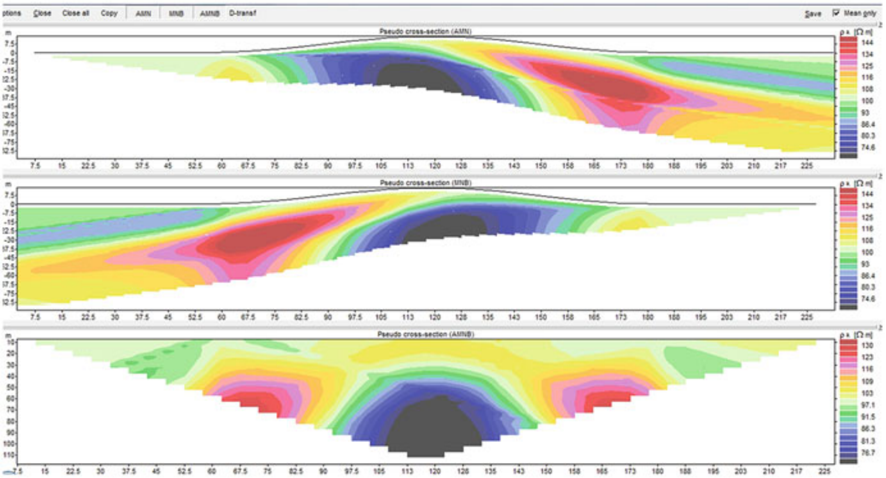

Fig. 5.10 Geoelectrical pseudo-section for a homogeneous medium above a relief with 20° inclination angle

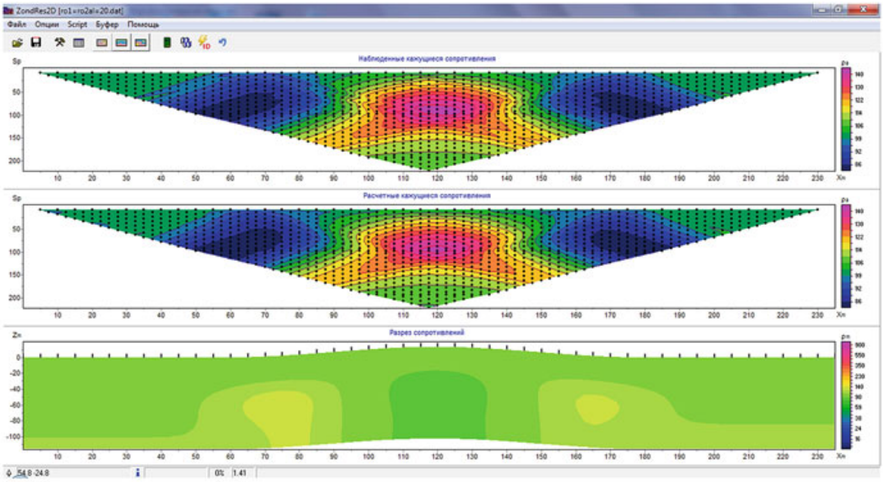

Fig. 5.11 Geoelectrical section obtained by the inversion program Zon2DRes for 20° inclination angle. A homogeneous medium was obtained

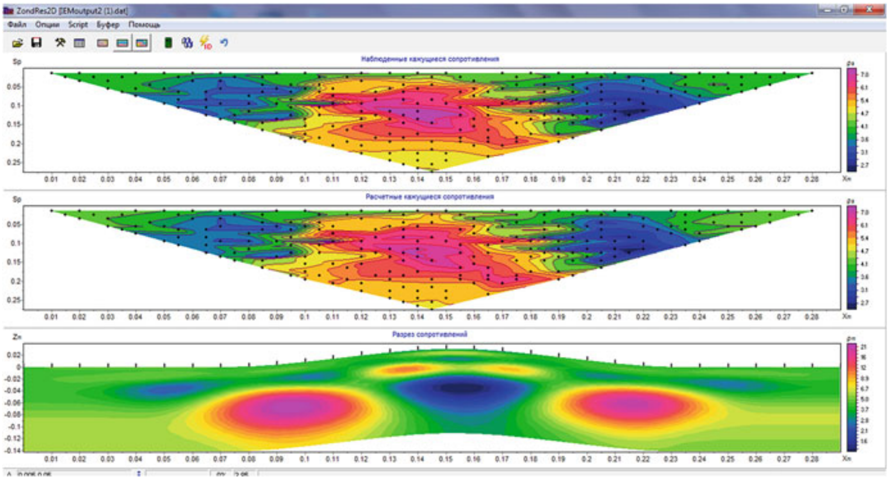

Fig. 5.12 Geoelectrical section obtained by the inversion program Zon2DRes for 40° inclination angle. Several artifacts distort homogeneity

conduct a series of experiments in which the parameters are R_q and N. This helps us to obtain stable results that do not depend on the nature of the triangulation or the size of the computational domain.

Based on the established computing parameters for each angle of inclination, it is possible to calculate the apparent resistivity in two different scenarios: (1) If the

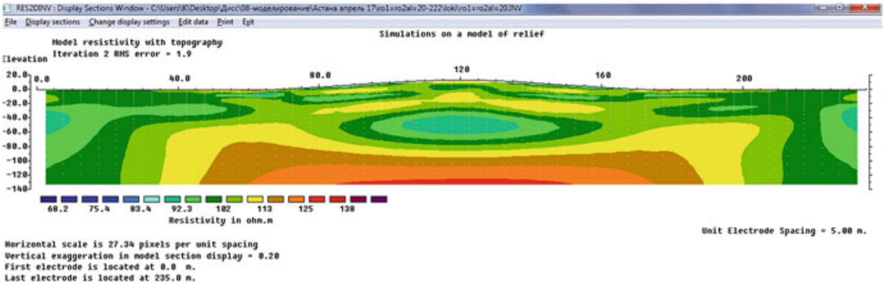

```
Simulations on a model of relief
Model resistivity with topography
Iteration 2 RMS error = 1.9
Unit Electrode Spacing = 5.00 m.
Horizontal scale is 27.34 pixels per unit spacing
Vertical exaggeration in model section display = 0.20
First electrode is located at 0.0  m.
Last electrode is located at 235.0 m.
```

Fig. 5.13 Geoelectrical section obtained by the inversion program Res2Dinv for 20° inclination angle. Several artifacts distort homogeneity

surface of the relief is smooth and the inclination angles do not exceed 20°, the parameters $R_q = 1$, $\alpha = 8$, and $N = 32$ are permissible. (2) If the surface contains high tilt angles and abrupt shape transitions, it is necessary to increase the computing area to $R_q = 10$, $\alpha = 8$, and $N = 60$. Despite the preliminary values of the recommended calculation parameters, it is desirable to perform additional modeling in which the calculation parameters (the number of layers of triangles and the size of the calculation area) are changed for each relief. It is preferable to use a high-performance technique with parallel computing, because the matrix arising in the BEM is dense and occupies a large amount of memory.

5.2 The BEM for a Two-Layered Medium with a Ground Surface Relief

5.2.1 Mathematical Model

In this section, we consider a medium with piecewise constant 2D distribution of electrical conductivity (see, for instance, Fig. 5.14). Let the medium comprise two layers with electrical conductivity coefficients σ_1 and σ_2 (corresponding to the specific resistances ρ_1 and ρ_2). Suppose the lower layer is disposed horizontally at h depth and the upper layer has an embossed surface. Let the form of the surface satisfy the conditions supposed in Sect. 5.1.1.

In practice, the voltage is applied to the medium through two source electrodes, designated A and B. However, by virtue of the principle of the superposition of electric fields, we consider only the potential created by a single point source A.

Let Γ_1 be a ground surface and Γ_2 the contact boundary of media with conductivities σ_1 and σ_2 (Fig. 5.14).

We look for a potential field sought as the sum of the simple layer potentials:

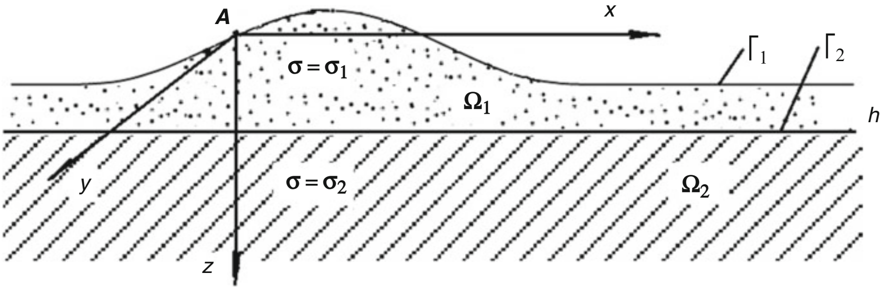

Fig. 5.14 Model of a two-layered medium with ground surface relief. See text for description of the symbols

$$u(M) = \frac{I}{2\pi\sigma_1 R_0 \mid AP \mid} + \frac{I}{4\pi\sigma_1 R_0}\left(\iint\limits_{\Gamma_1} \frac{q_1(P)}{\mid MP \mid} d\Gamma_P + \iint\limits_{\Gamma_2} \frac{q_2(P)}{\mid MP \mid} d\Gamma_P\right). \tag{5.20}$$

The factor I/($\sigma_1 R_0$) appears here as the dimensional scale for the dimensionless functions of the simple layer potential. The integral terms in (5.20) correspond to the simple layer potentials of the densities q_1 and $q_{2.}$ According to the properties of the simple layer potential, $U(P)$ satisfies Laplace's equation in domain $\Omega_1 \cup \Omega_2$ except for borders Γ_1, Γ_2 and point A (Fig. 5.14). Function $U(P)$ is required to satisfy the boundary condition at inner boundary Γ_2 between two materials and on surface Γ_1 of the medium. The first of these conditions specifies the conservation of the current through the contact boundary and is written as

$$\sigma_1 \frac{\partial U}{\partial n}\bigg|_1 = \sigma_2 \frac{\partial U}{\partial n}\bigg|_2. \tag{5.21}$$

The indices $i = 1, 2$ mean that the normal derivatives are taken from the side of the medium with the corresponding value of the conductivity.

Now, we write (5.21) in terms of the simple layer potentials:

$$u_i(M) = \iint\limits_{\Gamma_i} q_i(P) \frac{d\Gamma_P}{\mid MP \mid}, \quad i = 1, 2$$

We take into account the discontinuity of the normal derivatives of the simple layer potential on different sides of the surface. The change in the normal derivative of the potential taken at the inside and outside of region Ω_2 is equal to the density of a simple layer multiplied by 4π (2.5). If the normal to the boundary Γ_2 is directed from medium 2 to medium 1, then

$$\left.\frac{\partial u_2}{\partial n}\right|_2 - \left.\frac{\partial u_2}{\partial n}\right|_1 = 4\pi q_2(M)$$

and the following equalities hold:

$$\begin{aligned}\left(\frac{\partial u_2}{\partial n}\right)_2(M) &= 2\pi q_2(M) + \iint\limits_{\Gamma_2} q_2(P)\frac{\cos\psi_{MP}}{|\,MP\,|}d\Gamma_P \\ \left(\frac{\partial u_2}{\partial n}\right)_1(M) &= -2\pi q_2(M) + \iint\limits_{\Gamma_2} q_2(P)\frac{\cos\psi_{MP}}{|\,MP\,|}d\Gamma_P.\end{aligned} \tag{5.22}$$

The derivatives of the simple layer potential at the second boundary are discontinuous, but the derivatives of the potential of the other sources remain continuous. Therefore, the continuity condition for a normal current passing through a surface Γ_2 is written as

$$\sigma_2\left.\frac{\partial u_2}{\partial n}\right|_2 = \sigma_1\left.\frac{\partial u_2}{\partial n}\right|_1 - (\sigma_2 - \sigma_1)\left(\frac{4\pi\sigma_1 R_0}{I}\left.\frac{\partial U_0}{\partial u}\right|_{\Gamma_2} + \frac{\partial u_1}{\partial n}(P)\right). \tag{5.23}$$

Substituting (5.22) into (5.23), we obtain

$$2\pi q_2(M) = \frac{\sigma_2 - \sigma_1}{\sigma_2 + \sigma_1}\left(\iint\limits_{\Gamma_2} q_2(P)\frac{\cos\psi_{MP}}{|\,MP\,|}d\Gamma_P + \frac{4\pi\sigma_1 R_0}{I}\frac{\partial U_0}{\partial n}(M) + \frac{\partial u_1}{\partial n}(M)\right).$$

Therefore, the following integral equation is obtained:

$$q_2(M) = \frac{\kappa}{2\pi}\iint\limits_{\Gamma_2} q_2(P)\frac{\cos\psi_{MP}}{|\,MP\,|}d\Gamma_2 + \frac{\kappa}{2\pi}\left(\frac{4\pi\sigma_1 R_0}{I}\frac{\partial U_0}{\partial n}(M) + \frac{\partial u_1}{\partial n}(M)\right). \tag{5.24}$$

Here, $\kappa = \frac{\sigma_2-\sigma_1}{\sigma_2+\sigma_1}$ denotes a reflection coefficient at the boundary between medium 1 and medium 2. Substituting the potential for source electrode A and $u_1(P)$ into expression (5.24), we obtain

$$\begin{gathered}q_2(M) = \frac{\kappa}{2\pi}\iint\limits_{\Gamma_2} q_2(P)\frac{\cos\psi_{MP}}{|\,MP\,|}d\Gamma_2 + \\ \frac{\kappa}{2\pi}\iint\limits_{\Gamma_1} q_1(P)\frac{\cos\psi_{MP}}{|\,MP\,|}d\Gamma_1 + \frac{\kappa}{\pi}\frac{\partial}{\partial n}\frac{1}{|\,MA\,|}, M\in\Gamma_2\end{gathered} \tag{5.25}$$

The boundary condition at the medium's ground surface is derived from the condition that other normal currents (with the exception of the current from the point source) do not flow into medium 1. Let us write the expression for the normal current that enters medium 1:

$$\frac{I}{4\pi}\left(\left.\frac{\partial u_1(M)}{\partial n}\right|_{\Gamma_1}+\left.\frac{\partial u_2(M)}{\partial n}\right|_{\Gamma_1}\right)+\sigma_1\left.\frac{\partial U_0}{\partial n}\right|_{\Gamma_1}=\frac{I}{2\pi}\delta(\mathbf{r}). \tag{5.26}$$

The current flowing into the medium is expressed in terms of the normal derivative of the potential, which is taken from the side of the medium. Due to the properties of the simple layer potential, the normal derivative of the potential has a discontinuity on the surface of Γ_1. Let the normal be directed outside of medium 1. The normal derivative at the inner side of the surface is expressed as

$$\left.\frac{\partial u_1(M)}{\partial n}\right|_{\Gamma_1}=2\pi q_1(M)+\iint\limits_{\Gamma_1} q_1(P)\frac{\cos\psi_{MP}}{\mid MP\mid}d\Gamma_1(P) \tag{5.27}$$

Substituting (5.27) into (5.25), we obtain

$$\left(2\pi q_1(M)+\iint\limits_{\Gamma_1} q_1(P)\frac{\cos\psi_{MP}}{\mid MP\mid}d\Gamma_1+\left.\frac{\partial u_2(M)}{\partial n}\right|_{\Gamma_1}\right)+\frac{4\pi\sigma_1}{I}\left.\frac{\partial U_0}{\partial n}\right|_{\Gamma_1}=2\delta(\mathbf{r})$$

This yields another integral equation

$$\begin{aligned} q_1(M)=&-\frac{1}{2\pi}\iint\limits_{\Gamma_1} q_1(P)\frac{\cos\psi_{MP}}{\mid MP\mid}d\Gamma_1-\frac{1}{2\pi}\iint\limits_{\Gamma_2} q_2(P)\frac{\cos\psi_{MP}}{\mid MP\mid}d\Gamma_2\\ &+\frac{1}{\pi}\left(\delta(\mathbf{r})-\left.\frac{\partial}{\partial n}\frac{1}{\mid MA\mid}\right|_{\Gamma_1}\right), M\in\Gamma_1. \end{aligned} \tag{5.28}$$

Thus, we have two integral relations (5.25) and (5.28) for two unknown functions of the simple layer densities $q_1(P)$ and $q_2(P)$, defined at the ground surface Γ_1 and the contact boundary Γ_2, respectively.

5.2.2 *The Numerical Method*

The numerical solution of the system of integral equations is obtained by discretizing the integrals in (5.25) and (5.28). We limited the infinite surfaces Γ_1 and Γ_2 by their finite parts, which represent the regions of the oval shape. The boundary Γ_1 is mapped on the plane on which the irregular triangular mesh is constructed. The grid is condensed along the axis *Ox* at the part corresponding to the measurement line where the field potentials are computed. From the differences in the potential values along the profile, the apparent resistivity of the medium is calculated, as is customary in geophysical experiments.

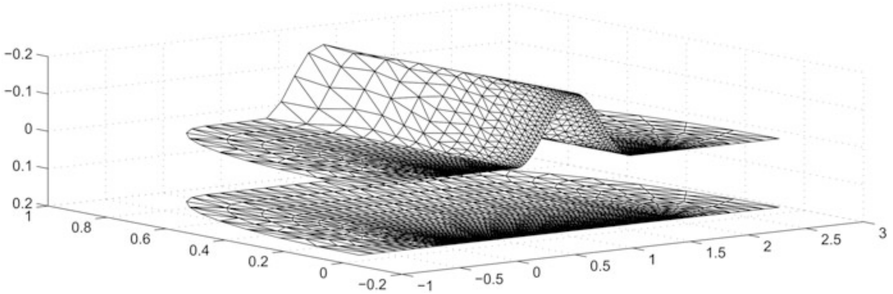

Fig. 5.15 Typical triangulation of the computed region (the positive z-direction is directed downward)

A typical triangulation of the calculations domain is shown in Fig. 5.15. The unknown functions $q_1(P)$ and $q_2(P)$ are computed at the nodes of triangulation. The integrals in the right-hand sides of (5.25) and (5.28) are approximated by using the values of the integrands at the grid nodes, taking into account the areas of the triangles.

Approximation of the integrals in (5.25) and (5.28) by their discrete analogs leads to the following system of linear algebraic equations:

$$q_i = \frac{\kappa_{1,2}}{2\pi} \sum_{j=1}^{N} q_j A_{ij} + \frac{\kappa_{1,2}}{\pi} B_i, \quad i = \overline{1, N} \tag{5.29}$$

Here, N is the total number of triangulation nodes at external and internal borders Γ_1 and $\Gamma_{2,}$; the factor $\kappa_{1,2}$ depends on the type of boundary to which the node belongs. If the node is at $\Gamma_{1,}$ the coefficient is 1; otherwise, it is equal to the value of reflection coefficient κ. Values A_{ij} represent the coefficient of mutual influence of points i, j. Values A_{ij} are formed by expressing integrals in discrete form. The system of (5.29) can be solved both by direct methods and by iterative methods. Both of these methods have been checked to verify that the solution does not depend on the choice of solution method.

Testing of the calculation algorithm was conducted using two methods: checking the implementation of the “reciprocity principle” for four-electrode array AMNB sounding and comparing the results of calculations with known solutions for a two-layered medium.

5.2.2.1 Test 1: Reciprocity Principle

In modern ERT equipment, the roles of electrodes as measuring or source electrodes can be exchanged in different experiments. Thus, it is possible to diversify the types of measuring electrode arrays available without large monetary expenditures. To optimize the switching of equipment and accelerate measurements in geophysics, the principle of reciprocity is applied. Based on this principle, the potential difference between the points MN, measured by some AMNB array, does not change if the roles of the pairs AB and MN are changed to make the source electrodes measuring electrodes and make the measuring electrodes source electrodes. Therefore, it is possible to reduce the number of measurements by changing the roles of the electrodes and using the principle of reciprocity.

To test our algorithm, the reciprocity principle was verified numerically. Let $k = 0,\dots, K$ be a series of equidistant positions of electrodes on a measuring line of length L. Assume that the source and sink electrodes A and B occupy the positions $k = 0$ and $k = 1$. Then, numerical experiments for A and B give the values of potential difference ΔU_{ij} between electrodes M_i, and M_j, $i = 2,\dots, K - 1$; $j = 2,\dots, K - 1$. If electrodes A and B are now located in positions M_i and M_j, $i = 2,\dots, K - 1$; $j = 2,\dots, K - 1$ in another series of experiments, the potential difference between the electrodes with numbers 0 and 1 should be equal to ΔU_{ij} obtained in the previous experiment.

This test was conducted using a four-electrode array by exchanging the source electrodes (A, B) with the pair of measuring electrodes (M, N) and calculating the potential difference between the points M and N. The value of K was set at 25. Calculations were made for the source electrodes A and B for two cases: (a) placed at positions 0 and 1; and (b) placed at positions 4 and 5. In the first case, the successive positions of the measuring electrodes M_i, M_{i+1} were considered. Then, the roles of the electrodes were changed, placing A and B at the points M_i and M_{i+1} and calculating the potential difference ΔU_{01} between the positions 0 and 1. The average relative difference between the obtained values ΔU_{01} and $\Delta U_{i,i+1}$ for the potential difference did not exceed 2%. The left part of Fig. 5.16a, b shows the sequence of values ΔU_{ii+1}, $i = 2,\dots, K - 1$ for the positions of source electrodes 0 and 1. The right-hand part of Fig. 5.16a, b plots the results obtained when the source electrodes (A, B) were exchanged with the measuring electrodes (M, N).

The same procedure was executed for the calculation of the second test (case b) for the position of the source electrodes A and B at positions 4 and 5. In contrast to the first case, the potential difference between the electrodes M_0M_i, $i = 1,\dots, K$ was computed excluding the values $i = 4, 5$. The experiments were then conducted by exchanging the roles of the pairs AB and MN.

The relative deviation of the respective values of the potential difference in the second test did not exceed 2%. Thus, both tests demonstrated the implementation of the principle of reciprocity. The test results of case (b) are shown in Fig. 5.16c, d.

Thus, the tests show the implementation of the principle of reciprocity in our numerical models.

5.2.2.2 Test 2: Two Horizontally Layered Media

A numerical solution of the system (5.29) was tested on a known solution for a two-layered medium (Koefoed 1979). The results are presented in Fig. 5.17a, b. The calculations were made for the three-electrode system AMN for a two-layered

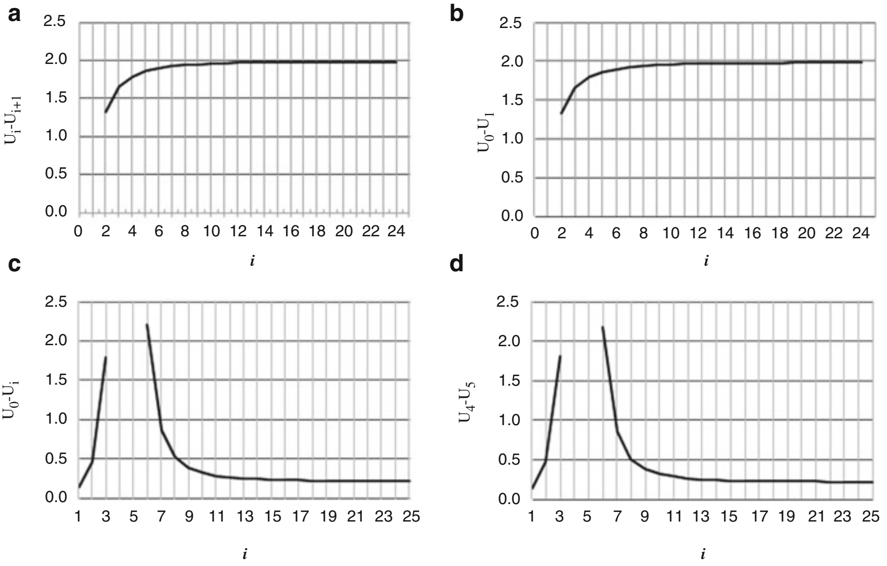

Fig. 5.16 (**a**) Potential differences $U_i - U_{i+1}$, depending on i (number of positions of MN). (**b**) Potential difference $U_A - U_B$ after exchange of the roles of AB and MN with A placed at 0 and B placed at 1. (**c**) Differences of potential $U_0 - U_i$ depending on i (number of positions of N). (**d**) Difference of potential $U_4 - U_5$ in the exchange of roles AB and MN; A is placed at 0; i is the position number of B. (Reproduced from Mukanova et al. 2017)

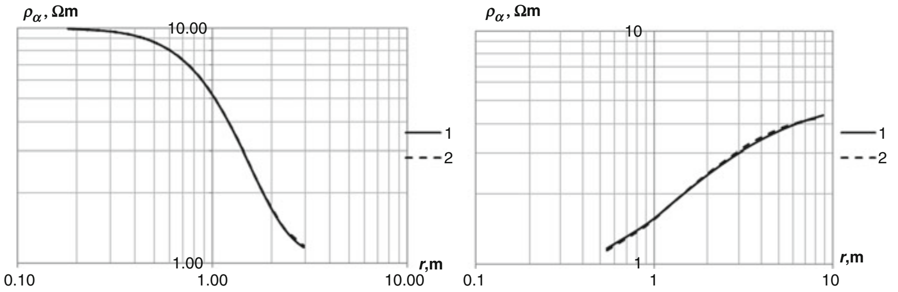

Fig. 5.17 The function of the apparent resistivity for models with a conductive base (left) and a high-resistivity base (right). *Curve 1* is a solution built by Koefoed (1979); *curve 2* is a solution obtained by solving the system (5.29). (Reproduced from Mukanova et al. 2017)

medium model with a flat surface with a high-resistivity base ($\rho_1 < \rho_2$) and a conductive base ($\rho_1 > \rho_2$).

The influence of the depth of the second layer was checked for both decreasing resistivity and rising resistivity models. The maximum relative error in calculations of the apparent resistivity was not greater than 2%.

This test allows us to determine the admissible dimensions of the computational domain and the degree of thickening of the mesh necessary to achieve the desired accuracy of approximately 1–2% in the apparent resistivity function.

5.2.3 *Influence of a Second Layer on the Measured Data and Inversion Results*

It was found that, if the resistivity of the second medium is less than that of the first, the size of the computational region can be less than if the second medium has a resistivity substantially (~100×) larger than the first. In the calculations, a certain length scale was used as the unit of length, and all the geometric parameters of the model (height of the relief, depth of the second layer, and length of the measuring profile) are expressed in this unit. The symmetry with respect to the abscissa axis is taken into account, allowing the number of nodes of the mesh to be halved. The resistivity of the first medium is used as a unit of resistivity. For instance, in the case of $\sigma_2 = 10\sigma_{1,}$ the dimensions of the oval, which has been triangulated, are equal to 4×2. Here, the length of the line along which the grinding of the mesh is conducted is equal to 2, and the number of nodes at this line varies over the range 200–300. The mesh was expanded when removed from the central line. If the expansion coefficient is 8 (i.e., if the size of the largest cell is approximately eight times greater than the size of the smallest cell), these parameters are consistent with the number of triangles, or approximately 16,600. For media with $\sigma_2 = 0.001\sigma_1$, the dimensions of the computational domain are 9×6, with 320 points on the condensation line and a condensation coefficient equal to 25. The total number of nodes in this case is approximately 10,400. The calculation time for the iterative method does not exceed 1 min on a personal laptop, whereas a direct method of solving a system of linear equations requires approximately 40 min.

Figure 5.18a, b show solutions of the system of integral equations for the shape of the relief, which is given analytically by the following formula:

$$z(x) = \begin{cases} 0.06\left(\cos\left(2\pi(x+0.25)\right)-1\right), & -0.25 \le x \le 0.75 \\ 0, & x \notin [-0.25, 0.75] \end{cases}$$

In this case, the relief has a shaft shape, as shown in Fig. 5.14, with the underlying layer at a depth of $z = 0.5$ and a conductivity $\sigma_2 = 10\sigma_{1.}$ The discontinuity at one point of the solution in Fig. 5.18a corresponds to the point of application of the pointwise source electrode.

The shape of the surface relief and the apparent resistivity, calculated along the profile with length equal to 2 and placed in a direction transverse to the relief, is shown in Fig. 5.19.

To determine the effect of the relief on the sounding curves, the results of numerical simulation for a two-layered medium with a relief of the ground surface were considered. Numerical simulations were made for reliefs in the form of a shaft

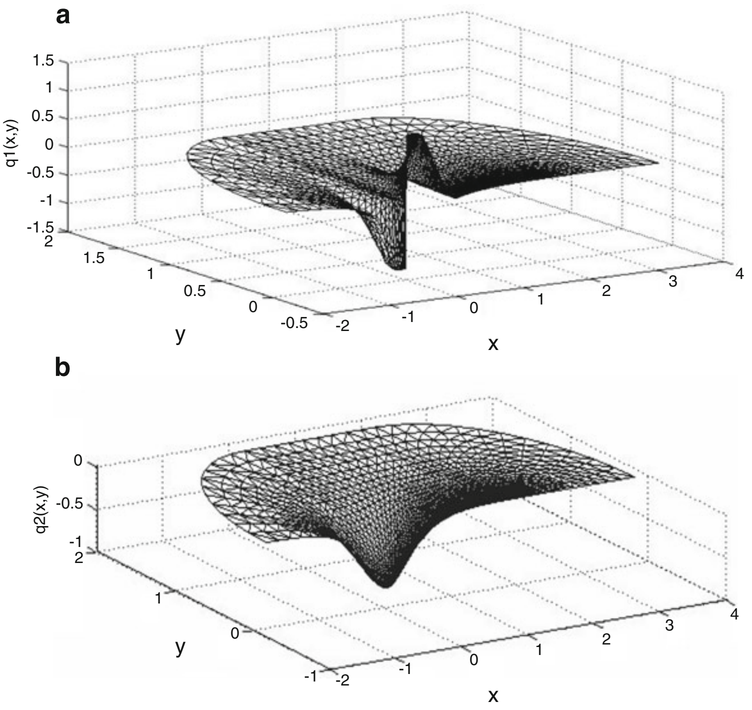

Fig. 5.18 (**a**) Distribution of the density of a simple layer $q_1(P)$ at the surface Γ_1. (**b**) Distribution of the density $q_2(P)$ at the surface Γ_2

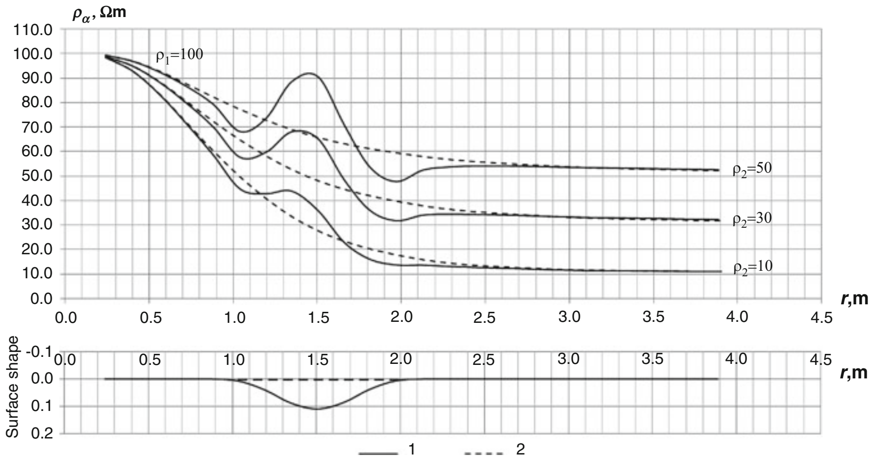

Fig. 5.19 The shape of the surface relief and the apparent resistivity curves for a model of a two-layered medium with a relief (*1*) and for a model of a two-layered medium with a horizontally plane surface (*2*). (Reproduced from Mukanova et al. 2017)

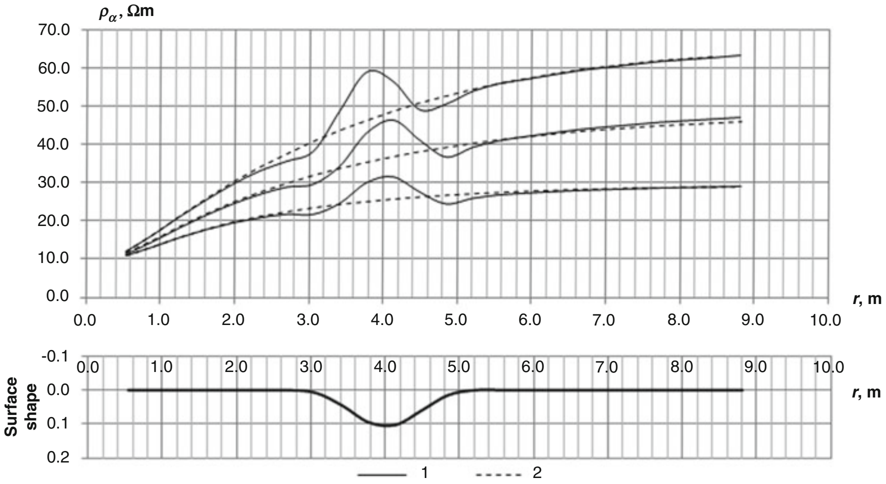

Fig. 5.20 Surface relief shape and apparent resistivity curves for a model of a two-layered medium with a relief (*1*) and for a model of a two-layered medium with a horizontally flat surface (*2*). (Reproduced from Mukanova et al. 2017)

(Fig. 5.12) and a valley with an underlying layer at a depth of $h = 0.5$. To determine the effect of the resistivity of the underlying layer on the apparent resistivity (ρ_a) anomaly associated with the relief, we performed the calculations by changing the resistivity values of the underlying layer for models with conductive and high-resistivity bases.

Figure 5.19 shows the simulation results for a medium with a conductive underlying layer with the relief of the ground surface in the form of the valley and without relief (horizontal plane) for resistivity values $\rho_2 = 10, \quad 30, \quad \text{and } 50\ \Omega\text{m}$ of the underlying layer. The resistivity of the first layer is set at $\rho_1 = 100\ \Omega\text{m}$.

The simulation results for the same medium with a higher resistivity basis for the values of the resistivity of the upper layer $\rho_1 = 10\ \Omega\text{m}$ and the underlying layer $\rho_2 = 30, \quad 50, \quad \text{and } 70\ \Omega\text{m}$ are shown in Fig. 5.20.

Figures 5.21 and 5.22 show the results of calculations similar to those performed in the previous models, but for the relief in the form of a shaft (Fig. 5.13).

The depth of the second layer, h, also influences the sounding curves. To study the influence of the depth of occurrence of the second layer, we performed numerical simulations on a two-layered medium with a relief for different values of h. Figure 5.23 shows the simulation results for values $h = 0.25$, 0.5, and 0.75 m for a decreasing resistivity model where $\rho_1 = 100$ and $\rho_2 = 10\ \Omega\text{m}$.

For all cases, the obtained apparent resistivity curves go to the asymptotic values of the second layer ρ_2. Evident anomalies are present in the vicinity of the irregularities of the relief. The vertices of convexity or concavity of the relief form are marked at the sounding curves with a minimum or a maximum, respectively. It should be noted that in the case of a relief in the form of a valley, the anomalies are

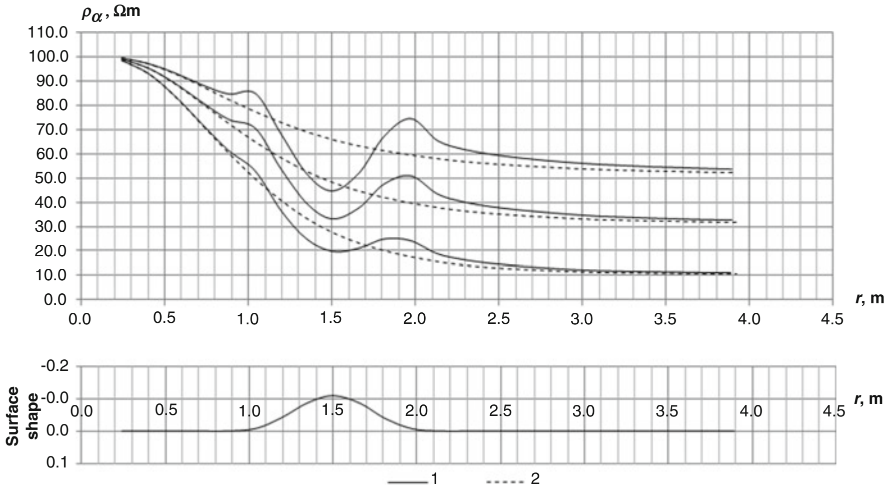

Fig. 5.21 Surface relief shape and apparent resistivity curves for a two-layered medium with a horizontally flat surface (*1*) and for a two-layered medium with a relief (*2*). (Reproduced from Mukanova et al. 2017)

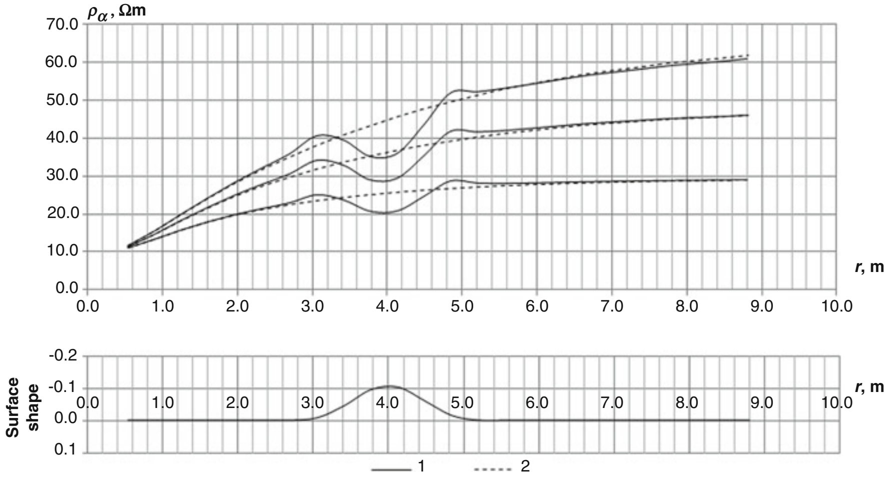

Fig. 5.22 The shape of the surface relief and the apparent resistivity curves for a model of a two-layered medium with a relief (*1*) and for a model of a two-layered medium with a horizontally plane surface (*2*). (Reproduced from Mukanova et al. 2017)

more pronounced than in the case of a relief in the form of a hill. We also note that when performing numerical calculations to reach the asymptotic values of the second layer for the model with a high-resistivity base, the computational domain was set to twice that for the model with a low-resistivity base.

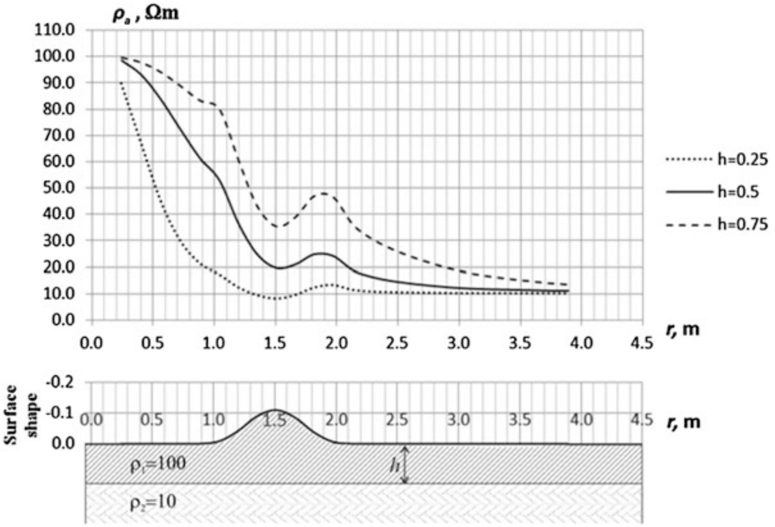

Fig. 5.23 Influence of the occurrence depth (h) of the second layer on the apparent resistivity curves. (Reproduced from Mukanova et al. 2017)

Calculations show that the apparent resistivity anomalies associated with the relief are more pronounced when the resistivity of the underlying layer is smaller than that of the upper layer and when the lower layer is closer. Conversely, if the underlying layer has a resistivity that is much higher than that of the upper layer, the influence of the relief is less pronounced.

To define the influence of the relief on the inversion results, we calculated apparent resistivity curves for a relief form similar to that depicted in Fig. 5.14. Numerical simulations were performed for the following parameters: length of the measuring line ($AB = 235$ m), number of electrodes ($K = 48$), depth equal to the height of the relief ($h = 20.9$ m), elevation angle (40°), resistivity ($\rho_1 = 100$ and $\rho_2 = 10$ Ohm m), and MN (5 m). The forward problems were solved for both three-electrode arrays, AMN and BMN. The successive positions of the electrode arrays correspond to common practice for ERT: source A moves from left to right, and B moves in the opposite direction in steps of MN. The pseudo-section obtained for the listed parameters is shown in Fig. 5.24.

The synthetic data shown in Fig. 5.24 were entered into 2D resistivity imaging programs. We applied the programs Res2DInv and ZondRes2D. The inversion results obtained from the data by Res2DInv and ZondRes2D are depicted in Figs. 5.25 and 5.26, respectively. As can be seen in Figs. 5.25 and 5.26, the influence of the relief yields distortions in the interpretation data, especially in the Res2DInv program. In the case of the inversion program ZondRes2D and for the considered example, the distortions are less expressed (Fig. 5.26). Indeed, the similarity of the original model and the inversion results shown in Fig. 5.26 serve as an additional verification of our numerical method.

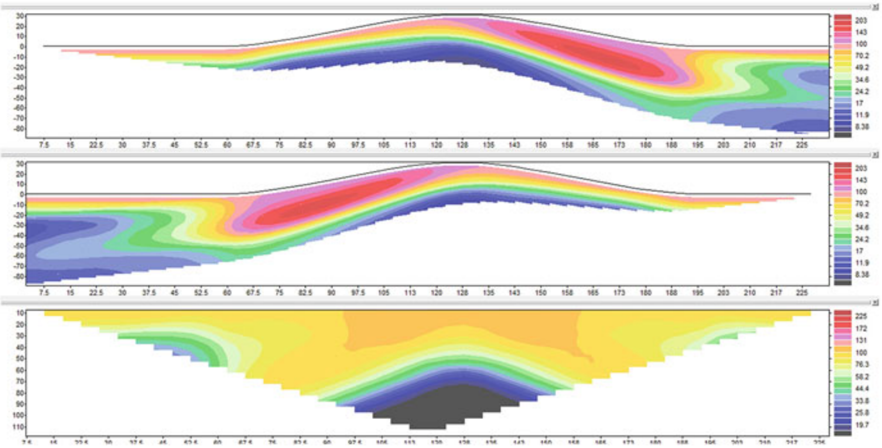

Fig. 5.24 Pseudo-section calculated for a model of a two-layered medium with ground surface relief

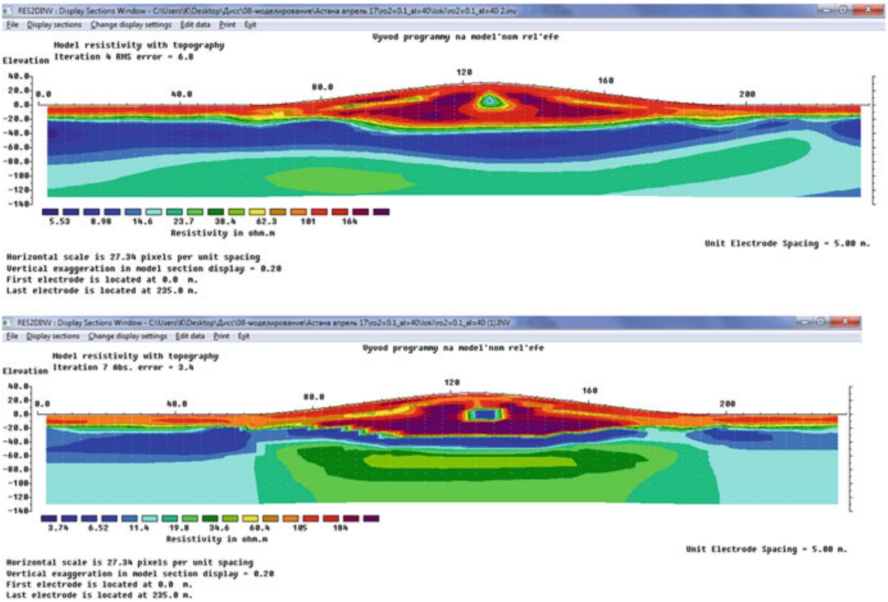

```
Vyvod programmy na model'nom rel'efe
Model resistivity with topography
Iteration 4 RMS error = 6.8
Unit Electrode Spacing = 5.00 m.
Horizontal scale is 27.34 pixels per unit spacing
Vertical exaggeration in model section display = 0.20
First electrode is located at 0.0  m.
Last electrode is located at 235.0 m.
```

```
Vyvod programmy na model'nom rel'efe
Model resistivity with topography
Iteration 7 Abs. error = 3.4
Unit Electrode Spacing = 5.00 m.
Horizontal scale is 27.34 pixels per unit spacing
Vertical exaggeration in model section display = 0.20
First electrode is located at 0.0  m.
Last electrode is located at 235.0 m.
```

Fig. 5.25 Interpretation data obtained by the program Res2DInv for a model of a two-layered medium with ground surface relief

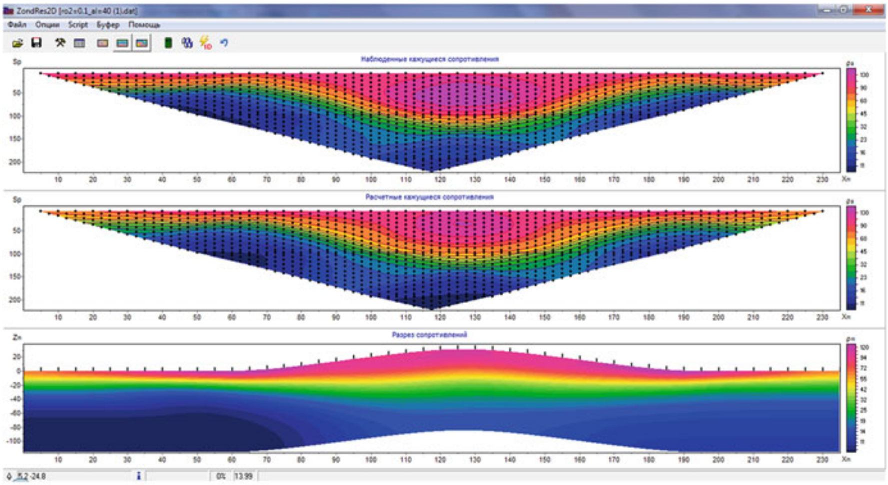

Fig. 5.26 Interpretation data obtained by the program ZondRes2D for a model of a two-layered medium with ground surface relief

5.3 The BEM for 3D Media: Influence of the Third Coordinate on Measuring Data and Interpretation Results

As noted above, the derivation of integral equations for the 3D case does not differ from the 2D case; therefore, it is not described here. The system of equations for the case of a two-layered medium with a 3D surface relief and an underlying layer has the same form as (5.25) and (5.28) of the previous section.

5.3.1 Triangulation and Approximation of the Ground Surface

For the numerical solution of the system of integral equations, the relief of the surface must be approximated. In the examples considered in this section, the algorithm for solving the integral equation of the ERT survey above a homogeneous medium with a relief of the surface is realized for analytically defined relief shapes. In practical applications, the relief parameters are determined by the step along the profile (the distance between electrodes) and by the height of the localization of the electrodes placed along the investigated profile; the parameters are measured under field conditions. A surface relief function is constructed based on this data. This function must satisfy the requirements necessary for the numerical realization of the method of integral equations. First, for each point of the surface, the normal to the surface must be defined; in addition, at intermediate points, it is necessary for the function not to have discontinuities or large gradients. As shown by Zaporozhets

(1938), the presence of jumps on the surface leads to the appearance of large parasitic anomalies on the sounding curves, a situation that is highly undesirable for further interpretation. For numerical simulations, the most favorable case is that in which the surface can be represented by a single formula in the form of a smooth function with a very simple form. Then, we must ensure the condition of strict approximation; that is, our surface must pass through the given points (heights).

For 2D inversion data, there are many methods for approximating the shape of the relief specified from the experiments. However, for the 3D case, the choice of methods is not large. Let us remark on that subject. Assume that we want to approximate the surface in the form of a linear combination of some basis functions:

$$Z(x, y) = \sum_{i=1}^{n} \lambda_i \varphi_i(x, y)$$

It can be shown that for any set of basic functions $\{\varphi_i(x, y)\}_{i=1}^{n}$, $(n > 1)$ there are many different points $\{(x_i, y_i)\}_{i=1}^{n}$ such that the linear system of equations for determining the coefficients becomes singular. This result is called the Haar theorem. The problem can be solved if a basis composed of shifts of one basic function symmetric with respect to the center is used as an interpolating function. This approach was first used by Hardy (1971), who called it the method of radial basis functions (RBFs). This method was applied to the mapping problem when it was necessary to construct a continuous function that represents a surface based on a set of scattered measurements of the heights of a set of points on a topographic surface. From our point of view, RBFs are the best choice for describing the surface relief and for the subsequent application of BEM in the 3D case. The use of RBFs for the approximation of multidimensional surfaces was proposed and applied by Broomhead and Lowe (1988). We will not dwell on a description of the method but simply recommend its application.

5.3.1.1 Triangulation of a 3D Surface

Another algorithmically difficult problem is the construction of a triangulation of the surface so that the vertices are condensing in the vicinity of the measuring line, grid nodes are placed equidistantly between electrodes, and the electrodes are located in the grid nodes. Triangulation should be conducted for an arbitrary shape of the relief given from the actual measurements.

With the use of RBFs, we can achieve a uniform surface description using an analytically defined function. Therefore, without considering the question of the approximation of the relief, let us consider the problem of constructing a triangulation on a 3D surface. Suppose, however, that the surface is such that it satisfies the conditions of the theorems outlined in Chap. 4.

Thus, we can represent the surface $z = Z(x, y)$ as a sufficiently smooth function of two variables (x, y). We now describe the main ideas of the triangulation of the computational domain that we have used in our simulations.

First, the whole computing area is constructed so that its projection onto the *Oxy* plane forms an oval made up of two semicircles and a rectangle, as in Fig. 5.2. The triangulation is then constructed layer by layer, beginning with the triangles closest to the measuring line. Let the projection of the measuring line AB on the *Oxy* plane form the segment [0, $L_{\max}$] on the *Ox* axis. The very first layer of nodes is placed on the measuring line with some step $h_q{}^0$. This step is chosen so that the measuring electrodes fall into the grid nodes. The length of the measuring line is set equal to 2 in dimensionless variables. The location of the nodes on the relief is determined in a similar manner as in Sect. 5.1 for each cross-section of the relief by the plane $y = y_j$. The Cauchy problem for the ODE for each plane curve formed by the intersection of the surface Γ with the plane $y = y_j$ is solved by the Runge–Kutta method:

$$\begin{aligned}
&dq = \sqrt{dx^2 + dz^2} = \sqrt{1 + Z'^2\left(x, y_j\right)}dx,\\
&\frac{dx}{dq} = \frac{1}{\sqrt{1 + Z'^2\left(x, y_j\right)}}, \quad q \in [q_{i-1}, q_i]\\
&q_0 = 0, q_i = q_{i-1} + h^j_{\text{й}}\\
&x(0) = 0,\\
&x(q_{i-1}) = x_{i-1}
\end{aligned} \tag{5.30}$$

In this way, we define the grid nodes such that their projection on the plane *Oxy* is located in a rectangle $y \in [-R_q, R_q]$, $x \in [0, L_x]$. The grid step h^j_q on each layer is increased so that the grid is uniform in logarithmic coordinates. To construct a grid on semicircles, the grid nodes are arranged layer by layer at the intersection of the surface Γ with cylinders of radius $r_j = |y_j|$ These curves are given by parametrization

$$x(t) = -r_j \sin t, \;\; y(t) = r_j \cos t, \;\; t \in [0, \pi]$$

on the left semicircle and by

$$x(t) = r_j \sin t, \;\; y(t) = r_j \cos t, \;\; t \in [0, \pi]$$

on the right semicircle.

The following ODEs determine the Cartesian coordinates of the surface points on the semicircle:

$$\begin{aligned}
&dq = \sqrt{dx^2 + dy^2 + dz^2} = \sqrt{r_j^2 + Z_x^2(x(t), y(t)) \cos^2 t + Z_y^2(x(t), y(t)) \cos^2 t}dt,\\
&\frac{dt}{dq} = \frac{1}{\sqrt{r_j^2 + Z_x^2(x(t), y(t)) \cos^2 t + Z_y^2(x(t), y(t)) \cos^2 t}}, \quad q \in [q_{i-1}, q_i]\\
&q_0 = 0, q_i = q_{i-1} + h_i^j\\
&t(0) = 0,\\
&t(q_{i-1}) = t_{i-1}.
\end{aligned} \tag{5.31}$$

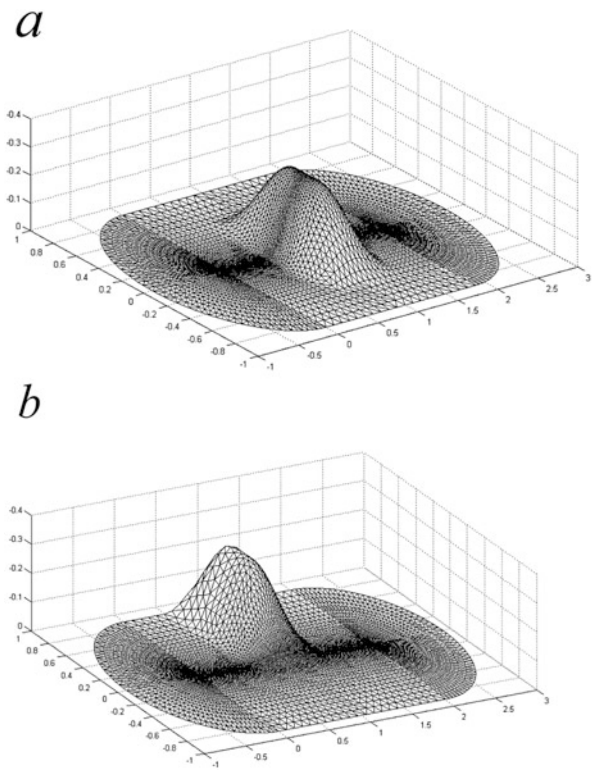

Fig. 5.27 Triangular mesh at the models of the 3D surface for the measuring line (**a**) passing along the symmetry line of the relief and (**b**) shifted in parallel

The solution of (5.31) determines the parameter t for each grid value of the curvilinear coordinate q. This coordinate has the meaning of the length of the curve measured along the intersection of the surface with a cylinder of radius $|y_j|$ for each semicircle on the projection of the oval. The Cartesian coordinates of the triangulation nodes are calculated using the parameter t. After determining the positions of the nodes, triangles are constructed on them. Figure 5.27a shows an example of the triangulation constructed in such a way for the case in which the measuring line passes along the axis of symmetry. Fig. 5.28 shows the corresponding example of a numerical solution, that is, the distribution of the densities of a simple layer on a triangulation of boundaries Γ_1 and Γ_2. The calculation parameters are as follows: the second layer is flat; the resistivities are 10 and 1 Ohm for the first and second layers, respectively; the angle of the relief is 40°; and the relief shape is set analytically in the form $z = f(x)\, g(y)$, where the functions $f(x)$ and $g(y)$ are given by the following expressions:

$$f(x) = \begin{cases} A\,(\cos\,(\pi^{-1}(x - x_0)) - 1), & x \in [x_0, x_0 + 1] \\ 0, & x \notin [x_0, x_0 + 1] \end{cases}, \qquad (5.32)$$

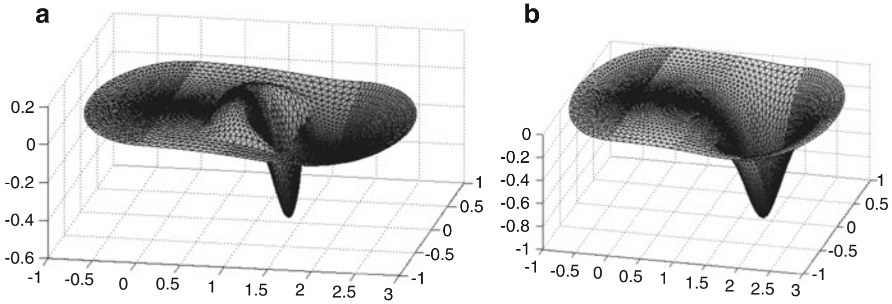

Fig. 5.28 Distribution of simple layer densities at the outer (*Figure* **a**) and inner (*Figure* **b**) boundaries

$$g(y) = \begin{cases} 1, & y \in [-a, a] \\ 0, & y \in [a+\Delta, \infty] \cup [-\infty, -a-\Delta], \\ g_1(y), & y \in [-a-\Delta, -a] \cup [a, a+\Delta] \end{cases} \tag{5.33}$$

Here, function $g_1(y)$ is constructed to ensure the smoothness of the relief. We took a polynomial of the second order for $g_1(y)$.

As a test, in this case it is convenient to compare the solution with those obtained for the 2D relief and for two-layered media with horizontal interfaces. These tests were performed successfully.

5.3.2 Numerical Results

Figure 5.27b shows examples of the triangulation and solution of the system of integral equations (5.25) and (5.28) for a 3D surface in which the measuring line does not pass through the center of symmetry.

To see how the modeling results are affected by the presence of the third coordinate, it is better to consider a homogeneous relief. For this, it is sufficient to set $\rho_1 = \rho_2$ in the program. We considered the relief given in the form $Z(x, y) = f(x)\, g(y)$ by (5.32) and (5.33). The value of x_0 is set equal to zero, the height of the relief is determined through the given angle of inclination, the width of the relief along the x-axis is equal to one dimensionless unit, and the width along the ordinate axis is specified by the parameters $a = 0.1$ and $\Delta = 0.2$. The total width of the relief along the ordinate axis is $2(a + \Delta)$ units.

To test the program, we simply compared the results with those obtained for the program described in the previous section for 2D relief. When the width of the relief was close to the size of the computing area, the results coincided with the 2D case.

The results showed that if the width of the relief is comparable to half the measuring line, then the difference between the apparent resistivity for the 2D case

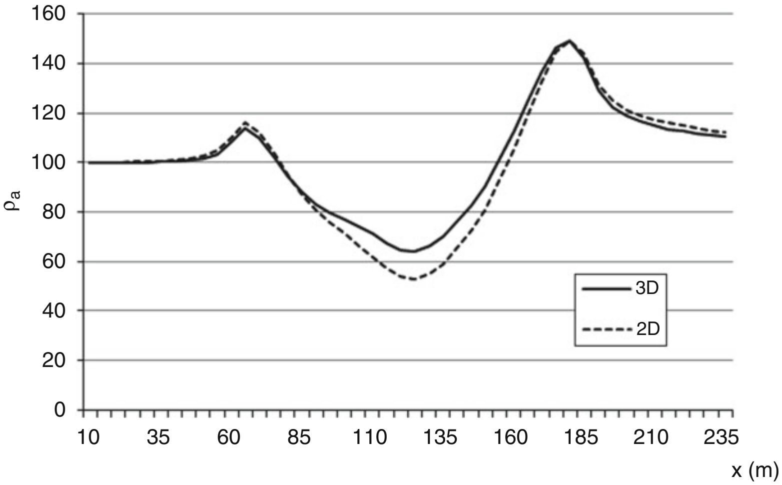

Fig. 5.29 Influence of a third coordinate on symmetrical 3D relief

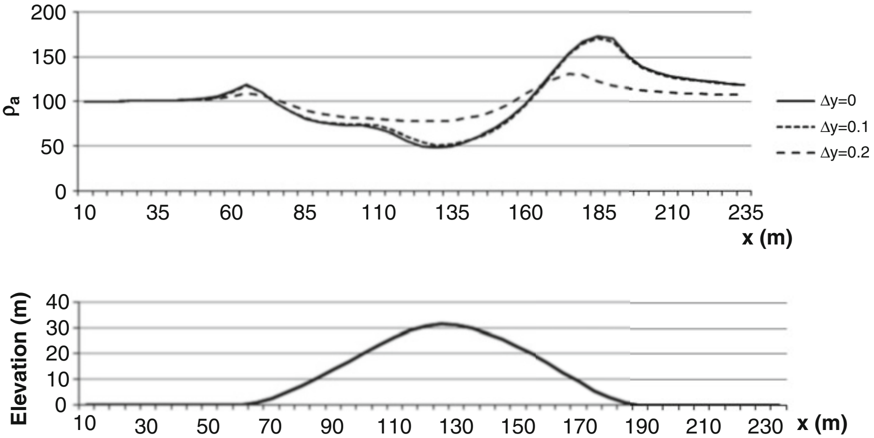

Fig. 5.30 Apparent resistivity curves obtained for a relief angle of 40°and for different values of the shift Δy

and the 3D case is greater than 10% (Fig. 5.29). In this model, the angle of inclination is equal to 30°.

The dependence of the apparent resistivity on the third coordinate y is more clearly expressed if the measuring line does not pass along the symmetry line of the relief but is shifted in parallel. Fig. 5.30 shows the apparent resistivity curves obtained for a relief angle of 40° and for different values of the shift Δy of the measuring line parallel to the axis of symmetry Ox.

In the case shown in Fig. 5.30, at $\Delta y = 0.2$ the line passes the relief along a flat base; however, the apparent resistivity curves “sense” the presence of the relief nearby.

References

D.H. Broomhead, D. Lowe, Multivariable functional interpolation and adaptive networks. Complex Syst. **2**, 321–335 (1988)

R.L. Hardy, Multiquadric equations of topography and other irregular surfaces. J. Geophys. Res. **76** (8), 1905–1915 (1971)

O. Koefoed, *Geosounding principles: resistivity sounding measurements* (Elsevier, Amsterdam, 1979)

T. Mirgalikyzy, B. Mukanova, I. Modin, Method of integral equations for the problem of electrical tomography in a medium with ground surface relief. J. Appl. Math. (2015)

B. Mukanova, T. Mirgalikyzy, D. Rakisheva, Modelling the influence of ground surface relief on electric sounding curves using the integral equations method. Math. Prob. En., Article ID 9079475, (2017). https://doi.org/10.1155/2017/9079475

V.M. Zaporozhets, Vliyaniye rel’yefa na rezul’taty zamerov soprotivleniy (Ed. S.G. Komarov and L.P. Gorbenko), Elkgr, 4(12) (1938)

Conclusions and Future Directions of Research

In this monograph, we discussed the modeling of direct ERT problems with the help of the IEM and the BEM. Media with a piecewise-constant electrical conductivity distribution were considered. Our results show that this method can be applied to media with a complex internal structure and surface relief. We considered problems stated for 2D and 3D media structures. In all cases, the electrical field generated in a medium is 3D. The BEM demonstrates a high efficiency in this type of field computation. Numerical simulations showed that the apparent resistivity anomalies associated with relief lead to distortions of the interpretation results when using 2D inversion programs. Modeling using the BEM allows one to estimate the level of false anomalies that appear due to the presence of topography. Numerical modeling is necessary for accurate account of the effect of topography on the results of vertical electrical sounding due to the very large electric field anomalies over the topography. These anomalies can exceed 100–200% of the background level. Under these conditions, a small software imbalance of inversion may lead to false anomalies in the geoelectric section. Further research should be conducted on the calculation of the effects of relief in field experiments and on models for more complicated media structures. Consequently, the elimination of false interpretation results and anomalies produced by topography must rely on future solutions.

Numerous problems have not been discussed in the framework of the methods considered here. In particular, we did not consider the mathematical problems of the IEM related to media in which the relief and the boundaries of the media are angular. Several years ago, in collaboration with A. G. Yakovlev, the author (Prof. I. Modin) showed that the density of an electric charge increases as the point approaches an angular point. However, the total charge cannot grow to infinity; thus, the singularity near an angle is at least integrable. Therefore, to correctly calculate the electric field near the corner points, it is necessary to thicken the grid. Meanwhile, under real conditions, there are absolutely no ideal sharp angles; as a result, an anomaly of an

B. Mukanova, I. Modin, *The Boundary Element Method in Geophysical Survey*,
Innovation and Discovery in Russian Science and Engineering,
https://doi.org/10.1007/978-3-319-72908-4

electric field does not grow to infinity. Although we did not discuss the construction of a triangulation scheme adapted to the kinks and corner points of contact boundaries, such a construction is quite feasible in the framework of the ideas outlined here.

The reduction of a 3D problem to a 2D problem via a Fourier transform (Section 4.1) was solved in a sufficiently general form for media with planar internal boundaries. However, mathematical questions regarding the correctness of the Fourier transformation were not discussed. In addition, we did not dwell on the problems of the Fourier transform using discrete filters or the justification of this technique.

The questions that arise when solving these interpretation problems based on mathematical models formulated using integral equations remain open. Moreover, there are interpretation programs that provide smoothed results. Based on existing computational technologies, it is possible to approximate these data via a piecewise-constant conductivity distribution and even automate this process. Furthermore, on the basis of the ideas outlined here, it is possible to formulate direct ERT problems and, for the obtained model, to develop programs for their solutions. However, at the present time, we are not aware of programs that are capable of performing such computations.

The authors of this monograph are ardent supporters of both the IEM and BEM. This is because these methods are fundamentally different from the FDM and FEM, which are currently predominantly used by software developers to solve direct and inverse ERT problems, and because they can generate entirely different simulations.

In addition, the BEM is more economical in terms of its required computational costs for a large class of models; thus, the IEM program can solve such problems with a large margin of accuracy. This makes it possible to obtain solutions that are more adequate when solving inverse problems. As such, the artifacts in inversion results can be determined confidently. It is also possible to state with a high degree of confidence that the IEM produces fairly accurate solutions for curvilinear (non-planar) boundaries. Together with D. B. Yakovlev, one of the authors (Prof. I. Modin) tested the IEM on a hemisphere and on a submerged spherical inclusion (this problem was solved analytically by A. I. Zaborovsky). For this purpose, a special program called SFE1DR was developed. The corresponding tests of the method exhibited a high accuracy and effectiveness.

The numerical simulation methods considered here showed high computational efficiencies, and they were adapted precisely for piecewise-constant distributions of the electrical properties of media. The described methods can be used to model 3D media containing complex structures. The principle of constructing a grid adapted to the relief and measuring equipment can be useful for the development of different programs and applications in geophysical practice.